Enhancing the function of iPS-derived neurons: implications for disease modelling.

PhD thesis by David Rushton

Student no. 0930549

Supervisors:

Prof. P. J. Kemp

Prof. N. D. Allen

DECLARATION

This work has not been submitted in substance for any other degree or award at this or any other university or place of learning, nor is being submitted concurrently in candidature for any degree or other award.

Signed …… (candidate) Date ……

STATEMENT 1

This thesis is being submitted in partial fulfillment of the requirements for the degree of ……(insert MCh, MD, MPhil, PhD etc, as appropriate)

Signed …… (candidate) Date ……

STATEMENT 2

This thesis is the result of my own independent work/investigation, except where otherwise stated.
Other sources are acknowledged by explicit references. The views expressed are my own.

Signed …… (candidate) Date ……

STATEMENT 3

I hereby give consent for my thesis, if accepted, to be available for photocopying and for inter-library loan, and for the title and summary to be made available to outside organisations.

Signed …… (candidate) Date ……

STATEMENT 4: PREVIOUSLY APPROVED BAR ON ACCESS

I hereby give consent for my thesis, if accepted, to be available for photocopying and for inter-library loans **after expiry of a bar on access previously approved by the Academic Standards & Quality Committee.**

Signed …… (candidate) Date ……

Table of Contents

Acknowledgments:

I would like to acknowledge my supervisors, Prof. P. Kemp and Dr. N. Allen, for their continued input and advice into my PhD, as well as other members of both labs for their help.

I would also like to acknowledge Prof. C. Svendsen for the kind gift of the iPS cell lines used in this study.

My PhD studentship was funded by the Medical Research Council (MRC) UK and mostly performed at Cardiff University. An MRC centenary award grant was also awarded which allowed me to briefly study at the Regenerative Medicine Institute at Cedars Sinai Medical Centre (Los Angeles USA) under Prof. C. Svendsen.

In addition to funding from the MRC, the Cure Huntington's Disease Initiative (CHDI) provided funding for this project.

Summary:

A critical deficit in many studies using iPS cell-derived neurons is the electrophysiological properties of these cells. Using short differentiation protocols this deficit is more significant, likely due to a lack of differentiated astrocytes in these cultures. As a strategy for combatting this deficit, this study utilises astrocyte secreted factors, in the form of astrocyte conditioned medium (ACM). ACM generated cultures of neurons producing spontaneous activity more reminiscent of neurons *in vivo* after only 3 weeks of differentiation. Further, this study finds that voltage activated Ca^{2+} currents are enhanced at a very early time point using ACM and these channels, along with $GABA_A$ receptors, are vital to neuronal functional maturation. This demonstrates an endogenous mechanism present in the early stages of functional development, where neurons exhibit excitatory responses to GABA which drive the activation of voltage activated Ca^{2+} channels. In addition to finding that astrocyte secreted factors evoke a gain of this endogenous, activity led mechanism for functional maturation, this study also investigates methods of enhance functional maturation by manipulating Ca^{2+} influx. However, in the absence of ACM, direct manipulation of this endogenous mechanism appeared limited by GABA becoming an inhibitory neurotransmitter as the cells functional matured. These strategies for enhance functional maturation are then assessed using iPS cell-lines generated for a Huntington disease study, finding that $GABA_A$ and increased Ca^{2+} concentration in the medium evoked both increased and more consistent functional properties in theses neurons at week 2. In addition to developing enhanced protocols for neuronal differentiation, a novel protocol for producing cultures of iPS cell-derived astrocytes in the absence neurons. These cultures could provide an invaluable tool, alongside iPS cell-derived neurons, for modelling neurodegenerative disease mechanisms in both cell types.

Chapter 1: Introduction

Pluripotent cells and disease modelling.

In vitro modelling of diseases provides a more rapid and easily manipulated platform for understanding disease mechanisms and developing testing potential therapies. However, tissues from patients with neurodegenerative diseases are unavailable for ethical and practical reasons. Therefore, we must look to other methods for generating human, disease specific tissues for *in vitro* modelling of neurodegenerative diseases.

The advent of induced pluripotent stem (iPS) cell technologies has opened new powerful opportunities for both disease modelling and drug discovery. The enormous potential of iPS cells comes from their ability to produce any cell type (pluripotency), combined with the ability to derive these cells from any individual [189]. Limited use has been made of human embryonic stem cell technologies to develop *in vitro* disease models, as it is necessary either to use very rare embryos which genetically carry the disease, or to manipulate genetically the cells at the individual gene level, or using nuclear transfer [27,83,87,188]. By contrast, iPS cells are now routinely generated from many healthy people and patients with genetic diseases, which allows comparisons between multiple wild-type and disease lines. Firstly, this provides a level of assurance that any findings in a dish are disease related and not abnormalities arising from each line's genetic background, or from the iPS reprogramming procedure. Secondly, experimental findings made in iPS cell lines can be related to clinical information of the patient, from which the cell lines were derived, potentially giving insight into different disease manifestations.

Focusing on neurodegerative diseases, many studies are now demonstrating disease-specific phenotypes, which can be observed across many disease-specific iPS cell lines and that correlate well with previous clinical and animal studies (table 1.1). IPS cell studies are both providing new insights into disease mechanisms and helping to confirm the relevance of pathophysiological mechanisms observed in other disease models. Further, using reliably observed disease-specific phenotypes as assays, iPS cell models provide novel cell platforms for high throughput drug screening. IPS cell models are also far faster and cheaper to use in drug discovery than animal models. They are more effective compared to standard high-throughput screening based on assay development in industry standard cell lines, such as

HEK293, HeLa or CHO cells. IPS cell-derived models provided unparalleled relevance and versatility.

Disease	Stressors	Assays	References
Huntington's	▪ Glutamate ▪ BDNF withdrawal	▪ Ca^{2+} dishomeostasis ▪ Caspase-9 activity ▪ Apoptosis	[218]
Parkinson's	▪ Hydrogen peroxide ▪ MG-132 ▪ 6- hydroxydopamine	▪ Caspase-3 activity ▪ Ubiquitin positive puncta ▪ Impaired mitochondrial Parkin uptake ▪ Increased PGC1-α expression ▪ Increased oxidative stress-related gene expression ▪ Increased α-synuclein expression	[25,139,173]
Rett syndrome		▪ CDLK5 expression ▪ Reduced synaptogenesis ▪ Altered electrophysiological characteristics ▪ Reduced neuronal cell soma	[3,119]
Spinal Muscular Atrophy (SMA) 1	▪ Valproic acid ▪ Tobramycin	▪ Nuclear gem numbers (SMN protein complexes)	[57]

		▪ SMN protein expression ▪ Reduced motor neuron population ▪ Reduced synapse number	
Disease	**Stressors**	**Assays**	**References**
Alzhiemer's	▪ docosahexaenoic acid	▪ Intracellular Aβ peptide aggregation ▪ BiP and Caspase 4 ▪ Expression studies for stress markers ▪ Reactive oxygen species generation ▪ Cell survival	[97]
Amyotrophic Lateral Sclerosis (ALS)		▪ TDP-43 protein aggregation	[24]
Familial dysautonmia		▪ Reduced neurogenesis ▪ Reduced neuronal migration ▪ IKBKAP splicing defect	[108]
Schizophrenia		▪ Reduced glutamate receptor expression ▪ Reduced neurite outgrowth ▪ Reduced PSD95 protein expression	[22]

Table 1.1: A list of iPS cell-derived models for neurodegenerative diseases which have reported disease-specific phenotypes.

The ideal approach for iPS-cell modelling of neurodegenerative diseases is to use a rapid and reliable differentiation protocol that produces functionally mature cells of the correct type, enabling disease-specific phenotypes to be readily observed. Whilst a disease may take many years (or decades) to manifest in patients, it has been found that disease phenotypes can be promoted in cell models by applying appropriate stressors (table 1.1 [24,25,218]). These stressors are most often based on disease-specific observations from previous models of the disease. For example, glutamate pulses and withdrawal of BDNF are used as stressors in Huntington's disease models (table 1.1 [218]). This system also provides the basis for rapid drug screening potential therapeutics [84]. Standardised protocols could be written to provide plates of iPS cell-derived neurons across multiple disease and wild type lines. Then, disease-specific stressors can then be employed to induce a disease phenotype and used as an assay for the potency of potential therapeutic drugs. This has the advantages of being fast and can be simultaneously used on many different patient derived cell lines. Therefore, by limiting further research to drugs found effective in iPS cell-derived models, it is possible to minimise the cost of animal testing to fewer, more promising drugs. Another fascinating feature of iPS cell-derived models being used for drug testing is that potential therapeutics can be tested for different causes and manifestations of each disease, allowing for new drugs to be targeted for different patients. This is particularly evident with many neurodegenerative diseases, as many are known to have multiple causes, for example Parkinson's disease, where iPS studies have thus far focussed on both PINK1 and LRKK2 mutations [25,139,173].

IPS cells are fundamentally capable of producing a powerful model system for drug discovery, since they can provide any cell type from any individual. However, to realise the full potential of this technology, there are still some hurdles to overcome. Firstly, methods for inducing pluripotency have required improvement, becoming more efficient and effective. Initially, iPS-cell reprogramming was performed using retroviral insertion of pluripotent factors, leaving a permanent new copy of these genes in the genome [189]. In theory, these genes should become inactivated during development; however, some studies have found this not to be the case resulting in some level of transcription of the reprogramming genes post-differentiation. This issue was solved by the use of non-integrating vector reprogramming techniques that have allowed cells to be reprogrammed

without leaving a permanent genetic mark on the cells [38]. However, even though epigenetic remodelling underpins the mechanisms of reprogramming and differentiation, significant differences are observed between iPS-cell lines and embryonic stem cell lines using whole-genome DNA methylation maps, which often correlate with the somatic cells from which they were reprogrammed [10,117,156]. This provides evidence for inconsistent gene-regulatory differences between iPS-cell lines and natural embryonic stem cells. Further, this perhaps explains observations that certain iPS-cell lines favour certain lineages, and could influence the functional properties of differentiated cells post differentiation, resulting in iPS cell line specific abnormalities [161]. This highlights the need to investigate diseases using multiple patient and wild-type iPS cell lines. Over time, reprogramming techniques and methods for assessing pluripotent stem cells are becoming more efficient and effective, allowing for more lines to be generated, more rapidly and with greater consistency.

This study is focused on the terminal differentiation and functional maturation of iPS cell-derived neurons, and it is here that we find other significant hurdles in iPS-cell technology. Firstly, an iPS-cell model requires cells of the correct type to be differentiated, ideally the correct mix of specific cell types typical of the tissue that is being modelled. In the case of neurodegenerative diseases, we would ideally produce a mix of the correct neuronal sub-types and glial cell types. However, many studies are finding only comparatively low yields of particular cell types, often after even very lengthy differentiation protocols [8,29,134,218]. Secondly, it is crucial that iPS-cell differentiation protocols generate cells that show mature functional attributes, which are necessary for these cells to form the basis of iPS cell-derived models that accurately recapitulate the correct neuronal tissue, and neurodegenerative diseases, in a dish. In particular, for models of neurodegenerative diseases to be informative, it is essential that iPS cell-derived neurons are electrophysiologically active and communicative through a synaptic network. These properties are critical to the function of neurons and also integral to the pathological dysfunction of cells in many neurodegenerative diseases. There have been a deluge of protocols developed for directed differentiation of different neuronal sub-types from iPS cells. However, largely these studies have focussed on generating cultures with a population of cells expressing cell markers with varying levels of specificity, starting with pan-neuronal markers, such as β3-tubulin and microtubule associated protein 2 (MAP2), followed by markers of specific neuronal sub-

types. Few studies have performed in depth analyses of the elecltrophysiological properties of iPS cell-derived neruons, and even more rare are studies where electrophysiological function used as a tool for differentiation protocol development[91,130,190].

Developing Neuronal differentiation protocols

Neuronal differentiation from iPS-cells occurs in 3 phases: neutralisation, differentiation and maturation. Neuralisation, is partial differentiation to produce neural progenitor cells, which are capable of differentiation to any cells within the neural lineage. Neuralisation is currently most efficiently achieved by inhibition of transforming growth factor β (TGF-β) and bone morphogenic protein (BMP) signalling, by targeting both the SMAD 2/3 and SMAD1/5/8 pathways, using small molecules [30,214]. These neural progenitor cells are then differentiated, resulting in the cells exiting the cell cycle and initially producing cultures of immature neurons.

Following differentiation, immature neurons must mature to develop the necessary machinery for functional electrophysiological activity and synaptogenesis. Key to these processes is the regulation of gene expression by the transcription factor, cAMP response element-binding protein (CREB). CREB activity is a central, and rate-limiting step in the multiple pathways which drive neuronal development, survival and synchronous functional integration [1,49,50,55,80,86,128,135,151]. CREB activity is regulated by serine phosphorylation at three sites (ser 133, ser 142 and ser 143). CREB phosphorylation determines its ability to bind to CREB-response elements (CRE) in gene-promoters, either as homo- dimers with itself, or as hetero-dimers with the closely related CREM (cAMP response element modulator) protein. CRE site occupancy then drives gene-regulatory changes in conjunction with other transcription factors [28,46,74,75,99,124,170]. Sustained ser133 phosphorylated CREB temporally correlates with the expression of immature, but postmitotic, neuronal markers (for example doublecortin and neuroD) and the loss of mitotic neural progenitor cell markers [68,80,86]. The expression of immature neuronal markers becomes replaced over time by mature neuronal markers involved in neurotransmitter release and synaptic function. These changes in neuronal marker expression correlate with a loss of stable CREB

phosphorylation and a switch to activity-dependent, transient CREB phosphorylation [72,80,86,128].

There are three well documented pathways that regulate the phosphorylation of CREB, and together these pathways integrate developmental and activity-dependent cell signalling as stimuli for differentiation, survival and electrophysiological maturation. Brain derived neurotrophic factor (BDNF) is a secreted neurotrophic growth factor which initiates terminal differentiation and is maintained to allow neuronal survival [37,90,103]. BDNF is a ligand for the tyrosine kinase B (TrkB) receptor, which upon binding initiates a protein kinase cascade leading to CREB phosphorylation. However, the TrkB receptor is also gated by cAMP, allowing for a second level of control of TrkB activity [21,90,149,174]. During development, neurons express different pools of adenylyl-cyclases which are differentially activated or inactivated by calcium influx through calmodulin and G-protein coupled receptor activity [42,77,121,172,184]. There is evidence to suggest that this cAMP gating increases the activity-dependence of neurotrophin signalling over time during maturation, due to changes in the expression of different adenylyl-cyclase isoforms [102,140]. Studies have shown that CREB phosphorylation is also stimulated by ionotropic neurotransmitter responses, including those elicited by glutamate and GABA [68,86,88,89,197,199]. Key to this mechanism is the influx of Ca^{2+} ions in response to neurotransmitter binding, which results in activation of calmodulin dependent kinases (CamK), which phosphorylate CREB [47,50,155,177,192,199]. Ionotropic glutamate responses directly result in calcium influx, since ionotropic glutamate receptors are cation channels, but ionotropic GABA receptors are ligand gated chloride channels. Voltage-activated calcium Ca^{2+} channels provide Ca^{2+} influx in response to membrane depolarisations, usually excitatory neurotransmitter responses. Therefore, GABA-dependant depolarisation is able to elicit Ca^{2+} influx indirectly by activation of voltage-gated Ca^{2+} channels. However, Cl^- currents are hyperpolarising in adult neurons, which would inhibit depolarisation instead of activating voltage activated Ca^{2+} channels. The direction of Cl^- currents in mature neurons is due to mature neurons highly expressing the potassium-chloride symporter 5 (KCC2), which co-tranports Cl^- ions out of the cell (driven by the outward K^+ gradient), compared to the potassium-sodium-chloride co-transporter 1 (NKCC1) which co-tranports Cl^- into the cell (driven by the inward Na^+ gradient). This difference in the expression of these two ion transporters maintains a Cl^- reversal potential more

polarised than the resting membrane potential [12,14,67]. However, due to changes of both NKCC1 and KCC2 expression during development, the Cl^- concentration gradient is augmented over time, resulting in Cl^- currents moving from depolarising to hyperpolarising compared to the resting membrane potential. This means that the response to GABA by immature neurons is initially excitatory, and capable of eliciting voltage activate Ca^{2+} channel activity in immature neurons.[67]. In addition to ionotropic neurotransmitter responses, metabotropic neurotransmitter receptors can also drive CREB phosphorylation [32,53,94]. G-protein coupled receptors increase cAMP production through the activation of adenylyl cyclases, this then stimulates protein kinase A (PKA) phosphorylation of CREB [52,128]. This provides a mechanism for metabotropic neurotransmitter receptors to influence CREB phosphorylation.

Studies on CREB-phosphorylation and CREB activity suggest that the integration of these pathways is not merely additive. It appears that CREB activity responds differently to tonic and transient neurotransmitter, or neurotrophin–dependant stimulation [89,128]. One potential distinguishing factor could be differential phosphorylation of different sites on the CREB protein. However, currently little is known about the mechanisms for phosphorylating the ser 142 and ser 143 sites [128]. Another factor influencing the different responses to tonic and transient neurotransmitter stimulation is that voltage activated Ca^{2+} channels inactivate during persistent depolarisation and ionotrophic neurotransmitter receptors desensitise with persistent neurotransmitter stimulation. Functionally, this means that a neuron must repolarise in preparation for further electrophysiological events, providing a short delay before the following Ca^{2+} influx. Therefore, the electrophysiological activity-dependent pathways to CREB phosphorylation will respond differently to transient and persistent stimulation.

CREB phosphorylation also appears to have different effects on neuronal functional development dependant on the developmental stage. This has resulted in sometimes conflicting results when studying the effects of CREB phosphorylation and synaptogenesis, as in one experiment it appears to inhibit a process that it later in development appears to promote[1,144,195]. It is unknown whether this disparity is primarily due to an increase in transient activity linked CREB phosphorylation, or loss of sustained CREB phosphorylation. It

is also unknown if differential phosphorylation of the different phosphorylation targets on the CREB protein are involved in this change. Importantly however, this allows CREB phosphorylation to orchestrate a synchronous development of functional maturation across multiple stages of functional maturation in neurons.

Neurotrophins, including BDNF, initiate neurogenesis though the activation of a protein phosphorylation cascade. During maturation, electrophysiological activity becomes a more important driving force for development in neurons, by providing Ca^{2+} influx and neurotransmitter response-dependant CREB phosphorylation. Critical to this mechanism are neurotransmitters and voltage activated Ca^{2+} channels. Evidence suggests, that immature excitatory GABA responses provide an important stimulus to sustain stable levels of phosphorylated CREB for neurogenesis [128]. The loss of stable phosphorylated CREB correlates well with the GABA-response switching from excitatory to inhibitory, and the appearance of NMDA receptor activity (a sub-type of glutamate receptor). Indeed, transient CREB phosphorylation in mature neurons is reliant on BDNF and glutamatergic synaptic drive stimulating action potentials [18,55]. At later developmental stages, very different responses to persistent glutamate stimulation are observed compared with transient stimulation. Synaptic glutamate receptors respond to transient synaptic glutamate release, providing depolarisation (excitatory post synaptic potentials, EPSPs) for action potential initiation. In addition to promoting electrical activity, these transient, synaptic glutamate responses provide Ca^{2+} influx, which promotes neuronal survival via CREB phosphorylation. However, persistent synaptic glutamate release also results in the activation of post-synaptic receptors. Further, by contrast to synaptic glutamate receptors, post synaptic NMDA receptor stimulation elicits Ca^{2+} dependent apopotosis, not survival[78,120]. This implies Ca^{2+} influx from different sources having different, or perhaps in some cases no, effect on CREB phosphorylation. However, during development it is entirely unclear when, or how, these different sources for Ca^{2+} influx come to evoke different responses.

Difficulties in synchronising the terminal differentiation of iPS-derived neural progenitor cells have resulted in long differentiation protocols, containing persistent progenitor cell populations, which results in inconsistent maturity in cultured neurons. One approach to address this problem has been to supplement differentiation media with the γ-secretase

inhibitor DAPT (N-[N-(3,5-Difluorophenacetyl)-L-alanyl]-S-phenylglycine t-butyl ester), in order to promote cell cycle exit by blocking notch-signalling. This has resulted in a more synchronous and faster initiation of terminal differentiation [20,138]. However, a second issue confounding terminal differentiation protocols has been the temporal separation of neurogenesis and gliogenesis. *In vivo,* neurons require significant influences from astrocytes to become fully functional (see introduction, Astrocytes and Neuronal Functional Development). Critically, astrocytes are instrumental in both the formation and maintenance of synapses [201]. Although neural progenitor cells are ultimately capable of producing both neurons and astrocytes, initially astrocytic genes are repressed by DNA methylation, making this fate choice impossible [96,180]. However, following a period of neurogenesis, a switch in progenitor cell fate is regulated by signals, including hypoxia, retinoic acid and notch signalling, and these signals induce the transcriptional regulators NFIA (nuclear factor 1 A-type) and CREB to release the methylation repression of astrocytic genes, allowing astrogliogenesis to ensue [6,31,36,62,180,182]. In many current differentiation protocols, there is a lengthy delay before a balance between astrocytes and neurons are observed in stem cell-derived cultures, and in short differentiation protocols very few astrocytes are observed [8,17,218]. Consequently, current differentiation protocols, in the short term, lack astrocytic influences on developing neurons. Therefore, introducing astrocytes or astrocyte secreted factors to the differentiation protocol could be an effective strategy for more rapidly inducing functional maturation in stem cell derived neuronal cultures. At present, no studies have found specific astrocyte secreted factors which can be added to a defined protocol which replicates the developmental influence of astrocytes (see Introduction, Astrocytes and Neuronal Functional Development).

By studying the electrophysiological characteristics of differentiating neurons treated with astrocyte-derived factors, we may better understand the mechanisms by which astrocytes influence neuronal development. Further, by understanding these mechanisms, and how they relate to other mechanisms in neuronal development, in which CREB appears central, we may be able to develop protocols which can be more directly influence functional development.

Astrocytes and neuronal functional development.

Astrocytes are the most abundant subtype of glia in the central nervous system. They are morphologically intricate and are continuously remodelling very fine projections armed with a plethora of receptors which surround neurons and capillaries. Astrocytes form highly organised tissues; an individual astrocyte is both responsible for and possessive of its microenvironment. Their constant morphological renovation and their diverse compliment of receptors gives astrocytes immense capacity for monitoring their microenvironments. Therefore, it is not surprising that the original idea that astrocytes only filled space and transported nutrients to neurons was a gross underestimation of the cell type's role. By contrast, it is now known that neurons and astrocytes are intimately and elaborately linked developmentally, functionally and metabolically [5,162,203].

Focussing on the influence of astrocytes on the functional development of neurons, many studies have shown that astrocytes facilitate neuronal maturation [203]. Studies using high resolution microscopy in hippocampal slices, have shown that astrocytes' projections closely interact with dendritic outgrowths from neurons and, through Eph-Ephrin signalling, drive morphological maturation and survival of dendritic spines whilst negatively regulating new immature dendrites [142]. Neurons *in vitro*, both stem cell-derived and *ex vivo,* demonstrate an excitable phenotype with somewhat polarised membranes and voltage activated currents. However, crucial to developing fully functional *in vitro* models, oftentimes very little synaptogenic activity is observed [69]. Indeed, alone, iPS-derived neurons *in vitro* produce few synapses, which is reflected by only few cells showing spontaneous activity. Co-culture of neurons with astrocytes has been shown to increase dramatically the formation and maintenance of fully functional synapses in many studies [154,200,201]. Further, studies have shown that astrocyte projections contact and interact with neurons *in vitro*, and through a protein kinase C dependant mechanism these increase dendritic puncta formation, expression of synaptic markers and generation of miniature synaptic currents [76].

As well as contact-dependant interactions, studies have also identified secreted factors from astrocytes that enhance and accelerate neurogenesis, neurite outgrowth and synaptogenesis in neurons. However, in stem cell derived cultures, the extent and mechanisms of their actions are not well understood [31,39,200]. Wnt3 is one such factor,

although involved in the patterning of the nervous system early in development, it has been found to be expressed in adult hippocampal astrocytes and plays a crucial role in hippocampal neurogenesis [112]. Another astrocyte secreted factor, thrombospondin 1A, has been found to be pro-synaptogenic when exogenously applied to neuronal cultures, but these synapses were found to be post-synaptically inactive, implying that thrombospndin 1A is alone is insufficient to produce active neuronal networks [40]. There is likely a large compliment of factors secreted by astrocytes which influence neurons in different ways, it is also likely that certain members of this cocktail are both region and situation specific. Therefore, choosing astrocytes from the correct region and developmental stage may be important if they are to be used to benefit neuronal cultures. However, astrocyte regional specification is currently very poorly understood [133]. Astrocytes may also change the panel of factors they secrete in response to certain events, for example brain trauma, which might be a feature expected of astrocytes which have been harvested by dissection [23,100].

To model accurately neurodegenerative diseases *in vitro,* it is of critical importance that functional synapses be developed and maintained in culture. These specific structures are an essential functional feature of mature neurons *in vivo*, and especially complex in the central nervous system. To this end, astrocyte secreted factors have been employed, in the form of astrocyte conditioned medium (ACM), as a strategy to enhance functional maturation and synaptogenesis in iPS cell-derived neurons using a full complement of astrocyte-secreted factors.

Electrophysiological properties of neurons.

Studying the electrophysiological properties of differentiated neurons is essential to producing accurate models for neurodegenerative diseases. There are many functional properties of neurons which, as a whole, allow neurons to both transmit and process information as part of neuronal circuits. Together, these functional properties form the complex, and diverse, electrophysiological phenotypes of neurons. These diverse features of neurons are also implicated in the pathophysiological mechanisms for many neurological diseases (see table 1.1). Therefore, studying in-depth the development of these features in iPS cell-derived models for neurodegenerative diseases is essential to assessing their validity as models. To this end, it is necessary for the development of better differentiation protocols which focus on producing more functional neurons. In addition to the mature function of these cells being absolutely essential to disease modelling, electrophysiological properties also play pivotal roles in the functional maturation of these cells due to the numerous links between electrophysiological activity, CREB phosphorylation and, ultimately, functional development.

Firstly, neurons must be capable of maintaining and manipulating the voltage across their membranes. Therefore, it is important to understand how ionic concentration gradients and ion channels are used by neurons to manipulate membrane voltage, using ATP as an energy source. In addition to setting the voltage across the membrane at rest, a cell must be able to produce action potentials, a moving wave of voltage-gated ion channel led depolarisation followed by repolarisation. Therefore, it is essential to understand the electrophysiological machinery required to produce action potentials using energy stored in ionic concentration gradients. Action potentials are important information carriers in neurons, and neuronal circuits. Therefore, fine tuning action potential propagation is required of neurons in the central nervous system to integrate many signals, forming the basis for information processing within neuronal circuits. It is important to understand how multiple electrophysiological parameters are woven together to augment the sensitivity of neurons to action potential generation, and how this information is passed between neurons at synapses.

Ion channels and the membrane voltage

Membrane voltage is fundamental to electrophysiological activity in neurons. Finely controlled changes in membrane voltage are essential for both transmitting and processing information across neuronal circuits. Therefore, understanding the electrophysiological parameters which cause and control membrane voltage is crucial to understanding how complex electrophysiological phenotypes arise in neurons.

Ionic concentration gradients are used to generate voltages. ATP is used to pump ions across the membrane to produce concentration gradients, thereby storing energy from ATP in the form of electrochemical potential energy.

Ion channels provide a conductance to ionic concentration gradients across the membrane, which by allowing a path for the current to flow allows the concentration gradient to apply a voltage across the membrane. The electochemical potential energy is slowly released by ion channels, producing a current through these ion channels. The reversal potential is the voltage required to oppose the electric field generated by the concentration gradient of an ion, resulting in no net current across the membrane for that ion. The reversal potential for the ion is calculated using the Nernst equation, and from this the driving force for the ion can be calculated (V_m - E_{ion}).

$$E_{ion} = \frac{RT}{zF} \cdot \ln \frac{[ion]_{out}}{[ion]_{in}}$$

The Nernst voltage equation, where: T is the absolute temperature (K), R is the ideal gas constant, z is the valence of the ion, F is the Faraday constant and E_{ion} is the reversal potential for that ion.

Ion channels are trans-membrane proteins with a channel pore through the membrane which conducts ions. They can show different levels of ion-selectivity and can be opened or closed based on different conditions, for example, the binding of a ligand molecule or voltage. Some of these ion channels are also rectifying, meaning they will only permit a current in one direction; this is electrically similar to a diode, but with no appreciable built-in potential.

The current across the membrane for an ion is proportional to the driving force for the ion (V_m-E_{ion}) and the conductance of the membrane to that ion (in accordance with Ohm's law). This has the effect that ion channels provide a larger current the further from the reversal potential for an ion the real membrane voltage is (also known as the larger the driving force). However, the gradient of this relationship between driving force and current is determined by the conductance of the ion.

Each ion channel has a single channel conductance that is relatively small, usually between 1 and 100pS. However, the membrane has many of each ion channel across the membrane that can all be considered in parallel, so the total conductance is the single channel conductance multiplied by the number of ion channels. We can model a single concentration gradient and ion channels as a battery, and represent the ion channels with a resistor (figure 1.1).

$$G_{total} = G_{single\ channel} \cdot Number\ of\ ion\ channels$$

$$R = \frac{1}{G} \quad \therefore \quad \frac{1}{R_{total}} = \frac{1}{R_{single\ channel}} \cdot number\ of\ ion\ channels$$

$$I = V \cdot G \quad \therefore \quad I = \frac{V}{R}$$

Top: the relationship between the total conductance across the membrane and both the number of ion channels and their single channel conductance. Middle: the relationship between conductance and resistance, and therefore the relationship between membrane resistance and both the number of ion channels and their single channel resistances. Bottom: Ohm's law with respect to current as a relationship with voltage, and either resistance or conductance. Note: conductance = G, resistance = R, current = I, and voltage = V.

In the case of a single ionic concentration gradient, this concentration gradient alone will determine the voltage across the membrane. However, a cell membrane maintains concentration gradients for Na^+, K^+, Cl^- and Ca^{2+} ions, with ion channels which conduct them. Therefore, all of these concentration gradients are providing currents through the membrane. The further from each ion's reversal potential the real membrane voltage, the

greater the driving force, and therefore the larger current for that ion. Therefore, it is the reversal potential and relative conductance of the membrane to each of these ions that determines the actual membrane voltage. This is because the relative conductance to each ion influences how much each ion's driving voltage contributes to the membrane voltage, by augmenting the magnitude of current generated by the ion with changes in driving force. We can model this using a batteries equal to the reversal potential for each ion, each in series with a resistor representing the conductance of the membrane to each ion, and then each of these in parallel (figure 1.1). Assuming the resistance to each ion was the same, we would observe a membrane voltage equal to the average of these voltages, as each concentration gradient (battery) would be contributing equally to the total voltage. However, where the ion channel resistances are different, then each ionic driving voltage will have different contributions to the total voltage by each battery (figure 1.1). The total voltage will be the sum of the battery voltages each weighted by the proportion of the total conductance which is in series with each battery. The total voltage is therefore defined by the following equation, for this model:

$$V_{membrane} = E_K \cdot \frac{G_K}{G_{total}} + E_{Na} \cdot \frac{G_{Na}}{G_{total}} + E_{Cl} \cdot \frac{G_{Cl}}{G_{total}} + E_{Ca} \cdot \frac{G_{Ca}}{G_{total}}$$

Where E_{ion} is the battery voltage representing each ionic gradient, G_{ion} represents the series conductance with each battery and G_{total} is G_{ion}. Note, this concept was well established before it's application in electrophysiology.

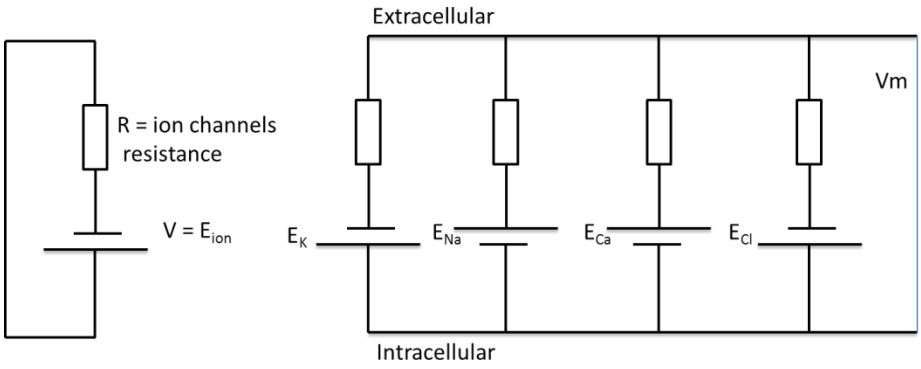

Figure 1.1: Developing models for membrane voltage dependant on each ions membrane conductance and reversal potential (driving voltage). On the left, an individual ionic

concentration gradient and conductance represented. On the right, all 4 of the major electrophysiologically active ions represented.

Using this model, we can understand how the membrane both maintains and manipulates membrane voltage. Firstly, the cell stores energy as concentration gradients to each ion across the membrane. These provide electric fields with different magnitudes and directions across the membrane; these can be used to control membrane voltage by manipulating the relative conductance to each ionic concentration gradient. Further, changes in membrane voltage can be enacted by altering the conductance of the membrane to these ionic concentration gradients by opening or closing ion channels.

To understand and model exactly how these concentration gradients and conductances function across biological membranes, it is necessary to consider the current across a biological membrane as the flux of charged particles in a concentration gradient. Therefore, is not as simple as modelling each ions contribution to membrane voltage as a constant voltage source applied over a resistor. There are two forces which drive flux (the movement of particles, in this case ions) across the membrane, which are: the diffusion of particles down a concentration gradient by pedesis, and secondly, the influence of an electric field on pedesis. Uncharged particles diffuse across a concentration gradient to result in a net flux towards areas of low particle density; this can be calculated using Flick's first law of diffusion.

$$J_{diffusion} = -\mu KT \cdot \frac{\Delta C}{\Delta X}$$

Flick's first law describing the flux due to the diffusion of a single uncharged particle with a single dimension concentration gradient. J is the particle's flux, D is the diffusion coefficient (D=μKT - μ = mobility, K = the Boltzman constant and T = absolute temperature), C is the concentration and X is the diffusion distance.

The addition of an electric field and charged particles influences this random motion, as it applies a vector force on any charged particle within the field, which scales linearly with the magnitude of the electric field. Ohm's law states, that the flux is proportional to the voltage

applied, the charge density of the ion in solution and the mobility of the ion in solution. The charge density of the ion in the solution is the valence of the ion, multiplied by it's concentration and the elementary electronic charge (z, c and e respectively). So, charge density multiplied by particle mobility (μ) and potential difference (E), give us a term for the flux due to an electric field (J).

$$J_{electrophoretic} = -\mu \cdot zce \cdot \frac{\Delta E}{\Delta X}$$

Flux due to the electric field: μ = mobility constant, E = potential difference, X = distance, z= ion charge, e = elementary electric charge and c = concentration.

This summation of these two forces is termed electrodiffusion, and the Nernst-Plank equation uses the summation of these two fluxes to calculate the total flux, accounting for both factors [60].

$$J = -\mu KT \cdot \frac{\Delta C}{\Delta X} - -\mu zce \cdot \frac{\Delta E}{\Delta X}$$

The Nernst-Planck equation. J= flux, μ = particle mobility, K = the Boltzmann constant, T= temperature, ΔC = change in concentration, ΔX = distance, z=ion valence, c= total concentration, e= electron charge, ΔE= change in potential.

Later, Goldman, Hodgkin and Katz derived a limited solution to the Nernst-Planck equation for the flux through ion channels across a biological membrane, given any membrane voltage. This equation highlights an interesting feature of ionic concentration gradients, the flux due to an electric field and the force due to the concentration gradient do not scale equally in response to changes in membrane voltage. In the case of no concentration gradient (equal inside and outside concentrations), the relation between voltage and flux is linear, as predicted by Ohm's law. This is because the only the flux is only due to an electric field. However, flux due to a concentration gradient influences the relationship between flux and membrane voltage, resulting in a non-linear relationship between flux and voltage. This means that, the gradient of the relationship between flux and voltage is also a function of the driving force (the difference between membrane voltage and the ions reversal potential). Where the voltage is pushing the ion against its concentration gradient, the

change in flux becomes smaller for the same change in voltage the further from the reversal potential the membrane voltage becomes. Conversely, where the voltage and the concentration gradient are pushing ions in the same direction the opposite relationship is true, the change in flux elicited by a change in voltage increases the further the membrane voltage is from the reversal potential. Therefore, in the case of a concentration gradient, the flux against membrane voltage curve is not linear, shows soft-rectification against currents opposing the ion's concentration gradient, gain of currents with the ion's concentration gradient, and crosses the X-axis at the point of the ion's reversal potential. This phenomenon is known as Goldman-Hodgekin-Katz rectification [81].

$$J = P_i z_i^2 \cdot \frac{V F^2}{RT} \cdot \frac{[i]_{in} - [i]_{out} e^{(zVF}{}_{RT)}}{1 - e^{(zVF}{}_{RT)}}$$

The Goldman-Hodgekin-Katz Flux equation. J= flux, P= permeability, z= valence, F= Faraday constant, R= the ideal gas constant, T= temperature, V= voltage.

To understand how these ionic concentration gradients assert a voltage across the membrane, we must consider the energies involved where ions are moving across the membrane. From a thermodynamics standpoint, the net flux of an ion in either direction is either spontaneous or not, and can only be spontaneous in one direction. Therefore, we must consider the Gibbs free energy of ions in the solution inside and outside of the cell moving across the membrane. At equilibrium, where there is no movement across the membrane, these free energies must be equal, as there is no spontaneous net movement. Therefore, the direction of the difference between the Gibbs free energy for the flux of ions across the membrane from either side of the membrane defines which direction the ions must flow. The free energy for the movement of these ions must also be considered using the two concepts of electrodiffusion. The free energy for ions moving in an electric field is simply the electronic density (per mole) multiplied by the magnitude of the electric field.

$$G_{electrophoretic} = E \cdot z\, e\, N_{Avagadro}$$

G is the free energy for the particles due to the electric field, E is the electric field strength, Z is the ionic valence. The constant e is the elementary electronic charge, multiplied by

Avagadro's number, meaning the charge of mole of ion, this term can be replaced with F, Faraday's constant.

$$G_{electrophoretic} = zF \cdot E$$

The energy due to diffusion can be considered an adiabatic thermodynamic process (no transfer of heat, enthalpy is therefore determined by work done in another respect). Ideal gas law shows the relationship between volume, pressure and temperature relationship for gasses. The entropy change of an expanding gas can be considered the integral of pressure against volume, from the initial to final volume. Therefore, the entropy change per mole is calculable when knowing the temperature is constant. This means, the Gibbs free energy for diffusion from each side of the membrane is considered in the case where there is none of the molecule on the opposing side. This means the free energy for diffusion is the difference between inside and outside the membrane.

$$V = \frac{mRT}{p}$$

Where V = volume, m = gaseous mass, R = the ideal gas constant, T = temperature and p = pressure.

$$\Delta S = \int_{V_i}^{V_f} p \ dV$$

Integral, S = entropy, changed between initial volume (V_i) and final volume (V_f).

$$\frac{\Delta S}{m} = \frac{RT}{p} dV \quad \therefore \quad \Delta S = mRT \int \frac{1}{V} dV = mRT \ln \frac{Vf}{Vi}$$

$$G_{diffusion\ to\ 0M} = RT \cdot \ln c$$

$$G_{diffusion} = G_{diffusion\ outside} - G_{diffusion\ inside}$$

The free energy across the membrane due to electrodiffusion is the summation of both the energy for diffusion and energy as a result of the electric field, similar to flux.

$$\Delta G = G_{diffusion} + G_{electrophoretic}$$
$$= RT \cdot \ln(c_{outside}) - RT \cdot \ln(c_{inside}) + (zFE_{outside} - zFE_{inside})$$

Which can be simplified to:

$$\Delta G = zFV + RT \ln \frac{c_{out}}{c_{in}}$$

The voltage generated by a single concentration gradient can be considered the voltage at which the electric field generated by the concentration gradient is opposed, the reversal potential. This is the voltage at which the flux of ions is at equilibrium. Therefore, this equation must be rearranged to be voltage where ΔG is zero, and thus no spontaneous flux across the membrane from either side. This yields a thermodynamic proof of the Nernst equation, which is used to calculate reversal potential. It can alternatively (and more canonically) be derived from the Nernst-Plank equation, where, using the Nernst-Einstein relationship, converting molar flux into an electrical current (in Amperes), finding the solution at current = 0, then integrating against the membrane width to find the voltage at which current = 0 occurs. However, in my opinion, this thermodynamic proof offers an alternative insight into the nature of the equilibrium potential.

$$V_{equilibrium} = \frac{RT}{zF} \cdot \ln \frac{[ion]_{out}}{[ion]_{in}}$$

The Nernst equation.

Using a similar principal as when modelling the membrane using simple batteries and resistors, the Goldman-Hodgekin-Katz voltage equation is used to calculate membrane voltage, taking into account all of the permeable ions. The voltage equation uses the reversal potential, calculated using the Nernst equation, for each ion and the relative membrane permeability of each ion.

$$V_{membrane} = \frac{P_K}{P_{total}} E_K + \frac{P_{Na}}{P_{total}} E_{Na} + \frac{P_{Ca}}{P_{total}} E_{Ca} + \frac{P_{Cl}}{P_{total}} E_{Cl}$$

The Goldman-Hodgekin-Katz voltage equation: $V_{membrane}$ = membrane voltage, P_{ion} = permeability to an ion, P_{total} = G_{ion}, and E_{ion} = the reversal potential for each ion.

During the course of functional development iPS cell-derived neurons must develop mature ionic concentration gradients and the ion channels required to manipulate membrane voltage by altering the relative conductance of the membrane to each ion. Firstly, the cell

must maintain a polarised membrane potential at rest. Inside the cell it must maintain a high K^+ and low Na^+ solution, whereas the outside of the cell is a high Na^+ and low K^+ solution. Physiologically, the reversal potential for K^+ is very negative and for Na^+ is very positive, roughly -75mV and +66mV respectively. At rest, the membrane of a neuron is mostly permeable to K^+ ions, and very impermeable to Na^+ ions. Therefore, the reversal potential to K^+ ions will contribute most to the membrane potential of the neuron whilst at rest, which results in a resting membrane potential of approximately -70mV. The high conductivity of the membrane to K^+ at rest, in neurons of the central nervous system, is largely due to low voltage and Ca^{2+} activated K^+ channels known as M-channels and K^+ leak channels that are constitutively open known as K2p channels (tandem pore potassium channels). Neurons have significantly more polarised membrane potentials than most other cell types, due to the development of a relatively high K^+ leak current. This is likely a very important developmental step for permitting neuronal electrophysiological activity, and can easily be assessed using measurements of the native membrane potential at rest.

Membrane capacitance

Another essential property the cell membrane to electrophysiological activity is the capacitance of the membrane. The ability of ion channels coupled to ionic concentration gradients to manipulate membrane voltage has thus far been presented as time-independent. The notion that changes in the relative conductance to each ion's concentration gradient can be used to augment membrane voltage is true, but also only over time. The capacitance of the membrane is an essential electrophysiological parameter which influences the time-scale which ion channel currents manipulate membrane voltage.

To explain how membrane capacitance is used to allow a cell to influence the rate at which membrane voltage changes occur, it is first necessary to understand how a capacitor works. A capacitor is a none-conductive electrical component (to DC currents), which stores a difference in charge and, consequently, electrical energy. Any two conductors separated by an insulator will have a capacitance across them, meaning that when you apply a voltage between the two conductors you will store a relative opposite charge on each conductor. A relative positive charge will accumulate on one conductor which is attracted to a relative

negative charge on the opposite conductor. The insulator between cannot conduct a current, but the electric field generated by the relative difference in charge provides a force to store charge. This is the simplest model of capacitance, referred to as a parallel plate capacitor isolated by a vacuum. The amount of charge stored by the capacitor is proportional to the voltage across. This is because a higher voltage means there is a greater force holding a charge difference across the capacitor. The relationship between voltage and charge difference stored is linear, referred to as the capacitance, and measured in Farads.

$$Charge = Capacitance \cdot voltage$$

The capacitance of a simple parallel plate capacitor is inversely proportional to the distance between the two plates and proportional to the surface area of the two facing sides of the plates. However, this model assumes the insulator does not respond to the electric field, for example in the case of a vacuum. In practice, insulators are comprised of molecules with some level of motility and either induced or innate charge differences within the molecules or particles of the insulator. This change in an insulator can be considered similar to iron filings or tiny magnets within a magnetic field; the molecules of an insulator can become aligned with the electric field, and therefore the whole insulator becomes polarised. However, this is very different from a conductor, which allows charges to move through it. This polarisation of the insulator by an electric field requires energy and charge from the source of the electric field, meaning the polarisation of the insulator can be considered an impedance to the electric field. Current is sunk into the capacitor from the voltage source to store energy and charge in the capacitor to polarise the insulating material. The more the insulator is able to respond to the electric field, the more energy can be stored by the insulator becoming polarised and the greater the impedance which is applied to the electric field. The measure of how much the insulating material responds, in terms of electric field impedance, is known as permittivity and a dielectric is an insulator which shows permittivity. A dielectric separating the conductive surfaces of a capacitor will influence the storage of charge across the capacitor, as the dielectric will store it's own electric field from the source. The polarisation of the insulator, as well as the stored charge on the plates of the capacitor, produces an internal electric field which increases the force storing charge in

the capacitor. Therefore, dielectrics increase the capacitance of the capacitor compared to a vacuum and the higher the permittivity of the dielectric the larger this effect becomes.

$$C = \varepsilon \cdot \frac{A}{d}$$

The capacitance of a parallel plate capacitor; C = capacitance, ε = permittivity of the insulator, A = plate area and d = distance between the plates (thickness of the insulator).

Applying a voltage to a capacitor charges the capacitor, this means storing an amount of charge determined by the voltage and the capacitance. How quickly the capacitor becomes charged is determined by the current (charge per second) entering the capacitor. The voltage across the capacitor only becomes equal to the input voltage once the capacitor is charged, as the capacitor's internal electric field is not taking energy and current from the input voltage. Conversely, when you remove the input voltage the capacitor's internal electric field initially maintains the voltage across it, resulting in a current if there is a conductive path in parallel with the capacitor. This current, over time, depletes the internal electric field across the capacitor, resulting in this field decaying.

To add both concepts into one general case, we can consider the capacitor acting to initially resist, and therefore attenuate over time, any changes in voltage across it. This attenuation of voltage changes over time is because any changes in the voltage across the capacitor must first alter the internal electric field of the capacitor so that it matches that of the input voltage. The internal electric field of the capacitor is determined by the charge stored in the capacitor. Therefore, the charge stored across the capacitor must be changed before the internal electric field and input voltage match. This is done by current either entering or leaving the capacitor, known as charging or discharging, respectively. Another way of considering this disparity between the internal electric field and the input voltage, is that the internal electric field results in a net voltage between the input voltage and the plate of the capacitor, sometimes referred to as the "back voltage". Therefore, a current will flow into (or out of) the capacitor in accordance with the back voltage. The current due to the back voltage results in the capacitor either charging or discharging until the back voltage, the difference between the capacitors internal electric field and input voltage, has decayed. Because a capacitor is non-conductive (to DC currents), the only current across a capacitor is

transient to facilitate changes in the charge stored across it, and thus the voltage across it. The transient current into or out of a capacitor is determined by the size of the capacitance, the magnitude of the voltage back voltage, and the resistance in series with the capacitor. Because current is charge over time and voltage is a function of charge and capacitance, therefore voltage becomes a function of current over time (the integral of current) and capacitance.

$$\Delta V = \frac{1}{C} \cdot \int_{t0}^{tn} i \; dt$$

$$i = C \, \frac{\Delta V}{\Delta t}$$

For this reason, where voltage changes are very fast (or appear instantaneous) a very large current is required, and often limited by the power supply or a resistance in series with the capacitor. Voltage changes in fact cannot occur instantaneously across a capacitor, as this would require infinite current. More importantly however, changes in voltage across the capacitor are a function of the integral of current over time. A perfect capacitor that does not leak and does not break down at high voltages would continue to add charge whilst a static current is applied, and the voltage would increase linearly with time. This would result in a larger electric field being built up inside the capacitor due to the additional charge. This means that individual short currents may each only influence the capacitor's voltage by a relatively small amount, but many such currents may cumulatively influence voltage significantly.

Any resistance in parallel with the capacitance, whether as a result of the capacitor leaking or an actual component, will result in charge escaping the capacitor. The current leaving the capacitor is determined by the voltage generated by the capacitors electric field and the parallel resistance. A larger resistance will result in a smaller current, meaning that the charge will escape the capacitor slower. As charge escapes the capacitor through this current, the electric field across the capacitor weakens. This means the current across the resistor escaping the capacitor changes with time as the electric field weakens. Therefore this means the discharging of a capacitor is an exponential decay over time. The current charging the capacitor is determined by the resistance in series with the capacitor. The

voltage at the capacitor is determined by a hypothetical potential divider formed by the series resistor and the impedance of the internal electric field of the capacitor. However, the impedance of the internal electric field of the capacitor becomes larger as the capacitance charges, because it takes more energy to store the same quantity of charge the closer the capacitor is to being charged. This means that the voltage divider starts with a low voltage across the capacitor, due to the low impedance into the capacitor, and increases in an inverse exponential fashion as the impedance into the capacitor becomes larger compared with the series resistor.

$I = \frac{V_i}{R} \cdot e^{-t\ RC}$

Discharging: $V_n = V_i \cdot e^{-t\ RC}$

Charging: $V_n = V_i - V_i\, e^{-t\ RC}$

Now that the properties of a capacitor are understood, it is necessary to understand how the capacitance of the membrane occurs and influences the electrophysiological properties of the cell. The lipid bi-layer of the membrane is a very good insulator, but it is also very thin and has dielectric properties, which makes the membrane of the cell an excellent capacitor. This is important for the electrophysiological function of the membrane, as the capacitance of the membrane allows the membrane to store charge differences and maintain an electric field. Therefore, the membrane voltage is not merely a function of the voltages generated by ionic concentration gradients and the relative conductance of the membrane to each ion, but also of absolute conductance of the membrane and time. This is because change in voltage across the membrane is a function of current over time, larger currents will influence membrane voltage faster than smaller ones. This allows the membrane to store changes in voltage for short periods of time. Therefore, a more accurate view of membrane voltage is that the Goldman-Hodgekin-Katz voltage equation predicts the eventual membrane voltage (if the conditions remain the same), but the absolute permeability of the membrane to the ions determines how quickly this voltage is met. Further, over a period of time individual currents may cumulatively change the membrane as the charge from each of

the previous currents is still stored at the membrane. However, leak currents at rest will over time cause these changes in voltage to decay. The rate at which a permeable ion influences the membrane voltage can be represented as a time constant:

$$t_{ion} = \frac{C}{G_{ion}}$$

The thickness and permittivity (approximately 10Fcm^{-1}) of the plasma membrane are relatively uniform, although slight variations are possible due to protein concentration and changes to the lipid mix [153,216]. This means that the capacitance per unit area of the membrane will be very uniform. This has allowed a specific capacitance of the membrane to be calculated, and has been demonstrated to be around 1 μFcm^{-2}. Therefore, the membrane capacitance is proportional to the cell surface area and influenced by cell size and complexity. The membrane capacitance is easily calculable using transient currents observed at the start and end of a voltage step, as a result of the membrane charging and discharging, respectively.

The capacitance of the membrane adds an additional dimension to the influence ion channels have on membrane voltage. Rate of change of voltage is proportional to absolute permeability of the membrane to an ion. Therefore, small currents alter membrane voltage slower than larger currents, and multiple separate currents which occur over a short time-scale can have a cumulative influence on membrane voltage.

Action potentials

In addition to maintaining a resting membrane potential, changes in the relative conductance of the membrane to ions is critical to action potential propagation. Action potentials are a moving wave of depolarisation, allowing electrical conduction across the entire membrane of the neuron. The propagation of an action potential is evoked by a smaller localised depolarisation, usually at a post synaptic membrane. An action potential has two distinct stages, firstly the cell depolarises to membrane potentials above 0mV and then repolarises back to the resting membrane potential. In contrast to leak ion channels which set the membrane voltage at rest, during an action potential, high rates of change of voltage are required. This means, large conductance is used to rapidly change membrane voltage, with large currents, but also consuming larger amounts of energy.

Voltage activated Na^+ channels provide the conductance required for depolarisation. Voltage activated Na^+ channels are gated by voltage, the channel pore is gated by the movement of a positively charged trans-membrane segment of the protein. Slight depolarisations of the membrane potential move this voltage-sensitive segment (S4) of the protein slightly away from the intracellular side of the membrane, resulting in a protein-wide conformational change which opens the channel pore. The conductance of the membrane to Na^+ ions increases rapidly at this point, so that the reversal potential for Na^+ becomes the dominant voltage across the membrane. This results in this this part of the membrane becoming almost immediately depolarised. However, also in response to depolarisation an internal region of the channel protein is attracted towards the intracellular region of the channel pore. This internal region then plugs the channel pore from the inside, preventing further Na^+ flux a short period of time following Na^+ channel opening. The plug-region of the protein will only release itself from the channel pore in response to repolarisation, meaning the Na^+ channel cannot open again until the cell has repolarised. It is these functional regions of the Na^+ channel protein that result in the channel having three distinct states: closed, open and inactivated [81]. The closed state is where the channel pore is closed, leaving the channel ready to open in response to depolarisation. Following a small depolarisation the channel enters the open state, where Na^+ ions are flowing through the channel pore. Lastly, whilst the channel pore is still in the open configuration the plug region of the protein plugs the channel pore resulting in the

inactivated state, from this state the channel must close again in response to membrane repolarisation before being able to activate again. Open and inactivation are as a result of changes to the conformation of two regions of the protein, and these conformational changes are voltage dependant. It is possible using voltage-clamp electrophysiology to specifically measure the relationship between these two events and membrane voltage. Studies have also shown that different sub-types of voltage activated Na^+ channel have different opening and inactivating voltages, however for each channel there is a relatively small difference between their activating and inactivating voltages [167].

Inactivation of Na^+ channels is essential for the transition from the depolarising stage of the action potential to the second, repolarising, stage of the action potential. Inactivation closes the large membrane conductance to Na^+, meaning that K^+ is once again the most permeable ion, meaning that eventually the membrane voltage will return to its resting value. However, the resting (constitutively open) K^+ conductance is relatively small, thus allowing for a smaller current and less energy being used at rest. This means that the current due to the resting K^+ conductance alone would take a very long time to restore the resting membrane voltage, due to the charge stored across the membrane capacitance. Therefore, the cell employs voltage activated K^+ channels to rapidly repolarise the cell using a much larger current. These channels activate slightly slower and at a more depolarised voltage than voltage activated Na^+ channels, so that they come into effect as the Na^+ current is inactivating. The voltage activated K^+ channels have a very significantly larger conductance than the resting K^+ conductance, resulting in a much larger current that is able to rapidly change the voltage across the membrane. These K^+ channels inactivate only after a much longer timescale, and would not be expected to inactivate during an action potential, as the resting membrane potential should have been reached, meaning the channels will close before inactivation occurs. The K^+ conductance is sufficient to significantly under-shoot the threshold voltage for an action potential, and often undershooting the resting membrane potential itself due to an even more extreme bias towards K^+ being the most dominant ion whilst the massive voltage gated K^+ conductance is open. This is important for allowing the voltage activated Na^+ current to recover for the generation of a second action potential.

An action potential, although considered a single signalling event is not a static single event. Action potentials travel across a neuron, caused by the depolarisation in a local region of the membrane activating nearby voltage activated Na^+ channels in a travelling wave. The nature of this action potential wave is modelled use active-cable theory models. However, it is critical for a neuron to produce functional pools of both Na^+ and K^+ channels in order to generate action potentials. It is also crucial for a neuron to express the correct mixture of sub-types of both ion channel to facilitate the correct behaviour in response to different voltage changes. These channels can be studied directly using voltage clamp protocols, and the ability of a cell to fire action potentials can be studied using forced depolarisation using current steps.

Neuronal excitability

An important parameter for neurons is their sensitivity to action potentials. Taking together, the electrophysiological parameters which influence membrane voltage over time and the machinery which initiate action potential propagation, this section will discuss how these parameters form an integrated system for fine tuning action potential generation. This system is essential for reliably and efficiently processing and conducting information in the nervous system. In the case of many neurons in the central nervous system it becomes increasingly complex, as multiple sources of information are integrated as changes in voltage over time to influence action potential propagation.

Sensitivity to action potential generation means how much energy is needed to initiate an action potential. Action potentials are usually propagated at post-synaptic membranes in response to ligand activated ion channel activity. The ligand gated ion channels (ionotropic neurotransmitter receptors) provide the depolarising stimulus required to activate Na^+ channels. This initiates the action potential wave through the cell. Ligand activated ion channels are tied to ionic concentration gradients, but they are only activated in response to neurotransmitters binding to a region of the protein. Neurotransmitters are secreted from vesicles binding to the pre-synaptic membrane, they then cross the synaptic gap to bind to

their associated ligand gated ion channels. In response to neurotransmitter binding, they induce small currents at the post synaptic membrane to influence membrane voltage. The current injected by these ligand gated ion channels is determined by the driving force for the ion they conduct and the collective conductance of the open ligand gates ion channels. Further, within a brief space of time the membrane capacitance will store the charge contributions of these neurotransmitter responses, resulting in a cumulative depolarisation. Therefore, a single synaptic event need not, and usually does not, evoke an action potential. Neurons have carefully developed their specificity and sensitivity to chemical stimuli at a synapse, by developing the magnitude of voltage changes in response to neurotransmitter binding and their sensitivity to them in terms of action potential propagation. If the synapse were too sensitive the neuron would be firing more action potentials than necessary, which would be energy inefficient. If the synapse were too insensitive then signalling between neurons would become slow and unreliable. The balance between energy efficiency and sensitivity is a debated subject amongst neuroscientists.

Ion channels opening results in increased conductance across the membrane. However, the resistance of the membrane at rest (inverse of conductance), due to leak conductance, is considered the input resistance. The input resistance is important, because it influences, along with the membrane capacitance, the magnitude of voltage response across the membrane due to currents. In accordance with Ohm's law, a higher input resistance will result in a larger change in voltage in response to the same current. When integrated by the membrane capacitance, this means that the rate of change of voltage is faster the higher the membrane resistance is (for the same current). The absolute membrane resistance changes significantly over voltage, as voltage activated ion channels significantly reduce membrane resistance when open. However, it is the input resistance at rest caused by leak conductance, which is obviously considerably larger, that is important for setting the sensitivity to an action potential.

The sensitivity of a synapse is essentially how easily the post synaptic membrane initiates an action potential in response to excitatory post-synaptic activity. There are several factors which control this sensitivity, and to explain how they integrate into a system for finely

tuning action potential propagation it is necessary to model the membrane's capacitance, resistance and the ion channels involved.

Firstly, to propagate the action potential a stimulus must raise the membrane potential of the cell from the resting membrane potential to the threshold for an action potential. Therefore, the most obvious factor influencing sensitivity is how large the difference is between the resting membrane potential and the threshold for an action potential. Simply, the more the voltage across the membrane has to change in order to reach threshold the more charge has had to be moved, meaning more energy used. Therefore, to increase sensitivity, one might expect the resting membrane potential and threshold voltage for an action potential to be relatively close. However, the threshold for activating an action potential is set by the activation voltage of voltage activated Na^+ channels. This means, the threshold voltage and resting membrane voltage cannot be too close, because voltage activated Na^+ channels inactivate at a similar voltage to their inactivation. This would mean that, if the resting membrane potential were too depolarised (too close to threshold) the voltage activated Na^+ current would be inactivated, and thus ineffective at driving an action potential. Therefore, there has to be at least a minimal difference between the resting and threshold voltages. However, there is some evidence to suggest that neurons do minimize the difference between resting membrane voltage and threshold voltage in certain membrane regions. There are different sub-types of Na^+ channel which respond to different voltages, in terms of both activation and inactivation. Immunostains have observed that one of the typical neuronal type Na^+ channels, $Na_{v1.6}$, tends to be localised at dendrites (in the CNS) and nodes of Ranvier (in mylinated neurons) [26]. Further, studies using TTX (tetrodotoxin) resistant forms of the protein to isolate and study the voltage dependant activation and inactivation of $Na_{v1.6}$ and another common neuronal Na^+ subtype $Na_{v1.2}$ demonstrated that $Na_{v1.6}$ activated at a significantly more polarised membrane potential than $Na_{v1.2}$ [167]. This would suggest deliberate localisation of $Na_{v1.6}$ in places where the cell needs a low threshold voltage to increase sensitivity, including post synaptic membranes. If this is the case then perhaps populations of $Na_{v1.6}$ are acting as pre-amplifiers to the cell, responding to the smaller stimuli at synapses to induce an action potential, which is then easily sufficient to spread by activation of other Na^+ channel sub-types across the rest of the neuron.

Another important aspect of synaptic sensitivity is how readily changes in membrane voltage occur in response to current injection from ligand gated ion channels. The magnitude of the current is determined by the collective conductance of the channels and the driving force for the ion across the membrane. We must also consider the resistance of the passive leak channels, also referred to as the input resistance, and the driving force for the leaky ions. Kirchoffs current law states that the currents passing a node must always cancel to preserve the conservation of charge. Therefore, the current into the membrane capacitance, current across the passive conductance and the synaptic current injection must meet a net 0 current. This means that all of the current from the opening of synaptic, ligand gated ion channels must either flow across the leak resistance, or it must flow into the membrane capacitance (see figure 1.2).

$$I_{synaptic} + I_{capacitance} + I_{passive} = 0$$

Each term in isolation:

$$I_{synaptic} = G_{synaptic} \cdot V_m - V_{reversal} \text{ and } G_{synaptic} = G_{single\ channel}\, n_{receptors\ open}$$

$$I_{passive} = G_{passive} \cdot V_m - V_{reversal}$$

$$I_{capacitance} = C_m \frac{\Delta V}{\Delta t}$$

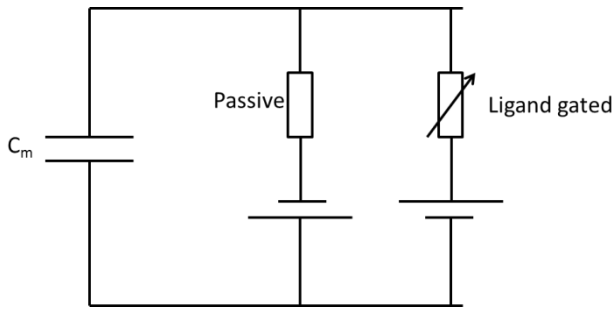

Figure 1.2: A schematic representing the key properties of the membrane which together form a circuit which allows depolarisation due to ligand binding. Firstly, the ligand gated ion channel is represented as a variable conductance, which increases upon ligand binding. A battery represents the driving force of the ion, or ions, which the ligand gated ion channel conducts. Secondly, the passive leak conductance of the membrane, and driving force of the

leak conductance is represented in parallel to the representation of the ligand gated ion channel. Lastly, the capacitance of the membrane is parallel to both.

In the absence of a membrane capacitance the synaptic injected current must be equal and opposite the current through the leak channels. In this case, the change in voltage evoked by neurotransmitter binding would be instantaneously building and decaying. However, this is useful because it tells us the eventual membrane voltage once, should the membrane capacitance fully charge. In this regard we can consider the leak and synaptic channels to be in series, and therefore a voltage divider. However, we must then consider the voltages due to the leak and synaptic currents to be in series, and in opposite directions. The voltage across the membrane at this point is the summation of the voltage across the synaptic and leak resistance, which if both were equal resistances would be equal and opposite and the voltage across the membrane would be the average of the leak and synaptic driving forces. However, the leak resistance is far larger than the synaptic resistance, meaning the synaptic resistance will contribute most to membrane voltage.

The resistance across the synaptic ligand gated channels and the ionic driving force determine the current injected by the synaptic event. This be modelled by a voltage source representing the driving force for the ions and a variable resistance representing the ligand gated ion channels. As previously discussed, in the absence of the membrane capacitance the voltage across the membrane would instantaneously change in response to current injection proportional to the membrane resistance, according to Ohm's law and the driving force of the leak ions.

The voltage driving the leak current is essentially the average of the reversal potentials for ions conducting at rest, weighted by the relative permeability to each by the leak channels. Therefore, it is approximately equal to the membrane potential at rest, with a high resistance in series. This higher resistance compared to that of the ligand gated ion channels has the consequence that the voltage due from the synaptic currents contributes more to membrane voltage.

$$V_m = (V_{synaptic} \cdot \frac{R_{synaptic}}{R_{synaptic} + R_{leak}}) + (V_{leak} \cdot \frac{R_{leak}}{R_{synaptic} + R_{leak}})$$

$$I = \frac{V_{synaptic} + V_{leak}}{R_{synaptic} + R_{leak}}$$

As previously shown, the current is split between the input resistance and charging the capacitance of the membrane, because the input resistance and capacitance are in parallel. The combined resistance of the capacitance and input resistance in parallel however, are in series with the synaptic current. Although it is useful to remember a capacitor does not have a real resistance, the back voltage due to impedance to changes in its electric field has the same effect when considering only one time point during the capacitors charging. Further, the effective resistance into the capacitor increases as the capacitor approaches fully charged. This means that initially the effective resistance of the leak channels and capacitor in parallel is very low, and increases asymptotically to the resistance of the leak channels. Therefore, initially as the capacitor starts to charge the synaptic current is actually very high, but the change in membrane voltage is very small, this is because most of the voltage drop is across the synaptic resistance now as the membrane resistance (due to the charging of the capacitor) is very small. Once fully charged, the capacitance of the membrane is cannot accept more charge and the current may now only flow across the input resistance. Therefore, as the capacitor charges the current flowing into the capacitor falls, as the imaginary resistance of the capacitor increases (exponentially). This means that asymptotically all of the current flows through the membrane leak resistance, which is a much larger resistance, resulting a smaller synaptic resistance, but a larger change in membrane voltage.

$$i_c = C\frac{\Delta V}{\Delta t} \;\; \therefore \;\; i_{leak} = i_{synaptic} - C\frac{\Delta V}{\Delta t}$$

For a time point during capacitor charging:

$$I_{synaptic} = \frac{V_{synaptic}+V_{leak}}{R_{synaptic}+R_{input}//R_{capacitor}}$$

The voltage across the membrane is a function of the current and resistance across the membrane, and until charged the capacitance of the membrane can be considered a resistance in parallel with the input resistance, starting at 0 and ending with infinity and increases exponentially against time in-between. This means that the voltage across the membrane is also an inverse exponentially increasing function of time, until it reaches a maximum determined by the input resistance. Splitting the voltage divider between the voltage across the synaptic and leak resistances gives us two terms, $V_m - V_{leak}$ and $V_m - V_{synaptic}$, as well as being able to represent the change in V_m across the capacitor. Applying Kirchoffs current law, but represented in terms of voltage, it is possible to construct an equation for voltage changes across the membrane due to ligand gated ion channels. Note that the resistance charging the capacitance is that of the synaptic resistance and leak resistance in parallel, because it is charging with respect to the membrane voltage (and, in all cases a voltage divider is functionally identical to the parallel resistance with a source voltage equal to that generated by the voltage divider, figure 1.2). Therefore, I can design a time constant for the membrane voltage, consider the starting membrane potential at rest and a final membrane potential determined by the synaptic and input resistances in the steady state when the capacitor has charged.

$$\frac{V_m - V_{leak}}{R_{input}} + C_m\frac{\Delta V}{\Delta t} = \; I_{synaptic} \; = \frac{V_m - V_{synaptic}}{R_{synaptic}}$$

$$\tau = C_m \frac{R_{synaptic} \cdot R_{input}}{R_{synaptic} + R_{input}} \quad or \ \tau = \frac{C_m}{G_{synaptic} + G_{input}}$$

$$V_m = V_{final} - V_{final}\, e^{-\frac{t}{\tau}}$$

The rheobase current is the minimum current, if sustained indefinitely, required to raise the membrane potential from rest to the threshold to fire an action potential. Therefore, the rheobase current is the current required to raise the membrane voltage from resting to the threshold in the absence of capacitance (V_{final}). The rheobase current is determined by the input resistance and is not influenced by the capacitance. However, in practice synaptic currents are too short to raise the membrane potential to V_{final} as a single event, and thus require the membrane capacitance to store the voltage contributions of multiple currents to raise the voltage to the threshold. However, the input resistance in parallel with the membrane capacitance allows the charge across the membrane to leak, so that the voltage decays back to the resting membrane potential. This means, that after a synaptic current the voltage will fall back to the resting membrane potential. However, this decay will be slower than the voltage gain during the synaptic current because it is discharging through the input resistance alone, not both the synaptic channels and the input resistance in parallel.

$$V_m = V_{leak} \cdot e^{-t/C_m R_{input}}$$

The difference between the gain and decay speed of a synaptic input is directly proportional to the ratio of synaptic and leak resistances. However, this has the effect that within a limited time the membrane will add up the changes in voltage due to multiple synaptic currents before they decay. This allows a series of short and small synaptic currents to be added to depolarise the cell sufficiently. Consequently, this also adds an additional level of complexity to neuronal excitability. It is therefore necessary to consider that there are multiple different methods of eliciting the voltage change required to start an action potential. Firstly, the cell can use a small continuous current, the rheobase current, to elicit an action potential, but this would be incredibly slow. Secondly, the cell can use one very large current to elicit an action potential almost immediately, this would be significantly faster, but has little flexibility to fine tune sensitivity. Put simply, by this second method an

action potential would always happen in response to synaptic input, and would result in two neurons in series firing action potentials at exactly the same rate in all circumstances, which would limit the ability of a neuronal circuit to process information. Thirdly, the synapse could rely on the frequency of synaptic currents to control membrane voltage and sensitivity. Due to membrane integration, bursts of individual synaptic currents will raise the membrane voltage almost as quickly as a single short current. Further, a persistent frequency of synaptic events would also produce a persistent depolarisation, which means that a smaller burst of synaptic events would be required to reach threshold. However, there are neurotransmitters which are hyperpolarising compared to the resting membrane voltage, meaning the frequency of these hyperpolarising stimuli could reduce sensitivity.

Voltage gated Ca^{2+} channels

Another set of voltage activated channels are the voltage activated Ca^{2+} channels. Ca^{2+} signalling in the cell plays a pivotal role in many electrophysiological processes, but is also critical to many molecular cell mechanisms and regulation of gene expression. Considering its role in both electrophysiological and molecular signalling, it is not surprising that it provides an important link between electrophysiological activity and gene expression. Ca^{2+} influx is vital to neuronal development, stimulating CREB phosphorylation in response to electrophysiological activity [45,99]. However, it also plays a role in neurodegenerative diseases, including apoptosis in Huntington's disease [212]. Therefore, investigating the function of Ca^{2+} channels is important for developing models for neurodegenerative diseases, but also potentially for developing improved protocols for functionally maturing iPS cell-derived neurons. There are 5 different sub-types of Ca^{2+} channel, L-, N-, P/Q-, R- and T- type channels, all of which are expressed in neurons (table 1.2).

L-type Ca^{2+} channels are amongst the most prevalent of neuronal Ca^{2+} channels. There are 4 L-type Ca^{2+} channel genes, Cav 1.1 to 1.4, which can be distinguished by their electrophysiological characteristics. Cav 1.1 and 1.2 are high-voltage activated, whereas Cav 1.3 and 1.4 are activated at relatively lower voltages, and considered highly sensitive [116]. Voltage activated Ca^{2+} channels usually show significantly slower activation and inactivation compared to Na^{+} channels. Most neurons express one of either Cav1.2 or 1.3 where they

contribute to a diverse set of functions. Cav1.3 responds to smaller depolarisations than Cav1.2, this means that Cav1.2 will respond only to action potential propagation, whilst Cav1.3 responds to changes in voltage that are sub-threshold for an action potential[116]. Further, although both channels generally contribute little to the depolarisation evoked during a neuronal action potential, Cav1.3 is capable of providing a small enhancement to synaptic depolarisations to facilitate the voltage reaching the threshold for an action potential. Crucially, L-type Ca2+ channels are capable of providing Ca2+ influx in response to both action potential propagation and sub-threshold depolarisations, depending on which sub-types are expressed. These Ca^{2+} influxes function primarily as a link between electrophysiological function and other functions of the cell, including gene expression, influencing synaptogenesis and cell survival [50,66,120,164]. L-type Ca^{2+} channel activity has also been shown to accelerate the differentiation of neurons from neural stem cells, resulting in more functionally active neurons [45]. Indeed, the function of voltage activate Ca^{2+} channels in neuronal development best explains the link between depolarising activity and the development of neuronal function [51]; an idea consistent with the potential effects of both neuronal activity and Ca^{2+} influx on BDNF potency [21,114,174]. This link between BDNF signalling and Ca^{2+} influx, is attributed to Ca^{2+} modulating adenylyl cyclase activity and cAMP gating the function of the TrkB receptor [48,159].

Another prevalent sub-type of Ca^{2+} channel in neurons is the N-type. These Ca^{2+} channels associate with the snare protein A syntaxin 1 at pre-synaptic membranes [110]. Snare proteins and N-type Ca^{2+} channels interact functionally as part of a complex, providing a link between N-type Ca^{2+} channel activity and synaptic vesicular release [110,131,157,178,207]. Demonstrating this link, studies have shown that synaptic vesicle release is inhibited by N-type Ca^{2+} channel blockade [16,85].

T-type Ca^{2+} channels are low voltage activating, and have a relatively small single channel conductance compared to other voltage activated Ca^{2+} channels [152]. There are three T-type Ca^{2+} channels: Cav3.1, 3.2 and 3.3. Cav 3.1. Cav3.2 shows a distinctive change in activation and inactivation rates with changes in membrane voltage. Near the activation threshold voltage of these channels, around -60mV, they show very slow rates of activation and inactivation. However, both activation and inactivation get faster as voltage increases, until

around -30mV where the activation rate stabilises at significantly faster rates than other Ca^{2+} channels [152]. This allows T-type Ca^{2+} channels to produce a very short depolarising spike which elicits a fast train of action potentials, known as burst spiking [152]. By contrast, Cav3.3 is expressed in far fewer neuronal sub-types and shows very slow inactivation [7]. These channels are essential for regulating the oscillatory frequency of the thalamus [7]. Therefore, the expression of these different T-type Ca^{2+} channels is important for defining features in the spontaneous activity of neurons, as they can facilitate burst spiking and biphasic membrane potentials in some neuronal sub-types. However, pharmacologically T-type channels are more difficult to identify, because of the poor specificity of the common T-type Ca^{2+} channel blocker mibedrafil.

The R-type Ca^{2+} channel, Cav2.3, is a high voltage activating channel expressed in most of the central nervous system [148]. This channel is differentially found at pre- and post- synaptic regions of neurons in different neuronal sub-types [148]. Functionally, R-type Ca^{2+} channels provide activity-linked Ca^{2+} influx, similar to L-type channels. Their localisation to spines, both axonal and dendritic depending on the neuronal sub-type, allows these channels to produce localised Ca^{2+} influxes and support plasticity [211].

P/Q- type Ca^{2+} channels in neurons have functional similarities with N-type channels. P/Q-type channels are high voltage activated Ca^{2+} channels that associate with SNARE proteins similar to N-type channels [33,157].

The different sub-types can generally be identified electrophysiologically using specific antagonists:

Name	Gene (α_1 subunit)	Antagonist
L-type ($Ca_{v1.1-1.4}$)	CACNA1- *S,C,D or F*	Nifedipine
N-type ($Ca_{v2.2}$)	CACNA1B	ω-Conotoxin
P/Q-type ($Ca_{v2.1}$)	CACNA1A	ω-Agatoxin
R-type ($Ca_{v2.3}$)	CACNA1E	SNX 482
T-type ($Ca_{v3.1-3.3}$)	CACNA1- *G,H or I*	Mibedrafil (less selective)

Table 1.2: A list of the voltage-gated Ca^{2+} ion channels, their genes and typical antagonists used to study them.

Neurotransmitter receptors

Neurotransmitters are an essential part of neuronal function, providing mechanism for information transfer between neurons. IPS cell-derived neurons must develop the capability to both secrete and respond to neurotransmitters to accurately model neuronal tissues, and potentially neuronal circuits, which may play pivotal roles in many neurodegenerative diseases.

There are two basic types of neurotransmitter receptor, metabotropic and ionotropic. Metabotropic receptors respond to neurotransmitter binding by initiating a series of intracellular molecular events, usually using a G-protein as an intermediate [143]. By contrast, ionotropic receptors are ion channels which are gated by the binding of a neurotransmitter, also called ligand gated ion channels (these were previously discussed with regards to neuronal excitability). Ionotropic receptors can also be sub-divided into those which provide depolarising and hyperpolarising currents in response to ligand binding. Depolarising ionotropic receptors are permeable to cations; they vary from being broadly permeable to Na^+, K^+ and Ca^{2+}, to being somewhat selective. The mean reversal potential of these ions is more depolarised than the resting membrane potential of the cell, resulting in a depolarising current when they open. Hyperpolarising ionotropic receptors are ligand gated Cl^- channels. In mature neurons, a concentration gradient of Cl^- ions is maintained such that Cl^- currents are hyperpolarising from the resting membrane potential. However, during the course of differentiation, the concentration gradient is significantly augmented, resulting in a switch from depolarising to hyperpolarising compared to the resting membrane potential (see Introductions, Electrophysiological properties of neurons, Neurotransmitter receptors, GABA receptors).

In the central nervous system there are several common neurotransmitters, including: glutamate, γ-aminobutyric acid (GABA), glycine, acetylcholine (ACH), serotonin and dopamine. Receptors can be located at the post synaptic membrane or extrasynaptically.

Extrasynaptic receptors respond to neurotransmitter release at the synapse with significant delay as the neurotransmitter diffuses from the main cleft and provide different functions for augmenting sensitivity.

Glutamate receptors

There are multiple types of both ionotropic and metabotropic glutamate receptor. Ionotropic glutamate receptors are generally categorised by non-physiological ligands which are specific to each subtype. Specifically: α-Amino-3-hydroxy-5-methyl-4-isoxazolepropionic acid (AMPA), kainic acid (kainate) and N-Methyl-D-aspartic acid (NMDA). Ionotropic glutamate receptors are permeable to cations, but NMDA receptors are somewhat more selective for Ca^{2+} [107]. All three sub-types of ionotropic glutamate receptor are excitatory, eliciting depolarisation in response to glutamate. NMDA receptors also require the binding of either Glycine or serine, depending on the neuronal sub-type, as a co-transmitter and are almost as sensitive to aspartate as they are glutamate [107]. Further, NMDA receptors are unique in that at the resting membrane potential Mg^{2+} ions flow into, and block, the open channel pore, which prevents a current in response to ligand binding [132].However, membrane voltage changes from AMPA or Kainate receptor-driven activity will cause conformational changes in the NMDA receptor to release the Mg^{2+} ions and unblock the channel [123,210]. AMPA or Kainate receptors provide immediate current responses at post synaptic membranes, whereas at rest, Mg^{2+} ions heavily inhibit responses from NMDA receptors, but as activity increases the NMDA current rapidly becomes uninhibited due to Mg^{2+} leaving the channel pore [11,65]. Extrasynaptic NMDA receptors provide continuous activity dependant Ca^{2+} influx, this stimulates protein kinase activity at the post-synaptic membrane to induce a phosphorylation-dependant increase in the activation of K^+ channels and AMPA receptors, increasing synaptic sensitivity immediately, providing one mechanism for phase 1 long-term potentiation [185]. Over longer periods of time this results in gene-regulation changes effecting the same K^+ channels, AMPA receptors and also modulating synaptic structural proteins, increasing synaptic sensitivity more permanently, resulting in the second phase long-term potentiation [185]. In some neuronal sub-types, metabotropic glutamate receptors mediate long-term potentiation. This mechanism also allows neurons of the central nervous system to initiate responses from two spatially distant but temporally similar signals on the dendritic arborisations of the cell. If spatially close, the membrane

would easily integrate the two currents and reach threshold. However, given a large enough spatial distance, each response may have decayed. Therefore, back-propagating, sub-threshold depolarisations remove the inhibition of NMDA receptors along a dendritic arborisation, enhancing their activity for subsequent, sub-threshold depolarisations. This results in the dendritic arborisation becoming more sensitive, and allowing an integration of both signals where membrane capacitance alone could not have due to spatial distance; this concept is known as coincidence detection [92,183].

There are three sub-types of metabotropic glutamate receptor. Group 1 are localised post-synaptically, and increase the sensitivity of the post-synaptic membrane by increasing NMDA-receptor activity as well as other ion channels [41,59,179]. Group 2 and 3 are usually localised pre-synaptically, and depress both NMDA-receptor activity and neurotransmitter release at the synapse [2,181]. Further characterisation can be performed using specific pharmacological antagonists for of these sub-types. Group 2 and 3 providing a feedback for neurotransmitter release and group 1 augment synaptic plasticity and excitability.

GABA receptors

There are two classes of GABA receptor, ionotropic $GABA_A$ and metabotropic $GABA_B$ receptors. $GABA_A$ receptors are ligand gated Cl^- channels and their activity results in a direct hyperpolarisation of the membrane by Cl^- influx. Now considered part of the $GABA_A$ class, there is also a sub-class of GABA receptors which are exclusively composed of rho-type subunits, known as $GABA_{A\text{-}P}$. $GABA_{A\text{-}P}$ receptors are pharmacologically differentiated by their insensitivity to allosteric modulators of general $GABA_A$ receptors, such as benzodiazepines and barbiturates [105]. $GABA_B$ receptors are G-protein coupled receptors, and hyperpolarise the membrane indirectly through increased activation of inwardly rectifying K^+ currents and further inhibit neurotransmitter release by inhibiting pre-synaptic voltage activated Ca^{2+} currents [93].

GABA is active in very early stages of neurogenesis [205]. However, initially $GABA_A$ activity results in GABA-dependant depolarisation, rather than hyperpolarisation. Therefore GABA is an excitatory neurotransmitter at these early stages of development [12,197]. In response to

repeated GABA stimuli, expression of the Na^+,K^+ & $2Cl^-$ co-transporter 1 (NKCC1) is reduced, and expression of the K^+ & Cl^- co-transporter 2 (KCC2) is increased. The net effect is a developmental change in the Cl^- concentration gradient, changing the reversal potential of Cl^- relative to the cell's membrane potential at rest [67,196]. This results in GABA becoming an inhibitory neurotransmitter later in post-natal neuronal development.

Further, excitatory GABA has been shown to promote synaptogenesis and integration of new neurons (which have not yet developed a mature, inhibitory GABA response) in the adult central nervous system [68]. This is likely due to GABA-dependant depolarisations driving Ca^{2+} influx, which then enhances synaptogenesis.

Huntington's disease

In addition to studying the development of electrophysiological maturity in iPS cell-derived neurons, this study also aims to develop enhancements in differentiation protocols to produce more functionally mature neurons. Using iPS cell lines generated for a Huntington's disease study, this study will attempt to use these protocol enhancements to produce a more consistent, and more mature functional outcome at a standardised time point.

Huntington's disease (HD) is a genetically dominant neurodegenerative disease, directly caused by an expansion of a CAG codon repeat in the Huntingtin gene [4]. The CAG repeat encodes a string of glutamine (Q) residues in the primary structure of the protein, which causes a severe abnormality in the protein's structure. Increases in the length of this repeat correlate well with both the age of onset and severity of the disease. This relationship between the disease manifestation and CAG repeat length is likely due to increasingly aberrant protein structure as the repeat length increases [4]. The disease results in motor control loss and chorea due to a progressive loss of Medium spiny neurons in the striatum. It is currently unclear the normal function of the Huntingtin protein is, and studies have linked the protein to multiple different processes. It is therefore unclear whether the disease phenotype is as a result of loss of the protein's function or gain of aberrant functions, or both. However, these effects may be linked to the protein being cleaved within the poly Q-repeat, resulting in a truncated version of the protein. Further, the likelihood of

this cleavage appears to increase with poly Q repeat length, which potentially provides a mechanistic link between Q-repeat length and disease progression [166]. A combination of protein-protein interaction and localisation studies, including yeast 2 hybrid, co-immuno precipitation and affinity chromatography, have shown the Huntingtin protein interacts with transcription factors, membrane trafficking proteins and some signalling proteins [111]. These interactions include, direct association with the machinery for clatherin vesicle endocytosis at synapses and interaction with the dynein-protien complex during vesicle transport along axonal microtubules [79]. Further, a study has shown inhibition of axonal transport with increased CAG repeat length due an increased toxic function of the truncated Huntingtin protein [186]. This directly implicates Huntingtin protein in transport to the plasma membrane and potentially a disease related phenotype involving mis-regulated movement of ion channels to or from the membrane. It has been speculated that this could lead to an electrophysiological phenotype, most likely at or near the synaptic membranes, which perhaps inlcudes augmented transport of different neurotransmitter receptors to the synaptic and post-synaptic membranes. Huntingtin also has a role in regulating apoptosis through inhibition of Caspase-9 activity, a reduction in this function potentially evoking an increase in the cell's sensitivity to Ca^{2+} dependant apoptosis [163]. Huntingtin has many functions in the cell, and it appears likely that the disease is induced by both toxic new functions of the protein and loss of its wild type function. Therefore, developing iPS cell-derived models for this disease requires generating functional cells which readily reproduce these phenotypes.

Neurotransmitter excitotoxicity is one of the leading hypotheses which attempts to explain the increased apoptosis of medium spiny neurons in HD. Work in transgenic mice has shown increased NMDA type Glutamate receptor dependant excitotoxicity with expanded CAG repeats [212,213]. Further, studies have found increased extrasynaptic NMDA currents in HD cells, which correlates with increased rates of apoptosis, assayed using increased tunnel positive cells, caspase 3 activity and caspase 9 activity [212]. Perhaps the increased rates of apoptosis are due to both to mis-regulated transport of NMDA receptors and increased sensitivity to increased intracellular Ca^{2+} as an apoptotic stimulus due to mis-regulation of caspase activity. [125,147].

Astrocyte function has also been linked to the mechanisms in Huntington's disease. Studies in mice have shown glutamate uptake by astrocytes is impaired, as well as increased Ca^{2+} dependant glutamate release by astrocytes [63,109,113,118]. The increased availability of glutamate for extrasynaptic NMDA receptor activation and increased NMDA receptor density at the membrane, taken together result in much larger Ca^{2+} influx from extrasynaptic NMDA receptors. Further, Medium spiny neurons of the striatum are also more sensitive to Ca^{2+} influx driving Caspas-9 mediated apoptosis. Interestingly, Ca^{2+} responses from synaptic glutamate receptors have been shown to be neuro-protective, compared to post-synaptic receptor activation which appears to be excitotoxic [78,171,215]. This is likely due to the specific compartmentalisation of the two separate Ca^{2+} influxes having different effects on cAMP synthesis and therefore CREB activation, perhaps influencing different pools of adenylyl cyclase which are differentially regulated by Ca^{2+} [78,146]. In addition to augmented glutamate activity, HD also significantly reduces BDNF expression in the striatum, reducing the pro-survival influence of BDNF [64]. Therefore, Huntington's disease disturbs the balance of post-synaptic and synaptic NMDA receptor Ca^{2+} influxes, resulting in reduced Trk-B receptor activity, reduced CREB activation, increased Ca^{2+} dependent caspase-9 activity and increased apoptosis.

Medium spiny neurons of the Striatum

Approximately 95% of the neurons of the striatum are medium spiny neurons, the remainder being cholinergic interneurons. However, it is medium spiny neurons that are selectively lost as a result of Huntington's disease. Since the functional properties of medium spiny neurons underpin the disease mechanisms, it is vital that these functional properties be investigated in any iPS-cell derived model for the disease.

Medium spiny neurons are GABAgenic neurons, meaning they secrete GABA from pre-synaptic membranes to supress activity, by hyperpolarisation, in subsequent neurons. Activity in medium spiny neuron is finely controlled by multiple neurotransmitters, including GABA, glutamate, ACH and dopamine.

Action potential activity in striatal medium spiny neurons is dependent on a bi-phasic membrane potential. Short trains of action potentials are observed during an up, depolarised state, which is near to the threshold for action potential initiation. These short trains and up-states are separated by longer stretches of a more polarised membrane potential closer to the reversal potential for K^+ ions. The initiation of action potentials during the up-state is determined by the voltage during the up-state; they do not generate any spontaneous activity if the up-state is not depolarised sufficiently [208]. The amplitude of the upstate is determined by the magnitude of depolarisation from the glutamatergic synaptic input and the magnitude of repolarisation caused by KCNQ channels [176,208]. Since the magnitude of the KCNQ current is regulated by muscarinic receptor activity (hence they are often called M-channels), the magnitude of the up-state can be regulated by ACH from cholinergic interneurons [176]. This allows cortical stimulation of cholinergic interneurons to augment the length of action potential trains in medium spiny neurons, in addition to the hyper-polarising stimulus of GABA from fast spiking interneurons [98,187]. However, in functionally immature medium spiny neurons GABA and ACH may show different effects on activity. Firstly, the resting membrane potential may be significantly more depolarised, meaning that M-channel activation may actually increase activity by reducing Na^+ channel inactivation. Secondly, GABA is initially an excitatory neurotransmitter, which would allow GABA to initially evoke action potentials.

Medium spiny neurons of the striatum can be differentiated by the expression of either D1 or D2 type dopamine receptors [101]. Both types of medium spiny neurons respond to dopamine secreted from projections which extend from dopaminergic neurons of the Substantia Nigra. In response to dopamine stimulation, Dopamine- and cAMP-regulated neuronal phosphoprotein (DARPP-32) mediates the modulation of multiple currents to augment the activity of medium spiny neurons [101]. D1-type dopamine receptors up regulate DARPP32 activity through cAMP-dependant phosphorylation, by contrast D2-type dopamine receptors down-regulate DARPP32 activity [115,141,204]. This allows each type of medium spiny neuron to orchestrate opposite responses to dopamine, where dopamine results in a depression of activity in D2-type medium spiny neurons but increases activity in D1-type medium spiny neuron.

The differential responses of medium spiny neurons of the striatum to dopamine are an important functional aspect of striatal physiology. The striatum functions as part of two parallel circuits in the basal ganglia, the indirect and direct pathways. How these two circuits integrate to a common function is most easily imagined in the case of motor control in the caudate of the striatum. Each pathway is a series of inhibitory and excitatory synapses culminating a negative (indirect pathway) and a positive (direct pathway) stimulus for the motor region of the cortex, which controls the motor output. Glutamatergic projections from the cortex provide the input into the striatum for both the direct and indirect pathways. Once in the striatum, the two pathways are distinguished by the sub-type of medium spiny neuron which are used, the direct pathway utilises D1-type medium spiny neuron and the indirect pathway utilises D2-type medium spiny neurons, this separation is crucial to the regulation of each pathway [54]. The direct pathway results in increased output from the thalamus to the cortex, which is a positive stimulus for motor action in the cortex [54]. D1-type medium spiny neurons from the striatum repress, via GABAergic projections, activity in neurons of both the external globus pallidus and substantia nigra reticulata[54]. Reduced activity from the external globus pallidus and substantia nigra are translated to reduced GABAergic output by both in the thalamus. By contrast, the indirect pathway results in reduced output from the thalamus to the cortex, acting to repress motor action [54]. D2-type medium spiny neurons inhibit neurons of the internal globus pallidus that have GABAergic projections into the sub-thalamus [54]. The sub-thalamus then has glutamatergic projections which excite neurons of the external globus pallidus and substantia nigra [54]. Therefore, where the direct pathway is inhibiting GABAergic projections of the globus pallidus and substantia nigra, the indirect pathway is stimulating these inhibitory outputs to the thalamus, resulting in reduced output from the thalamus to the cortex. D1 and D2 type neurons are at the start of the direct and indirect pathways, respectively. This allows dopamine secretion in the striatum to simultaneously augment the sensitivity of each pathway at their start. Due to the different responses of D1- and D2- type medium spiny neurons to dopamine, this means that dopamine in the striatum will increase the output of the direct pathway and reduce the output of the indirect pathway. This puts the substantia nigra in a position to fine tune the strength of each pathway through the basal ganglia, and therefore the sensitivity of the system overall to initiate motor activity.

DARPP-32 provides a dopamine-dependant mechanism for mediating of activity in D1 and D2 type medium spiny neurons. This mechanism influences function of multiple ion channels by intracellular modifications, which together augment the cell's electrophysiological activity. In the D1 type medium spiny neurons, dopamine stimulation increases the peak currents for L-type Ca^{2+} channels, increases NMDA receptor peak currents, decreases $GABA_A$ currents, traffics more AMPA receptors to the membrane, reduces N-type Ca^{2+} channel peak currents and augments Nav1.2 currents [54]. By contrast, in the D2 type medium spiny neurons, dopamine stimulation results in reduced L- and N-type Ca^{2+} channel currents, reduced AMPA receptor peak currents, increases K_{ir3} currents and augments Nav1.2 currents [54]. These changes allow dopamine to increase the sensitivity of D1 type medium spiny neurons and simultaneously reduce the sensitivity of D2 type medium spiny neurons. Cholinergic interneurons also express dopamine receptors, which augments their activity, increasing the secretion of ACh to supress medium spiny neuron activity by increasing KCNQ current magnitudes [193].

Aims of the study

This study aims to provide new insights into the development of electrophysiological function of iPS-cell derived neuronal cultures. Astrocyte secreted factors, in the form of astrocyte conditioned medium (ACM), will be used as a strategy for improving the function of short protocol-derived neuronal cultures. The benefits to electrophysiological function evoked by ACM will be closely scrutinised as a protocol for enhancing short differentiation protocols. Further, enhanced functional properties evoked by ACM will be considered as defined strategies for directly enhancing functional maturation by activity-linked means.

In addition to enhancements developed for short protocol differentiation of neurons from iPS cells, protocols will be considered for deriving astrocytes from iPS cells. iPS cell derived astrocytes could prove invaluable as a tool for enhancing iPS cell derived neuronal cultures and for modelling disease mechanisms in either cell type in mixed cultures.

Further, enhanced short differentiation protocols will be assessed by examining the consistency and functional maturity activity observed in iPS-cell derived neurons developed for studying Huntington's disease (HD).

Chapter 2: Methods

Electrophysiology

The electrophysiological phenotype of differentiating neurons was characterised using whole cell patch clamp at weeks 1, 2 and 3 post plate-down. Recordings and protocols were performed using an Axopatch 200B amplifier (Molecular Devices, Sunnyvale, California, USA), an Axon Digidata 1320 DAC/ADC converter (sampling at 10 Khz) and the accompanying Clampex 9.2 software (Molecular Devices, Sunnyvale, California, USA) with a Bessel low-pass filter applied at 10 Khz. The Axopatch 200B amplifier supports both current and voltage clamp, during current clamp the amplifier dictates the current through the membrane and records evoked voltage changes. Conversely, in voltage clamp the amplifier dictates the membrane voltage across the membrane and records evoked currents. The analyses of all recordings were performed offline using Clampfit 9.2 software (Molecular Devices, Sunnyvale, California, USA). Glass micropipettes for patch clamp were drawn from WPI borosilicate glass capillaries (WPI,) using a Narishige PP-830 two stage pipette puller (Narishige Int. Ltd., London, UK), the heat settings used to draw pipettes were aiming at producing tip resistances (when in the bath solution) between 5 and 8 MΩ. Although not routine, micropipettes were heat polished when facing certain more difficult cell cultures or time points using a Narishige Microforge, the heat settings of the pipette puller were also adjusted to account for changes in resistance due to heat polishing the tip. The internal solution contained (in mM, all from Sigma-Aldrich, Poole, Hants., U.K.) 117 KCl, 10 NaCl, 2 $MgCl_2$, 1 $CaCl_2$, 11 EGTA, 2 Na_2.ATP and 11 HEPES, and the external solution (ECS) contained (in mM, all from Sigma-Aldrich, Poole, Hants., U.K.) 135 NaCl, 5 KCl, 5 HEPES, 10 glucose, 1.2 $MgCl_2$ and, 1.25 $CaCl_2$. The pH of both solutions were measured using a digital pH meter, and then by stepwise addition of aqueous NaOH (1 M) to the external solution or KOH (1 M) for the internal solution the pH was increased to 7.4. The junction potential generated by

these solutions was calculated using clampfit 9 as 3.9 mV, which was considered relatively small. To assure the quality of the whole cell patch data, recordings were made only from cells where the access resistance was below 25 MΩ and the leak current was very small (aiming for a total resistance above 1 GΩ at rest, held at -70 mV). Recordings were performed at room temperature and in the ECS, but each coverslip of cells was replaced after 3 hours.

Cells which had clear and accessible cell bodies which appeared alive were selected for electrophysiological measurement. Although no deliberate bias was used to select cells with very obvious and mature neuronal morphologies, cells which were clearly undifferentiated, dead or showing morphology very different to neurons were ignored.

Membrane capacitance was calculated using the shape of the transient current elicited during the charging or discharging of the capacitance. The change in the charge stored across the capacitance is the integral of the current over time during this transient current. The capacitance therefore could be calculated using the change in charge stored across the capacitance divided by change in voltage. The series resistance, or access resistance to the cell by the patch pipette, was considered the only considerable resistance in series with the membrane capacitance. Therefore the non-linear change in current during the charging of the capacitor had a time-constant determined by the capacitance and the access resistance of the cell. In practice, the patch-clamp amplifier used a variable capacitance and resistance in the positive feedback of the amplifier, which iteratively changed the values of its series resistance and capacitance until they matched that of the cell and pipette. This allowed this circuit to charge whilst the membrane capacitor discharged and discharge as the membrane capacitor charged, cancelling out the effects of membrane capacitance during voltage clamp recordings, as well as measuring these parameters. Very high access resistances (above 25 MΩ) resulted in the cell being rejected as such high access resistances would result in voltage-inaccuracies due to the effective voltage divider caused by the access resistance and ion channels.

Using current clamp the membrane potential at rest and the presence, or absence, of spontaneous action potentials were recorded. The current was maintained at 0pA in standard ECS over 1-2 minutes of recording, allowing for a recording of the cells natural

electrophysiological behaviour. The resting membrane potential was calculated by taking the mean voltage during the recording. Spontaneous action potentials were represented by depolarising spikes that reached or exceeded 0mV and then rapidly returned to the baseline voltage. To measure the ability to fire action potentials (induced action potentials), a current step protocol was employed; continuous current injection was used to artificially hold the membrane voltage at approximately -70 mV, from this a 100 ms current step was applied to depolarise the cell, which increased stepwise from 0 pA to 180 pA in 10 pA increments and then between each step at least 100 ms was allowed for recovery. Induced action potentials were represented by rapid depolarising spikes that were elicited during a more gradual depolarisation caused by the membrane capacitance charging in response to the current step. Cell input impedance was measured using sub-threshold voltage injections during current step protocols and Ohm's law, this data was corroborated by low voltage data in voltage ramp protocols and Ohm's law. The analysis of action potential shape and threshold is explained in the Analysing induced action potentials section of the methods.

Using voltage clamp, the magnitude and presence of both voltage activated Na^+ and K^+ currents were measured. A voltage step protocol was used to activate both currents, from being held at -70 mV a 200 ms step was applied which increased from -120 to +50 mV in 10 mV increments per sweep. Eight pre pulses (P/N = 8) were used prior to each so that the leak current can be subtracted from the final current recording online using Ohm's law. Isoosmotic replacement (135 mM) of NaCl with N-methy-D-glutamine chloride (NMDG, Sigma-Aldrich, Poole, Hants., U.K.) was used to confirm the presence of voltage activated Na^+ currents by removing the ion which the channels are permeable to. The addition of 10mM tetraethyl ammonium chloride (TEA, Tocris, Bristol, Avon, U.K.) to the ECS was used to confirm the presence of voltage activated K^+ currents because TEA is a potent antagonist of voltage activated K^+ channels. In the absence of NMDG, Na^+ currents were represented as a fast activating inwards spike at the start of voltage steps above -40 mV, the magnitude of the Na^+ current at each voltage was measured using the peak inwards current at the start of the voltage step. In the absence of TEA, K^+ currents were a slower activating current rose to an outwards plateau during voltage steps above -20 mV, the average current during this plateau was measured to give the magnitude of the K^+ current. The presence or absence of spontaneous miniature synaptic currents was assessed using continuous recording for 10

minutes in voltage clamp, holding at -80, -20 or +20 mV to avoid the generation of action potentials. To further distinguish these currents from whole action potentials 0.1 µM Tetrodotoxin (TTX, Tocris, Bristol, Avon, U.K.), a potent antagonist of voltage activated Na^+ channels, was added to the ECS. The addition of 10 µM bicuculline (Tocris, Bristol, Avon, U.K.), an antagonist of $GABA_A$ receptors, was used to determine the presence of GABA-dependant synaptic activity. Miniature synaptic currents, regardless of the type of synapse involved, were observed as small inwards (downwards) rapidly activating and more steadily inactivating currents, roughly -50 pA peak at -80 mV due to the concentration gradients of the ions in the patch clamp solutions. At +20 mV their currents were in the opposite direction. The voltage dependant profile of activation and steady state inactivation for the cells' Na^+ current was measured using a dual voltage step protocol; from a holding of -90 mV a 200 ms variable (from -120 to 0 mV in 5 mV increments) step was performed followed by a 100 ms constant 0 mV step. The current evoked by the first step was used showed the voltage dependant activation of the Na^+ current, whilst the current evoked by the second step was used to show the voltage dependant inactivation of Na^+ current as this current was lost as the first step increased in magnitude. In order to increase accuracy the errors in the step voltages were removed offline by subtracting the junction potential (calculated using Clampfit 9.2) was subtracted and the voltage loss due to the series resistance (the access resistance into the cell) was accounted for mathematically (see series resistance compensation equation). Using the adjusted voltage, evoked currents and the driving force for Na^+ at each voltage in the patch clamp solutions, the evoked Na^+ currents were converted mathematically to conductance and then normalised them against maximal conductance (G/Gmax). For both the activation and inactivation of Na^+ channels the normalised conductance was plotted against adjusted voltage and the point at which the two curves transect was recorded as the voltage of the peak Na^+ window current (referred to as the Na^+ window).

$$V_m = V_t \cdot \frac{V_t{}_I - R_{series}}{V_t{}_I}$$

Series resistance compensation equation. Vm = membrane voltage, Vt = total voltage, Rseries = series resistance and I = current.

In order to record voltage activated Ca^{2+} currents, temporal isolation of the voltage activated Ca^{2+} currents from voltage activate Na^{+} currents was achieved using their different activation voltages on a voltage ramp protocol; from a holding of -70 mV the voltage stepped to -120 mV momentarily and then performed a continuous linear change in voltage over time from -120 to 50 mV over 500 ms. A modified ECS containing 27 mM $BaCl_2$ (Sigma-Aldrich, Poole, Hants., U.K.), isoosomotically replacing NaCl, was used to amplify the magnitude of voltage activated Ca^{2+} channels and inhibit their steady state inactivation, this was used to both confirm their identity and increase their visibility. The addition of 2 µM nifedipine (Tocris, Bristol, Avon, U.K.) was used to determine the contribution of L-type Ca^{2+} channels to the total evoked Ca^{2+} current. The presence of ionotropic GABA ($GABA_A$) receptors was determined by a current evoked by a 5s application (using an Intracel RSC160 rapid perfusion system) of 300 µM ɣ-amino buyturic acid (GABA, Sigma-Aldrich, Poole, Hants., U.K.) in ECS during voltage clamp with a holding voltage of -70mV. To produce a current-voltage relationship curve of the GABA evoked current, 300 µM GABA was applied using the rapid solution changer during the step of a voltage step protocol; a 10 second voltage step from a holding of -70 increasing in 20 mV increments from -100 to 20 mV.

The patch-clamp protocols were performed in such an order as to minimise the effects of each protocol on other electrophysiological parameters being measured. To this end, the current clamp protocols (gap free and current steps) were performed first, as these protocols did not involve the addition of pharmacological reagents. Importantly these protocols were used to measure the neuron's native membrane potentials, spontaneous activity and their native ability to fire induced action potentials. Following this, the voltage-clamp protocols were performed, most of which required solution application from the rapid solution changer. Firstly, the voltage step protocols were used to measure the voltage activated Na^{+} and K^{+} currents, and the activation and inactivation profiles for the Na^{+} current. However, both the NMDA and TEA used during these experiments were shown to have very fast and effective wash-off. A voltage gap-free protocol was then used to measure miniature synaptic currents, if any were observed then bicuculline and TTX were applied,

which again both showed effective and rapid wash-off. Following this $GABA_A$ currents were assessed whilst being held at -70 mV and then Ca^{2+} currents using a voltage ramp protocol and high $BaCl_2$ solution. The GABA showed rapid wash-off, but the $BaCl_2$ solution sometimes showed inhibition of voltage activated K^+ currents which washed off more slowly. Therefore, following each cell being measured, subsequent cells were then chosen away from the flow of the rapid solution changer flow to reduce the effects of solutions applied during the previous sample.

Analysing induced action potentials

During functional maturation the shape of induced action potentials varies significantly. The shape of action potentials varies in the speed and extent of both depolarisation and repolarisation. A mature neuronal action potential should show a very fast depolarisation resulting in a peak significantly above 0 mV, followed by a rapid repolarisation which reaches voltages significantly more polarised than the threshold voltage. By contrast, immature neurons show slow events that reach voltages only very slightly above 0 mV and do not significantly hyperpolarise the cell. During functional maturation these multiple features of action potentials are augmented, resulting in action potential shapes that are increasingly fast and sharp.

Qualitatively it is relatively easy to recognise an immature neuronal action potential compared to a mature one (figure 2.1 A). Developing a quantitative measure for action potential sharpness is more complex, as there are many individual features of action potentials which can be measured and together give an accurate picture of the action potential shape. Ideally however, we would generate a standard method of analysis which takes into account these multiple factors and can be considered a direct measure of sharpness and depolarisation extent.

To assess and develop a standard method for action potential shape 10 evoked action potentials were selected which showed increasing sharpness qualitatively (figure 2.1 A and B). Since action potential sharpness is essentially as a direct result of the rates and length of depolarisation and repolarisation over voltage, orbital plots where the differential of voltage against time (dV/dT) is plotted against voltage (figure 2.1 B). These plots show us how the rapidly the membrane voltage changes during the action potential. Time progresses around

the orbit in these graphs. The orbital graph starts with a slightly changing voltage due to graduated change in voltage elicited by the current step protocol. Once threshold is reached, an upwards inflection is observed as the voltage activated Na^+ channels open and the depolarisation phase of the action potential begins. This rises to a positive peak representing the maximal rate of depolarisation before declining back towards 0 mV/ms. The point at which it reaches 0 mV/ms represents the very peak of the action potential where the Na^+ channels inactivate and the K^+ channels become the dominant force and begin to repolarise the membrane potential. This leads to a negative peak which represents the repolarisation of the cell, significant voltage activated Ca^{2+} currents will split this peak into a less negative plateaux followed by a more negative peak when the Ca^{2+} channels have inactivated. The peak then decays back towards 0 mV/ms, in the case of a mature action potential this is significantly more polarised than the threshold.

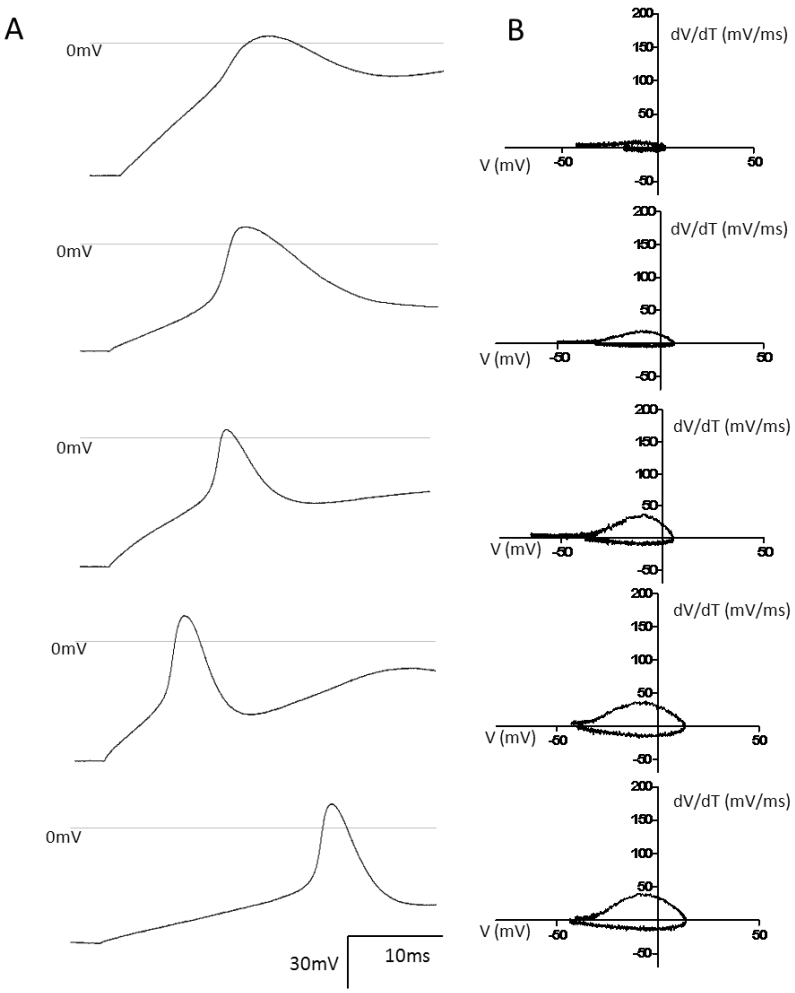
A
0mV
0mV
0mV
0mV
0mV
30mV
10ms
B
dV/dT (mV/ms)
V (mV)
200
150
100
50
-50
-50
50

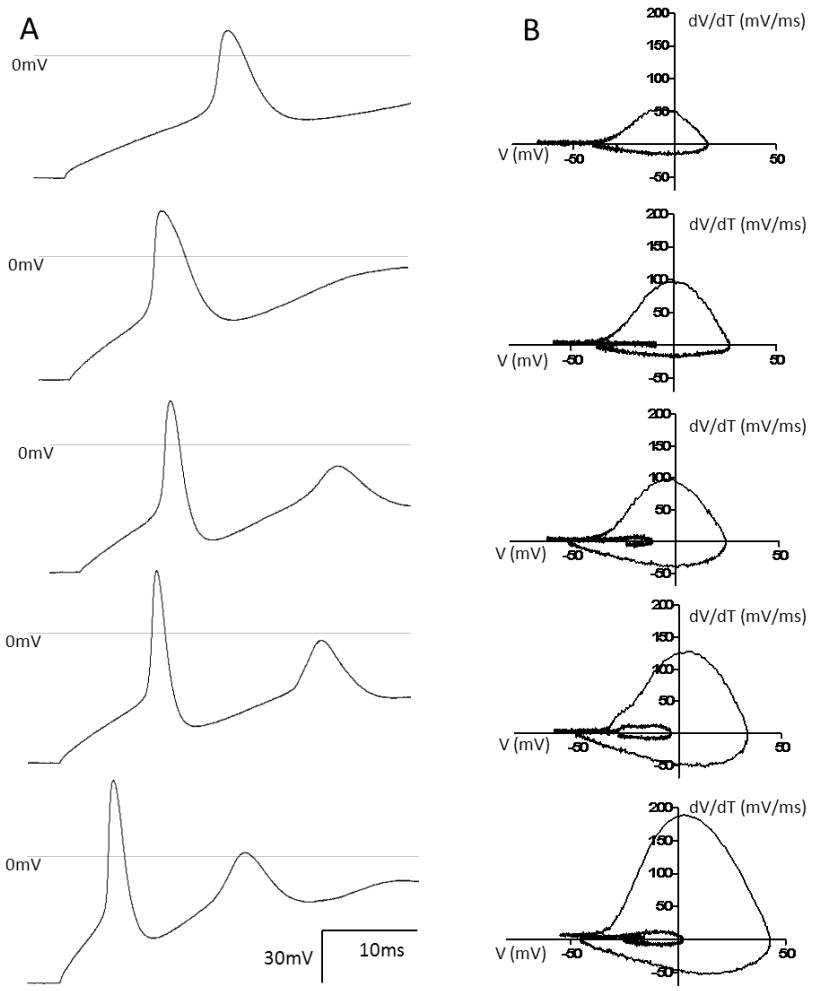

Figure 2.1: A series of evoked action potentials assessed for their maturity, from least sharp to most sharp.

A) Voltage traces during the current-step protocol showing the evoked action potential.

B) Orbital graphs (dV/dT against V) for each of the evoked action potentials from panel A.

From the voltage trace (voltage against time) during an evoked action potential we can directly measure a few characteristics. Firstly, the width of the action potential at half height is a measure of how fast the action potential occurred. To measure this we calculated the voltage half way between threshold and peak, then the difference between the times at which this voltage is reached during depolarisation and then repolarisation. In this study the half voltage was chosen between the peak and the threshold, instead of between the peak and the peak overshoot after repolarisation, because the threshold value was found to be more consistent and many immature action potentials showed no overshoot following

repolarisation. To assess the extent of the action potential depolarisation and repolarisation, the peak voltage and extent of overshoot can be measured directly. Using the orbital graphs, it is possible to measure the maximal rates of both depolarisation and repolarisation during an action potential. Interestingly however, the modulus of the area inside the orbital graph is determined, in part, by all of these factors. The height of the upper peak is the rate of depolarisation, the height of the lower peak is the rate of repolarisation and the width of both peaks is the extent of depolarisation. So therefore, the area inside the orbit can be considered to be proportional to the speed and the extent of the action potential. However, the rates of both depolarisation and repolarisation are highly sensitive to noise during the action potential. Therefore, the data was smoothed by substituting averages for every 5 data points in.

Number	Peak (mV)	Undershoot (mV)	Width (ms)	Peak dV (mV/ms)	Peak –dV (mV/ms)	Orbit Area (mV^2/ms)
1	4	0	10	10.1	-5	269
2	8.9	-0.4	7.4	31.1	-7.3	722
3	5.3	-2.2	4.4	35.5	-9.8	1172
4	13.6	-5.6	3.2	41	-15.2	1727
5	14	-7.6	3.4	39.7	-16.3	1738
6	16.3	-4.1	3.4	73	-23.1	2612
7	27.5	-8.1	3.1	98	-22.6	4365
8	24.3	-13.8	1.9	103	-44.2	5542
9	33.8	-15.2	1.5	144	-51.1	8201
10	43.3	-15.7	1.4	189	-56.2	10884

Table 2.1: Measured shape properties of 10 action potentials from figure 2.1. Peak: the absolute highest voltage achieved during the action potential. Undershoot: Following repolarisation how far was the membrane voltage hyperpolarised compared to threshold. Width: the difference in time from the half height voltage (between threshold and peak) during depolarisation to hyperpolarisation. Peak dV: Peak positive rate of change of voltage (max depolarisation rate). Peak –dV: Peak negative rate of change of voltage (max

repolarisation rate). Orbit area: The modulus of the sum of the integrals of dV/dT against V from threshold to overshoot, resulting in the area inside the orbit.

Following these analyses, it is immediately clear that they correlate well with each other, where action potentials are qualitatively appear sharp, short widths (at half height) are observed. Further, this correlates well with increased maximal depolarisation and repolarisation rates (table 2.1, figure 2.1). These data also correlate well with a higher peak voltage and undershoot following repolarisation. The area inside the obit (sum of the modulus of the integrals of dT/dV against V) also correlates very well with all of these measures. Further, the area under the curve appears most able to distinguish differences in the action potential shape across all levels of maturity. This is because certain measures become less able to distinguish action potential shapes as they reach plateaux at either end of the spectrum, or are simply more variable. For example, peak depolarisation and peak voltage show plateaus when assessing action potentials 1-5 whereas the peak repolarisation shows a plateau when assessing action potentials 8-10. The half width shows very little sensitivity and appears only useful to demonstrate very significant differences in shape. The area inside the orbit however, remains sensitive across all maturities whilst correctly identifying very similar action potentials, for example in the case of 4 and 5. This is largely because the area inside the orbit is actually dependant on multiple of the above factors. Therefore, the area inside the orbit is potentially a powerful quantitative technique for providing a single measure of action potential maturity.

The threshold for an action potential is the voltage at which the action potential is initiated due to the response of voltage activated Na^+ channels. The threshold can be estimated using the original voltage trace, but this is fairly inaccurate. The dV/dt vs. V orbits generally shows a more obvious inflection at the very start of the threshold voltage, because the orbital graph is representing the action potentials in terms of rate of change of voltage. The second order differential was also attempted but produced very variable results from some action potential shapes.

Calcium imaging

To produce a more complete profile of the functional expression of voltage activated Ca^{2+} channels, Fura-2 Ca^{2+} imaging was used to detect depolarisation dependant Ca^{2+} influx at week 1. Fura-2 AM (Invitrogen) was loaded into cells for 30 minutes at 37 ^{o}C at 4 µM in culture medium (with 0.04% DMSO, Sigma-Aldrich, Poole, Hants., U.K.). Once loaded, the cells were moved to a perfusion chamber mounted on the stage of an inverted Olympus IX-70 microscope (Olympus Microscopy, Essex, U.K.) and continuously perfused in ECS. Fura-2 was alternately excited by 50-100 ms pulses of light at 340 and 380 nm using a monochromator (Cairn Instruments, Faversham, Kent, U.K.) through a 400x quartz, oil immersion objective. The resulting re-emission at 505 nm evoked by excitation at either 340 or 380 nm was recorded using a CCD camera (Hamamatsu Orca, Hamamatsu Photonics K.K., Hertfordshire, U.K.) every 3 seconds, online 2x binning was used to increase the signal intensity at the expense of resolution but without sacrificing the signal to noise ratio. Off-line, the image acquisition software (OptoFluor, Cairn Instruments, Faversham, Kent, U.K.) was used to analyse the captured images, measuring the fluorescent intensities evoked by excitation at 340 and 380 nm within regions of interest which circled the cell bodies of neurons. The background fluorescence from each excitation frequency was independently measured using regions of interest circling an empty region of the coverslip. The background fluorescence was then subtracted from the fluorescence intensities measured at each of the cell bodies of interest. The ratio of fluorescence intensities (i380/i340, background subtracted) was calculated against time for each cell and used as an indication of changes in intracellular Ca^{2+} concentration over time. A 10 s application of a modified ECS where 50mM KCl was added (high K^{+}), isoosmotically replacing NaCl, was applied directly to the cells using the rapid perfusion system. The high K^{+} solution was used to depolarise the cells, evoking Ca^{2+} influx through voltage activated Ca^{2+} channels, which was measured as a sharp increase in the ratio of the fluorescent intensities (i380/i340) of Fura-2. Following a high KCl application and given 200 s to recover in ECS, the same high K^{+} solution was applied with the addition of a specific antagonist to one sub-type of voltage activated Ca^{2+} channels (10 µM nifedipine, 0.1 µM conotoxin, 0.1 µM agatoxin and 0.1 µM SNX482 (all from Tocris, Bristol, Avon, U.K.) for L-, N-, P/Q- and R- type channels respectively) and again allowed to recover in ECS. Subsequently high K^{+} solution applications were added alternately with high K^{+}

applications with different antagonists to voltage activated Ca^{2+} channel sub-types, and allowed to recover for 200s inbetween. For each application of high K^+ solution, with or without an antagonist, the area under the Fura-2 fluorescent ratio (i380/i340) against time curve was calculated by taking the sum of the integrals of each 3s linear line joining each data point from the start of the application to the ratio having reached baseline. The baseline Fura-2 fluorescent ratio was calculated by linear regression of the Fura-2 fluorescent ratio prior to an application of high K^+ and after the cell has returned to baseline following high K^+ application (usually approximately 150 s). The integral of the baseline Fura-2 fluorescent ratio line was then calculated between the same time limits as the integral of the actual curve during an application of high K^+, to give the assumed area under the curve had the application not occurred. The assumed area under the curve had a high K^+ application not occurred was then subtracted from the actual area under curve for each high K^+ application, leaving only the increase in intracellular Ca^{2+} due to the high K^+ application. The antagonist free high K^+ applications were used to demonstrate the presence and magnitude of each cell's voltage activated Ca^{2+} response, and further to show run down of this response with time. Linear regression was used to calculate the run down over time for the high K^+ induced Ca^{2+} influx which was used to estimate the expected area under curve for each high K^+ application without the antagonist, from which the observed area under curve (with the antagonist) could be subtracted to calculate the amount of inhibition. The amount of inhibition was used as a measure of the contribution to the total Ca^{2+} influx from each sub-type of Ca^{2+} channel.

Fura-2 based Ca^{2+} imaging was also used as an indirect measure of the direction of chloride currents from $GABA_A$ stimulation. During neuronal development, in response to GABA stimulation, the Cl^- concentration gradient switches from being depolarising (Cl^- moving outwards) to hyperpolarising (Cl^- moving inwards). Therefore, GABA responses switch from being excitatory to inhibitory for neurons firing an action potential. Using the same Ca^{2+} imaging set up as before (above), the cell responses to GABA were measured indirectly, using the Ca^{2+} influx due to GABA-evoked depolarisation. In this protocol, 10s applications (using the rapid perfusion system) of high K^+ solution, 300 µM GABA both in normal ECS and a low Cl^- ECS, NaCl was isoosmotically replaced with Na · isethionate (Sigma-Aldrich, Poole, Hants., U.K.). The high K^+ solution was used as a positive control for voltage activated Ca^{2+}

cells, to exclude cells not able to respond. In the presence of the low Cl^- then the Cl^- concentration gradient will always be outwards (depolarising) and therefore elicit a response from the voltage activated Ca^{2+} channels. By contrast a Ca^{2+} response to GABA in ECS will only be observed in cells where their native concentration gradient to GABA is outwards (depolarising). Therefore a cell which showed a Ca^{2+} influx response to GABA in both ECS and low Cl^- have a natively excitatory response to GABA, whereas cells which only showed a Ca^{2+} response to GABA in low Cl^- have a natively inhibitory response to GABA.

Immunostaining

The media was aspirated off, replaced with 4% paraformaldehyde (Sigma-Aldrich, Poole, Hants., U.K.) and fixed for 10 minutes at 4 ^oC in a lab refrigerator. The cells were then washed 3 times in PBS before the blocking solution (PBS (Sigma-Aldrich, Poole, Hants., U.K.) with 10% BSA (Sigma-Aldrich, Poole, Hants., U.K.) and 1% Triton X-100 (Sigma-Aldrich, Poole, Hants., U.K.)) was added and incubated for 1 hour at room temperature. Following the blocking solution, 3 PBS washes were performed and the primary antibodies prepared (PBS with 10% BSA, 1% Triton X-100 and primary antibody at the dilution in Table 2.1). The samples were incubated over night at 4 ^oC with the primary antibodies. The following day the primary antibodies were removed and the cells were given 3 PBS washes, the secondary antibodies were then added (PBS with 10% BSA, 1% Triton X-100, secondary antibodies at the dilution in Table 2.2, and 10% normalised serum of the same species (Life Technologies, Paisley, U.K.)) and incubated at room temperature for 1 hour. Three PBS washes were performed and the Hoechst nuclear stain was added for 30 minutes at room temperature. The cells were PBS washed 3 times and then mounted in a drop of fluoromount G (Life Technologies, Paisley, U.K.) solution on a glass microscopy slide. Samples were then mounted in fluoromount G on microscopy slides were dried at 4 ^oC overnight, then stored like that in a slide rack. The cells were imaged on a Leica DMI microscope with Leica fluorescent microscopy camera (Leica, Milton Keynes, Buckinghamshire, U.K.).

Target	Cell Type	Manufacturer	Dilution	Species	Lot No.
Map2ab	Neuron	Sigma-Aldrich	1:200	Mouse	048k4836
β3 tubulin	Neuron	Sigma-Aldrich	1:1000	Mouse	088k4799
GFAP	Astrocyte	Dako	1:1000	Rabbit	Z0334
S100β	Astrocyte	Abcam	1:500	Mouse	AB66028
Nestin	Progenitor	Millipore	1:1000	Rabbit	LV1635955
DARPP32	Neuron(MSN)	Cell Signalling	1:400	Rabbit	2306

Table 2.2: A list of primary antibodies used.

Target	label	Manufacturer	Dilution	Species	Lot. No.
Rabbit	AF 488	Life Technologies	1:2000	Donkey	A21203
Mouse	AF 594	Life Technologies	1:2000	Donkey	A21206

Table 2.3: A list of secondary antibodies used.

Cell Culture

Coating and preparing, coverslips, culture dishes and multi-well plates

Human induced pluripotent stem (iPS) and embryonic stem (ES) cell cultures were grown on matrigel coated 6-well plates or 6cm dishes. The matrigel (BD Biosciences, Oxford, U.K.) was diluted (using the recommended dilution factor for each batch of matrigel) in DMEM:F12 (1:1, Life Technologies, Paisley, U.K.), as quickly as possible to avoid the thawing matrigel from aggregating, the plates or dishes were then flooded with 2 ml of diluted matrigel. The plates or dishes were then incubated at 37 ^{o}C for 1 hour before being aspirated off immediately before adding cells.

Poly-L-lysine (PLL) was used as a substrate for stem cell derived neuronal and astrocyte differentiation plate downs. The PLL (Sigma-Aldrich, Poole, Hants., U.K.) was diluted to 100 µg/ml in sterile water (Invitrogen), placed on the coverslip as an 80 µl droplet and then incubated at 37 ^{o}C for 30 minutes. The PLL droplet was then aspirated off the coverslip and the coverslip was left to dry in a tissue culture hood overnight. The coverslip was then washed with a droplet of PBS to remove excess. In addition to PLL coating the coverslips were coated with laminin. The laminin (Stemgent, Cambridge, MA, U.S.A.) was diluted to 50µg/ml in PBS (Life Technologies, Paisley, U.K.), placed on a 13mm glass coverslip as an 80 µl droplet and then incubated at 37 ^{o}C for at least 30 minutes. The laminin was not removed until ready to drop cells on the coverslips, when ready the laminin on the coverslip was aspirated, the coverslip was quickly washed with an 80 µl PBS droplet and then the cells placed on the coverslip to avoid the laminin drying. The PBS droplet was then aspirated immediately prior to adding the cells.

In the latter part of chapter 3, where the rosette differentiation was used, Poly-D-lysine and Matrigel were used in preference to PLL and Laminin. The coverslip was poly-D-lysine (Sigma-Aldrich, Poole, Hants., U.K.) coated using the same protocol as poly-L-lysine (above). The coverslip was matrigel coated using the same protocol as for coating tissue culture plastic with matrigel (above) for the iPS and ES cells, except using 80 µl droplets on the coverslips instead of flooding the well.

Poly-hema was used to coat tissue culture flasks to avoid the EZ-sphere cultures from adhering to them. The poly-hema (Sigma-Aldrich, Poole, Hants., U.K.) was dissolved in 95% ethanol with sterile water at 10 mM overnight by incubation at 37 ^{O}C. The poly-hema was then added to tissue culture flasks, 3 ml for a T25 flask, and left to dry in a tissue culture hood overnight with each flasks screw top open.

Human iPS and ES cell culture:

Fibroblasts extracted from an individual not genetically predisposed (33 and 18 CAG repeats, referred to as HD33) to Huntington's disease and a sibling suffering with adult Huntingdon's disease (66 and 18 CAG referred to as HD66) as well as two childhood onset patients with much longer repeat lengths (extended alleles of 109 CAG repeats and 180 CAG repeats, referred to as HD109 and Q180 lines respectively) were all reprogrammed by retroviral insertion of klf-4, Oct3/4, c-myc and sox-2 [218]. Genetic analysis revealed no further repeat expansion or contraction as a consequence of reprogramming and cell culture and normal karyotypes [218]. These induced pluripotent stem cells (iPS) cells were a kind gift of Prof. Clive Svendsen of the Regenerative Medicine Institute at Cedars Sinai Medical Centre (Los Angeles, California, USA). As well as the human iPS cell lines, H9 human embryonic stem (ES) cell cultures were also cultured. Both the human ES and iPS cells were cultured in Matrigel (BD Biosciences, Oxford, U.K.) coated 6 well tissue culture plates in mTeSR 1 medium (Stem Cell Technologies, Grenoble, France), in a standard tissue culture incubator (37 ^{O}C, 5% CO_2). To avoid differentiation the pluripotent stem cell colonies were visually inspected using a phase contrast microscope every day, any differentiating colonies were removed physically with a sterile p200 pipette tip. Every week the cells were passaged into new Matrigel coated 6 well tissue culture plates using Versene(Life Technologies, Paisley, U.K.) and cell scraping.

Astrocyte isolation, culture and conditioned medium

Striatal astrocytes were isolated from P1 or P2 post natal mice (wild type, Black 6). Striata were dissected and then triturated using a 1 ml pipette in Hank's buffered saline (Peprotech, London, U.K.) to fragment the tissue. A single cell suspension of striatal cells was then produced by enzymatic dissociation using TrypLE express (Life Technologies, Paisley, U.K.) and DNAse1 (0.1 mg.ml-1, Sigma-Aldrich, Poole, Hants., U.K.) for approximately 20 minutes at 37 ^{o}C with intermittent trituration by 1ml pipette. The digestion was stopped by centrifuging the cells to a pellet (1000 rpm, 1.5 minutes) and washing out the enzyme with astrocyte growth medium (DMEM supplemented with 1% Glutamax (Life Technologies, Paisley, Strathclyde, U.K.), 10% fetal bovine serum (Sigma-Aldrich, Poole, Hants., U.K.) and 1% of a cocktail of penicillin, streptomycin and fungizone (Anti-Anti, Life Technologies, Paisley, Strathclyde, U.K.). The cells were cultured in standard tissue culture flasks in a standard tissue culture incubator (37 ^{o}C, 5% CO_2) and given astrocyte growth medium twice a week. The cultured striatal cells were allowed to reach confluency before being passaged at a 1:3 ratio using TrypLE express. Following the second passage and being grown to confluency, the astrocytes were used to condition medium for use as the medium for differentiating neuronal cultures. To condition medium, the astrocyte medium was aspirated and the astrocytes were washed with PBS, to remove any remaining astrocyte medium and avoid contamination in the neuronal medium. The astrocytes were then cultured in the base neuronal medium (DMEM:F12 (1:3 or 1:1, see neuronal differentiation medium) and 2% B27) for 3 days. The medium was then removed and filtered through a disposable Nalgene 0.22 µm suction filter (120-0020 Sterilization Filter, Nalgene), then frozen at -80 ^{o}C in 25 ml aliquots for later use. Using quantitive ELISA (Quantikine Mouse CCL2/JE/MCP-1 immunoassay, R & D Systems, Abingdon, Oxon., U.K.) for an astrocyte secreted factor found not to be influenced by Huntington's disease, CCL2 (chemokine C-C motif ligand 2), the astrocyte conditioned medium was standardised by dilution with neuronal base medium. The standardised conditioned medium was then mixed 1:1 with neuronal base medium and supplemented with factors defined in the neuronal differentiation media section.

EZ sphere differentiation

Induced pluripotent stem cells and human embryonic stem cells were partially differentiated into an easy to maintain, non-adherent culture of neural progenitor cells known as EZ spheres [56]. The EZ spheres were made form physically lifted ES or iPS cell colonies (using a cell scraper) from the Matrigel coated 6 well plates using a cell scraper and were allowed to settle at the bottom of a 14 ml Falcon tube. The medium was then replaced with EZ-sphere medium (In Stemline (Sigma-Aldrich, Poole, Hants., U.K.), 100 ng.ml-1 EGF (Millipore GF144, Merck Millipore, Billerica, MA, U.S.A.) 100 ng.ml-1 bFGF (Millipore GF003, Merck Millipore, Billerica, MA, U.S.A.) and 5 µg.ml-1 heparin (H3149, Sigma-Aldrich, Poole, Hants., U.K.)), washed with the same medium again to remove any remaining MtESr medium and the cells were then placed in poly-hema (see poly hema coating) tissue culture flasks. The EZ spheres were fed with EZ sphere medium every other day and passaged weekly using a mechanical tissue chopper (Mcllwain tissue chopper, Mickle Engineering, Gromshall, UK) in 0.2 mm by 0.2 mm pieces. The EZ spheres were allowed to grow through at least 4 passages prior to use, and mostly only used between 10 and 30 passages as this resulted in the most consistent differentiation.

The EZ spheres were used to produce terminally differentiating cultures of neurons. To inhibit apoptosis during plate down, prior to plating 1µM Rho Kinase inhibitor Y-27632 (ab120129, Abcam, Cambridge, U.K.) was added to the EZ sphere medium for 20 minutes at 37 ^{o}C. The EZ spheres were then disaggregated by incubating them in 2ml TrypLE express at 37 ^{o}C in a heated water bath for between 5 and 10 minutes, depending on how quickly a single cell suspension was formed. The enzyme was then washed out twice in neural differentiation medium by centrifuging the cells to a pellet (1000rpm, 1 minute). The cells were then counted using a haemocytometer and phase contrast light microscope, dead cells were excluded by staining the cells by mixing them 1:1 by volume with trypan blue (Life Technologies, Paisley, U.K.). The cells were then plated at a density of 20,000 cells per well in 80µL drops on poly L-lysine (see PLL coating) and laminin (see laminin coating) coated coverslips in 24 well tissue culture plates. After between 2 and 4 hours in a drop on the PLL-Laminin coverslips the wells were flooded with 400µL of differentiation medium (see neuronal differentiation media). The differentiated neurons were culture for up to 3 weeks, having a full media change every 3 days.

Astrocyte EZ differentiation, culture and hACM

EZ spheres were differentiated into astrocytes using a novel 3 step protocol. Similar to neural differentiation the EZ spheres were disaggregated with TrypLE express and plated on PLL-Laminin coverslips at a density of 40,000 cells per well. In the first week the cells were bathed in DMEM:F12 (1:1) medium with 2% B27 and 10 µM Ara-C (Tocris Bristol, Avon, U.K.), resulting a loss of mitotic cells, the medium was replaced every 3 days. Following the first week the medium was changed with DMEM:F12 (1:1) medium with 2% B27 and 10µM leukaemia inducible factor (human recombinant LIF-1, Life Technologies, Paisley, U.K.) and replaced every 3 days. Following the second week the medium was changed with DMEM:F12 (1:1) with 10% foetal bovine serum (FBS, Life Technologies, Paisley, U.K.) and 10µM LIF-1, this medium was then changed every 3 days and used as the standard medium for continually culturing the human astrocytes. The cells could then be lifted from the glass coverslips using TrypeLE express and passed into standard Nuncylon coated tissue culture flasks. The cells were then passaged every week using TrypeLE express. After 1 passage the cells could be used for producing astrocyte conditioned medium, using the same protocol as employed for the mouse isolated astrocytes.

From rosette neuronal differentiation

Human iPS or ES cultures which have reached 70% confluence in 6 well, matrigel coated plates or 6cm culture dishes were used for differentiation, this is considered day 0. To remove factors present in the mTeSR medium the cultures were washed 3 times in PBS. From Day 0 to 4 the cultures were given the first differentiation (advanced DMEM:F12 (1:1) with 2% B27, 10 µM SB431542 (ab120163, Abcam, Cambridge, U.K.), 1 µM LDN 193189 (04-0019, Stemgent, Cambridge, MA, USA) and 1.5 µM IWR1 (3532, Tocris Bristol, Avon, U.K.)) medium, which was replaced daily. The cells were treated with 10 µM ROCK (Rho Kinase) inhibitor Y-27632 for 1 hour at 37 ^{o}C, then rinsed with PBS twice before being passaged at a 1:2 ratio using neat accutase into more matrigel coated plates and rinsed with ADF (DMEM:F12 (1:1) with 2% B27). From day 4 to 8 the cells were fed daily with the first differentiation medium (see above) and 10 µM ROCK inhibitor (Y-27632). At day 8 the cells were passaged again and fed with the second differentiation medium (advanced DMEM:F12 (1:1) with 2% B27, 0.25 µM LDN 193189 and 1.5 µM IWR1). At day 16 the cells had formed neural rosettes which could be expanded for a limited number of passages, frozen or

continued to terminal differentiation. Terminal differentiation was performed on nitric acid etched, poly D-lysine and matrigel coated glass coverslips in 24 well tissue culture plates. The neural rosettes were disaggregated using accutase at 37 ^{o}C for 5 minutes, then collected by centrifugation, re-suspended in advanced DMEM:F12 with 2% B27 and counted (using trypan blue to ignore dead cells). The cells were re suspended at 1x10^{6} cells per ml and plated on the glass coverslips in 80µL drops, which were left at 37 ^{o}C for 2-4 hours before being flooded with 500 µL of neural differentiation medium for week 1 (see neuronal differentiation medium). The medium was changed every 2 days, after 1 week the media was changed to the second neural differentiation medium (see neuronal differentiation medium).

Neuronal differentiation media

For chapters 1 and 2 a low Ca^{2+} (0.6 mM) base medium was chosen, to which any modifications were added, consists of DMEM:F12(DMEM:F12 (1:3, Life Technologies, Paisley, Strathclyde, U.K.) with 2% B27 (+ RA, Miltenyi Biotec Ltd., Bisley, Surrey, U.K.), 1% none essential amino acids (Life Technologies, Paisley, Strathclyde, U.K.), 10ng/ml brain derived neurotrophic factor (BDNF, Peprotech, London, U.K.), 10 ng/ml glial derived neurotrophic factor (GDNF, Peprotech, London, U.K.) and 200 µM ascorbic acid (Sigma), 10 µM DAPT (Tocris, Bristol, Avon, U.K.) was also added for week 1 only. This medium was also chosen for the ACM experiments, although BDNF, GDNF, ascorbic acid and DAPT were added post-conditioning. In order to test the effects of calcium on differentiation an additional 0.6 and 1.2 mM $CaCl_2$ was added to the medium, resulting in 0.6 mM Ca^{2+} medium (control), 1.2 mM Ca^{2+} medium and 1.8 mM Ca^{2+} medium. The higher 1.8 mM Ca^{2+} medium (with 1.2 mM $CaCl_2$ added) was found to be more effective and therefore used in subsequent experiments involving specific blockade of ion channels. Both the ACM and 1.8 mM Ca^{2+} media were supplemented with nifedipine, agatoxin, conotoxin, SNX482 and bicuculline individually to specifically block L-, P/Q-, N- and R- type Ca2+ channels, and $GABA_A$ channels respectively. GABA and Bay K8644 (Tocris, Bristol, Avon, U.K.) were added to the control (0.6 mM Ca^{2+}) to specifically activate $GABA_A$ and L- type Ca^{2+} channels respectively. In addition to simple pharmacological experiments to assess the activation /

inhibition of one channel, experiments were also performed where inhibition was combined with activation of a different channel to affect a rescue of function. Specifically, to the high Ca^{2+} (1.8 mM) both conotoxin and GABA were added to block N- type Ca^{2+} channels and activate $GABA_A$ receptors, and, separately, both bicuculline and Bay K8644 were added to block $GABA_A$ channels and activate L-type Ca^{2+} channels.

In chapter 3 initially a moderately higher Ca^{2+} (1.25 mM) medium was chosen for modelling the development of HD: DMEM:F12 (1:1) with 2% B27, 1% none essentially amino acids, 10 ng/ml BDNF, 10 ng/ml GDNF, 200 μM ascorbic acid and 10 μM DAPT (Tocris, Bristol, Avon, U.K.) for the first week. Astrocyte conditioned medium was also created for this medium from the mouse isolated astrocyte cultures. In latter experiments however, the EZ-sphere differentiation was dropped for a straight from iPS-cell differentiation, with a neural rosette intermediate which could be frozen down and thawed when needed (see from rosette differentiation). In addition to dropping the use of EZ spheres, the differentiation medium was also altered, incorporating techniques developed in chapter 2, as well as other work to enhance the functional outcome of differentiation. This new differentiation occurred in two steps, the first medium for week 1 (Advanced DMEM:F12 (1:1, Life Technologies, Paisley, U.K.) with 2% B27, 200mM L-glutamine (Life Technologies, Paisley, U.K.), 2 μM PD0332991 (Tocris, Bristol, Avon, U.K.), 10 μM Forskolin (Tocris, Bristol, Avon, U.K.), 3 μM CHIR 99021 (Tocris, Bristol, Avon, U.K.), 300 μM GABA (Tocris, Bristol, Avon, U.K.), +0.6 mM $CaCl_2$ (to 1.8 mM, Sigma-Aldrich, Poole, Hants., U.K.), 10 ng/ml BDNF, 200 μM ascorbic acid and 10 μM DAPT). And then a second medium for all subsequent weeks (Advanced DMEM:F12 (1:1) with 2% B27, 200 mM L-glutamine, 2 μM PD0332991, 3 μM CHIR 99021, +0.6 mM $CaCl_2$ (to 1.8 mM, Sigma-Aldrich, Poole, Hants., U.K.), 10 ng/ml BDNF and 200 μM ascorbic acid).

Statistics

For continuous data-sets where 2 means were compared the data were checked for an approximate fit to a Gaussian distribution. Assuming an approximately Gaussian distribution a two sample unpaired, two tailed, T-test was performed. If the data distribution was significantly distinct from a Gaussian distribution then data transformations were considered in order to apply a T-test. However, if there was no obvious data transformation which resulted in an approximately Gaussian distribution then the medians were compared

using a Mann-Whitney U test. For binomial data sets comparing two proportions of cells, two-tailed Chi^2 tests were used. Statistics were reported as means or the probability value, test statistic and degrees of freedom (if relevant) were included for any statistical test performed. Statistics and graphical representations of the data were performed using either R (x64) version 2.14.0 with the default installed libraries or Graphpad Prism version 5.01 (La Jolla, Ca. USA.).

Chapter 3: Secreted factors from isolated mouse astrocytes enhance the extent of functional maturation in iPS-derived neurons.

Specific Introduction

Astrocyte secreted factors and neuronal differentiation

In vivo, astrocytes provide both contact and secreted signals to allow neurons to differentiate and functionally mature (see introductions, Astrocytes and Neuronal Functional Development). However, in the short protocol for differentiating neurons few astrocytes are observed, due to the delay between neurogenesis and astrogliogenesis in neural progenitor cells. The mechanisms by which astrocyte secreted medium (ACM) operate to enhance functional maturation in neurons is not yet fully understood. Further, no single secreted factor has demonstrated the ability to recapitulate the full effects of ACM in a defined protocol. Therefore, to assess the changes in the electrophysiological function evoked by a full complement of astrocyte secreted factors, conditioned medium was generated using post-natal isolated mouse astrocyte cultures. The conditioned medium from these astrocytes then conferred the full mixture of astrocyte secreted factors to the iPS cell-derived neuronal cultures. Therefore, the hypothesis was tested that the functional influences of astrocytes can be incorporated in short differentiation protocols using ACM, evoking increased functional maturity. Many different electrophysiological parameters have been analysed. However, most crucial to generating more functional iPS cell-derived neurons is increased spontaneous activity. Further, by investigating the functional properties of ACM neurons, if a significant functional enhancement is observed, it may be possible to assess which functional properties are responsible for ACM-evoked increases in spontaneous activity. It is also plausible that ACM evokes functional changes early in the differentiation protocol, which by augmenting electrophysiological activity at these early stages, enhance functional maturation over time.

Specific methods

Mouse astrocyte conditioned medium

Human iPS cell derived neurons were differentiated using a standard terminal differentiation protocol from EZ-sphere neural progenitor cell cultures. Post natal day 1 or 2 isolated astrocytes were cultured and expanded and then used to condition the neuronal base medium, producing mouse astrocyte conditioned medium (ACM, see methods). The astrocyte conditioned medium was then used in parallel with a standard, established differentiation protocol (see methods), for comparison. During the 3 week differentiation protocol for terminal differentiation, the cell physiological parameters were measured each week using a combination of whole cell patch clamp and fura-2 Ca^{2+} imaging.

Differentiation using mouse ACM

Cells from EZ-spheres were plated as a single cell suspension on PLL/laminin-coated glass coverslips and cultured in standard medium (Control). As expected, the cells appeared disperse and lacked any morphological complexity at day 1. During the first week, they remained disperse but began to extent neurites. At weeks 2 and 3, cells were more morphologically complex and tended to aggregate into colonies, extending processes between colonies of cells.

Voltage-activated Na^+ and K^+ channels and the ability to generate action potentials

Considered the most basic electrophysiological function of a neuron is the ability to generate an action potential. To assess the ability of each cell to generate an action potential, a current step protocol was employed, which measured changes in membrane voltage evoked by current injection. In order to measure induced action potentials (iAPs), the resting membrane was first clamped at approximately -70 mV, using continuous current injection, and followed by 100 ms depolarising current steps, which varied from 10 pA up to 120 pA (in 10 pA increments). The depolarisation of the membrane evoked by the current step was graduated in a non-linear fashion due to charging of the cell capacitor across the

pipette resistance (figure 3.1 A). This graduated depolarisation conveniently allowed for a more gradual rise of the membrane voltage until the threshold for an action potential was reached, allowing voltage threshold estimations to be performed later. The current injection required to depolarise the cell sufficiently to elicit an action potential was determined by the input resistance, since, in the absence of voltage activated ion channel activation, the extent of depolarisation (after the membrane capacitance had charged) is determined by Ohm's law. The input resistance of the membrane was measured using the voltage change elicited by sub-threshold steps. In the case of a successful action potential, a sudden rapid depolarisation, which overshot 0 mV, was observed once the threshold voltage was met, which was then followed by a rapid repolarisation which sometimes undershot the threshold voltage. On some occasions, the undershoot was sufficient to allow a second small action potential, this second action potential was often considered abortive, as it usually failed to reach 0 mV. In rare cases (and only in ACM), a full second action potential, or action potential train, was observed (see figure 3.1 A for examples of each type of response).

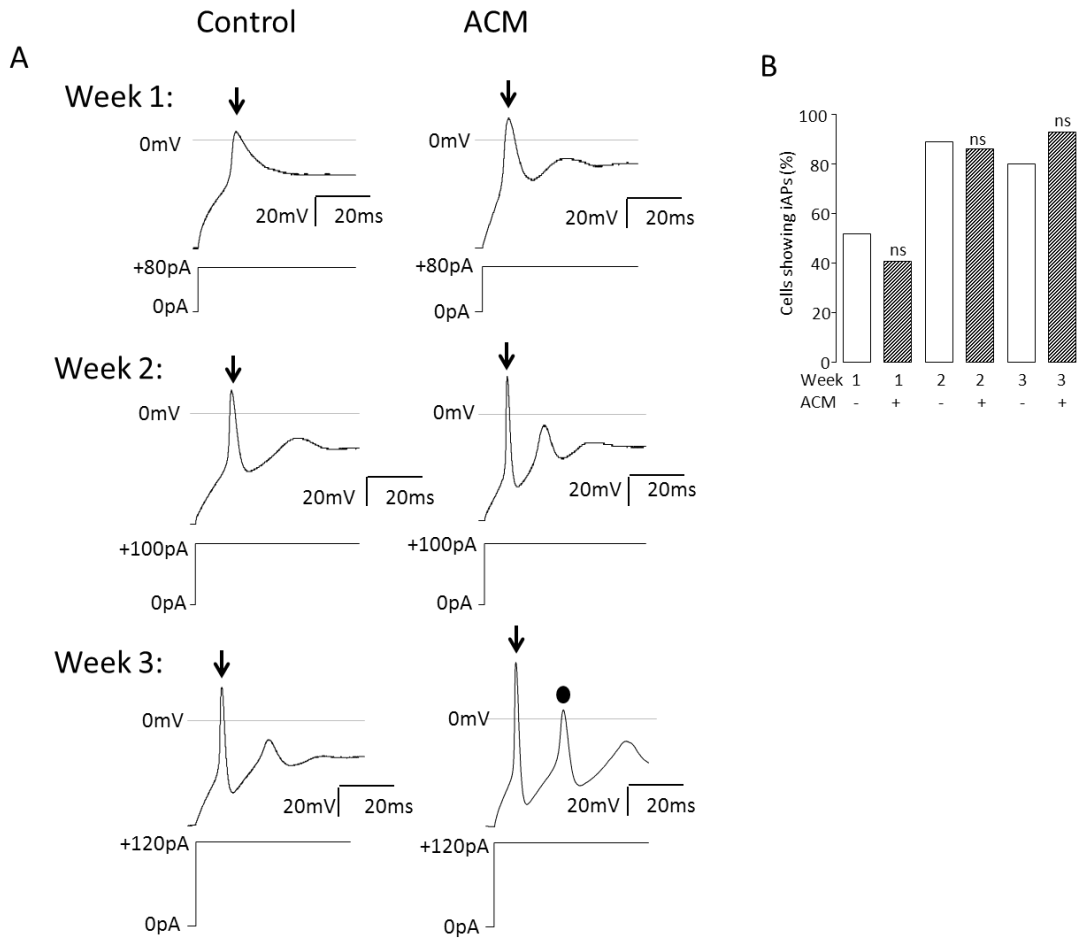

Figure 3.1: Evoked action potentials across all 3 weeks of differentiation in ACM and control medium.

A) Voltage recordings of induced action potentials (top) during current steps (bottom) for cells differentiated in control and ACM medium at each week of differentiation. Arrow indicates the first action potential, the circle indicates a second initiated action potential (only seen in ACM at week 3).

B) Bar graph showing the portion of cells able to fire a single (or more) action potential in response to the current steps protocol (% cells) for ACM and control cells over all 3 weeks (n = 122). Chi^2 tests were performed at each week.

The ability to fire action potentials was assessed using current step protocols over all 3 weeks of differentiation, in both control and ACM – treated cells. At week 1, roughly half of the cells in both ACM (ACM: 41.1% (n = 24)) and control medium (52.3% (n = 21), ns, chi^2= 2.52) were able to fire action potentials (figure 3.1B). At week 1, the cells showed slow depolarising events, starting at a relatively consistent threshold voltage, which reached a peak voltage slightly above 0mV (marked with an arrow) followed by a relatively slow repolarisation, which did not significantly undershoot the threshold voltage (figure 3.1 A). The remainder of cells at week 1, showed either no physiological response to the current step (so only measuring the slow depolarisation of the current injection charging the membrane capacitance) or they showed very small responses that could be considered abortive action potentials (where the action potential does not depolarise the cell sufficiently to reach 0mV). By week 2, almost all cells in both media (89.5% (n = 19) in control and 89.7% (n = 29) in ACM, ns, chi^2<0.001) demonstrated action potentials elicited by the current step protocol (figure 3.1B). More strikingly, these action potentials showed faster depolarisation, with peaks that reached more positive voltages, followed faster repolarisation stages that significantly undershot the threshold voltage (figure 3.1A). At week 2, in some cases in both cultures, but more prevalent in ACM-treated cultures (32% (n = 19) in control vs. 70%(n = 20) in ACM, P<0.05, Chi^2=5.8), the repolarisation overshoot was significant enough to allow an abortive second action potential, which although did not reach 0mV did show an initiation of a second electrophysiological event. At week 3, again almost all cells were able to fire action potentials (80% (n = 15) in control and 93% (n = 14) in ACM, ns, chi^2=1, figure 3B). These responses also showed fast depolarisations, more polarised peak voltages and faster repolarisation stages with larger undershoot. By week 3, most cells showed an initiation of a second abortive action potential (53% (n = 15) in control vs. 71% (n = 14) in ACM, ns, Chi^2=1). However, a significant number of the ACM-treated cells showed a second completed action potential (0% (n = 15) in control vs. 43% (n = 14) in ACM, P<0.01, Chi^2=8.1; marked with a dot, figure 3.1A), where the second action potential reached or exceeded 0 mV.

To fire an action potential it is necessary for the cell to possess the electrophysiological machinery for both voltage dependant depolarisation and repolarisation. In voltage clamp, the voltage step protocol was used to measure both the voltage activated Na^+ and K^+ currents simultaneously (see methods). Once the voltage step had reached approximately -40 mV, the opening of voltage activated Na^+ channels was observed as a rapidly activating and inactivating inward current (depolarising) at the start of the voltage step. K^+ currents were observed at approximately -30 mV as a slower activating outward current (repolarising) that reached a plateau, and did not inactivate significantly during the voltage step. The currents were measured during each voltage step was then plotted against the voltage of the step, producing a current-voltage relationship graph for both the Na^+ and K^+ channels. Where comparing multiple cells, the currents were converted to current density ($pA \cdot pF^{-1}$) and plotted against step voltage (figure 5). As a pharmacological confirmation for the voltage activated K^+ current, the voltage step protocol was repeated with ECS containing 10mM tetraethyl ammonium chloride (TEA), a potent voltage activated K^+ channel blocker (figure 3.2 A). Using this solution, an almost complete ablation of the outwards current was observed (figure 3.2 A and 3.2 B), confirming this current represents voltage activated K^+ channels in normal ECS. To confirm that the inward current was carried by Na^+ current, a modified ECS was used, in which NaCl has been isoosomotically replaced with N-methyl-D-glutamine chloride (NMDG), to which Na^+ channels are impermeable (figure 4A – NMDG). Using this solution, the fast inwards currents (figure 3.2 A and 3.2 B) were entirely abolished, confirming this current represents voltage activated Na^+ channels in normal ECS.

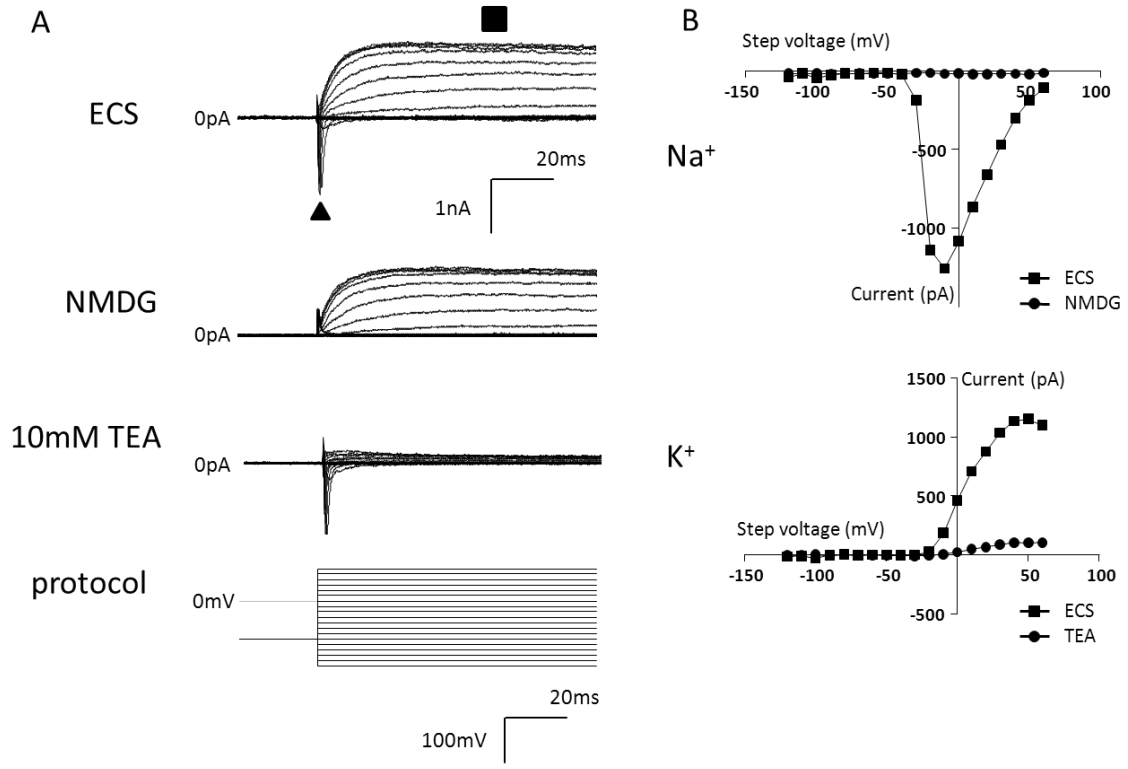

Figure 3.2: Confirming the identity of evoked fast voltage activating and inactivating depolarising currents and slower activating repolarising currents as Na^+ and K^+ channels, respectively using pharmacology and ionic substitution.

A) Exemplar current recordings during a voltage step protocol in standard ECS, NMDG solution and standard ECS with the addition of 10mM TEA, with the voltage protocol at the bottom. Showing control cells at week 2.

B) Example IV curves for the current recordings in 4A, showing the mean K^+ current density in standard ECS and with TEA (top) and peak Na^+ current in standard ECS and NMDG solution (bottom). Showing control cells at week 2.

Even though around half of the cells at week 1 did not have the ability to fire action potentials (see Figure 3.1 B), the majority of cells in both the ACM and control medium expressed measurable voltage activated Na^+ (73% (n = 11) in control and 88.9% (n = 27) in ACM, ns, chi^2=1.66) and K^+ (82% (n = 11) in control and 92.5% (n = 27), ns, chi^2=0.96) currents. This observation was maintained at week 2 (Na^+: 94% (n = 16) in control and 97%

(n = 32) in ACM, ns, chi^2=0.26, and K$^+$: 81% (n = 16) in control and 84% (n = 32) in ACM, ns, chi^2=0.08) and 3(Na$^+$: 92% (n = 12) in control and 91% (n = 11) in ACM, ns, chi^2<0.01, figure 3.3A). However, the magnitude of these currents (mean current densities) were very small at week 1 in both culture conditions (control: Na$^+$ = -27.0 ± 5.0 pA.pF^{-1} (n = 11); K$^+$ = 24.4 ± 4.7 pA.pF^{-1} (n = 11), and in ACM: Na$^+$ = -37.6 ± 4.4 pA.pF^{-1} (n = 27), ns, T= 1.93, df=39; K$^+$ = 31.9 ± 4.8 pA.pF^{-1}, ns, T=0.94, df=37, figure 3.4 C), perhaps explaining the disparity between the portion of cells with measurable Na$^+$ and K$^+$ currents and their ability to fire action potentials. Such a notion is confirmed by the transformed data in figure 3.3B, which shows frequency histograms of the magnitude of Na$^+$ and K$^+$ currents in the populations of cells either able or unable to fire action potentials within the total of (818 cells in total, figure 3.3 B).

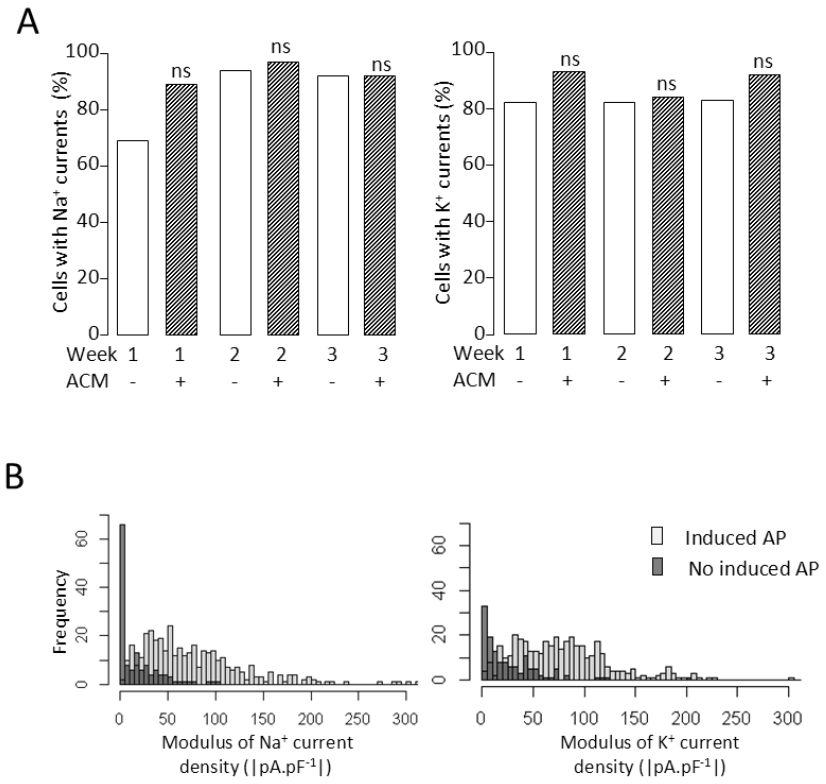

Figure 3.3: The number of cells showing observable Na$^+$ and K$^+$ channel currents over each week and how these current magnitudes are distributed between cells able and unable to generate action potentials.

A) Bar graphs showing the portion of cells with appreciable Na (left) and K (right) currents over all 3 weeks (% cells) for ACM and control cells over all 3 weeks.

B) Frequency histograms (ranges of 5pA·pF^{-1}) showing the modulus of the Na (left) and K (right) magnitude for cells with an inducible action potential compared to this without in all weeks and all conditions (n = 818).

Once the cells had reached week 2, both the Na^+ (control: from -27.0 ± 5.0 pA.pF^{-1} (n = 11) to -58. ± 7.5 pA.pF^{-1} (n = 13); ACM: 31.9 ± 4.8 pA.pF^{-1} (n = 27) to 53.9 ± 5.2 pA.pF^{-1} (n = 32)) and K^+ (control: from 24.4 ± 4.7 pA.pF^{-1} (n = 11) to 69.5 ± 8.3 pA.pF^{-1} (n = 13); ACM: 31.9 ± 4.8 pA.pF^{-1} (n = 27) to 53.9 ± 5.2 pA.pF^{-1} (n = 32), figure 3.4 D) current densities had increased, with significantly larger Na^+ currents observed in the ACM-treated cells compared to control (Na^+ P<0.05, T=2.05, df=46; K^+ ns, T=1.52, df=46, figure 6 C and D). This is consistent with nearly all cells being able to fire action potentials at week 2, when the currents in very few cells fell below the minimal levels required for an action potential. It may also be expected, that a higher magnitude of voltage activated K^+ current is required for cells to undershoot sufficiently to initiate a second action potential. Additionally, it was speculated that a higher minimal magnitude of Na^+ current for a second action potential would be required, because a portion of the Na^+ current will still be inactivated when the second action potential initiates. Therefore, it is not surprising that second, usually abortive, action potentials are only seen at week 2 and beyond, and are more prevalent in the ACM-treated cells at week 2. At week 3, the voltage activated Na^+ and K^+ currents had increased somewhat in the control treated cells (Na^+: -118.9 ± 24.9 pA.pF^{-1} (n = 12), and K^+: 119.5 ± 16.14 pA.pF^{-1} (n = 12), but not the ACM cells (Na^+: -68.0 ± 7.9 pA.pF^{-1} (n = 11), and K^+: 65.5 ± 9.9 pA.pF^{-1} (n = 11), figure 3.4C), resulting in significantly larger K^+ currents in the control cells (Na^+: ns, T=1.79, df=20, and K^+: P<0.01, T=2.85, df=20). However, this did not result in an apparent increase in second action potentials in the control cells compared to ACM (figure 3.1 A), in fact the opposite appeared true, implying undershoot by K^+ current is not the only factor influence the ability to initiate a second action potential.

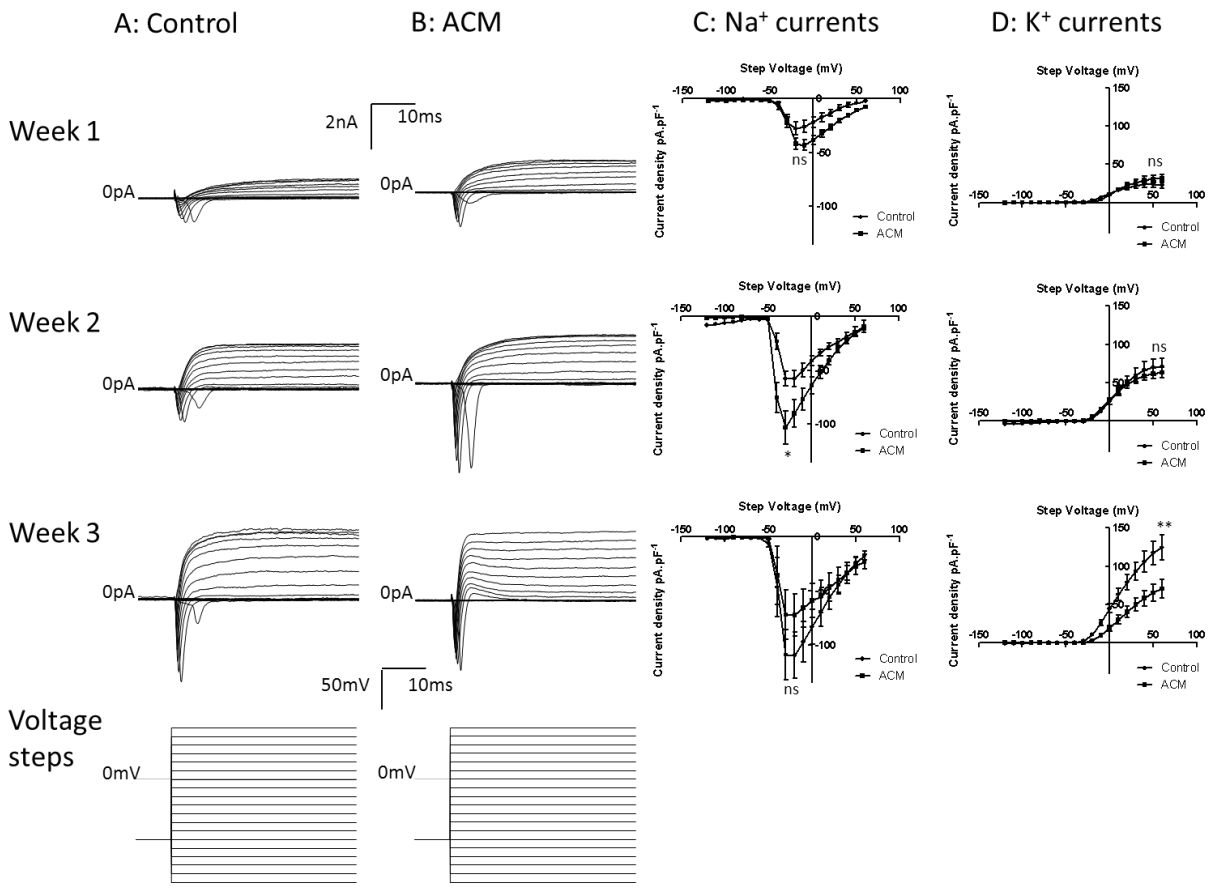

Figure 3.4: A comparison of the Na^+ and K^+ current densities in control and ACM treated cells across all 3 weeks of differentiation.

A and B) Exemplar current recordings during a voltage step protocol (bottom) for ACM (B) and control cells (A) from each week of differentiation at all weeks.

C and D) Mean current density against step voltage curves for the voltage activated Na^+ (left) and K^+ (right) currents from each week of differentiation, comparing the ACM (D) and control cells (C) at all weeks (n = 106 for each current). T-tests were performed comparing the mean peak currents.

Spontaneously generated action potentials and the membrane potential at rest

Mature neurons of the central nervous system *in vivo* are not just able to fire induced action potentials; they produce spontaneous action potentials in response to synaptic stimuli. Neuronal networks of the central nervous system are constantly active with rhythmic action potentials. To assess the generation of spontaneous activity in the differentiating neurons, the native membrane voltages were measured in current clamp with no current injection. Whilst recording the native membrane potential, a spontaneous action potential would be represented by a sharp depolarising spike (arrow) from the resting membrane potential that reached at least 0 mV (figure 3.5 B and C).

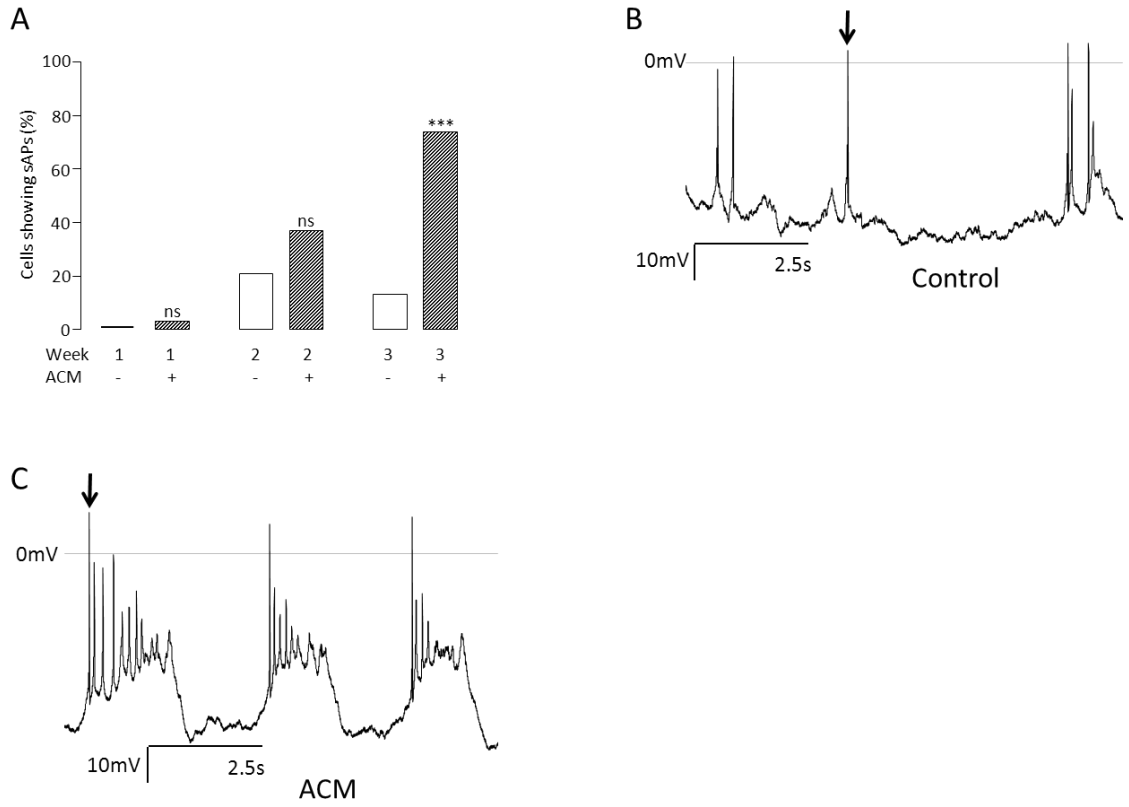

Figure 3.5: Observed spontaneous action potential generation in control and ACM-treated cells.

A) A bar graph showing the proportion of cells showing spontaneous action potentials whilst being held at I=0 in current clamp for both ACM and Control cells from each week of differentiation (n = 147). Chi^2 tests were performed at each week.

B) Exemplary voltage recording during current clamp (I=0) demonstrating a typical control cell at week 3, showing sparse action potentials and no biphasic membrane potential.

C) Exemplar voltage recording during current clamp (I=0) demonstrating a typical ACM-treated cell at week 3, showing both short trains of action potentials (arrow) and a biphasic membrane potential.

At week 1, very few cells showed any spontaneous activity (0% (n = 19) in control and 2.7% (n = 37) in ACM, ns, chi^2=0.71). This increased significantly at week 2 (29% (n = 21) in control and 37% (n = 35) in ACM, ns, chi=0.43), but actually declined in the control cells by week 3 (13% (n = 16), figure 7A). The ACM-treated cells showed a very similar trend at weeks 1 and 2. However, at week 3, a striking 74% (n = 19, P<0.001, chi^2=13.1) of the ACM cells generated spontaneous action potentials (figure 3.5A). In addition to more cells showing some level of spontaneous activity, the ACM-treated cells showed increased rates of spontaneous activity and were unique in having a biphasic resting membrane potential with action potential trains observed in the "up-state" (figure 3.5 B and C). Indeed, all 74% (n = 19) of the active ACM treated cells exhibited complex short trains of spontaneous activity and bi-phasic resting membrane potentials (figure 3.5 C). Although, as shown before with the current injection evoked action potentials, it is necessary for the cell to express a minimal level of Na^+ and K^+ current in order to fire an action potential, the development of the magnitude of these currents does not correlate temporally well with increases in spontaneous activity observed in ACM. Indeed, the control cells actually showed the larger Na^+ and K^+ currents at week 3, yet showed very low rates of spontaneous activity. Further, the ACM evoked no enhancement of the Na^+ and K^+ current densities at week 3, yet the result was a massive increase in spontaneous activity. This suggested that there were alternative mechanisms responsible for this ACM-evoked increase in spontaneous electrical activity, prompting an examination other cell physiological parameters in order to be able to explain this disparity.

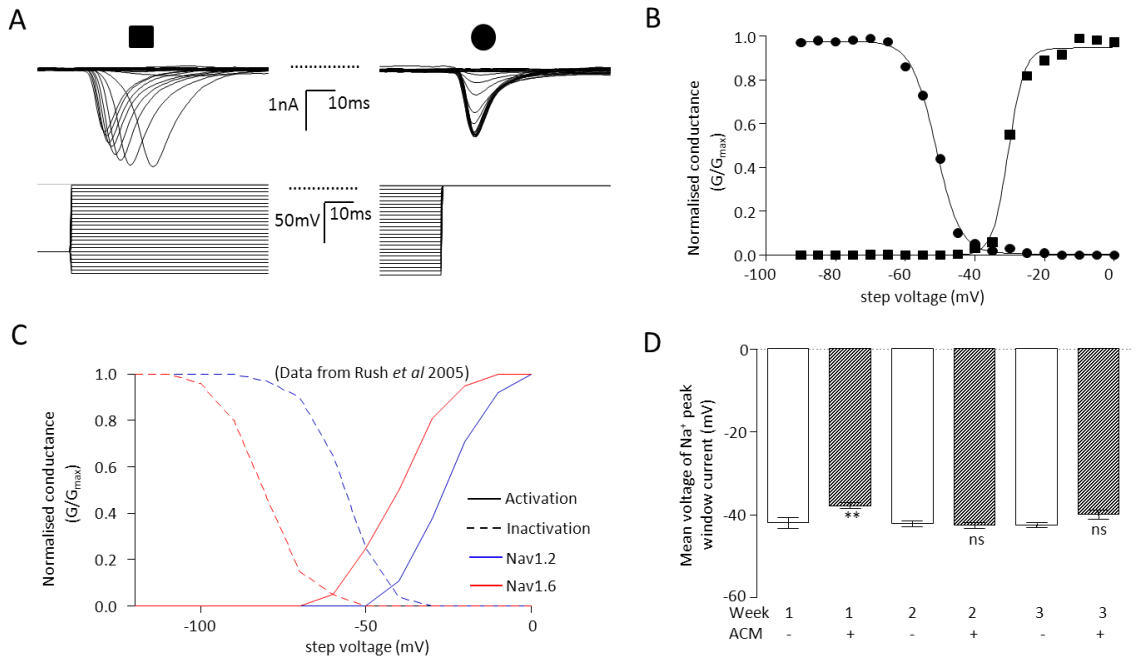

Figure 3.6: The voltage-dependant activation and inactivation relationships for the Na^+ currents observed in control and ACM-treated cells.

A) An exemplar current recording (top) during a dual step voltage protocol (bottom), showing the Na current response used to measure activation (square) from the first step and the current response used to measure inactivation (circle) from the second step. Example recording is a control cell at week 2.

B) An exemplar normalised conductance (calculated using the series resistance and junction potential compensated voltages and the observed currents) against step voltage (series resistance and junction potential compensated) graph, showing the fitted Boltzmann-Sigmoid curves fitted to both the voltage profile for activation and inactivation of the Na^+ current.

C) Data plotted from Rush et al. 2005 showing the isolated voltage-dependant activation and inactivation (solid and dashed, respectively) profiles for 2 neuronal sub-types of voltage gated Na^+ channel, Nav1.2 and Nav.1.6 (blue and red, respectively.

D) A bar graph showing the mean voltage at which the hypothetical peak-window current would occur (where the activation and inactivation curves cross) for the ACM and control

cells at each of the 3 weeks of differentiation (n = 77). T-tests were used to compare the mean Na window current at each week.

One property which may influence the generation of spontaneous activity in neurons is the voltage dependent activation and inactivation profiles for the voltage-activated Na^+ channels. A narrower gap between resting membrane potential and the voltage dependent activation of the Na^+ current could result in the cell becoming more sensitive to action potential propagation. However, if the gap between the resting membrane potential and voltage dependent inactivation of the Na^+ current were too small this may inhibit action potential generation, since the Na^+ current is inactivated. Additionally, cells with biphasic membrane potentials may actually benefit from the up-state approaching the threshold voltage for Na^+ channel activation, whilst benefitting from the down-state removing the inactivation of these channels. Therefore, it was speculated that a hyperpolarising shift, due to changes in the expression of Na^+ channel sub-types evoked by ACM, could increase the sensitivity of ACM-treated neurons to action potentials, especially during the up-state of their biphasic membrane potential.

The voltage-dependant profiles for both activation and steady-state inactivation of voltage activated Na^+ channels were measured using a dual voltage step protocol (in the presence of 10 mM TEA to avoid the confounding effects of voltage activated K^+ currents at more depolarised test potentials). From a holding voltage of -90 mV, the protocol started with a 100 ms voltage step (increasing from -110 mV to 0 mV in 5 mV increments per sweep) was used to both assess the voltage-dependant activation (square) of the Na^+ current and evoke inactivation (figure 3.6A). From this first step, the voltage was then immediately held at 0 mV for 100 ms, this step would only activate a Na^+ current if the first step had not already inactivated the channels (circle). The currents were then mathematically converted to normalised Na^+ conductance (G/Gmax, see methods) and plotted against the voltage of the first step (adjusted for series resistance and junction potential). The resulting curves were then fitted with a Sigmoid Boltzmann equation (figure 3.6B). The curve representing inactivation is inverse, meaning it represents the proportion of the conductance not inactivated (so available) at that voltage, it starts at 1 (no steady-state inactivation) before falling sigmoidally (described by a Botlzman function) to zero at voltages between -55 and -

40 mV (full steady–state inactivation. Conversely, the curve representing activation represents the proportion of the conductance opened by that voltage, before inactivation, it starts at zero and rises sigmoidally to 1 between -40 and -25 mV. Where the two curves meet is considered the voltage at which the peak Na^+ window current occurs (from now on referred to as the Na^+ window voltage); this is a voltage at which a hypothetical small continuous Na^+ current would be observed if Na^+ channels were transitioning from the closed to active states and from inactive to closed states. However, this does not occur because the transition from inactive to closed states also occurs at a much lower voltage and over a longer time scale. Using the Na^+ window voltage as a measure for both the voltage activation and inactivation of the cells' Na^+ current, no significant changes over time were observed in either ACM or control medium treated cells (figure 3.6D). Figure 3.6C compares shows data from Rush *et al.* 2005 showing the activation and inactivation profiles for two neuronal subunits of Na^+ channel Nav1.2 and Nav1.6, measured in isolation using genetically encoded TTX resistance [167]. The voltage-dependant activation and inactivation profiles observed in the iPS-derived neurons used in this study were compared with the data from Rush *et al.* 2005, finding very similar voltage profiles to that of isolated Nav1.2 when treated with either ACM or control medium (figure 3.6B and 3.6C). This implies that the iPS-derived neurons expressed primarily Nav1.2 over 1.6, as Nav1.6 shows voltage-dependant activation and inactivation over more polarised membrane potentials [167].

The Na^+ current-voltage activation profile is an important parameter to setting the voltage threshold for an action potential because an action potential is initiated at the voltage where the cells' voltage activated Na^+ channels open. Any depolarising current must therefore push the membrane voltage up from the resting membrane voltage to this threshold to start an action potential. As discussed previously, in the neuronal excitability section of the introduction, there are multiple factors which can potentially influence the sensitivity of a neuron to initiating an action potential. Firstly, the difference in the threshold voltage and the resting membrane potential, the larger the voltage change required reaching threshold the more current is required.

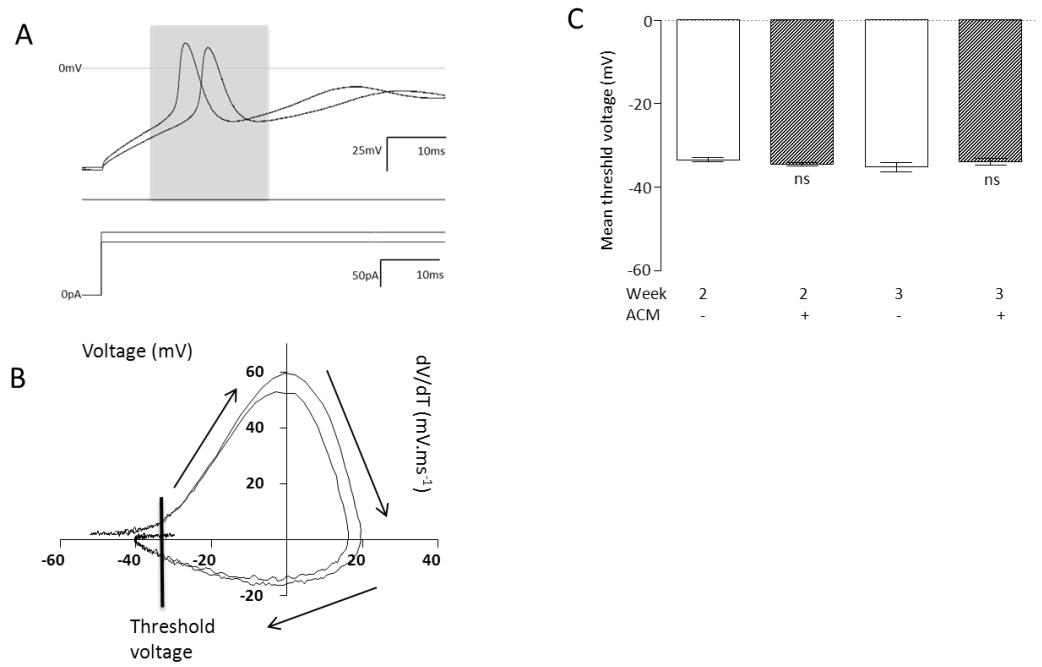

Figure 3.7: Calculating the threshold voltages for action potentials from cells differentiated with control or ACM treatment.

A) Exemplar current recordings from a week 2 control cell showing an induced action potential (top) during a current step protocol (bottom), the grey box indicates the region used to produce an orbital graph (B).

B) Exemplar action potential orbital graph, the first differential of voltage against time plotted against voltage. A line indicates the inflection used to approximate the threshold voltage and arrows indicate the direction of time on this graph.

C) A bar graph showing the mean estimated threshold voltage for both ACM and control cells from weeks 2 and 3 of the differentiation protocol (n = 29). T-tests were performed at each week.

The action potential threshold voltages were measured by analysing induced action potentials (figure 3.7A). The region of the voltage trace which contained an action potential was isolated and differentiated against time (dV/dT). The differential of voltage against time was then plotted against the voltage, resulting in an orbital graph of the action potential, which runs anticlockwise (figure 3.7B). The short, flat region at low voltages prior to the onset of the upstroke represents the slow rise in voltage caused by the membrane

capacitance charging across the input resistance during the start of the current step. Following this flat region, if an action potential was initiated, a sharp inflection was observed rising with time towards the top of the orbit. The inflection and linear rise represent voltage activated Na^+ channels opening and the magnitude of the Na^+ current increasing (so this occurs over a very short time scale). The top of the orbit represents the linear and maximal stage of depolarisation, the up-stroke of the action potential. Following the top of the orbit, the curve rapidly drops to the negative and starts to move in the opposite direction in the voltage axis. The rapid switch from positive to negative dV/dT represents the peak of the action potential, where the Na^+ channels are inactivating and the K^+ channels are opening. The negative peak of the orbit represents the maximal repolarisation by the K^+ channels, which then begin to close again as the voltage approaches the initial threshold. The shape of the action potential was assessed using 3 quantitive measures. Firstly, the peak depolarisation, which measured how far the cell had depolarised during the action potential. Secondly, the width of the action potential at its half height, this is a measure of how rapidly the action potential occurred. Lastly, the area inside the orbital graph was measured using the modulus of the sum of the integrals from threshold to completion of the action potential as well as the peak rates of depolarisation and repolarisation. This measure has the benefit of being determined by both the speed and extent of the depolarisation, and is more sensitive to changes in depolarisation speed. By week 3 the ACM treated cells were showing evoked action potentials that were narrower at their half height (2.7 ± 0.7 ms (n = 10) in control vs. 1.9 ± 0.1 ms (n = 11) in ACM, $P<0.05$) and reached a more depolarised peak (+24.7 ± 2.7 mV (n = 10) in control vs. +33.4 ± 2 mV (n = 11) in ACM, $P<0.0001$, table 3.1). These measures correlated with increased rates of depolarisation at weeks 2 and 3 observed in ACM-treated cells (60.6 ± 4.8 Vs^{-1} (n = 12) in control vs. 86.5 ± 7.6 Vs^{-1} (n = 16) in ACM at week 2 ($P<0.01$), and 81.8 ± 14.3 Vs^{-1} (n = 10) in control vs. 122.4 ± 11.5 Vs^{-1} (n = 11) in ACM ($P<0.05$) at week 3, table 3.2) and faster rates of repolarisation at week 3 (-36.3 ± 3.1 Vs-1 in control vs. -45.4 ± 2 Vs^{-1} in ACM ($P<0.05$), table 3.2). Using the area inside the orbit (sum of the modulus of the integrals of dV/dt against V during the action potential orbit), larger orbits by week 2 with the ACM (2700 ± 310 $mV^2 \cdot ms^{-1}$ (n = 12) in control vs. 4120 ± 410 $mV^2 \cdot ms^{-1}$ (n = 16) in ACM, $P<0.05$), which became more pronounced by week 3 (3480 ± 450 $mV^2 \cdot ms^{-1}$ (n = 12) in control vs. 6020 ± 700

$mV^2 \cdot ms^{-1}$ (n = 16) in ACM, P<0.0001, table 3.3). This quantitatively demonstrated that which had been observed qualitatively in figure 1, that the ACM-treated cells produced sharper, faster action potentials at both weeks 2 and 3. Further, this demonstrates the utility of the area inside the orbit as a one-measure for comparing neuronal action potential spikiness and maturity. The threshold voltage was approximated by eye by drawing a line through the start of the inflection at the start of the rise of the orbit. This was considered more accurate than using the original voltage against time graph and more reliable than taking the second differential of voltage against time plotted against voltage. No appreciable change in the threshold voltage was observed over time, or by treatment with ACM (see table 2).

Week	Control		ACM		Statistics (T- test)	
-	*Peak (mV)*	*Width (ms)*	*Peak (mV)*	*Width (ms)*	*Peak*	*Width*
1	14.7±2.1 (10)	13.4±1.5 (10)	15.7±2.3 (10)	11.7±1 (10)	ns	ns
2	21.1±3.4 (12)	4.8±1.2 (12)	26.3±1.3 (16)	3.5±0.5 (16)	ns	ns
3	24.7±2.7 (10)	**2.7±0.7 (10)**	**33.4±2 (11)**	1.9±0.1 (11)	P<0.05	P<0.0001

Table 3.1: The shape characteristics for both control and ACM, each is a mean with standard error, analysed with a T-test. Firstly the peak depolarisation, indicating the extent of an action potential, secondly the width of an action potential spike at half-height, indicating how rapidly the action potential occurred. Bold and underline text used to identify the significantly higher value in the comparison between ACM and control at the same week, sample sizes displayed in brackets.

Week	Control		ACM		Statistics (T- test)	
-	*+dV/dt (V/s)*	*-dV/dt (V/s)*	*+dV/dt (V/s)*	*-dV/dt (V/s)*	*+dV/dt*	*-dV/dt*
1	21.8±2 (10)	-11.1±0.8 (10)	24.5±1.8 (10)	-13.6±0.8 (10)	ns	ns
2	60.6±4.8 (12)	-31.3±2.3 (12)	**86.5±7.6 (16)**	-36.7±3.1 (16)	P<0.01	ns
3	81.8±14.3 (10)	-36.3±3.1 (10)	**122.4±11.5 (11)**	**-45.4±2 (11)**	P<0.05	P<0.05

Table 3.2: Peak rates of depolarisation +(dV/dt) and repolarisation (-dV/dt) in control and ACM-treated cells. The area inside the orbit is potentially useful measure for both the extent and speed of the action potential. Bold and underline text used to identify the significantly higher value in the comparison between ACM and control at the same week, sample sizes displayed in brackets.

Week	Control		ACM		Statistics (T- test)	
-	V_{thr} *(mV)*	*A(mV^2·ms^{-1})*	V_{thr} *(mV)*	*A(mV^2·ms^{-1})*	V_{thr}	A_{orb}
1	-34.8±2.2 (10)	1270±100 (10)	-34.1±2.5 (10)	1470±140 (10)	ns	ns
2	-33.3±0.6 (12)	2700±310 (12)	-34.5±0.4 (16)	**4120±410 (16)**	ns	P<0.05
3	-35±1 (10)	3480±450 (10)	-33.7±0.7 (11)	**6020±700 (11)**	ns	P<0.0001

Table 3.3: The mean voltage threshold (V_{thr}) for an action potential, approximated using an orbital graph, and the area inside the orbit (A(mV2·ms-1)) of this graph. The area inside the orbit is potentially useful measure for both the extent and speed of the action potential. Bold and underline text used to identify the significantly higher value in the comparison between ACM and control at the same week, sample sizes displayed in brackets.

These data demonstrate, that differentiating neurons develop action potentials with more mature shape over time, and that ACM-treatment is able to enhance the development of this property. These parameters are crucial to developing trains of action potentials and mature spontaneous activity, consistent with the nature of spontaneous activity observed in ACM-treated cells comparing more favourably with *ex vivo* neuronal cultures. However, as no change was observed in the threshold voltage, consistent with no observed change in the voltage-dependant activation of these cells' Na^+ current, this does not explain why more ACM-treated cells show spontaneous activity. Therefore, more electrophysiological

parameters affecting the propensity for neurons to produce spontaneous activity must be investigated in these cultures.

As discussed in the introduction, the input resistance determines how far the voltage will change in response to a current after the membrane capacitance has charged, in accordance with Ohm's law. This gives us the concept of the rheobase current, the minimal current of infinite length required to reach threshold. However, the capacitance of the membrane charging results in voltage changes occurring as a function of time. The time constant is a function of the capacitance and resistance (both synaptic channel resistance and input resistance). This means that the shorter the current, the more the magnitude of membrane capacitance determines the extent of depolarisation. The membrane capacitance was measured using the transient currents produced by the membrane capacitance at the start and end of a 10 ms, 10 mV step. The input resistance was calculated using the stable voltage change evoked by sub-threshold current steps.

Surprisingly, no significant increase in membrane capacitance was observed from week 1 to week 2, or comparing control and ACM at these weeks (table 3.4). However, at week 3 the ACM evoked a significantly larger membrane capacitance (14.4 ± 1.6 pF (n = 16) in control cells vs 21.4 ± 1.4 pF (n = 19) in ACM cells, $P<0.01$, table 3.4). This implies a loss of neuronal complexity at week 3 in the control cells, but does not in itself explain changes in spontaneous activity. In fact, for a larger membrane capacitance it is required that the current must be larger, longer or more frequent (see introductions) to result in the same change in voltage, for membranes with the same input resistance. More surprisingly, no appreciable increase in input resistance was observed either over time, or with ACM-treatment (see table 3.4). These data imply that from the same resting membrane potential one would expect a similar rheobasic current in ACM and control cells. However, due to a higher membrane capacitance in ACM-treated cells at week 3 a higher short-current requirement in ACM-treated cells.

Week	Control		ACM		Statistics (T- test)	
-	C_m (pF)	R_i (MΩ)	C_m (pF)	R_i (MΩ)	C_m	R_i
1	17.8±1.8 (25)	1128±181 (20)	18.6±1.5 (38)	1025±83 (20)	ns	ns
2	22.8±2.3 (19)	940±61 (19)	19.5±1.7 (35)	1060±86 (22)	ns	ns
3	14.4±1.6 (16)	993±130 (15)	**21.4±1.4 (19)**	1066±96 (14)	P<0.01	ns

Table 3.4: Mean and standard error for membrane capacitance (C_m) and input resistance (R_i), and differences between ACM and control analysed by T-test. Bold and underline indicates the significantly higher value in the comparison between ACM and control –treated cells of the same week, sample sizes displayed in brackets.

Although a resting membrane potential closer to the threshold voltage for an action potential will minimize the current required to reach threshold, the resting membrane potential must also be sufficiently hyperpolarised to remove the inactivation of the voltage activated Na^+ current, this sets a practical limit on how close the threshold and resting voltages can be together. Considering that ACM does not evoke significant changes in the cell capacitance, threshold voltage or the voltage at which the Na^+ current inactivates, it seemed logical that this increase in spontaneous activity was due to concordant changes in the resting membrane potential. Therefore, there could be two possible reasons for increased spontaneous activity in ACM based on the resting membrane potential alone. Firstly, if the ACM cells expressed more depolarised resting membrane potentials than control cells, but not so depolarised as to evoke inactivation of the Na^+ current, this could result in these cells to be more sensitive to depolarising stimuli. Alternatively, compared with ACM cells, if the control cells were depolarised sufficiently to inactivate the Na^+ current, then fewer of the control cells would be capable of firing spontaneous action potentials.

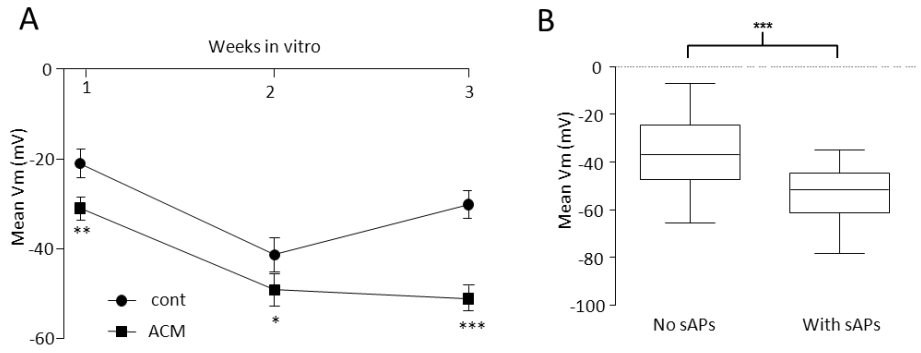

Figure 3.8: Comparing the resting membrane potential of control and ACM-treated cells across all 3 weeks, and then comparing the resting membrane potential of spontaneous active and non-spontaneous active cells.

A) A graph showing the mean resting membrane potential, measured during current clamp at I=0, for ACM and control cells over all 3 weeks of differentiation. T-tests were performed comparing control and ACM at each week.

B) A box and whisker plot for all cells showing the distribution of mean resting membrane potentials for cells showing spontaneous action potentials compared to those without across all weeks and conditions (n = 298).

The resting membrane potential of the cell was measured in current clamp by measuring the average voltage whilst the current was held at 0pA. The importance of the resting membrane potential is illustrated in figure 8 B, here the mean resting membrane potentials for cells which are spontaneous active and not spontaneous active are compared ($P<0.0001$, n = 298, figure 3.8B), independently of their time in culture or treatment. Importantly, these data show that the cells which were spontaneously active also had significantly more hyperpolarised resting membrane potentials (sAP vs no sAP). The resting membrane potentials of both ACM and control treated cells became more polarised from week 1 to week 2 (control: from -21 ± 3.2 mV (n = 19) to -41.3 ± 3.8 mV (n = 21), and ACM: from -31 ± 2.6 mV (n = 37) to -49.2 ± 2.2 mV (n = 35), figure 3.8 A). At all weeks the resting membrane potential of ACM-treated cells was significantly more hyperpolarised than control cells ($P<0.01$, $T=2.9$, $df=61$ at week 1 and $P<0.05$, $T=2.05$, $df=54$ at week 2). Most strikingly,

where at week 3 the control treated cells actually became relatively depolarised (from -41.3 ± 3.8 mV (n = 21) to -30.5 ± 3.1 mV (n = 16)), the ACM-treated cells stayed remained relatively hyperpolarised (from -49.2 ± 2.2 mV (n = 35) to -50.0 ± 2.8 mV (n = 19)). This resulted in a large and significant 19.5mV difference between control and ACM cells at week 3 ($P<0.0001$, $T=4.87$, $df=33$), which highly correlated with the pattern seen in the development of spontaneous activity over the 3 weeks (figure 3.8A and 3.5). These data are completely consistent with the Na^+ current activation and inaction curves which show that the voltage window of maximum Na^+ current is between -36 and -42 mV (figure 3.6B). Further, in the control cells, only 15% and 1% of the Na^+ current is available at their mean resting membrane potentials at weeks 2 and 3, respectively. In contrast, approximately 60% of the Na^+ current is available at both weeks 2 and 3 at their mean resting membrane potential for the ACM-treated cells. However, this cannot explain the large difference in spontaneous activity between weeks 2 and 3 in the ACM treated cells, suggesting that they have developed increased depolarising stimuli from synapapses, thus driving increased spontaneous activity. This notion is supported by the fact that biphasic resting potentials are seen exclusively in ACM-treated cells.

Voltage activated Ca^{2+} currents

Voltage activated Ca^{2+} currents were recorded during a voltage ramp, where from a holding of -70 mV the voltage was stepped down to -120 mV, then continuously increased to +60 mV during 500 ms. The voltage ramp resulted in the voltage activation of Na^{+}, K^{+} and Ca^{2+} channels. However, the voltage activated Ca^{2+} channels were too small to be easily detected in standard solutions. To amplify the Ca^{2+} currents, the extracellular solution (ECS) was replaced with a modified external solution containing 27 mM $BaCl_2$. The voltage activated Ca^{2+} current was usually not visible until after the addition of Ba^{2+}, where it was represented by an inward current that activated at around -20 mV and did not rapidly inactivate (figure 3.9A). The $BaCl_2$ solution also resulted in a partial inhibition of the voltage activated K^{+} current. The current traces were then plotted against voltage during the ramp to produce a current-voltage relationship. The leak current was manually subtracted by linear regression using the voltage and current relationship during the ramp before activation of voltage-dependant channels. The presence of L-type Ca^{2+} channels was confirmed by either a complete or partial inhibition of the Ba^{2+} current when 2 µM nifedipine was applied (figure 3.9A). The current was normalised for cell surface area using the cell capacitance ($pA \cdot pF^{-1}$). Peak, normalised inward current densities were quoted for each condition during the differentiation time-course.

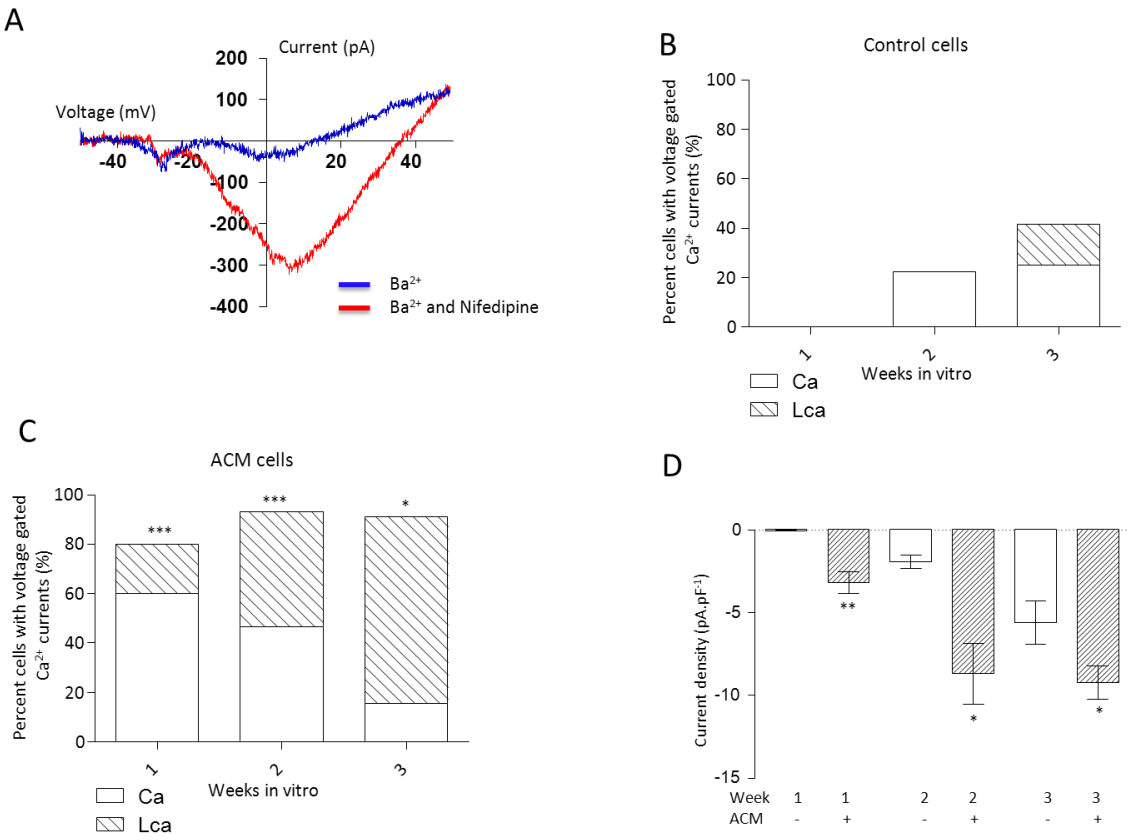

Figure 3.9: The proportion of cells showing, and magnitude of, voltage activated Ca^{2+} channels in control and ACM-treated cells.

A) Exemplar IV graph showing Ba^{2+} currents through voltage activated Ca^{2+} channels in $BaCl_2$ solution with and without 2μM nifedipine, from a control cell at week 2.

B) A bar graph showing the proportion of cells with voltage activated Ca^{2+} currents, and nifedipine sensitive Ca^{2+} currents in control cells from each week of differentiation at all 3 weeks of differentiation.

C) A bar graph showing the portion of cells with voltage activated Ca^{2+} currents, and nifedipine sensitive Ca^{2+} currents in ACM cells from each week of differentiation at all weeks of differentiation. T-tests were performed comparing ACM and control for all 3 weeks.

D) A bar graph showing the mean current density of Ba^{2+} currents in ACM and control cells from each week of differentiation, error bars show SEM.

The control cells at week 1 showed no detectable voltage activated Ca^{2+} currents (0% (n = 11), but slowly increased in both proportion and magnitude during the 3 week period (22.2% (n = 9), -1.9 ± 0.4 pA.pF^{-1} (n = 5) at week 2 and 41.7% (n = 12), -5.6 ± 1.3 pA. pF^{-1} (n = 8) figure 3.9 B and C). L-type Ca^{2+} currents were only observable at week 3 in the control cells (40%, n = 5). In contrast, even at week 1, 80% (n = 15, P<0.001, chi^2=16.34, 25% (n = 13) were L-type) of ACM-treated cells had detectable Ca^{2+} currents (-3.2 ± 0.6 pA. pF^{-1} (n = 15)). This trend continued into week 2 (93% (n = 23), P<0.01, chi^2= 8.67, 50% L-type (n = 21)), and their current density was now significantly larger than control (-8.7 ± 1.9 pA. pF^{-1} (n = 12, P < 0.05)). By week 3, almost all of the ACM-treated cells had not only Ca^{2+} currents but L-type Ca^{2+} currents (90.9% (n = 11), P<0.05, chi^2=4.4, 83% were L-type), but the currents had not increased in magnitude significantly from week 2 (-9.2 ± 1.0 pA. pF^{-1} (n = 9, P < 0.05)) and the control cells had begun to catch up. This implies a very significant and immediate functional enhancement by ACM-treated cells. Over all 3 weeks, the ACM-treatment produced a higher proportion of cells expressing functional voltage activated Ca^{2+} currents that were, on average, larger in magnitude than control. However this effect was most striking at week 1, which does not correlate well with the temporal pattern of the ACM-evoked increase in spontaneous activity.

To produce a more complete characterisation of the Ca^{2+} channels which were being up-regulated by ACM-treatment, Fura-2 Ca^{2+} imaging was employed. Fura-2 is a fluorescent reporter for Ca^{2+} concentration, excitation at two different wavelengths 340 nm and 380 nm results in a signal intensity for the molecule both bound to Ca^{2+} and unbound. Therefore, the ratio of emissions following excitation at each of those two wavelengths is proportional to the intracellular Ca^{2+} concentration. Voltage-activated Ca^{2+} channels were activated by 10 s pulses of a modified ECS, which had 50 mM KCl, isoosomotically replacing NaCl, resulting a shift of the K^+ ion reversal potential, and consequent cell depolarisation. A sharp rise in the ratio of emission (i340/i380) was observed as soon as the KCl solution was applied, which then immediately began to decay. To allow for cell recovery, each pulse was separated by 200 s, which was sufficient time to allow the Ca^{2+} concentration to return baseline. The area under the curve was calculated for each KCl solution application (see methods) and used as a measurement for the magnitude of the Ca^{2+} influx. Alternately antagonists to 4 different types of Ca^{2+} channel were added with the short pulses of high K^+; 2 µM nifedipine, 0.1 µM

conotoxin, 0.1 µM agatoxin and 0.1 µM SNX482 for L-, N-, P/Q- and R- type channels, respectively, figure 3.10 A). T-type Ca^{2+} channels were not included due to their activation being at voltages far more hyperpolarised than the membrane potential of the week 1 cells. KCl applications in the absence of an antagonist were used both before and after to calculate the expected size the Ca^{2+} response to KCl when the antagonist had been added. The difference between the expected and observed response was considered to represent the contribution of that specific sub-type of Ca^{2+} channel to the overall Ca^{2+} influx.

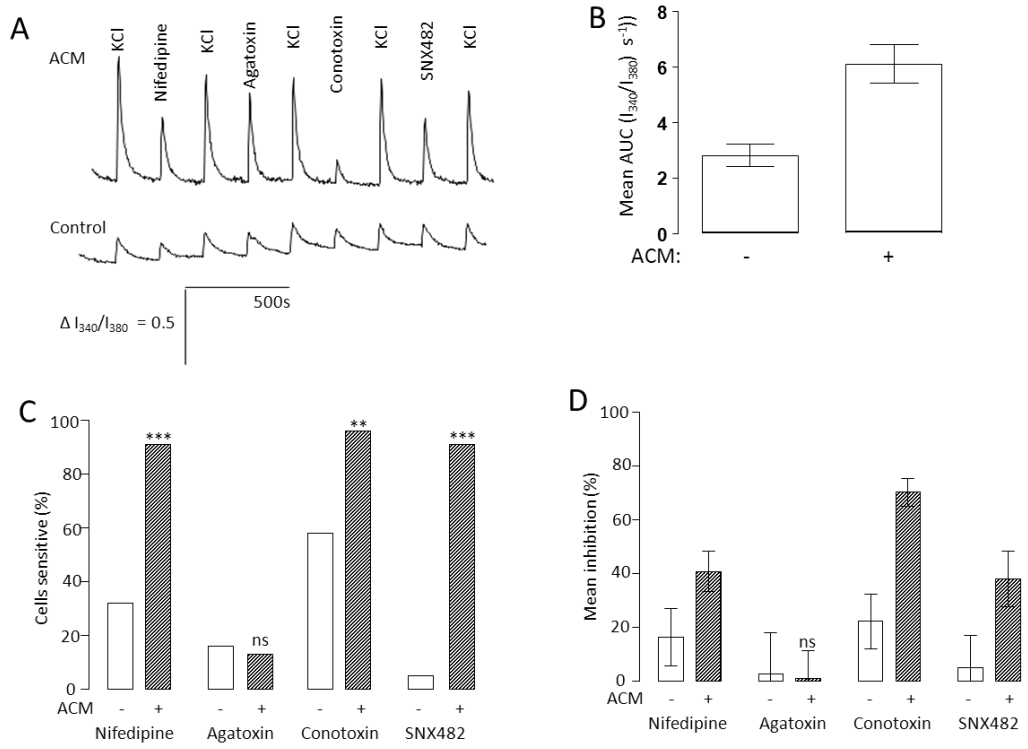

Figure 3.10: A Fura-2 Ca^{2+} imaging characterisation of week 1 Ca^{2+} currents in ACM and control-treated cells.

A) Mean Fura-2 ratiometric fluorescent intensities graph (i340/i380), background subtracted, for ACM (upper) and control (lower) cells. Labels above show the times at which high K^+ solution was applied, or high K^+ solution with an antagonist for a specific sub-type of Ca^{2+} channel. The antagonists used were: 2µM nifedipine, 0.1µM agatoxin, 0.1µM conotoxin, 0.1µM SNX482.

B) A bar graph showing the mean (±SEM) Fura-2 radiometric area under curve response to high K^+ solution, for both ACM and control cells at week 1 (n = 42).

C) A bar graph showing the portion of cells showing significant inhibition of the response to K^+ by each antagonist, for ACM and control cells at week 1 (n = 42).

D) A bar graph showing the mean (±SEM) percent inhibition of the K^+ response by each antagonist, for both ACM and control cells at week 1 (n = 42).

A further characterisation of the voltage gated Ca^{2+} channels was performed in ACM and control cells at week 1, at the time point where the most significant difference in the functional Ca^{2+} currents using patch clamp. This was also considered the most likely time point that Ca^{2+} influx from these channels influenced development. It was immediately evident that the ACM-treated cells had a much larger Ca^{2+} response to KCl solution (figure 3.10A). However, in contrast to data collected by patch-clamp, almost all of the cells from both treatments responded to high K^+ (figure 3.10 A and B, control: 89% cells at 2.8±0.4 AUC n = 19, ACM: 100% cells at 6.1±0.7 AUC n = 24). This was attributed to the Ca^{2+} imaging being a far more sensitive approach to measuring voltage activated Ca^{2+} channels, a notion supported by the very small size of the currents measured during patch clamp (figure 3.9B). When using the specific antagonists to assess individual sub-types of Ca^{2+} channel, it was observed that in the ACM treated cells almost all were sensitive to nifedipine (91.3% (n = 24)), conotoxin (95.7% (n = 24)) and SNX482 (91.3% (n = 24)), implying significant functional expression of L-, N- and R- type Ca^{2+} channels, respectively (3.10 C and D). In contrast, in the control treated cells, a significant number were conotoxin sensitive (58% (n = 19), $P<0.01$, $chi^2=9.22$), fewer were nifedipine sensitive (31.3% (n = 19), $P<0.0001$, $chi^2=16.86$) and virtually none were sensitive to SNX482 (5.3% (n = 19), $P<0.0001$, $chi^2=31.82$). In both conditions very few cells showed any sensitivity to agatoxin (15.8% (n = 19) in control and 12.5% (n = 24) in ACM, ns, $chi^2= 0.1$)), an antagonist of P/Q-type Ca^{2+} channels (figure 3.10 C and D). Additionally, ACM increased significantly the magnitude of the inhibition caused by each of the specific channel blockers (Figure 4 C). Thus, nifedipine-sensitive AUC went from 16.4 ± 10.7 % (n = 19) of the high K^+ response to 40.8 % ± 7.5 % (n = 23, $P < 0.001$), conotoxin-sensitive AUC went from 22.2 ± 10.1 % to 70.2 ± 5.1 % ($P < 0.001$) and SNX482-sensitive AUC went from 5.2 ± 11.7 % to 38 ± 10.4 % ($P < 0.001$). Importantly, these data show that a larger proportion of the ACM-treated cells had functional L-, N- and R- type Ca^{2+} channels, and that the ACM-treated cells had significantly larger functional responses from

each of these channel types. Importantly, the short applications of these potent antagonists showed immediate effects on the magnitude of Ca^{2+} influx response, but these effects appeared entire reversible as the responses to high K^{+} alone showed relatively little run-down. This is consistent to studies which have shown that short applications of these antagonists result in a reversible blockade.

Ionotropic GABA elicited currents and GABA synapses

In addition to voltage activated currents, neurons express ligand activated ion channels so that the cell is responsive to neurotransmitters. GABA as an inhibitory neurotransmitter is essential to striatal function, being an integral part to both the direct and indirect pathways for motor control. However, it is also likely that GABA has many roles in the development of neurons. As previously discussed, a significant increase in the functional expression of specific sub-types of Ca^{2+} channel was observed with ACM treatment. However, in the absence of a depolarising stimulus the Ca^{2+} channels alone will not function to allow Ca^{2+} influx.

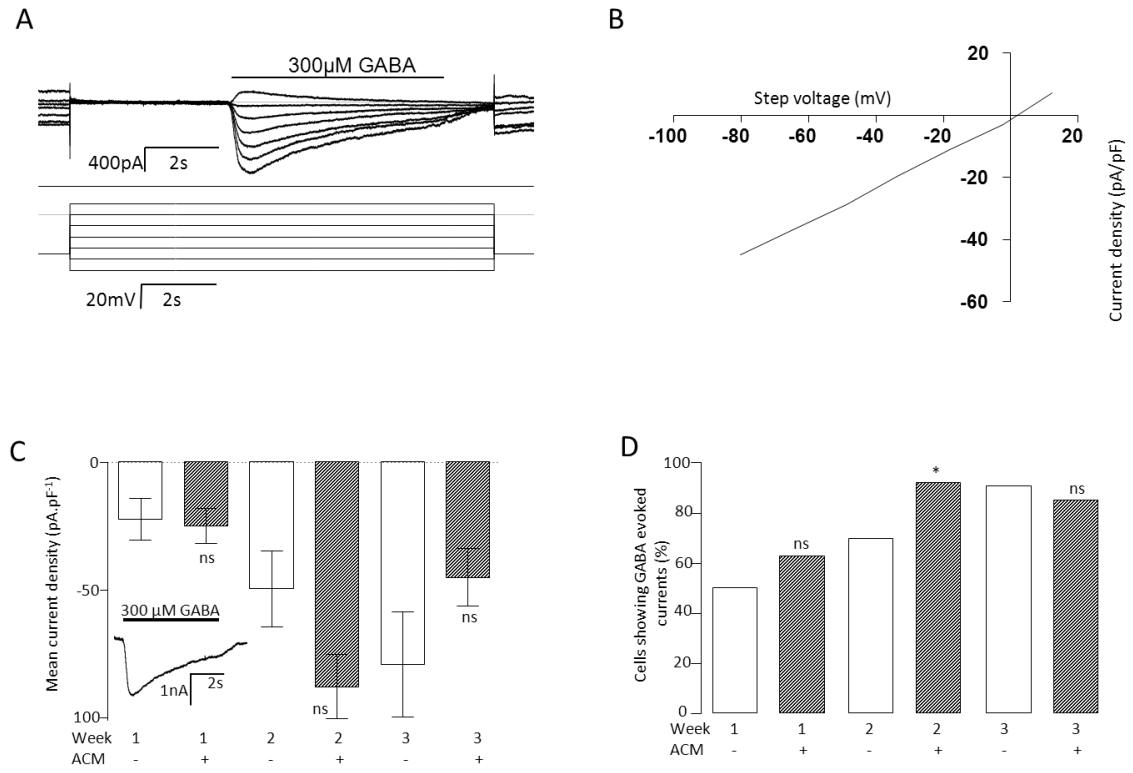

Figure 3.11: Measuring GABA-evoked currents in ACM and control treated cells.

A) A bar graph showing the mean peak current density (±SEM) for GABA evoked currents in both the ACM and control cells. The inset shows an exemplar current evoked by 300µM GABA whilst being held at -70mV in a week 2 control cell.

B) A bar graph showing the portion of cells with significant GABA evoked currents from both the control and ACM cells from each week (n = 95).

C) An exemplar current recording during a 10s voltage step protocol with a 5s addition of 300µM GABA.

D) An exemplar IV relationship curve for GABA evoked currents during a voltage step, showing a reversal potential close to 0mV.

Demonstrating that the GABA-dependant current was carried by Cl^- was achieved by applying GABA (5s, 300 µM) during a voltage steps (holding -70 mV, 10 s step increasing from -100 mV to 20 mV in 20 mV increments). The resulting GABA-dependant I-V current reversed at 0mV, as predicted in these solutions for a Cl^- current. (figure 3.11 A and B).

Whole cell ionotropic GABA currents were measured with cells voltage clamped at -70 mV, and during a 5s application of 300 µM GABA. At -70 mV, the GABA-dependant current was represented by a rapidly activating inward current which then slowly desensitised during the 5s GABA application and reversed upon GABA wash off (figure 3.11 C inset). Roughly half of the iPS cell derived neurons showed relatively small ionotropic GABA responses at week 1 in both cultures (control: 50% (n = 11), ACM: 63% (n = 24), ns, chi^2=0.46; figure 3.11 C and D). By week 2, almost all of the ACM cells responded (70% (10) in control and 92% (25) in ACM $P<0.05$, chi^2=4.54), whereas the control cells lagged slightly behind until week 3 (91% (12) in control and 85% (13) in ACM, ns, chi^2=0.29, figure 3.11 C and D). The magnitude of the $GABA_A$ currents increased sharply from week 1 to week 2 (Control: week 1 = -22.1 ± 8.2 $pA.pF^{-1}$ (n = 6) to week 2 = -49.4 ± 14.9 $pA.pF^{-1}$ (n = 7); ACM: week 1 = -24.8 ± 6.8 $pA.pF^{-1}$ (n = 8) to week 2 = -87.8 ± 12.5 $pA.pF^{-1}$ (n = 20)), but showed no significant difference between culture conditions (figure 3.11 C). At week 3 little change in the current magnitudes were observed in either culture (control = -79.1 ± 20.7 $pA.pF^{-1}$ (n = 11) vs. ACM = -44.9 ± 11.4 $pA.pF^{-1}$ (n = 7)).

In culture or *in vivo*, the resting membrane potential and the Cl^- concentration gradient determine whether GABA stimulation hyperpolarises or depolarises the cell. During patch-clamp, both the Cl- gradient and the membrane potential are set, meaning it was not possible to measure the natural response of the cells to GABA. In order to determine whether GABA would cause an inhibitory or excitatory drive to neurons at each time point during different differentiation protocols “in situ”, Fura-2 Ca^{2+} imaging was employed. This

allowed measurement of GABA-evoked responses to GABA in the presence of quasiphysiological conditions (i.e with physiological Cl^- gradient and Vm). Although GABA does not itself evoke a Ca^{2+} current, if GABA stimulation depolarised the cell, this was measureable as a Ca^{2+} influx through voltage activated Ca^{2+} channels. Confirmation that each cells did indeed, express voltage activated Ca^{2+} channels was achieved by an initial application of high KCl solution, as above. Further, the use of a modified low Cl^- external solution to change the Cl^-concentration gradient such that any Cl^- response would become excitatory, ensured that any false negatives in normal Cl^- could be excluded. Thus, 10s applications of KCl solution identified cells without Ca^{2+} channels, GABA with low Cl^- solution identified cells without $GABA_A$ receptors and GABA in normal ECS distinguished between cells which were inhibitory or excitatory to GABA. Where a cell responded to all 3 solutions the cell was considered to have an excitatory GABA response, where a cell only responded to KCl and GABA in low Cl^- solution it was considered to have an inhibitory GABA response. Cells with no KCl or GABA in low Cl^- response were removed from the analysis (figure 3.12 A inset).

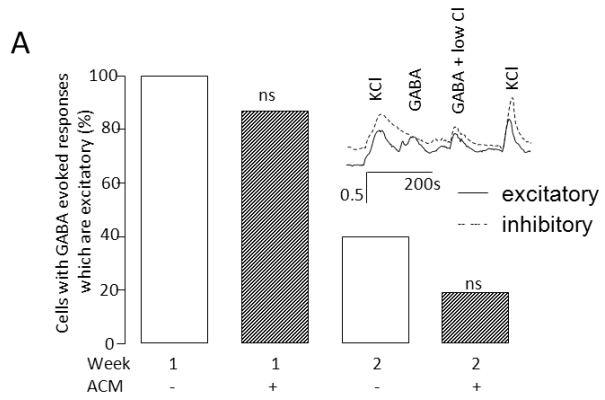

Figure 3.12: The proportion of cells showing excitatory GABA-evoked currents in control and ACM-treated cells across weeks 1 and 2 of differentiation.

A) A bar graph showing the percent cells with excitatory GABA responses (in terms of Ca^{2+} influx evoked during Ca^{2+} imaging by GABA in standard ECS), for both ACM and control cells across weeks 1 and 2 of the differentiation protocol (n = 58). The inset shows exemplar Fura-2 ratiometric fluorescent intensities graph (i340/i380) recordings, normalised against the background, the text indicating the addition of high K^+ solution, GABA in ECS and GABA in

low chloride solution for a cell exhibiting an inhibitory and excitatory response. Note the absence of a GABA evoked Ca^{2+} response in the inhibitory cell in standard ECS.

At week 1, almost all cells in either ACM and control cultures showed excitatory GABA responses, meaning that it produced a Ca^{2+} influxes to all 3 applications (100% (n = 17) in control and 87% (n = 15) in ACM, ns, chi^2= 2.4, figure 3.12A). However, by week 2 less than half of the cells in each culture demonstrated excitatory responses (40% (n = 10) in control cells and 18% in ACM (n = 16), ns, chi^2= 1.4), implying that already more than half of the cells had switched to become inhibitory. Further, a slight trend towards more cells having switched from excitatory to inhibitory GABA-responses in ACM may imply faster maturation in ACM-treated cells or simply increase Ca^{2+} responses to GABA in week 1, consistent with the observed increased Ca^{2+} channel function. This could potentially limit the ability of GABA to drive depolarisation-dependant Ca^{2+} influxes beyond week 2.

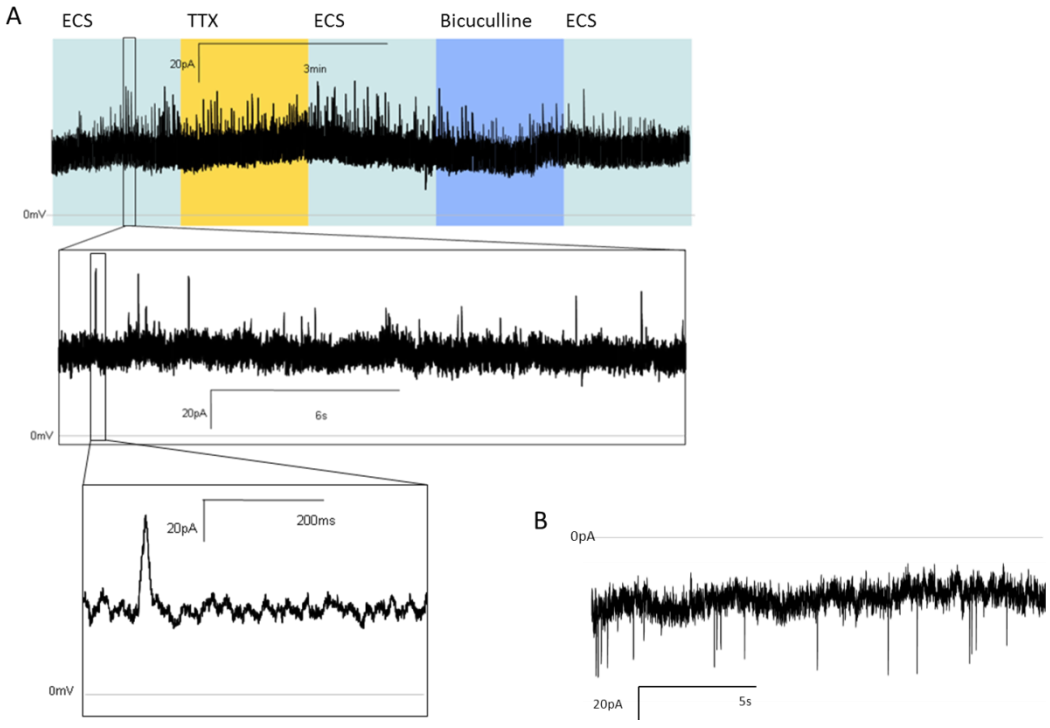

Figure 3.13: Exemplar miniature synaptic currents observed in week 3 ACM-treated cells.

A) Miniature spontaneous synaptic currents during voltage clamp at +20mV in standard ECS, and with the addition of 10µM bicuculline or 10µTTX from a week 3 ACM treated cell.

B) Miniature spontaneous synaptic currents from the same cell whilst being held at -20mV, from a week 3 ACM treated cell.

Differentiating neurons must also develop functionally mature and spontaneously active synapses, a critical function allowing neurons to conduct electrochemical signals within circuits and potentially important in the pathobiology of many neurodegenerative diseases. Spontaneous post-synaptic currents were measured using voltage clamp at either -20 or +20 mV, to ensure that the voltage activated Na^+ current was inactivated, therefore removing the possibility of action potentials. Further, TTX was added to further ensure that the events being observed were not as a result of action potentials. During these patch clamp experiments it was not possible to distinguish an excitatory (cation) synaptic current (EPSC) or an inhibitory (Cl^-) current (IPSC) as the reversal potentials of both cation-inselective channels and Cl^- channels were approximately 0mV. Therefore, regardless of their identity we observed their reversal when moving from -20 to +20 mV (3.13 A and B). Therefore to identify the crucial GABA responses 10µM bicuculline was added, a potent and selective antagonist of $GABA_A$ channels.

I compared the number of cells which showed some spontaneous synaptic currents over 10 minutes at -20 mV, finding that a few ACM-treated cells (30% (n = 10)) had developed active synapses at week 3 where the control cells had not (0% (n = 14)). Pharmacological tools were then used to identify those synapses which were GABA-ergic using bicuculline, finding that the vast majority of spontaneous synaptic events were bicuculline sensitive, but TTX insensitive (figure 3.13 A).

Chapter 4: The development of electrophysiological function in iPS-derived neurons is dependent on specific Ca^{2+} currents and GABA signalling.

Specific Introduction:

Ca^{2+} channel activity in ACM:

During the characterisation of iPS cell-derived neurons treated with ACM, an immediate increase in the function of voltage activated Ca^{2+} channels was observed. More importantly, ACM evoked a significant increase in spontaneous activity and more hyperpolarised resting membrane potentials at week 3. However, the increase in Ca^{2+} channel function did not correlate temporally with the more crucial increase in spontaneous activity. Ca^{2+} influx provides a functional link between electrophysiological activity and gene expression. Further, previous work has implicated Ca^{2+} channel activity in development and neurogenesis (see introduction – voltage activated Ca^{2+} channels). Therefore, it was speculated that the functional increase in Ca^{2+} currents early in development by astrocyte secreted factors was actually a mechanism by which the ACM-treated cells matured. At week 1 especially, the ACM-treated cells produced a much larger Ca^{2+} influx response to depolarisation; this increase in Ca^{2+} could drive functional changes in the developing neurons.

Effect of manipulation of GABA and Ca^{2+} channel function on differentiation and maturation

Specific blockade of Ca^{2+} channels or $GABA_A$ receptors in ACM

The hypothesis that the specific Ca^{2+} channels that are functionally up-regulated by ACM play a mechanistic role in the functional maturation observed with ACM-treatement was tested. Specific antagonists for each sub-type of Ca^{2+} channel that had been up-regulated by ACM were added individually: 2 µM nifedipine, 0.1 µM conotoxin and 0.1 µM SNX482 were added to the ACM to specifically antagonise L-, N- and R- type Ca^{2+} channels, respectively.

The electrophysiological function of the cells treated with ACM, and with each antagonist was assessed over 3 weeks of differentiation as previously described. Of particular interest was the function of differentiated cells at week 3, where the ACM-treated cells showed the most functional benefit from ACM and behaved most similar to the cells *in* vivo, with higher rates of spontaneous activity and hyperpolarised membrane potentials. Individual blockade of L-, N- or R- type Ca^{2+} channels were each sufficient to entirely inhibit the development of spontaneous activity (0% (n > 9) vs. 74% (n = 19), P< 0.0001, Chi^2 >13, figure 4.1A). The loss of spontaneous activity also correlated with less polarised resting membrane potentials (-50.8 ± 2.8 mV (n = 19) ACM, -27.3 ± 3.9 mV (n = 9) conotoxin, -21 ± 2.5 mV (n = 9) nifedipine, -25.5 ± 2.3 mV (n = 10) SNX 482, P<0.0001, T > 4.7, figure 4.1B). The hypothesis tested was that, at least one of the sub-types up-regulated by ACM would have such an effect on development. However, it is surprising that blockade of each of the 3 currents results in the same effect.

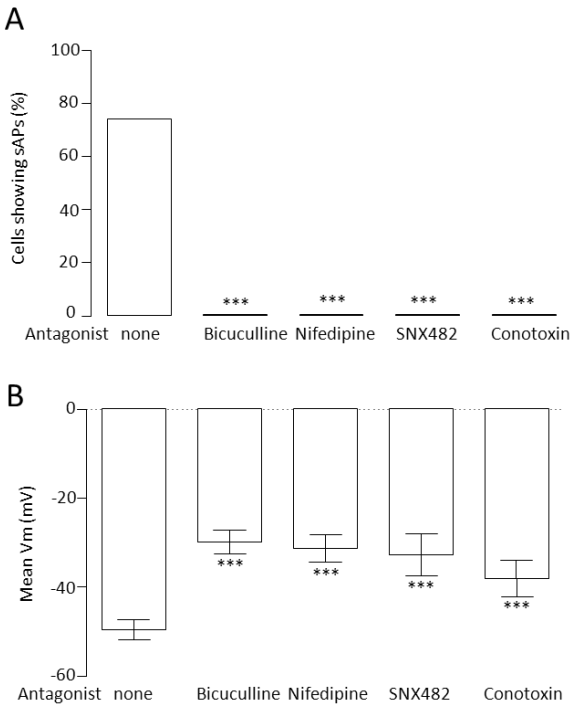

Figure 4.1: A comparison of resting membrane potentials and spontaneous activity in ACM and ACM treated with each of the following antagonists: 2 µM nifedipine, 0.1µM SNX482, 0.1µM conotoxin or 10µM.

A) A bar graph showing the portion of cells with spontaneous action potentials at week 3 in ACM, and with the addition of 2 µM nifedipine, 0.1 µM SNX482, 0.1 µM conotoxin or 10 µM bicuculline, compared by Chi^2 test against ACM.

B) A bar graph showing the mean resting membrane potential (±SEM) at week 3 in ACM, and with the addition of 2 µM nifedipine, 0.1 µM SNX482, 0.1 µM conotoxin or 10 µM bicuculline, compared by T-test against ACM.

It was also speculated that GABA signalling provides an important stimulus for driving Ca^{2+} influx by providing frequent depolarisation stimuli to open voltage activated Ca^{2+} channels. Therefore the hypothesis was tested that pharmacological blockade of $GABA_A$ channels, using 10 µM bicuculline, would have a similar functional effect to blocking the voltage activated Ca^{2+} channels, as it would remove the depolarising stimulus which Ca^{2+} channel activation depends on. Consistent with this notion, $GABA_A$ blockade mimicked blockade of each of the voltage activated Ca^{2+} channels by entirely inhibiting the development of spontaneous activity (0% (n = 10) vs 74% (n = 19), $P < 0.0001$, $Chi^2 = 15.2$, figure 4.1A) and resulting in a depolarised resting membrane potential (-27.1 ± 1.2 mV (n = 10) vs -50.8 ± 2.8 mV (n = 19), $P < 0.0001$, $T = 5.9$, figure 4.1B).

Manipulating Ca^{2+} influx using increased Ca^{2+} concentration and GABA

Voltage activated Ca^{2+} channels and $GABA_A$ receptors are important in the mechanism by which ACM improves functional maturation, as their specific blockade significantly impaired maturation in ACM. Therefore, would it be possible to directly enhance functional maturation by manipulating Ca^{2+} influx? The first strategy for increase Ca^{2+} influx directly was to increase the concentration of Ca^{2+} in the culture medium, which would increase the magnitude of Ca^{2+} influx when voltage activated Ca^{2+} channels were opened (see figure 2.2). The addition of 0.6 mM $CaCl_2$ and 1.2 mM $CaCl_2$ to the standard differentiation medium (which contained 0.6 mM Ca^{2+}), resulting in a 1.2 mM Ca^{2+} medium and a 1.8 mM Ca^{2+} medium.

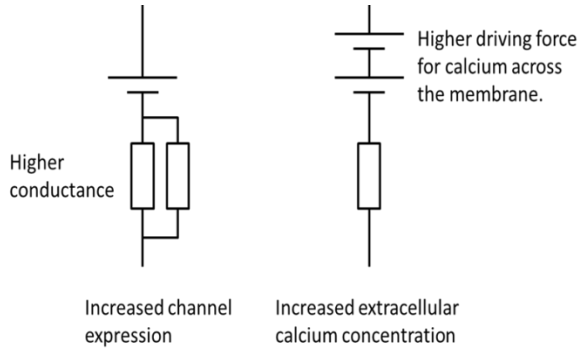

Figure 4.2: A schematic comparing the effect of increased ion channel density and increasing the external concentration gradient for the permeable ion, in this case calcium.

The electrophysiological function of iPS cell-derived neurons differentiated in these media with varying Ca^{2+} concentrations was assessed over a 3 week differentiation protocol, as previously described. At week 1, a significant polarisation of the resting membrane potential in both the 1.2 and 1.8 mM Ca2+ medium was observed (-19.8 ± 2.6 mV (n = 25) in 0.6 mM vs -37.2 ± 3.8 mV (n = 13) in 1.2mM and -41.4 ± 3.2 mV (n = 16), $P<0.0005$, $T > 3.7$, figure 4.3B). However, this did not evoke an increase in the proportion of cells firing spontaneous action potentials (0% (n = 25) in 0.6mM vs 7.6% (n = 13) and 0% (n = 16), figure 4.3C). Surprisingly, at week 1 the 1.8mM Ca^{2+} medium evoked a significant increase in the cells able to fire action potentials (50% (n = 22) in 0.6mM vs 58% (n = 12) and 88% (n = 16), $P < 0.01$, $Chi^2=5.8$, Figure 4.3A). At week 2, the control cells had improved and caught up with the higher Ca^{2+} media, meaning no differences were observed in the proportion of cells able

to fire induced action potentials (89% (n = 19) in 0.6 mM, 94% (n = 15) in 1.2 mM and 92% (n = 12) in 1.8 mM, figure 4.3A) and no significant differences in resting membrane potential (-39.3 ± 3.7 mV (n = 21) in 0.6mM, -41.8±2.5 mV (n = 16) in 1.2 mM and -47.5 ± 4.4 mV (n = 16), ns (P=0.09, T=1.3; P=0.17, Mann-Whitney U = 137), figure 4.3B). However, the 1.8 mM Ca^{2+} evoked a significant increase in the proportion of cells showing spontaneous activity at week 2 (29% (n = 21) in 0.6 mM Ca^{2+}, 37.5% (n = 16) and 56% (n = 16) in 1.8 mM Ca^{2+}, $P<0.05$, $chi^2=2.89$, figure 4.3C). At week 3 the increased Ca^{2+} media showed a decline in function similar to that of the control cells, with relatively depolarised resting membrane potentials (-30.5 ± 3.1 mV (n = 16) in 0.6 mM, -33.2 ± 4.6 mV (n = 5) in 1.2 mM and -34± 5.9 mV (n = 8) in 1.8 mM, figure 1B) and few cells showing spontaneous activity (12.5% (n = 16) in 0.6 mM, 20% (n = 5) in 1.2 mM and 25% (n = 8) in 1.8 mM, ns, figure 4.3C). Although increasing the driving force for Ca^{2+} did not reproduce exactly the effects of ACM, it did both increase spontaneous activity and polarised the resting membrane potential. The 1.8 mM Ca^{2+} medium also increased the rate at which cells were able to fire induced action potentials were generated. The discrepancy between ACM and increasing the Ca^{2+} concentration in the medium was that, like the control cells, the cells cultured in high Ca^{2+} medium functionally declined after week 2. This implies that beyond week 2 there is some functional change that either results in Ca^{2+} influx being ineffective to drive functional maturation, or that Ca^{2+} influx is diminished, which will be examined later in this chapter.

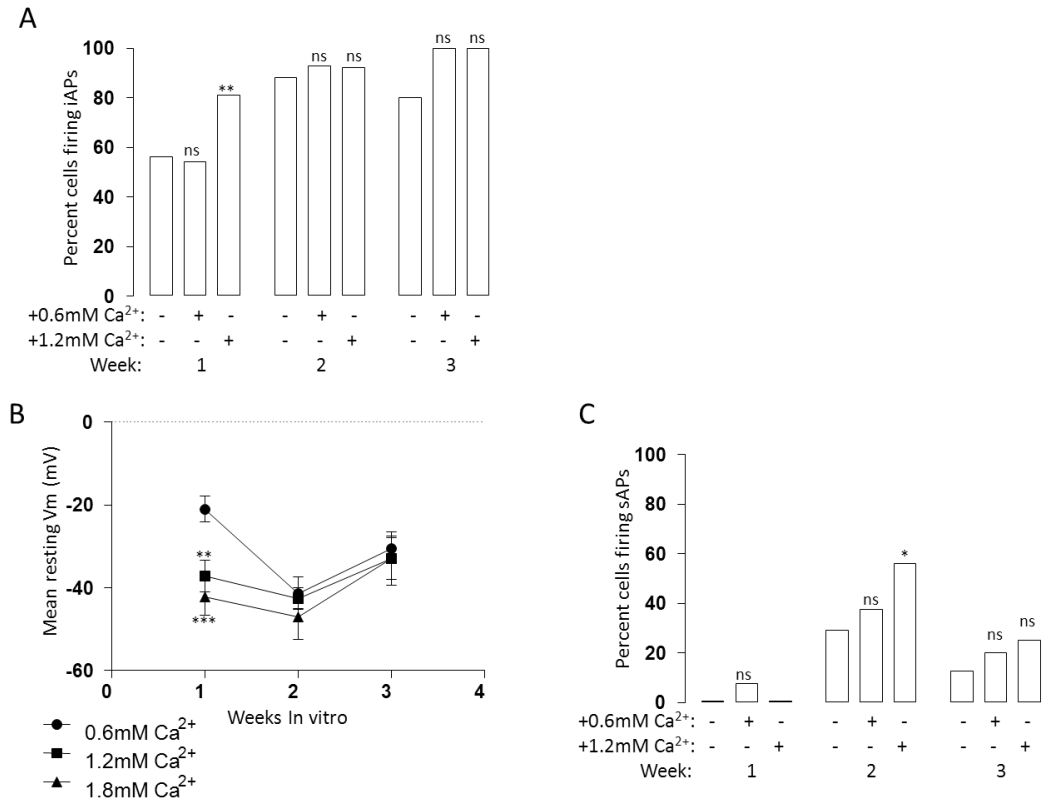

Figure 4.3: The proportion of cells able to fire induced action potentials, proportion firing spontaneous action potentials and the resting membrane potentials of cells treated with all 3 varying Ca^{2+} concentration media.

A) A bar graph showing the proportion of cells capable of firing induced action potentials over the 3 weeks of differentiation in the 0.6 (control), 1.2 and 1.6 mM Ca^{2+} media, compared using Chi^2 against 0.6mM medium.

B) A graph showing the mean resting membrane potential (±SEM) over the 3 weeks of differentiation in the 0.6 (control), 1.2 and 1.8 mM Ca^{2+} media, compared using T-test against 0.6mM medium.

C) A bar graph showing the portion of cells showing spontaneous action potentials over the 3 weeks of differentiation in the 0.6 (control), 1.2 and 1.6 mM Ca^{2+} media, compared using Chi^2 against 0.6mM medium.

The mechanisms driving Ca^{2+} influx in these cultures were investigated in the hopes of understanding why at week 3 the increased Ca^{2+} concentration ceased to enhance functional maturation. The functional Ca^{2+} channels using patch clamp and the function of $GABA_A$ channels using Ca^{2+} imaging were examined over the first 2 weeks of differentiation to find any changes over time which may explain changes in the nature of native Ca^{2+} influx in these cells over time. Cells were differentiated in the control and 1.8 mM Ca^{2+} medium (now referred to as the high Ca^{2+} medium). Further cells were differentiated using the same high Ca^{2+} medium with 10 µM bicuculline to block $GABA_A$ receptors, therefore testing the hypothesis that GABA signalling itself was required for any changes in Ca^{2+} influx or $GABA_A$ function over time. Over the first 2 weeks of differentiation, the proportion of cells with measurable Ca^{2+} currents was assessed using patch clamp with a voltage ramp protocol using high $BaCl_2$ solution to amplify and identify Ca^{2+} channel currents. At week 1, no control cells showed significant Ca^{2+} currents (0% (n = 9)) and 20% of cells showed Ca^{2+} currents (n = 10)) in high Ca^{2+} medium (figure 4.4A). However, at week 2, there was a significant increase in the proportion of cells with functional voltage activated Ca^{2+} channels in the high Ca^{2+} medium (22.2% (n = 9) in control medium and 100% (n = 7), $P<0.01$, $Chi^2=9.6$, figure 4.4A), which was almost entirely blocked by bicuculline (42% (n = 12), $P<0.05$, $Chi^2=6.5$, figure 4.4A). The number of cells with inhibitory and excitatory GABA responses was then assessed using Ca^{2+} imaging (see methods). Crucially, the high Ca^{2+} medium had accelerated the switch from excitatory to inhibitory; at week 1 roughly half of the cells had already made the switch from excitatory to inhibitory by week 1 (100% (n = 17) excitatory in control vs 52% (n = 17) excitatory in high Ca2+ medium, $P<0.01$, $Chi^2=10.5$), and were almost entirely inhibitory by week 2 (only 8.3% (n = 12) excitatory, figure 4.4B). In contrast, half of the cells were still excitatory at week 2 (40% (n = 10), $P<0.05$, $Chi^2=3.1$) and bicuculline was sufficient to slow the switch down that 80% were still excitatory at week 2 (80% n = 15, $P<0.001$, $Chi^2=13.2$, figure 4.4B).

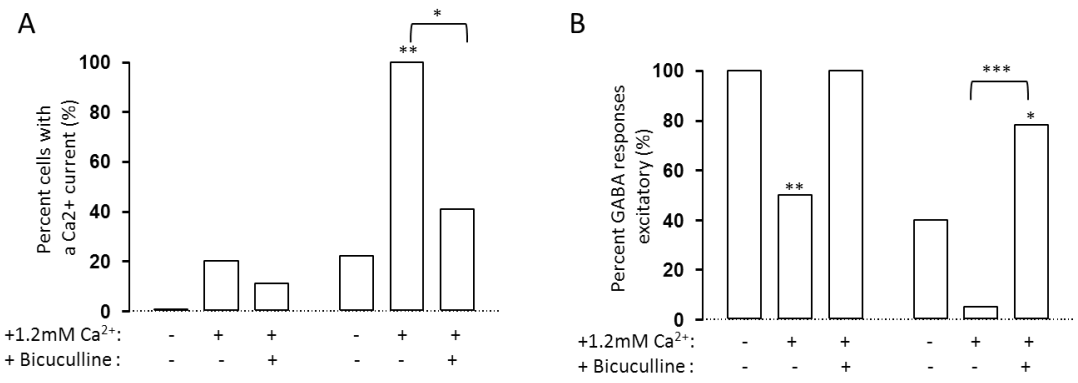

Figure 4.4: The proportion of cells with voltage gated Ca^{2+} channels and excitatory GABA responses in control, high Ca^{2+} and high Ca^{2+} with bicuculline media.

A) A bar graph showing the proportion of cells with a significant voltage activated Ca2+ current when measured using patch clamp at weeks 1 and 2 of differentiation, for cells cultured in control, 1.8 mM Ca^{2+} and 1.8 mM Ca^{2+} medium with 10 µM bicuculline (compared using Chi^2 test).

B) A bar graph showing the proportion of cells with excitatory GABA responses, measured using Ca^{2+} imaging, at weeks 1 and 2 of differentiation, for cells cultured in control, 1.8mM Ca^{2+} and 1.8 mM Ca^{2+} medium with 10 µM bicuculline (compared using Chi^2 test).

Increasing Ca^{2+} influx using the high Ca^{2+} medium resulted in increased functional expression of Ca^{2+} channels in differentiating neurons by week 2, similar to observations made in the ACM. However, the high Ca^{2+} medium also, and in contrast to ACM, significantly accelerated the switch from excitatory to inhibitory GABA responses; resulting in virtually no cells with excitatory GABA responses by week 2 in the high Ca^{2+} cultures. This has the functional consequence that by the second week, stimulation by GABA is no longer able to depolarise the membrane and drive Ca^{2+} influx in the high Ca^{2+} medium. This is consistent with both the control and high Ca^{2+} medium reaching a functional peak at week 2 and then declining, because GABA could no longer drive the Ca^{2+} influx to enable functional maturation. Further, blockade of $GABA_A$ receptors was sufficient to inhibit the development of functional Ca^{2+} currents and slow the switch from excitatory GABA to inhibitory GABA.

To test the hypothesis that GABA-evoked depolarisation specifically could drive Ca^{2+} influx dependant maturation, 300 µM GABA was added to the control (0.6 mM Ca^{2+}) medium to stimulate $GABA_A$ receptors as a second strategy for increasing Ca^{2+} influx. Also, testing the hypothesis in the increased Ca^{2+} medium that GABA stimulation is required for the Ca^{2+} influx, 10 µM bicuculline was added to the high Ca^{2+} medium again to block $GABA_A$.

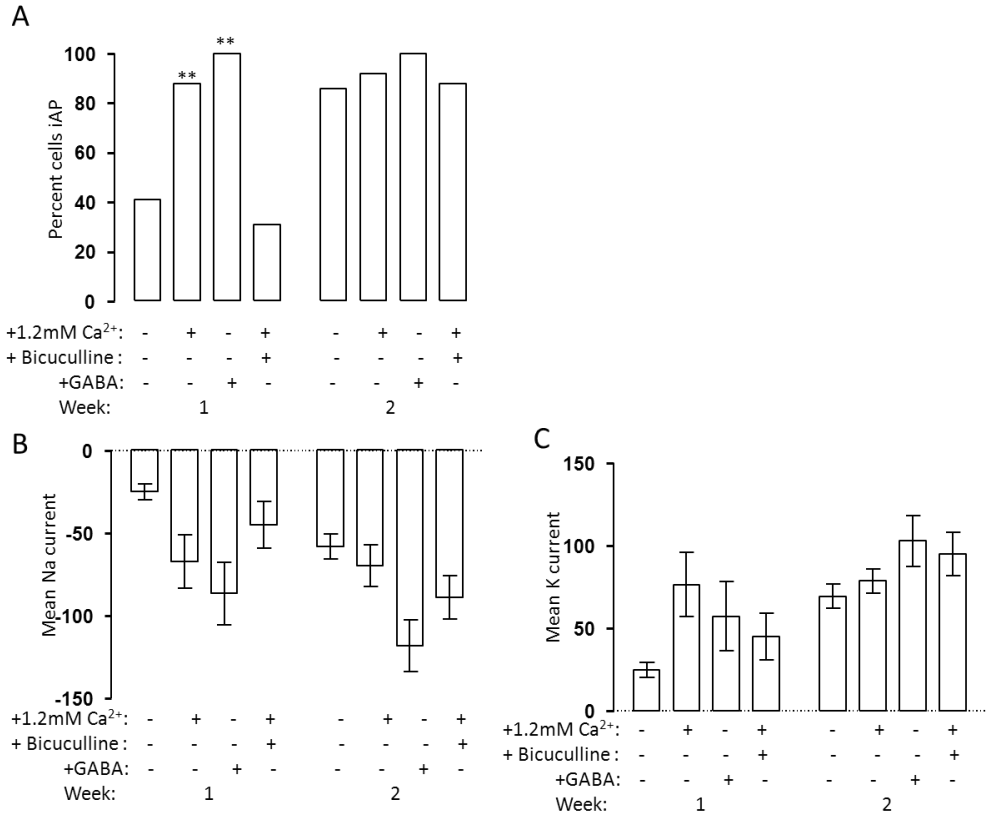

Figure 4.5: The proportion of cells able to fire induced action potentials, and the magnitudes of both Na^+ and K^+ channel current densities in the control, GABA, high Ca^{2+} and high Ca^{2+} with bicuculline media.

A) A bar graph showing the proportion of cells able to fire an induced action potential during a current step protocol in the control medium, high Ca^{2+} medium, high Ca^{2+} medium with 10µM bicuculline and the control medium with 300µM GABA.

B) A bar graph showing the mean peak Na current densities (±SEM) in the control medium, high Ca^{2+} medium, high Ca^{2+} medium with 10 µM bicuculline and the control medium with 300µM GABA.

C) A bar graph showing the mean K current densities (±SEM) in the control medium, high Ca^{2+} medium, high Ca^{2+} medium with 10 µM bicuculline and the control medium with 300 µM GABA.

Consistent with observations made using the high Ca^{2+} medium (88% (n = 16) in high Ca^{2+} medium), the GABA medium also accelerated the generation of cells able to fire induced action potentials at week 1 (100% (n = 8) with GABA vs. 50%(n = 22) in control medium, $P<0.01$, $Chi^2=7$, figure 4.5A). Further, blockade of $GABA_A$ receptors (using 10µM bicuculline) in the high Ca^{2+} medium inhibited the generation of cells able to fire action potentials at week 1 (88% (n = 16) in high Ca^{2+} medium vs 31%(n = 15) with bicuculline, $P<0.001$, $Chi^2=9.6$, figure 4.5A). Therefore, demonstrating that like ACM, the functional enhancements driven by increased Ca^{2+} concentration are $GABA_A$-dependant. These increases in cells able to fire action potentials also correlated well with increases in the magnitude of voltage activated Na^+ and K^+ currents in cells treated with either the high Ca^{2+} medium or GABA medium (Na^+: -86.6 ± 18 (n = 8) with GABA or -67 ± 15 (n = 10) with high Ca^{2+} vs -37.3 ± 13 (n = 6) in high Ca^{2+} with bicuculline and -27.0 ± 5.0 (n = 11) in control medium; K^+: 66.3 ± 10 (n = 8) with GABA or 76.6 ± 19 (n = 10) with high Ca^{2+} vs 47.9 ± 19 (n = 6) in high Ca^{2+} with bicuculline and 24.4 ± 4.7 (n = 11) in control medium (all $pA.pF^{-1}$), figure 4.5B and C). Further, significantly more hyperpolarised membrane potentials were observed in both the high Ca^{2+} medium and GABA media at week 1 (-19.8±2.6 mV (n = 19) in control medium vs -42.4±3.3 mV (n = 8) in GABA medium ($P<0.001$, $T=4.3$) and -41.4±3.2 mV (n = 16) in high Ca^{2+} medium ($P<0.001$, $T=5.2$)), which was blocked by bicuculline in the high Ca^{2+} medium (-41.4±3.2 mV (n = 16) vs -20.1±2.9 mV (n = 19) with bicuculline, $P<0.001$, $T=5.3$, figure 4.6B). Further, this improved resting membrane potential correlated with more cells showing spontaneous action potentials in the GABA medium (25% (n = 8) with GABA vs 0% (n = 25) in control, $P<0.01$, $Chi^2=6.9$), but surprisingly not the high Ca^{2+} medium (6.3% (n = 16) in high Ca^{2+} vs 0% (n = 25) in control, ns, $Chi^2=0.1$, figure 4.6A). At week 2 both the control medium treated cells had caught up, now almost all cells in all conditions were able to fire action induced potentials (89% (n = 19) in control vs 92% (n = 12), figure 4.5A) and showed somewhat closer resting membrane potentials (-39.3 ± 3.7 mV (n = 21) in control vs -47.1 ± 4.4 mV (n =

16), ns (P=0.09, T=1.3; P=0.17, Mann-Whitney U = 137), figure 4.6B). In contrast, the bicuculline treated cells by contrast still showed somewhat depolarised resting membrane potentials (-25.3 ± 2.2 mV (n = 16) in high Ca^{2+} and bicuculline medium vs -47.1 ± 4.4 mV (n = 16) in high Ca^{2+} medium, P<0.001, T=4.4; or -39.4 ± 3.7 mV (n = 21) in control medium, P<0.01, T=3, figure 4.6B), but were mostly able to fire action potentials (87.5% (n = 16) with bicuculline, figure 4.5A). This shows that blockade of $GABA_A$ had only ameliorated the effects of increased Ca^{2+} influx and had not stopped the cells from differentiating to cells with a basic neuronal phenotype. As previously discussed at week 2 the high Ca^{2+} medium evoked a significant increase in the portion of cells firing spontaneous action potentials. However, in the GABA medium similar levels of spontaneous activity moving from week 1 to week 2(25% (n = 8) to 33% (n = 9), figure 4.6A) were observed.

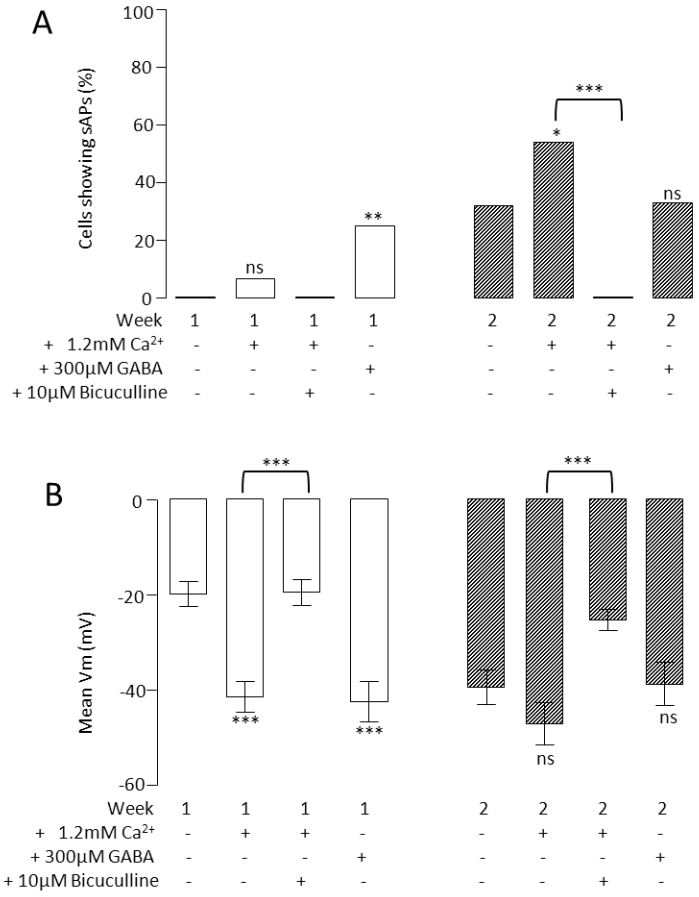

Figure 4.6: A comparison of the proportion of cells showing spontaneous activity and the polarisation of the resting membrane potential for cells treated with control, GABA, high Ca^{2+} and high Ca^{2+} with bicuculline media.

A) A bar graph showing the proportion of cells showing spontaneous action potential during a current clamp I=0 in the control medium, high Ca^{2+} medium, high Ca^{2+} medium with 10µM bicuculline and the control medium with 300µM GABA (compared using Chi^2 test).

B) A bar graph showing the mean resting membrane potential (±SEM) during current clamp in the control medium, high Ca^{2+} medium, high Ca^{2+} medium with 10µM bicuculline and the control medium with 300µM GABA (compared using T-test).

The high Ca^{2+} medium cells were then compared to control cells using immunohistochemistry at week 3 as another assay for neuronal development. Immunohistochemistry was performed using antibodies for β3 tubulin, map2ab as markers for young and more mature neurons respectively, and nestin for neural progenitor cells. Surprisingly, only approximately half of the cells stained positive for β3-tubulin, which was slightly increased with high Ca^{2+} medium compared to control (48.2% (n = 1129) vs 52.9% (n = 1158) $P<0.05$, $Chi^2= 5$, figure 4.7 and 4.8). This perhaps suggests many immature glial cells were also present in these cultures; these may have contributed a significant number of the population not staining for β3 tubulin. Also surprisingly relatively few of the cells were positive for the more mature neuronal marker Map2ab, although this was again increased slightly with the high Ca^{2+} medium (7.3% (n = 2968) vs 11.3% (n = 2908), $P<0.0001$, $Chi^2=28$, figure 4.7 and 4.8). A larger difference was observed when comparing the number of cells nestin positive, where significantly fewer cells were positive in the high Ca^{2+} medium (38.1% (n = 1129) vs 28.3% (n = 1158), $P<0.0001$, $Chi^2=24.5$, figure 4.7 and 2.8). This is consistent with the notion that the increased Ca^{2+} influx has a significant role in pushing neural progenitor cells to differentiate into neurons.

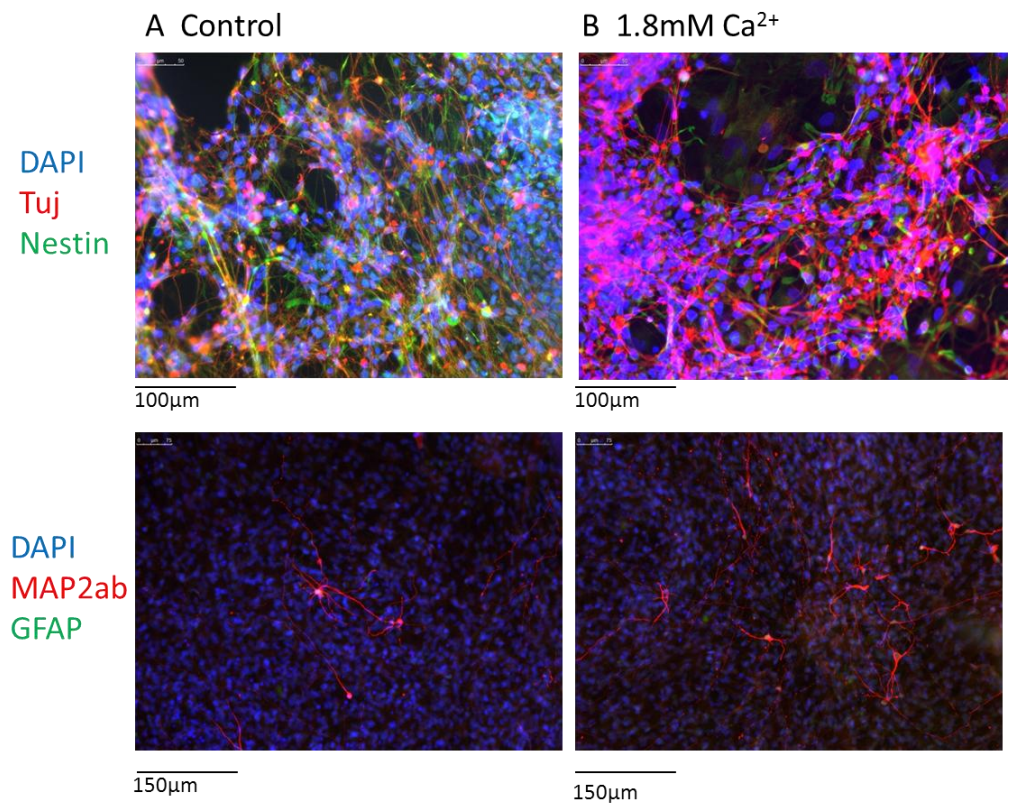

Figure 4.7: Immunohistochemistry for β3-tubulin, Map2AB and Nestin in control and high Ca^{2+} medium-treated cells.

A) Staining for DAPI (blue), β3-tubulin(red) and nestin (green) (top), and DAPI (blue), MAP2ab (red) and GFAP (green) (bottom) in cells differentiated for 3 weeks in the control medium.

B) Staining for DAPI (blue), β3-tubulin(red) and nestin (green) (top), and DAPI (blue), MAP2ab (red) and GFAP (green) (bottom) in cells differentiated for 3 weeks in the 1.8mM Ca^{2+} medium.

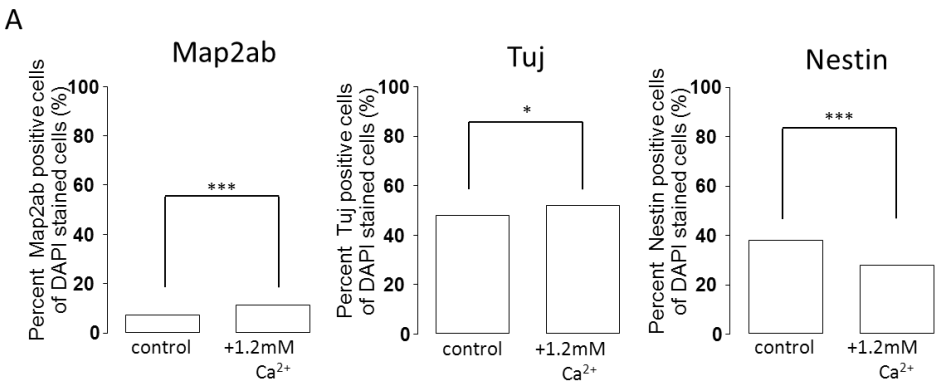

Figure 4.8: A) Bar graphs showing the portion of cells under immunostain which were positive to Map2ab, β3-tubulin (Tuj) and Nestin as a percentage of total cells (using DAPI stain) (compared using Chi^2 test).

Manipulating specific ion channels in the high Ca^{2+} medium

To assess the influence of each sub-type of voltage activated Ca^{2+} channel in the development of neuronal function in the high Ca^{2+} medium, each sub-type of Ca^{2+} channel was individually blocked. It was speculated that, similar to observations made in the astrocyte conditioned medium, that pharmacological blockade of specific sub-types of Ca^{2+} channel expressed in the control cells would have significant effects on the functional maturation of neurons in the high Ca^{2+} medium. Therefore the hypothesis was tested that blockade of either L- or N- type channels would block the development of spontaneous activity and result in a hyperpolarised resting membrane potential.

At week 1, blockade of L- or N-type Ca^{2+} channels had no significant effect on development of cells able to fire induced action potentials in the high Ca^{2+} medium (79% (n = 15) when blocking L-type and 64% (n = 11) when blocking N-type vs 87.5% (n = 16) without either, figure 4.9A). By contrast, $GABA_A$ blockade significantly impaired the development of inducible action potentials (31% (n = 15) with bicuculline vs 87.5% (n = 16) without, $P<0.001$, $Chi^2=9.6$, figure 4.9A), which it was thought drives Ca^{2+} influx by depolarising the cell in response to GABA. Therefore, it is surprising that N-, and L- type channel blockade appeared to not mimic $GABA_A$ blockade. However, blockade of P/Q-type Ca^{2+} channels had a moderate but significant effect on cells showing inducible action potentials at week 1 (50%

(n = 10), P<0.05, Chi^2=4.4, figure 4.9A). Which is further surprising as by the end of the first week very few cells were observed with functional P/Q-type Ca^{2+} channels; this could suggest a level of very early expression of P/Q-type channels, perhaps even at the neural progenitor cell stage. Into week 2, and the ability to fire induced action potentials was no longer inhibited by $GABA_A$ or Ca^{2+} channel blockade (90% (n = 11), 82% (n = 11) and 100% (n = 9) when blocking L-, N- and P/Q-type channels (nifedipine, conotoxin and agatoxin, respectively) respectively, or 87.5% (n = 16) when blocking $GABA_A$ channels (bicuculline), compared to 92% in high Ca^{2+} medium (n = 12), ns, chi^2<0.5, figure 4.9A). However, the blockade of L- or N-type Ca^{2+} channels did evoke a moderate depolarisation of the resting membrane potential at week 1 (-31.6 ±4 mV (n = 17) when blocking L-type and -32 ±4 mV (n = 12) when blocking N-type, vs -41.4 ±3.2 mV (n = 16) without, P<0.05, T>1.8, figure 4.9B). This is entirely consistent with $GABA_A$ channel blockade which resulted in a more significant depolarisation of the resting membrane potential (-20.1 ±2.9 mV (n = 19), P<0.001, T=5.3, figure 4.9B). A moderately depolarised resting membrane potential was also observed when P/Q-type Ca^{2+} channels were blocked (-32 ±4.8 (n = 10), P<0.05, T=1.88, figure 4.9B), again pointing to an early expression of these channels. By week 2, the cells treated with high Ca^{2+} medium and antagonists for L- or N-type Ca^{2+} channels showed even more depolarised resting membrane potentials (-21.8 ±2.8 mV (n = 13) when blocking L-type or -20.7 ±3.5 mV (n = 15) when blocking N-type, vs -47.1 ±4.4 mV (n = 16) without, P<0.001, T> 4.8, figure 4.9B) and were now very reminiscent of cells treated with $GABA_A$ blockade (-25.3 ±2.2 mV (n = 16), figure 4.9B). Blockade of P/Q-type channels were no longer showing any effect on the resting membrane potential by week 2 (-42.2 ±3.2 mV (n = 9), ns, T=0.3), consistent with the notion that they were only expressed at a very early stage. Crucially, and consistent with $GABA_A$ blockade, there was a complete ablation of spontaneous activity by either L- or N-type Ca^{2+} channel blockade (0% (n = 13) when blocking L-type or 0% (n = 10) when blocking N-type, vs 56% (n = 16) without, P<0.001, Chi^2>12, figure 4.9C). This was not observed with P/Q- type Ca^{2+} channel blockade (44% (n = 9)), which developed similar levels of spontaneous activity to the high Ca^{2+} medium.

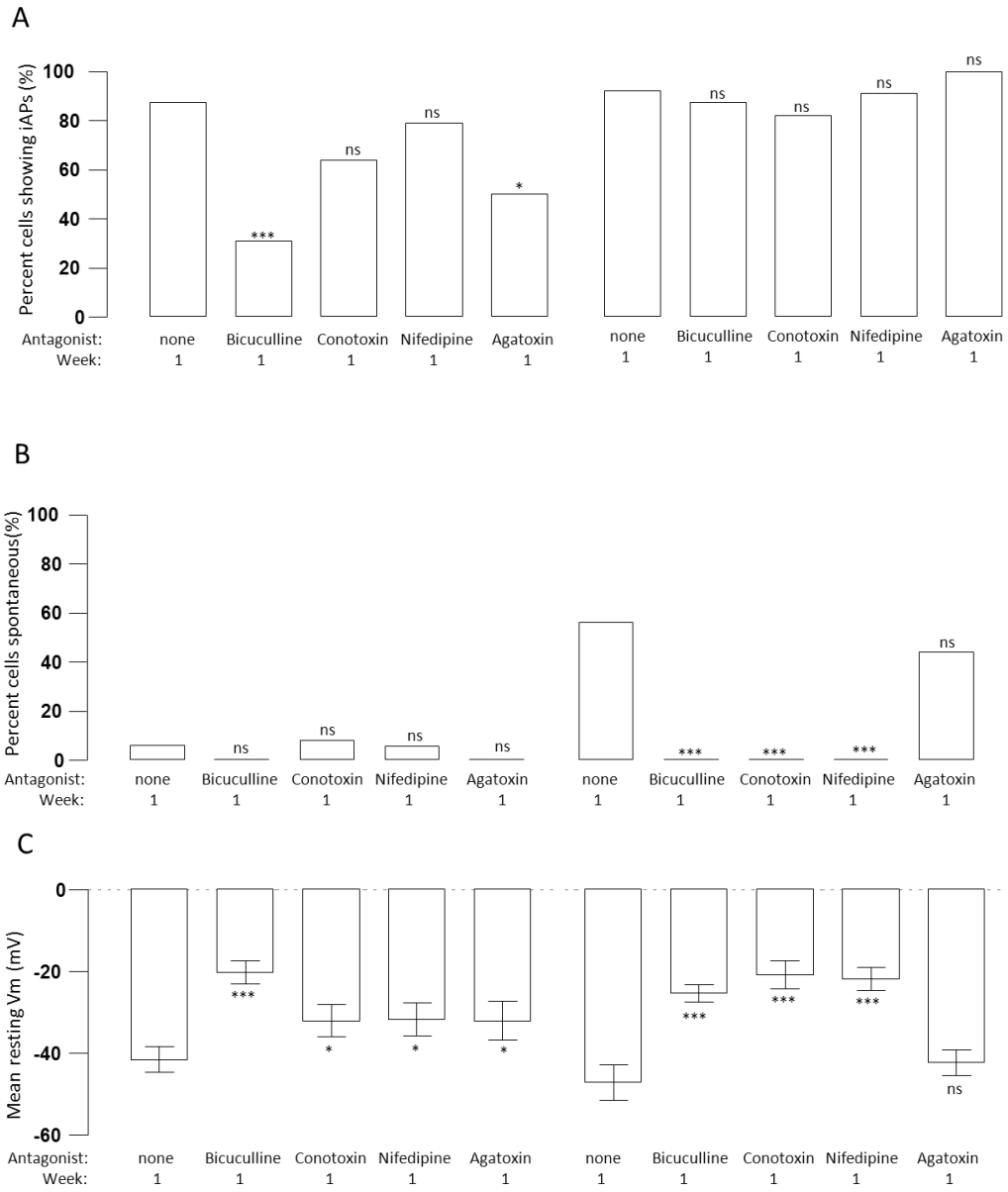

Figure 4.9: Comparison of proportion of cells showing spontaneous activity, proportion of cells showing induced action potentials and resting membrane potential of cells cultured in high Ca^{2+} medium and with the addition of 2 µM nifedipine, 0.1 µM agatoxin, 0.1 µM conotoxin or 10 µM bicuculline individually.

A) A bar graph showing the portion of cells able to fire an induced action potential during a current step protocol in the 1.8 mM medium, and with the addition of 2 µM nifedipine, 0.1 µM agatoxin, 0.1 µM conotoxin or 10 µM bicuculline (compared using Chi^2 test) at weeks 1 and 2.

B) A bar graph showing the portion of cells showing spontaneous activity in the 1.8mM medium, and with the addition of 2 µM nifedipine, 0.1 µM agatoxin, 0.1 µM conotoxin or 10 µM bicuculline (compared using Chi^2 test) at weeks 1 and 2.

C) A bar graph showing the mean resting membrane potential (±SEM) for cells cultured in the high Ca^{2+} medium and with the addition of 2 µM nifedipine, 0.1 µM agatoxin, 0.1 µM conotoxin or 10 µM bicuculline (compared using T- test) at weeks 1 and 2.

Increasing the Ca^{2+} concentration in the medium resulted in an immediate acceleration of the development to a basic neuronal phenotype, followed by a hyperpolarised resting membrane potential and a higher proportion of cells with spontaneous activity. It appears that at a very early stage P/Q- type Ca^{2+} channels contribute to the Ca^{2+} influx which drives the functional maturation. However, their expression has waned by the end of the first week. L- and N- type channel blockade do not appear to impact the initial development of a basic neuronal phenotype, in terms of generating an induced action potential. This is consistent with L- and N-type channels being only expressed in neurons, and so only after the development of a basic neuronal phenotype. Following this initial stage, the L- and N-type channels are both required for the neurons to mature from a basic phenotype to developing a polarised resting membrane potential and spontaneous activity. $GABA_A$ function appears to have a role at both stages. Firstly, blocking these channels slowed down the development of cells able to fire an inducible action potential. Following that, blockade of these channels entirely ablated the development of a more mature phenotype with a hyperpolarised resting membrane potential and spontaneous activity. This strongly suggests that GABA stimulation provides a pro-neurogenic, followed by a pro-maturation and pro-synaptogenic stimulus by driving Ca^{2+} influx, initially through P/Q-type Ca^{2+} channels and then later using the more typically neuronal L- and N- type channels. Beyond the initial differentiation to a basic neuronal phenotype, the data then suggest that GABA continues to provide a stimulus to drive further functional maturation, producing more polarised membranes and permitting more spontaneous activity. With more time however, GABA becomes an inhibitory neurotransmitter, and is no longer able to drive functional

maturation, resulting in an eventual functional decline in both the high Ca^{2+} and control media.

These data suggest that GABA signalling is central to the mechanism behind early functional maturation in iPS cell-derived neurons, as it provides a depolarising stimulus to activate voltage activated Ca^{2+} channels. For both L- and N- type Ca^{2+} channel blockade to individually have an equal effect on functional maturation to $GABA_A$ blockade, it seems appropriate to suggest that the two sub-types of Ca^{2+} channel have different, and equally critical roles in this mechanism. Previous studies have linked L-type Ca^{2+} channels to the post-synaptic membrane and provide Ca^{2+} influx in response to synaptic activity [116]. In contrast, N-type Ca^{2+} channels are linked to the pre-synaptic membrane and respond to action potentials reaching the pre-synaptic membrane to mediate synaptic vesicular release [85]. Therefore, it seems probable that N-type channels are required in this mechanism because they mediate the endogenous release of GABA and L-type channels are required as they produce the Ca^{2+} influx at the post-synaptic membranes in response to GABA-dependent depolarisation.

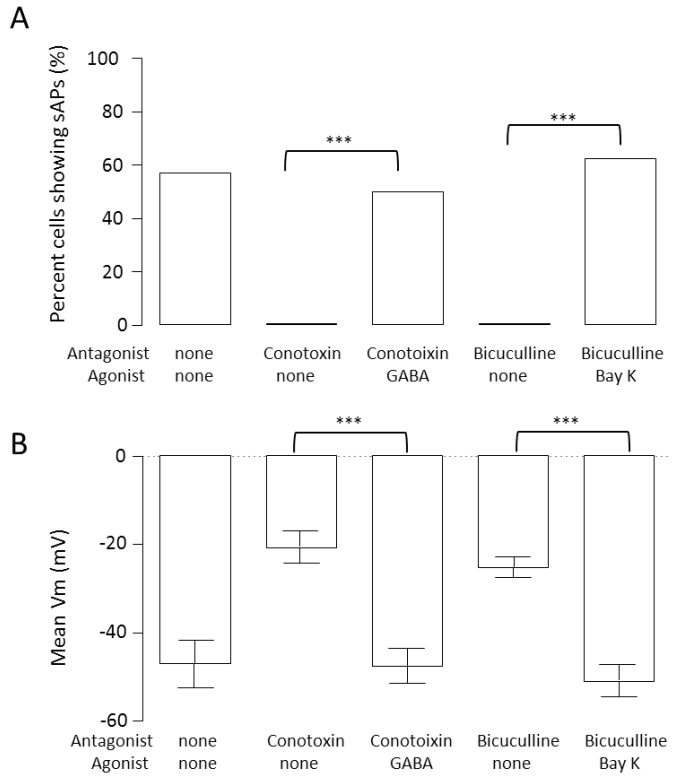

Figure 4.10: The ability of GABA to rescue functional development with conotoxin treatment and the ability of Bay K8644 to rescue functional development with niphedipine treatment.

A) A bar graph showing the proportion of cells (%) showing spontaneous activity in 1.8mM Ca2+ medium, and with the following: 0.1µM conotoxin; 0.1µM conotoxin and 300µM GABA; 10µM bicuculline and 10µM Bay K8644 at week 2 (compared using Chi^2 test).

B) A bar graph showing the mean resting membrane potential (±SEM) in 1.8mM Ca2+ medium, and with the following: 0.1µM conotoxin; 0.1µM conotoxin and 300µM GABA; 10µM bicuculline and 10µM Bay K8644 at week 2 (compared using T- test).

Following the experiments described above, the hypothesis that the addition of GABA to the high Ca^{2+} medium with conotoxin (N-type Ca^{2+} channel antagonist) could replace the GABA that is not being secreted because the Ca^{2+} influx from N-type Ca^{2+} channels are not initiating GABA-vesicle release was tested. Indeed, 300µM GABA added to the 0.1 µM conotoxin and high Ca^{2+} medium rescued the development of spontaneous activity (from 0% (n = 15) with conotoxin to 50% (n = 10) with both GABA and conotoxin, $P < 0.01$, chi2 = 9.38, figure 4.10A) and a hyperpolarised resting membrane potential (from -20.7 ± 3.5 mV (n = 15) with conotoxin to -47.6 ± 3.9 mV (n = 10) with both GABA and conotoxin, $P < 0.001$, T=5.1, figure 4.10B).

Another hypothesis, that the addition of BayK 8644 to directly activate L-type Ca^{2+} channels would remove the need for GABA-dependant depolarisation for Ca^{2+} influx to enhance functional maturity was tested. 10µM BayK 8644 added to the 10µM bicuculline and high Ca^{2+} medium rescued the development of spontaneous activity (from 0% (n = 19) with bicuculline to 62.5% (n = 8) with Bay K8644 and bicuculline, $P < 0.01$, Chi^2=14.6, figure 4.10A) and a hyperpolarised resting membrane potential (from -25.1 ± 2.2 mV (n = 19) with bicuculline to -51.0 ± 4.4 mV (n = 8) with Bay K8644 and bicuculline, $P < 0.001$, T=6.4, figure 4.10B).

Since GABA or BayK 8644 were able to completely ameliorate the effects of either conotoxin or bicuculline, respectively this suggests an order of events in this maturation mechanism.

N-type Ca^{2+} channels, blocked by conotoxin, are required for GABA-secretion. The secreted GABA activates $GABA_A$ receptors providing depolarisation sufficient to stimulate L-type Ca^{2+} channel activity. This suggests direct activation of L-type Ca^{2+} channels, with BayK 8644, results in the most direct strategy for using Ca^{2+} influx to drive functional maturation. Using BayK 8644 to directly activate L-type Ca^{2+} channels also has the benefit of not being dependant on GABA-signalling, which means it does not become ineffective at the time point at which GABA becomes inhibitory. Therefore, BayK 8644 stimulation in conjunction with an increased Ca^{2+} concentration medium could provide a powerful, but defined, mechanism for driving functional maturation in pluripotent stem cell-derived neurons. One limitation may be that, at the very early stages of the differentiation protocol very few cells have functional L-type Ca^{2+} channels. However, both GABA-stimulation and increased Ca^{2+} concentration are effective, likely due to early P/Q-type channel function. Therefore, as a suggested protocol, the use of a high Ca^{2+} medium with GABA treatment initially which is replaced by Bay K8644 may be a very effective strategy for rapidly producing electrophysiologically functional neurons.

Using dopamine in the differentiation protocol

Dopamine is an important neurotransmitter for striatal function. Projections from the substantia nigra innervate the striatum allowing the TH (tyrosine hydroxylase) positive projections to secrete dopamine across the striatum [206]. Medium spiny neurons of the striatum respond to dopamine which evokes different responses in each type of medium spiny neuron based on their expression of either D1 or D2 type dopamine receptors. Using the intermediate DARPP32, dopamine stimulation results in the attenuation of multiple ion channel currents crucial to medium spiny neuron function; these include NMDA-type glutamate receptors, L-type Ca^{2+} channels and $GABA_A$ receptors [54]. The attenuation of these currents by dopamine is different in each type of medium spiny neuron, acts as a fine-tuning mechanism for the two paths of motor control through the striatum; the direct and indirect pathways.

Focussing on development and maturation, dopamine receptor stimulation has been linked to CREB phosphorylation and may play an important role in functional maturation in the

developing striatum [32,53]. Therefore as a potential strategy for functionally enhancing iPS cell derived neurons of a striatal lineage, dopamine or co-culture with dopaminergic neurons were considered.

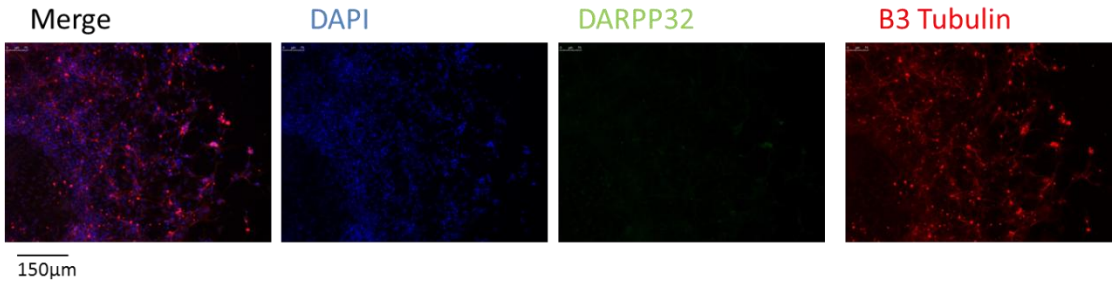

Figure 4.11:

A) Stains for DAPI (blue), DARPP32 (green) and β3-tubulin (red) in week 2 control differentiated neurons, colour channels separated and labelled above.

To determine if the differentiation protocol had indeed successfully specified a striatal lineage, the cells were immunologically studied for the presence of medium spiny neurons, the most numerous neuronal cell type in the striatum. Immunostains for DARPP32, an established cell marker for medium spiny neurons, revealed no detectable DARPP32 expression in the control cultures at week 2 (figure 4.11). This is consistent with results showing that even in far lengthier differentiation protocols less than 10% of cells express DARPP32, meaning very poor yields of crucial medium spiny neurons[8,29]. This implies the differentiation protocol had not specified a striatal lineage, and no medium spiny neurons were produced. However, despite DARPP32 playing a crucial role in the functional response of medium spiny neurons to dopamine, this does not rule out a separate developmental response to dopamine.

Co-culture of iPS cell-derived neurons from which had been developed, using a typical midbrain dopaminergic neuron differentiation protocol and neurons from the control differentiation protocol was attempted. However, the dopaminergic differentiation protocol resulted in relatively low yields of TH+ neurons and a mixture of neuronal and glial sub-types (data not shown). Therefore, to test only the effects of dopamine on development, avoiding the potential effects of neurons and astrocytes being added to the culture,

dopamine was added to the differentiation culture as a defined protocol. The hypothesis that 20 µM dopamine added to the differentiation medium could enhance neuronal function, of these none-striatal neurons, in terms of resting membrane potential and action potential generation was tested.

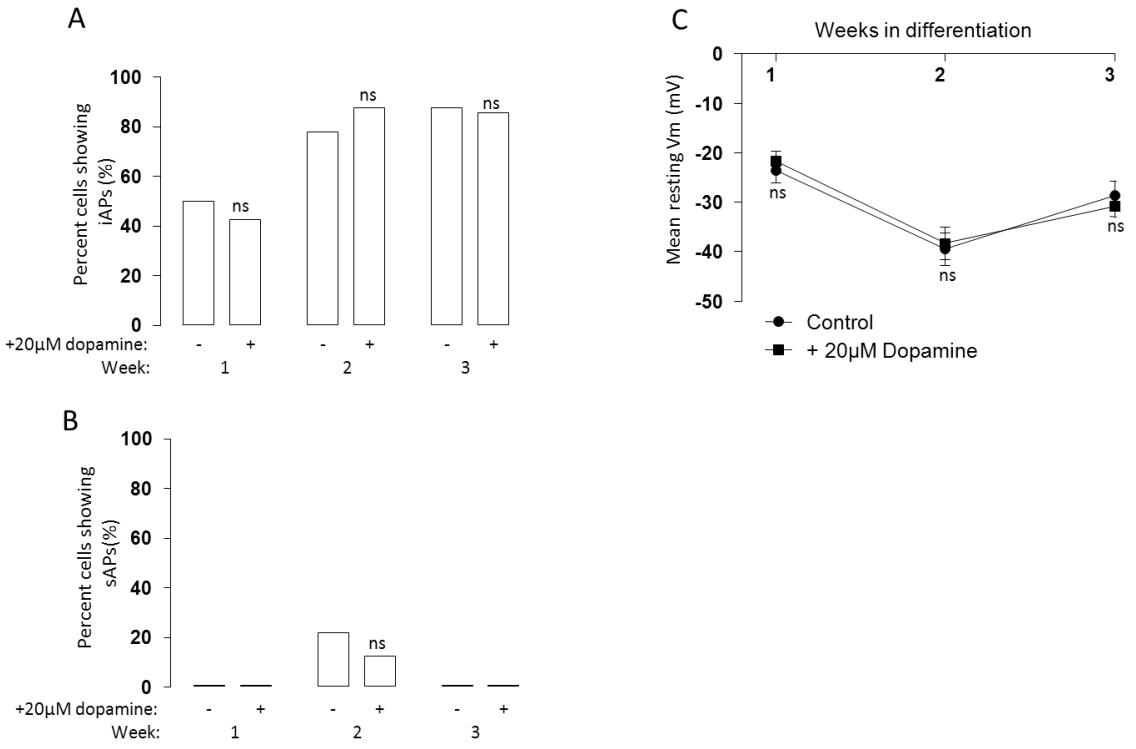

Figure 4.12: The electrophysiological properties of iPS cell-derived neurons cultured in the standard differentiation protocol, and with dopamine.

A) Bar graph showing the proportion of cells able to fire induced action potentials over 3 weeks of differentiation in control medium and control medium with 10 µM dopamine.

B) Bar graph showing the portion of cells showing spontaneous activity over 3 weeks of differentiation in control medium and control medium with 10 µM dopamine.

C) A graph showing the mean resting membrane potential (±SEM) over 3 weeks of differentiation in control medium and control medium with 10 µM dopamine.

Differentiated iPS-cell derived neurons using the standard differentiation protocol and with 20 µM dopamine added to the medium were compared electrophysiologically over the 3 week protocol previously described. Both the control and dopamine medium followed a very similar pattern of development. At week 1, roughly half of the cells in both media (50% (n = 8) in control and 43% (n = 7, ns) with dopamine) had developed the ability to fire induced action potentials (figure 4.12A). This increased to almost all cells at week 2 (78% (n = 9) in control and 88% (n = 8, ns) with dopamine). Which essentially continued into week 3 (88% (n = 8) in control and 85% (n = 7, ns) with dopamine, figure 4.12A). The dopamine also failed to evoke a significant change in the cell's resting membrane potential at any week. Following the same pattern as control cells, the dopamine cells started depolarised (-23.5 ±2.5 mV (n = 8) in control and -21.7 ±2.2 mV (n = 7), ns, figure 4.12B), then both produced a slightly more polarised membrane potential at week 2 (-39.5 ±3.2 mV (n = 9) in control and -38.3 ±3.3 mV (n = 8) with dopamine, ns), and then declined at week 3(-28.6 ±2.9 mV (n = 9) in control and -30.8 ±2.1 mV (n = 9) with dopamine, ns, figure 4.12B). Correlating with the pattern of development observed in the resting membrane potential, few cells were firing spontaneous action potentials at week 2 (22% (n = 9) in control and 12.5% (n = 8) with dopamine, ns, figure 4.12C), where the membrane potential was most polarised, however dopamine evoked no significant change.

This disproved the hypothesis that the addition of dopamine to the medium, at a standard working concentration of 20 µM, could positively influence the electrophysiological maturation of iPS cell-derived neurons. The failure of dopamine to influence maturation is most likely attributable to the cells not having been specified down a striatal lineage, resulting in cells that do not express dopamine receptors. However, this strategy may be worth revisiting as a mechanism for improving functional maturity when differentiation protocols, or direct reprogramming techniques, are developed which efficiently specify striatal medium spiny neurons.

Comparing BayK 8644 and mACM in human embryonic stem cell derived neuronal differentiation

Using the data described previously it is plausible that BayK 8644 treatment may be a viable strategy for producing a defined protocol to functionally enhance neurons, similar to ACM, or perhaps more rapidly. This protocol is based upon the notion that BayK 8644 will stimulate the previously investigated Ca^{2+} influx-dependant mechanism for functional maturation, but independently of GABA. Therefore, where GABA or increased Ca^{2+} concentration compared poorly to ACM-treatment at week 3, because of the GABA excitatory to inhibitory switch, BayK 8644 should continue to function. To further validate that this principle is sound, both BayK 8644 and mouse ACM were tested on human embryonic stem cells.

Human embryonic stem cells from the H9-line were partially differentiated using an established protocol for EZ-sphere culture. These EZ-spheres were cultured through between 6 and 11 passages before being used for terminal differentiation. The standard differentiation protocol was employed and also with 10 µM BayK 8644 and the mouse ACM previously described. The functional maturity of these cultures was assessed using patch clamp for the first 2 weeks of differentiation. However, reproducibly the embryonic stem cell-derived differentiations showed very poor survival into week 3.

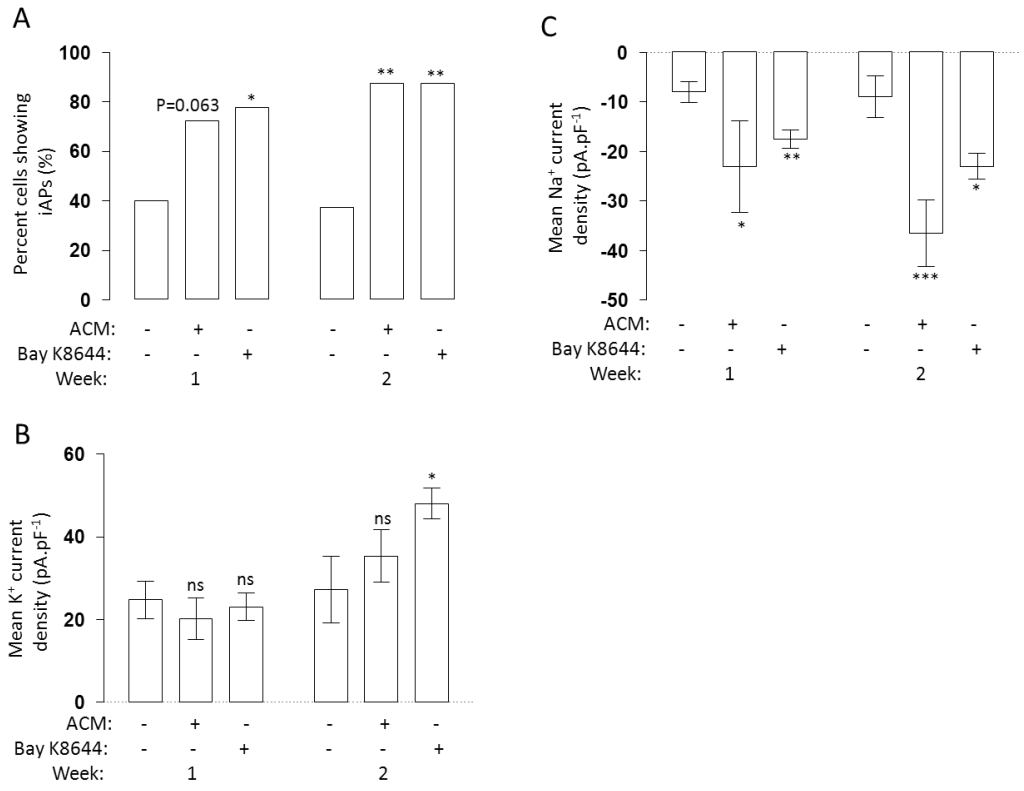

Figure 4.13: A comparison of the ability to fire induced action potentials, Na^+ current density and K^+ current density of human embryonic stem cell-derived (H9) neurons differentiated in control, BayK 8644 medium and ACM.

A) A bar graph showing the portion of cells able to fire induced action potentials during weeks 1 and 2 of differentiation terminal of H9 derived EZ spheres in ACM, 10µ Bay K8644 and control medium.

B) A bar graph the mean peak Na^+ current (±SEM) during weeks 1 and 2 of differentiation terminal of H9 derived EZ spheres in ACM, 10µ Bay K8644 and control medium.

C) A bar graph the mean K^+ current (±SEM) during weeks 1 and 2 of differentiation terminal of H9 derived EZ spheres in ACM, 10µ Bay K8644 and control medium.

Similar to the pattern of maturation seen in the iPS cell-derived neurons, by week 1 40% (n = 10) of the H9-derived neurons had developed the ability to fire induced action potentials. Again, similar to observations made in the iPS-cell derived cultures, the majority of the H9-derived cells had both voltage activated Na^+ and K^+ currents (88% (n = 9) with Na^+ currents, 100% (n = 9) with K^+ currents, figure 32A), but the magnitude of both current densities were

very small resulting in very immature shaped action potentials (-8.2 ± 2.1 pA·pF^{-1} (n = 8) mean Na^+ current density and 24.8 ±4.6 pA·pF^{-1} (n = 9) mean K^+ current density, figure 4.12 B and C). In contrast to the iPS cell-derived neurons, the control H9-derived neurons did not show a significant increase in their Na^+ and K^+ currents from week 1 to week 2 (from -8.2 ± 2.1 pA·pF^{-1} (n = 8) to -8.9 ±4.2 pA·pF^{-1} (n = 7) mean Na^+ current density and from 24.8 ±4.6 pA·pF^{-1} (n = 9) to 28.3 ±8 pA·pF^{-1} (n = 7) mean K^+ current density, figure 32B and C). This resulted in no increase in the portion of cells able to fire action potentials (from 40% (n-10) to 37.5% (n = 9)).

The ACM-treated cells from week 1 showed significantly larger Na^+ current densities (-23.2 ±9.1 pA·pF^{-1} (n = 9), P<0.05, T=1.8), and unsurprisingly most ACM-treated cells were able to fire action potentials by week 1 (73% (n = 11), P=0.0635, figure 32A, B and C). This trend continued into week 2, where the ACM-treated cells showed moderate functional increases in both their Na^+ and K^+ currents (-36.5 ±6.5 pA·pF^{-1} (n = 7) mean Na^+ current density and 35.4 ± 6.4 pA·pF^{-1} (n = 7) mean K^+ current density at week 2), the Na^+ currents were now much larger than control treated cells (P<0.001, T=6.1). Consequently all sampled ACM treated cells were able to fire action potentials (n = 8), compared to only 37.5% (n = 9) in control medium (P<0.01, Chi^2=8.2, figure 14 A, B and C).

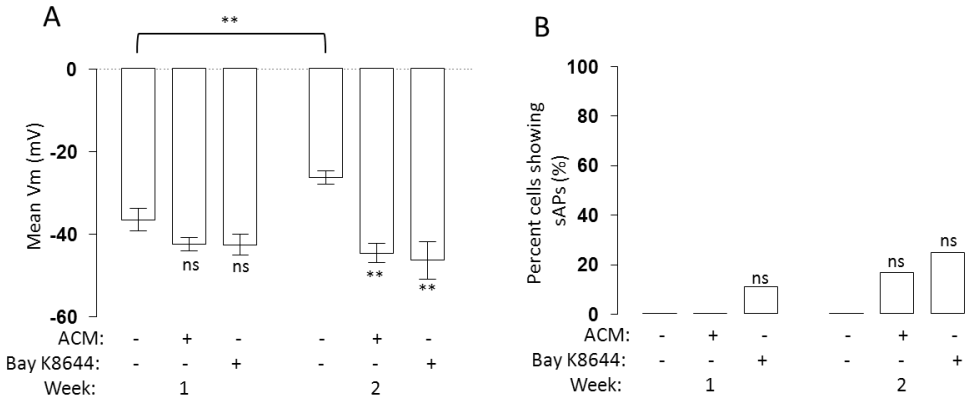

Figure 4.15: Resting membrane potentials and spontaneous action potentials in h9-derived neurons treated with control, BayK and ACM.

A) A bar graph the mean peak resting membrane potential (±SEM) during weeks 1 and 2 of differentiation terminal of H9 derived EZ spheres in ACM, 10µ Bay K8644 and control medium.

B) A bar graph showing spontaneous action potentials during weeks 1 and 2 of differentiation terminal of H9 derived EZ spheres in ACM, 10µ Bay K8644 and control medium.

When examining the cells treated with BayK 8644, a pattern of development similar to that of the ACM-treated cells was observed. At week 1 the BayK 8644 medium evoked a significant increase in voltage activated Na^+ currents (-17.5 ± 1.8 $pA \cdot pF^{-1}$ (n = 8), P<0.01, T=3.3, figure 4.15B), which resulted in a significant increase in the portion of cells able to fire an induced action potential (78% (n = 9), P<0.05, Chi^2=2.8, figure 4.15 A). This trend continued into week 2 where 100% (n = 8) of the BayK 8644 treated cells could fire induced action potentials and with a significantly larger Na^+ current density (-22.9 ±2.6 $pA \cdot pF^{-1}$ (n = 7), P<0.05, T=2.8, figure 4.15 B).

In contrast to the iPS-cell derived neurons, the control treated H9-derived neurons did not develop significant numbers of cells showing spontaneous activity. Even at week 2, none were firing spontaneous action potentials at week 2 (n = 9, figure 33B). This is consistent with the relatively few cells in the control medium able to fire induced action potentials at all. Further, this was confounded by the fact that those few which were able to fire an induced action potential generated, demonstrated very immature action potential shapes, likely due to the limited Na^+ and K^+ currents available. By contrast both the ACM and BayK-treated cultures showed low, but existing populations of spontaneously active neurons (12.5% (n = 8) and 25% (n = 8) in ACM and BayK medium respectively). Crucial to the development of spontaneous activity is the resting membrane potential. At week 1, all 3 cultures showed relatively hyperpolarised resting membrane potentials, which were sufficient to permit action potentials, assuming a cell has significant enough Na^+ and K^+ currents (-40 ±3.1 mV (n = 11) in control, -42.1 ±1.7 mV (n = 11) in ACM and -42.5 ±2.7 mV (n = 9) in BayK medium, figure 4.15A). However from week 1 to week 2, the control cells

actually became significantly less polarised (-26.2 ± 1.6 mV (n = 9), P<0.01, T=3.7), meaning virtually none of these cells had significant pools of closed, and not inactivate Na^+ channels. By contrast both the ACM and BayK treated cells showed slightly more hyperpolarised membrane potentials at week 2 (-43.24 ± 3.073 mV (n = 8) and -44.45 ± 5.579 mV (n = 8), in ACM and BayK treated cells respectively, P<0.01, T>3.3, figure 4.15A). The combination of larger Na^+ current and a hyperpolarised resting membrane potential therefore resulted in a few ACM and BayK treated cells being able to fire spontaneous action potentials. Unfortunately the H9-derived cells showed very poor survival over time, some were lost at week 2 and by week 3 insufficient cells were remaining for any meaningful observations.

The H9-derived neurons from H9-derived EZ spheres showed very poor function and survivability compared to the iPS cell-derived cultures. Therefore, a comparable pattern of development to observations made in the iPS cell-derived cultures was not seen. The control H9-derived cells never developed an enriched population of cells able to fire action potentials with a mature shape, and showed a functional decline after week 1 showing very depolarised resting membrane potentials. The astrocyte conditioned medium also showed a different pattern of development in the H9-derived cells. No significant population of spontaneous active cells was generated using these differentiation protocols. However, the ACM did restore a significant population of cells able to fire induced action potentials and evoke a polarisation of the membrane. Perhaps, if the cells had survived beyond the week 2 point, and continued to functionally develop, the ACM-treated cells would have generated a significant proportion of cells showing spontaneous activity by week 3. However, the BayK 8644 treated cells showed a very similar pattern of development to the ACM-treated cells, in terms of proportion of cells able to fire induced action potentials and resting membrane potential.

Chapter 5: Generating cultures of human iPS cell-derived astrocytes which produce functional astrocyte conditioned medium.

Specific introductions

Astrocyte differentiation

The mechanisms underlying many neurodegenerative diseases are not necessarily limited to neurons or single neuronal sub-types. Other cells of the central nervous system, including glial cells, play pivotal roles in these diseases. For example, in Huntington's disease, the excitotoxic loss of medium spiny neurons is in all likelihood caused in part by the increased sensitivity of medium spiny neurons to extrasynaptic NMDA receptor-driven apoptosis, but also due to reduced glutamate uptake by astrocytes [61,146]. Therefore, in many cases it will be crucial to incorporate astrocytes, or other glial cells, in models of neurodegenerative diseases in vitro. However, current protocols for stem cell derived astrogliogenesis are both lengthy and involve a significant time in co-culture with neurons. It may be very useful to produce enriched cultures of naïve astrocytes, which have not been cultured alongside neurons and do not risk introducing neurons or neural progenitor cells to the final model. This will allow clean integration of wild type astrocytes into a disease neuronal culture, or vice-versa, to produce the co-culture models that are experimentally appropriate.

Therefore, a rapid protocol for differentiating astrocytes in the absence of neurons was developed, using a well-defined culture of neural progenitor cells and source of iPS derived neurons, the same EZ-sphere populations that used to derive neurons. As a possible strategy for developing relatively pure iPS cell-derived astrocyte cultures, the following mechanism was considered: initially prevent neurogenesis by killing mitotic neural progenitor cells with Ara-C (cytosine arabinoside), followed be treatment with LIF-1 to initiate astrocyte differentiation [194]. Lif-1 was used in the second step to promote astrocyte differentiation, but producing an astrocyte precursor population which retains the ability to self-renew [96,19].

Specific methods

Astrocyte differentiation

Astrocyte differentiation was performed using the same EZ-sphere cultures of neural progenitor cells and plated on PLL-laminin coated coverslips (see methods). The base medium used was similar to neuronal differentiation, being based on DMEM:F12 (1:1) as well as 2% B27. However, differentiation occurred in 3 phases. Firstly neurogenesis was blocked using 10 µM Ara-C to inhibit the mitotic division necessary for neurogenesis for 1 week. Following this 10 µM LIF-1 was used to promote astroglial precursor development, to produce a self-renewing GFAP positive population of cells. Following a week the iPS cell-derived astroglial cell culture was transferred to more standard tissue culture flasks and cultured in FBS-based medium to allow the cultures to expand. The differentiation was assessed immunologically using antibodies for β3-tubulin, GFAP and S100β, for neurons, astroglial cells and more mature astroglial cells respectively.

Human astrocyte conditioned medium (hACM)

In addition to the presence of marker proteins for astrocytes, the ability of these iPS cell-derived human astrocyte cultures to produce human astrocyte conditioned medium (hACM) was tested. Using the same protocol as developed using the mouse astrocyte cultures base neuronal differentiation medium was conditioned using the iPS cell-derived astrocytes. Using the same protocol as before iPS cell derived neuronal cultures treated with hACM and control medium were assessed electrophysiologically over a 3 week differentiation at weeks 2 and 3.

Astrocyte differentiation protocol

Similar to the neuronal differentiation, a single cell suspension of dissociated EZ-spheres was plated onto PLL-laminin coated coverslips. The wells were flooded with a base medium known to allow survival of both neurons of astrocytes using the B27 supplement. To selectively kill mitotic cells, Ara-C (cytosine arabinoside) was added, a compound toxic to mitotic cells [194]. A cell-survival based dose response curve was produced for 1 week of Ara-C treatment with concentrations of (from 0.3 to 300 µM, expressed in the figure as log [Ara-C

(mM)]). Immunostaining for β3 tubulin was also used to assess the development of immature neurons in these cultures. A concentration of 10 µM Ara-C was then chosen as this resulted in sufficient cell survival, reducing the total cell pool to only half compared to control, but generated very few β3 tubulin positive cells (figure 5.1 A and B).

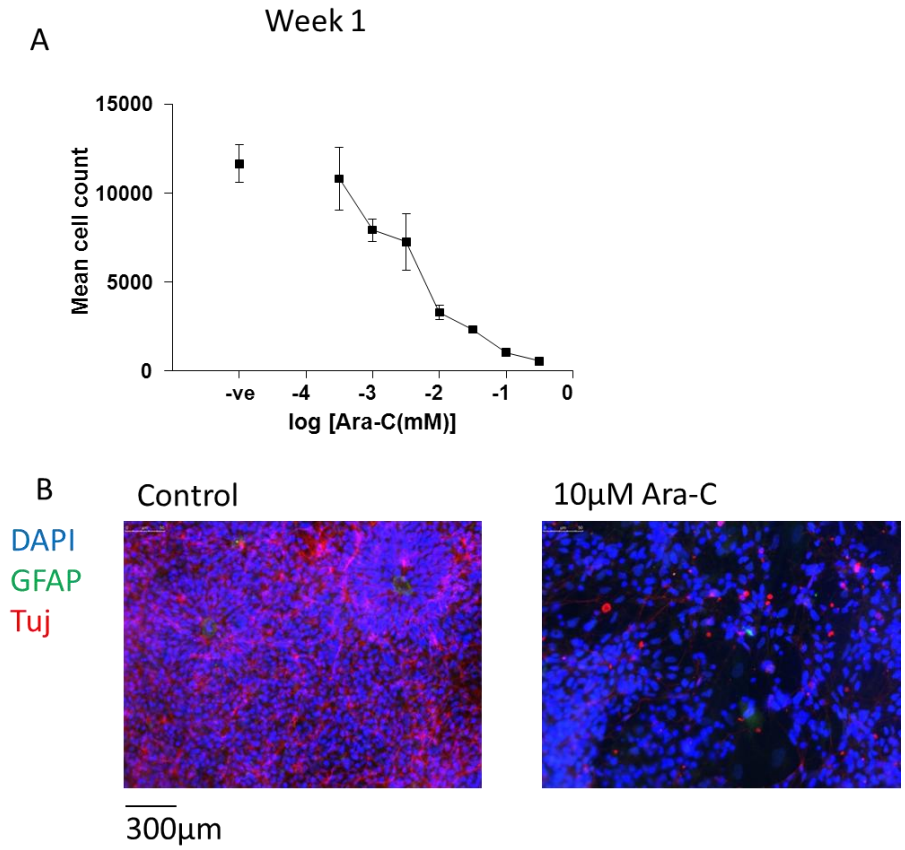

Figure 5.1: The survival and propensity to produce β3-tubulin positive cells with 1 week of Ara-C treatment.

A) A graph showing the mean cell count (±SEM) following 1 week of culture in varying concentrations of Ara-C.

B) Exemplar DAPI nuclear stain (blue), β3-tubulin immunostain (red) and GFAP immunostain (green) for cells in control medium (left) and treated with 10µM Ara-C (right) after 1 week.

The second stage of the new astrocyte differentiation protocol focused on maturing astroglial precursor cells with 10 µM human recombinant leukaemia inducible factor (LIF-1) in the same base medium, using the principle that Lif-1 induces the development of a self-renewing population of GFAP (glial fibrilary acidic protein) positive astroglial sub-type that may exhibit best neurogenic properties due to their developmental stage [19,122]. Following 1 week of LIF-1 treatment, 91% (n = 416) of cells were positive for the astrocyte marker GFAP, showing a highly enriched culture of astrocytes after only a total of 2 weeks in culture (figure 5.2). Further, although some GFAP positive cells were also weakly β3 tubulin positive, only 4% of the population were β3 tubulin positive but GFAP negative, indicating a very low rate of neurogenesis in these cultures (figure 5.2).

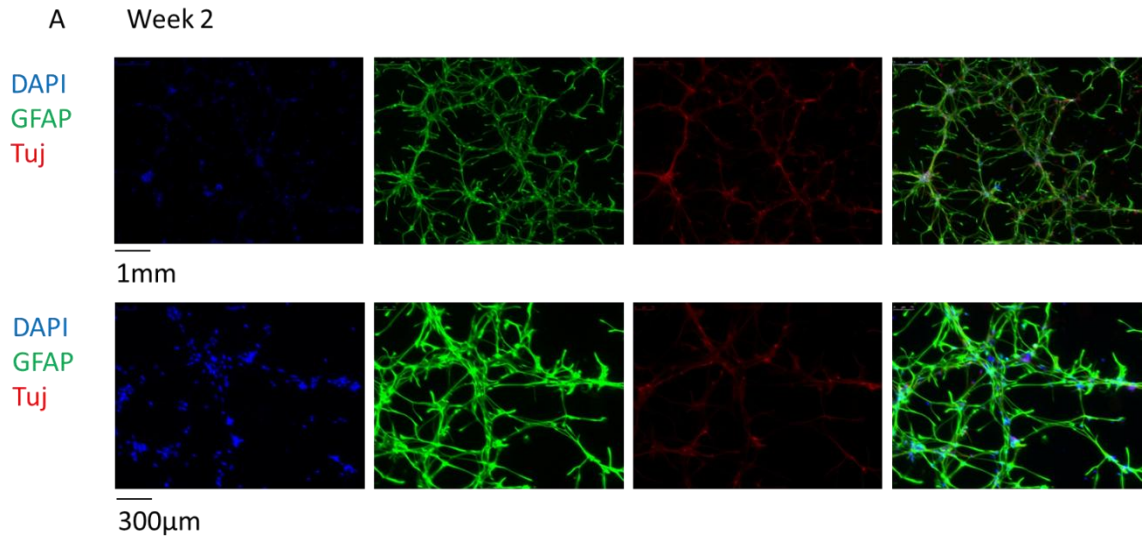

Figure 5.2: The production of highly pure GFAP+ cultures following 1 week Ara-C treatement and then 1 week Lif-1 treatment (total of 2 weeks).

A) DAPI, GFAP and β3-tubulin (Tuj) stains, blue, green and red respectively, for cells treated with Ara-C for 1 week followed by Lif-1 for 1 week at 5x and 10x magnification, colour channels have been split blue, green, red and merge respectively.

The 2 week protocol was repeated, but this time without the Ara-C treatment during the first week. This change to the first medium resulted in an obvious increase in total cells, but crucially an increase in β3 tubulin positive cells even following 1 week of LIF-1 treatment (figure 5.3 B). This demonstrates the importance of the initial treatment with Ara-C to limit neurogenesis to produce a more pure population of astrocytes.

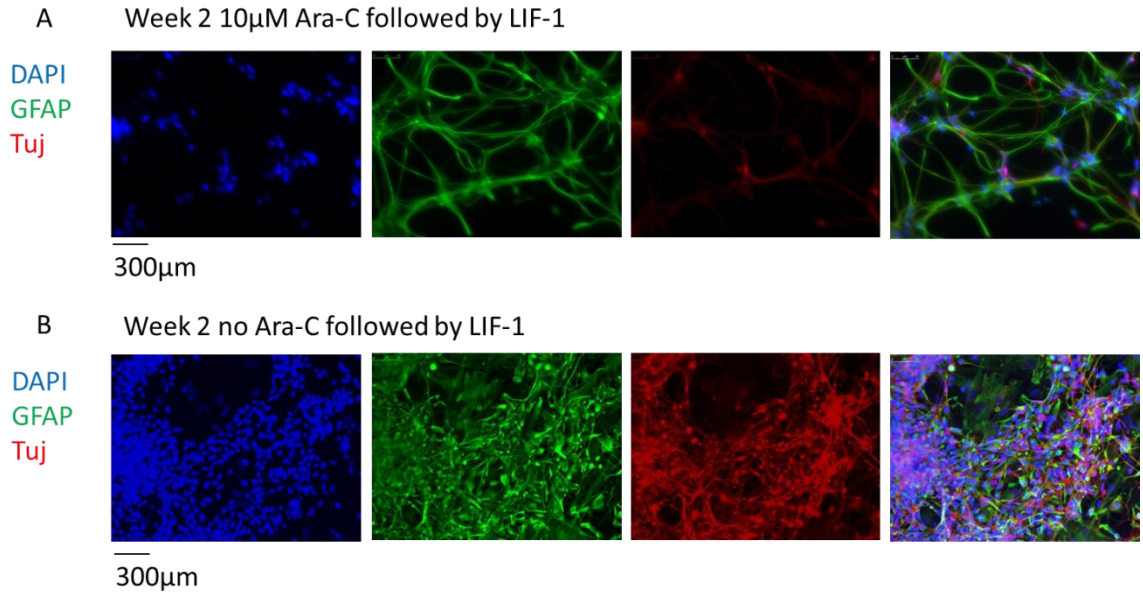

Figure 5.3: A comparison of GFAP+ and β3-tubulin+ cells using this protocol with and without Ara-C treatment.

A) DAPI, GFAP and β3-tubulin (Tuj) stains, blue, green and red respectively, following the 2 week protocol 1, colour channels have been split blue, green, red and merge respectively.

B) DAPI, GFAP and β3-tubulin (Tuj) stains, blue, green and red respectively, following the 2 week protocol 1 but without Ara-C treatment during the first week, colour channels have been split blue, green, red and merge respectively.

Following the 2 week protocol, the cells were then passaged and transferred to standard tissue culture flasks and the B27 in the base medium replaced with 10% FBS, which is known to support astroglial growth but not neurons or neuronal progenitor cells (see specific introductions – astrocyte differentiation). Following 1 week in the new FBS medium, 100% (n = 211) of cells were GFAP positive and 0% were β3 tubulin positive but GFAP negative. However, a low level of β3 tubulin was still observed in many GFAP positive cells. Further, immunostaining for GFAP and S100β, a second marker for astrocytes that is expressed later in development (figure 5.4A), again showed 100% of the cells were GFAP positive (n = 301) but, crucially, 91% of the cells were both S100β and GFAP positive (figure 5.4A). This is a clear indication that by week 3 this protocol had produced a highly enriched culture of mature astrocytes. The astrocytes were then cultured in the same medium for an additional 5 weeks, passaging the cells once per week, resulting in a total of 8 weeks differentiation. Again, almost all cells were both S100β and GFAP positive (figure 5.4B). This shows that the new protocol is capable of producing enriched cultures of astrocytes and can be expanded for at least 5 passages.

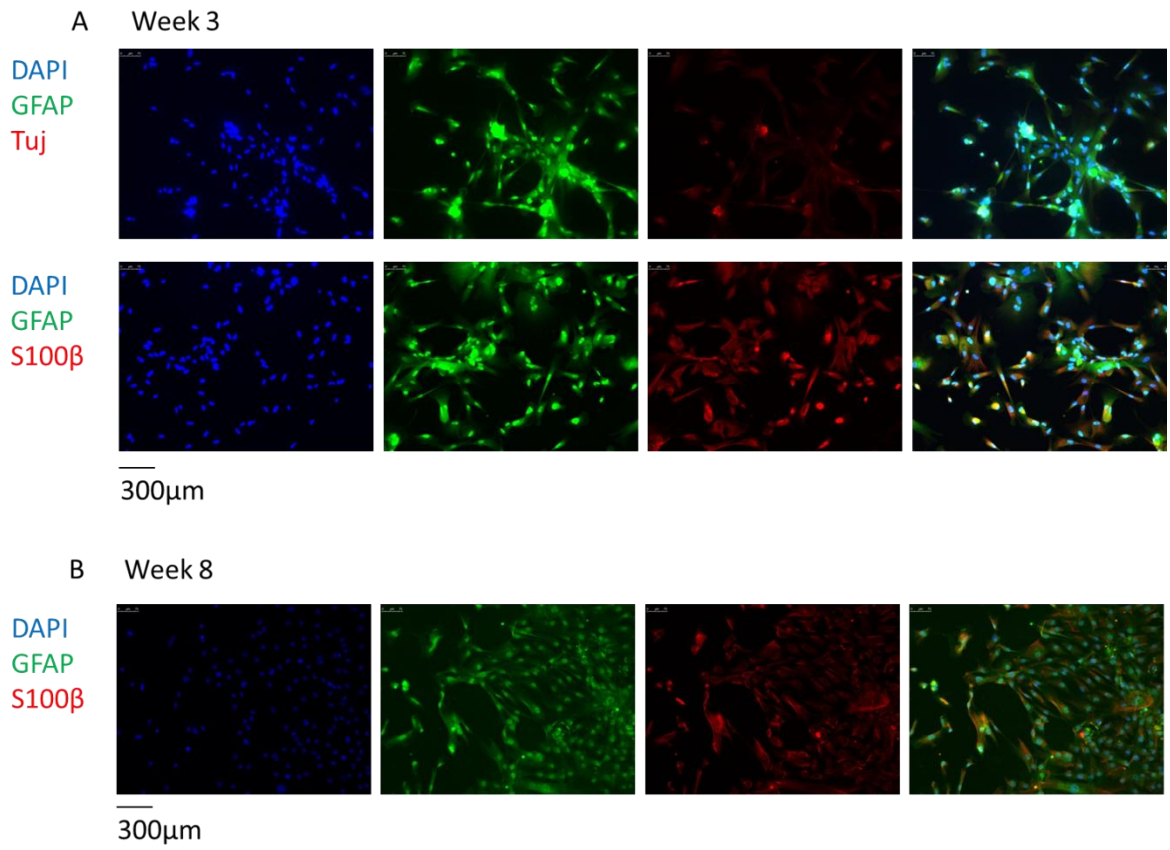

Figure 5.4: The expression of GFAP+ and S100B in these cultures following 3 and 8 weeks of culture.

A) DAPI, GFAP and S100B stains, blue, green and red respectively, following 1 week in the FBS and Lif-1 medium, colour channels have been split blue, green, red and merge respectively.

B) DAPI, GFAP and S100B stains, blue, green and red respectively, following 5 weeks (8 passages) in the FBS and Lif-1 medium, colour channels have been split blue, green, red and merge respectively.

Differentiation using human iPS cell derived astrocyte ACM (hACM)

Using a similar protocol to chapter 3, human iPS cell-derived astrocytes were used to condition base differentiation medium (human ACM, or hACM) for culturing iPS cell-derived neurons. The iPS-cell derived neurons treated with control medium and human iPS cell-derived astrocyte conditioned medium were compared electrophysiologically at weeks 2 and 3 of the differentiation protocol. Similar to the previous differentiation protocols, almost all cells were able to fire induced action potentials by week 2 (90% in control (n = 10) and 93% in human ACM (n = 15)) which was maintained to week 3 (80% in control (n = 10) and 100% in hACM (n = 9), figure 5.5 C). Consistent with results using mouse ACM, the human ACM did not accelerate the development of an induced action potential. However, although the control cells showed an equal proportion of cells able to fire action potentials we did observe a difference in the shape of action potentials in human ACM cells. Consistent with mouse ACM, we saw more mature action potentials in the human ACM-treated cells by week 3. The shapes of induced action potentials elicited in control and human ACM-treated cultures were compared quantitatively using the previously described method using the area inside orbital plots (figure 5.5 D). At week 2, the control and human ACM-treated cells exhibited relatively similar shape action potentials (2186 ± 395 $mV^2 \cdot ms^{-1}$ (n = 8) in control vs. 2526 ± 350 $mV^2 \cdot ms^{-1}$ (n = 9) in human ACM, ns). At week 3 however, the human ACM-treated cells exhibited a more mature shape (3419 ± 338 $mV^2 \cdot ms^{-1}$ (n = 8) vs. 4725 ± 549 $mV^2 \cdot ms^{-1}$ (n = 8) in human ACM, $P<0.05$, figure 5.5 A and F). In addition to the shape of the induced action potentials the threshold voltage at which the action potentials were initiated was estimated from the orbital plots. However, and in contrast to data using mouse ACM, this increased spikey-ness did not result in a significant proportion of cells firing a second action potential event following an induced action potential (0% (n = 8) in control vs. 12.5% (n = 8) in human ACM, ns). Consistent with previous data with the mouse ACM, the human ACM elicited no change in the action potential threshold at week 2(-31.4 ± 1.2 mV (n = 8) in control vs. -31.8 ± 0.8 mV (n = 9) in human ACM, ns) or week 3 (-32.9 ± 1 mV (n = 8) in control vs. -33.7 ± 1 mV (n = 8) in human ACM, ns, figure 5.5 E).

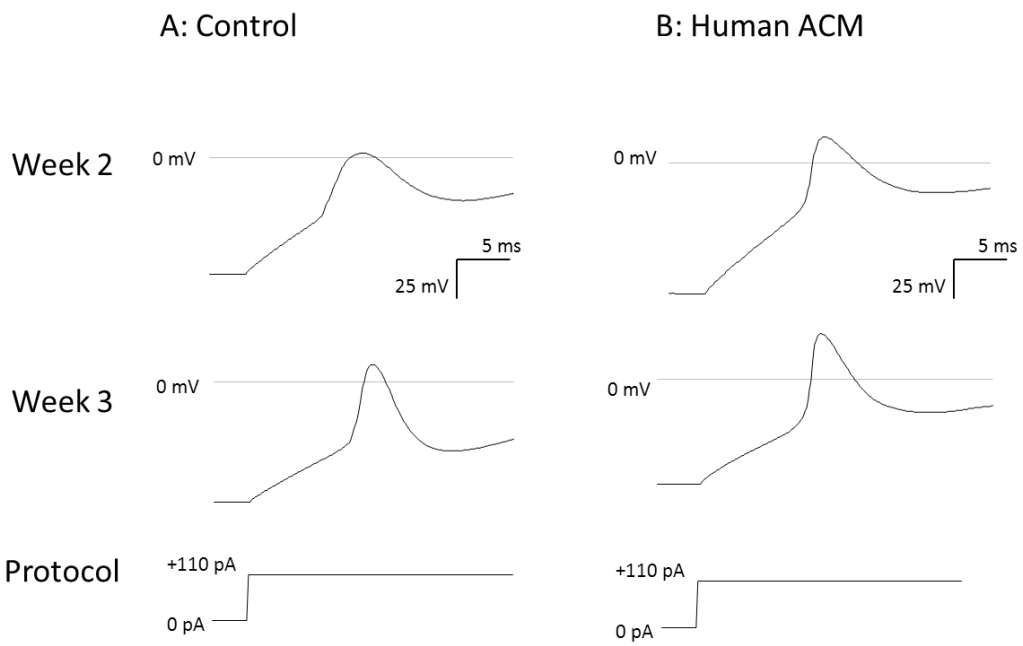
A: Control
B: Human ACM
Week 2
Week 3
Protocol
0 mV
5 ms
25 mV
+110 pA
0 pA

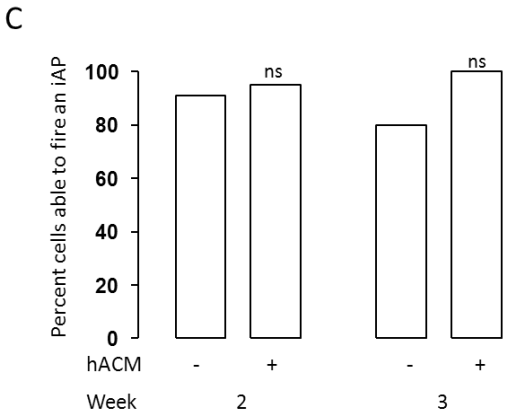
C
Percent cells able to fire an iAP
100
80
60
40
20
0
ns
ns
hACM
-
+
-
+
Week
2
3

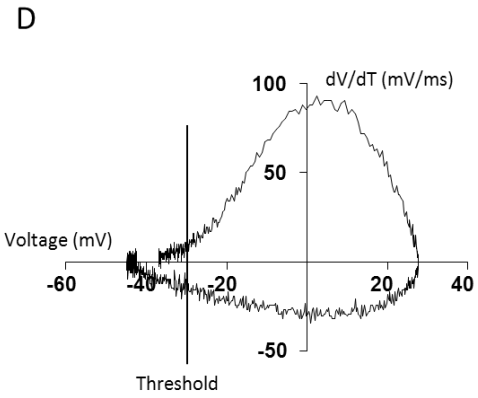
D
dV/dT (mV/ms)
100
50
-50
Voltage (mV)
-60
-40
-20
20
40
Threshold

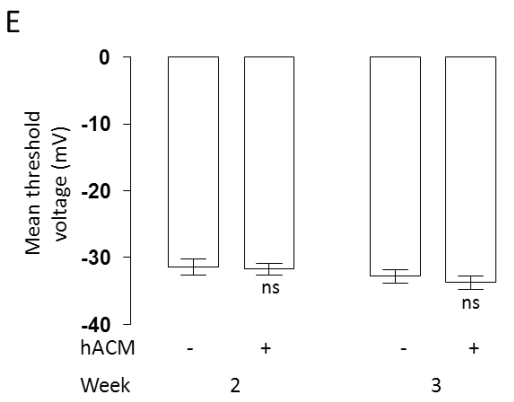
E
Mean threshold voltage (mV)
0
-10
-20
-30
-40
ns
ns
hACM
-
+
-
+
Week
2
3

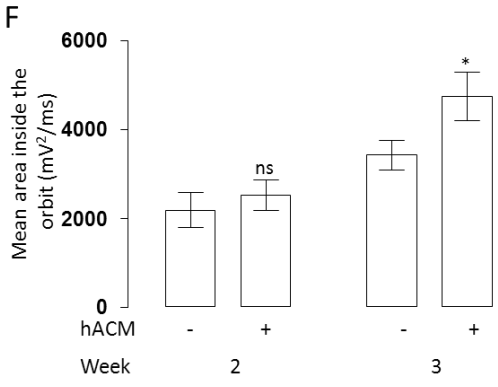
F
Mean area inside the orbit (mV²/ms)
6000
4000
2000
0
ns
*
hACM
-
+
-
+
Week
2
3

Figure 5.5: The development of induced action potentials in control and human ACM treated cells.

A) Exemplar voltage recordings from week 2 and 3 control treated cells during a current step protocol eliciting an action potential. The protocol is shown at the bottom.

B) Exemplar voltage recordings from week 2 and 3 human ACM treated cells during a current step protocol eliciting an action potential. The protocol is shown at the bottom.

C) A bar graph showing the portion of cells (%) showing induced action potentials (iAP) at weeks 2 and 3 for both control and human ACM treated cells.

D) An exemplar orbital graph (differential of voltage against time plotted against voltage) for a single action potential generated by a human ACM-treated cell at week 3. The approximate threshold voltage is indicated as a line.

E) A bar graph showing the mean (±SEM) estimated threshold voltages for elicited action potentials from both control and human ACM-treated cells at weeks 2 and 3. T-tests were performed for statistical differences between control and human ACM at each week.

F) A bar graph showing the mean area inside the orbit (see panel D for an example) for control and human ACM-treated cells at weeks 2 and 3, calculated using the sum of the modulus of the integrals of the orbital graph. T-tests were used to compare the control and human ACM-treated cultures at each week.

Using voltage clamp, the voltage activated Na^+ and K^+ currents responsible for action potential generation were measured (figure 5.6 A to D). By week 2, almost all cells in both the control and human ACM-treated cells developed significant voltage activated Na^+ and K^+ currents, consistent with their ability to fire induced action potentials. Consistent with similar shape induced action potentials in both control and human ACM cultures at week 2, both cultures showed every similar magnitude of both Na^+ and K^+ current densities (Na^+: -65.8 ± 11.1 $pA \cdot pF^{-1}$ (n = 7) in control vs. -61.9 ± 5.8 $pA \cdot pF^{-1}$ (n = 9) in human ACM, ns, and K^+: 43.3 ± 5.2 $pA \cdot pF^{-1}$ (n = 7) in control vs. 41.4 ± 5 $pA \cdot pF^{-1}$ (n = 9) in human ACM, ns, figure 5.6 E). At week 3, the human ACM had evoked a significant increase in the Na^+ current density compared with control (-89 ± 8.4 $pA \cdot pF^{-1}$ (n = 8) in control vs. -112.4 ± 7 $pA \cdot pF^{-1}$ (n = 8) in

human ACM, P<0.05). These data are consistent with faster depolarisation rates observed in week 3 human ACM-treated cells compared with control (29 ± 2.9 $V \cdot s^{-1}$ (n = 8) in control vs. 48.4 ± 4.6 $V \cdot s^{-1}$ (n = 8) in human ACM, P<0.01) and therefore an increase in the area inside the orbit (3419 ± 338 $mV^2 \cdot ms^{-1}$ (n = 8) vs. 4725 ± 549 $mV^2 \cdot ms^{-1}$ (n = 8) in human ACM, P<0.05, figure 5.5 F). However, magnitude of K^+ current density did not appreciably increase at week 3, which was not altered by human ACM (45.5 ± 4.6 $pA \cdot pF^{-1}$ (n = 8) in control vs. 48.4 ± 3.2 $pA \cdot pF^{-1}$ (n = 8) in human ACM, ns, figure 5.6F). Consequently, human ACM did not enhance the rates of repolarisation at week 3 (-27.9 ± 2.5 $V \cdot s^{-1}$ (n = 8) in control vs. -29.8 + 2.9 $V \cdot s^{-1}$ (n = 8) in human ACM, ns). This perhaps explains why few cells in control or human ACM were able to fire second full, or even abortive induced action potentials, because the K^+ current was relatively small resulting in slower repolarisation which did not undershoot as far (-3.8mV ± 2.6 mV (n = 7) in control vs. -2.9 ± 3.1 (n = 7) in human ACM, ns).

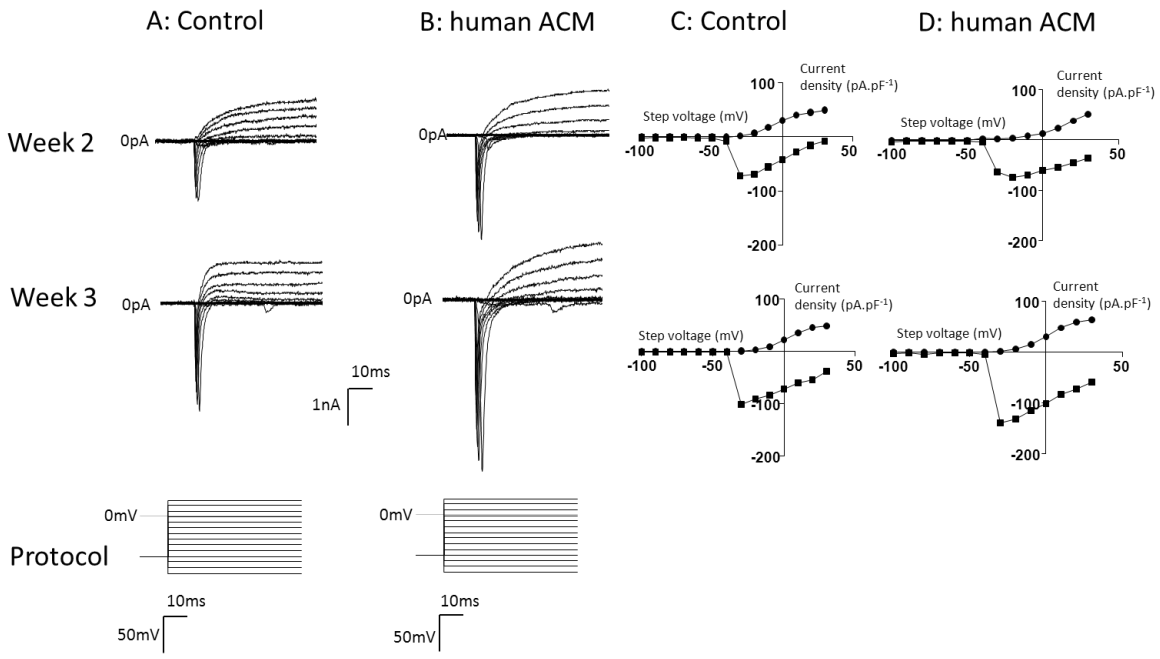

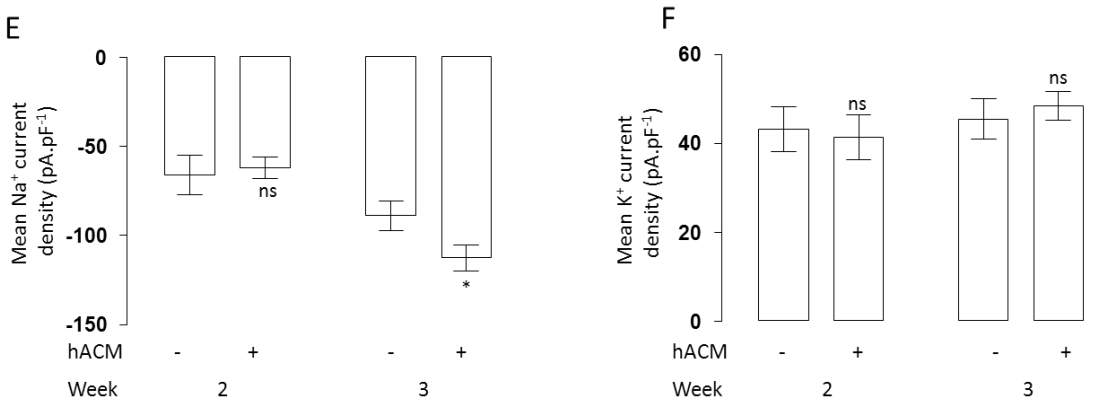

Figure 5.5: Na^+ and K^+ voltage activated currents evoked in neurons differentiated with human ACM (hACM).

A) Exemplar voltage recordings (top) in control cells at weeks 2 and 3 during a voltage step protocol (bottom), eliciting both voltage activated Na^+ and K^+ currents.

B) Exemplar voltage recordings (top) in human ACM-treated cells at weeks 2 and 3 during a voltage step protocol (bottom), eliciting both voltage activated Na^+ and K^+ currents.

C) Exemplar current density ($pA \cdot pF^{-1}$) against voltage graphs plotted for Na^+ (squares) and K^+ (circles) currents from control cells at weeks 2 and 3.

C) Exemplar current density ($pA \cdot pF^{-1}$) against voltage graphs plotted for Na^+ (squares) and K^+ (circles) currents from human ACM-treated cells at weeks 2 and 3.

E) A bar graph showing the mean (±SEM) maximum peak negative Na^+ current density elicited in both control and human ACM-treated cells at weeks 2 and 3. T-tests were performed for statistical differences between control and human ACM at each week.

F) A bar graph showing the mean (±SEM) maximum mean K^+ current density elicited in both control and human ACM-treated cells at weeks 2 and 3. T-tests were performed for statistical differences between control and human ACM at each week.

Similar to previous differentiations in the absence of protocols designed to enhance Ca^{2+} influx, relatively little spontaneous activity was present at week 2 in either culture (16% (n = 12) in control and 26% in human ACM (n = 15), figure 5.7A). Critically though, by week 3 the human ACM evoked a significant increase in the proportion of cells firing spontaneous

action potentials (0% (n = 10) in control vs. 66% (n = 9) in human ACM, p<0.01, figure 5.7A). However, unlike mouse ACM-treated cells, development of the biphasic resting membrane potentials and membrane potential trains was not evoked with human ACM (figure 5.7B to D). This is perhaps consistent with the data observing the evoked K^+ currents in these cells and the rates of repolarisation which were not enhanced by human ACM. By contrast, the mouse ACM had evoked a significantly enhanced rate of repolarisation at week 3, resulting in larger voltage-undershoots and greater recovery of the cells Na^+ current for further action potentials.

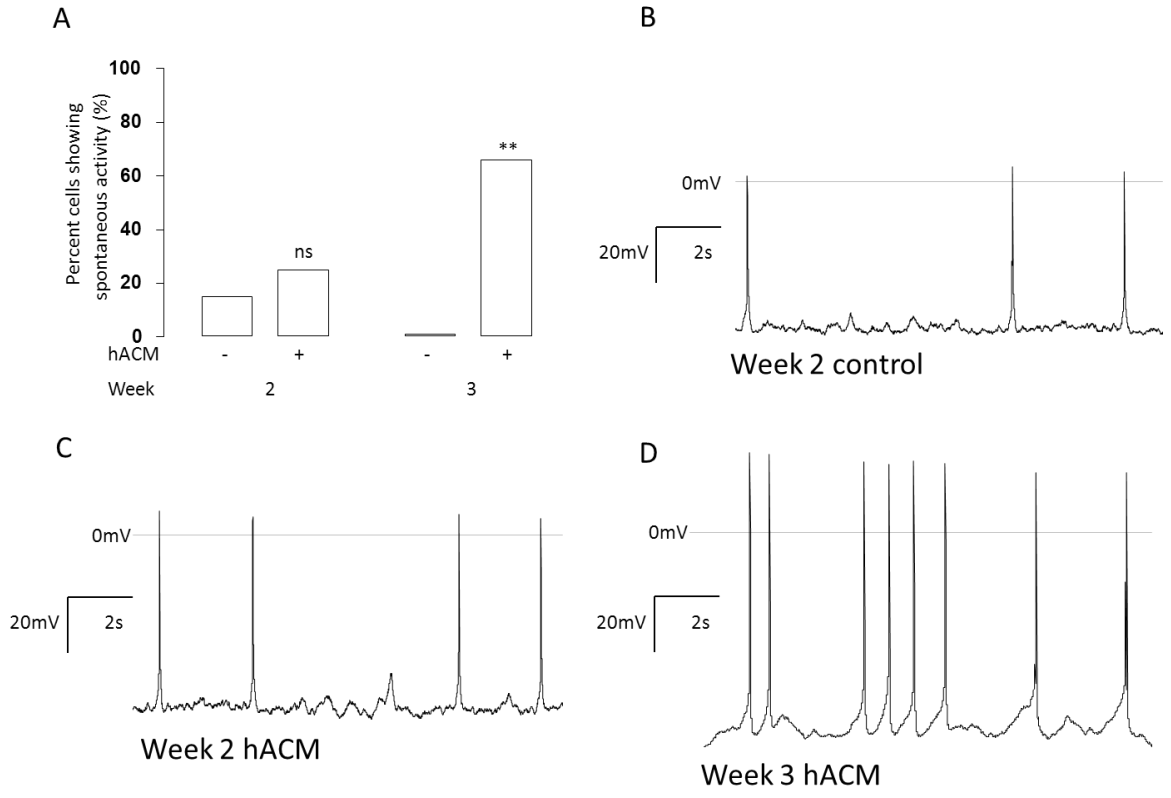

Figure 5.7: Spontaneous action potential generation in neurons differentiated using human ACM (hACM).

A) A bar graph showing the portion of cells (%) showing spontaneous activity in the human ACM and control treated cells at weeks 2 and 3 of differentiation, Chi^2 test was used to compare human ACM and control treated cells.

B) An exemplar voltage recording during current clamp I=0, showing spontaneous action potentials in a control treated cell at week 2.

C) An exemplar voltage recording during current clamp I=0, showing spontaneous action potentials in a human ACM treated cell at week 2.

D) An exemplar voltage recording during current clamp I=0, showing spontaneous action potentials in a human ACM treated cell at week 3.

The resting membrane potential was shown to be an important electrophysiological parameter which was enhanced by mouse ACM, and which contributed to the increase in spontaneous activity. In a similar pattern, the control treated cells showed a decline in resting membrane potential between week 2 and 3 (from -35.8 ± 2.2 mV (n = 12) to -31 ± 2.3 mV (n = 10)) where the ACM-treated cells showed a continued hyperpolarisation of the membrane potential from week 2 to week 3 (from -42.6 ± 4.5 mV (n = 15) to -44.9 ±1 mV (n = 9), figure 5.8A). This results in a significantly more hyperpolarised resting membrane potential in human ACM-treated cells at week 3 (-31 ± 2.3 mV (n = 10) in control vs. -44.9 ±1 mV (n = 9) in human ACM, $P<0.05$, figure 5.8A) compared to control cells. These data, with data demonstrating that the Na^+ current voltage dependant activation and inactivation profiles correlates had not changed over time or with human ACM, suggests greater Na^+ current availability in human ACM-treated cells at week 3 (figure 5.8 C and D). Therefore, this correlates well with both the increase in spontaneous activity observed at week 3 in human ACM treated cells and decline in spontaneous activity in control cells. Comparing these resting membrane potentials values to activation-inactivation profiles of the Na^+ current in these cells (figure 5.8 C and D), suggested that at the only 5% of the Na^+ current would be available in control cells whilst it would be 45% in human ACM-treated cells.

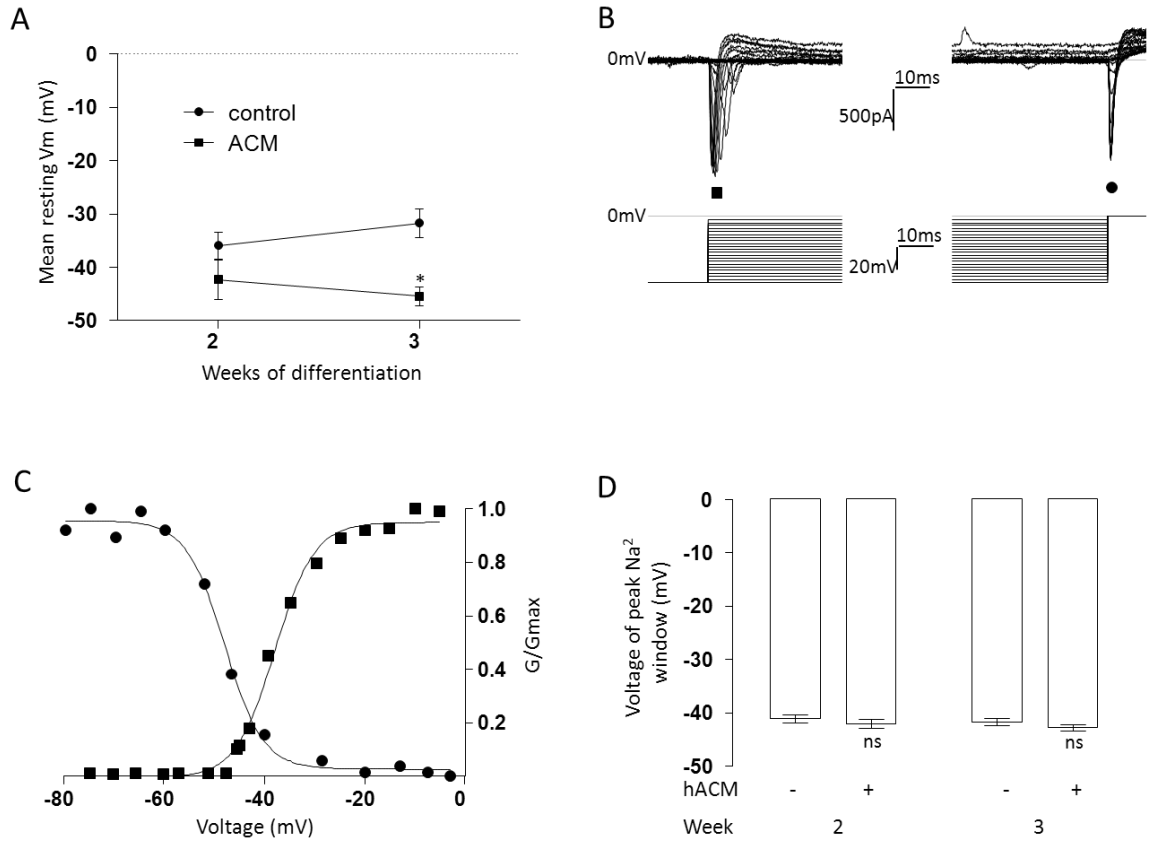

Figure 5.8: Resting membrane potentials and the voltage dependant profiles for activation and inactivation in iPS cell derived neurons treated with hACM and control.

A) A graph showing the mean resting membrane potential (whilst in current clamp at I=0) for both control and human ACM-treated cells at weeks 2 and 3. T-tests were performed to compare the mean resting membrane potential of control and human ACM-treated cells at each week.

B) Exemplar current recordings (top) during a dual-step voltage protocol (bottom) showing currents elicited by each step from a week 3 control cell. The first step is a variable and increasing step and the elicited current is used to measure voltage-dependant activation of Na^+ channels (square). The second step is static at 0mV and is used to measure the voltage-dependant inactivation of Na^+ channels as a result of the first step (circles).

C) Using the data from panel B, normalised conductance (G/G_{max}) curves are plotted against the voltage of the first step (adjusted for junction potential and series resistance) for both the inactivation (circles) and activation (square) voltage relationships. Sigmoid-Boltzmann

curves were then fitted to each relationship allowing for the hypothetical peak Na^+ window voltage to be estimated.

D) A bar graph showing the mean (±SEM) voltage of the hypothetical peak Na^+ window for both control and human ACM-treated cells at weeks 2 and 3. These values, as previously discussed in chapter 3, are used as a barometer for changes in both the activation and inactivation voltage profiles and consequently changes in the proportions of neuronal Na^+ channel sub-types.

Chapter 6: Using astrocyte secreted factors and manipulation of Ca^{2+} influx to develop a more functionally mature and consistent model for Huntington's disease.

Specific Introductions:

Having shown that neuronal maturation could be enhanced in iPS cell-derived cultures, these differentiation protocols were then tested on iPS cells derived from Huntington's disease (HD) patients. Firstly, it is important to develop a protocol which produces neuronal cultures which are more functional and is important in developing iPS cell-derived models for the disease. Secondly, the HD genotype could have an effect on the profile of functional development observed in these neurons, which could have a mechanistic role in the development of the disease. However, this also presents a challenge for using iPS cell models, as cells developing or maturing at different rates could influence the results when modelling the disease using stressors [218]. Therefore, assessing protocols for their functional consistency at a set time point is also important. Ideally a protocol should be chosen which results in similar levels of functional maturity across multiple patient and wild type –derived lines at a specific time point. This should be a standardised time point for disease modelling or drug testing experiments can be best performed.

Specific Methods:

Initially, three lines from a previous iPS derived HD study where disease-relevant phenotypes were observed [218]. A control 33 repeat line (the control line used previously, a HD-line developed from a sibling of the control line with HD (60 CAG repeats (Q60)) and a childhood onset line with 180 CAG repeats (Q180) [218]. These iPS cell lines were reprogrammed using an the older integrating protocol, characterised for a normal karyotype and pluripotency and then partially differentiated to a neural progenitor cell state grown in "EZ spheres" (see methods). These cells were differentiated using a standard differentiation protocol, with a physiological concentration (1.2 mM) Ca^{2+} in preference to the low Ca^{2+} medium used previously (0.6 mM). The change in Ca^{2+} concentration was expected to have little effect functionally; a comparison between 0.6 mM, 1.2 mM and 1.6 mM Ca^{2+} medium was performed in control cells in chapter 5. The lines were also differentiated using mouse astrocyte conditioned medium to enhance the functional maturation of the generated

neurons. However, the very high repeat line, the Q180 line, showed very poor survival beyond week 2 in control medium and fared worse still in ACM.

Advances in reprogramming and differentiation protocols were then tested, including manipulation of the Ca^{2+} influx dependant mechanism discussed in chapter 5. Firstly, new, none-integrating, iPS cell lines from the same HD patients and wild type individual were used, thus avoiding the effects of any genetic bleed through of the reprogramming factors affecting differentiation and maturation. In addition to these lines a second childhood onset line with 109 CAG repeats (Q109), this line allows a more continuous series of CAG-repeat lengths and could serve as a replacement for the poorly surviving Q180 line. Secondly, a neural-rosette differentiation protocol was employed in preference to EZ-sphere generation. The neural rosettes were generated using a small molecule based dual SMAD inhibition protocol to produce neural-rosettes (see methods), which unpublished data from our lab suggests is more efficient. Lastly, terminal differentiation was performed with the addition of the glycogen synthase kinase-3 inhibitor CHIR 99021, the cyclin dependant kinase-6 inhibitor PD0332991 and forskolin to increase cAMP synthesis at week 1 and increase CREB-phosphorylation (see methods) [9,106,145]. The hypothesis was tested that the combination of increased Ca^{2+} concentration and GABA in the medium to improve functional maturation and consistency across these HD-lines and in conjunction with the newer differentiation protocol. Another key difference between the standard differentiation protocol and this new protocol is the removal of the non-essential amino acids supplement, crucially removing 100µM L-glutamate, which by excitotoxicity could have led to the poor survival of the Q180 line in the previous protocol. This newer protocol will be regarded as the “advanced” protocol from now on.

The electrophysiological function of iPS-derived neurons from Huntington’s disease patients.

Using the standard differentiation protocol, from EZ-spheres, iPS cell-derived neurons were generated from 3 iPS lines (see specific methods). The control line used previously, an adult onset HD line (Q60) and lastly a childhood onset line (Q180). The HD109 line was not developed using the older and integrating reprogramming protocol, so therefore was not used when comparing the older standard protocol. The cells were terminally differentiated

in a standard differentiation medium and characterised electrophysiologically using patch clamp over the 3 week differentiation protocol. However, 180 repeats cell did not survive on coverslips to week 3, so for this line the characterisation was performed over the first 2 weeks only.

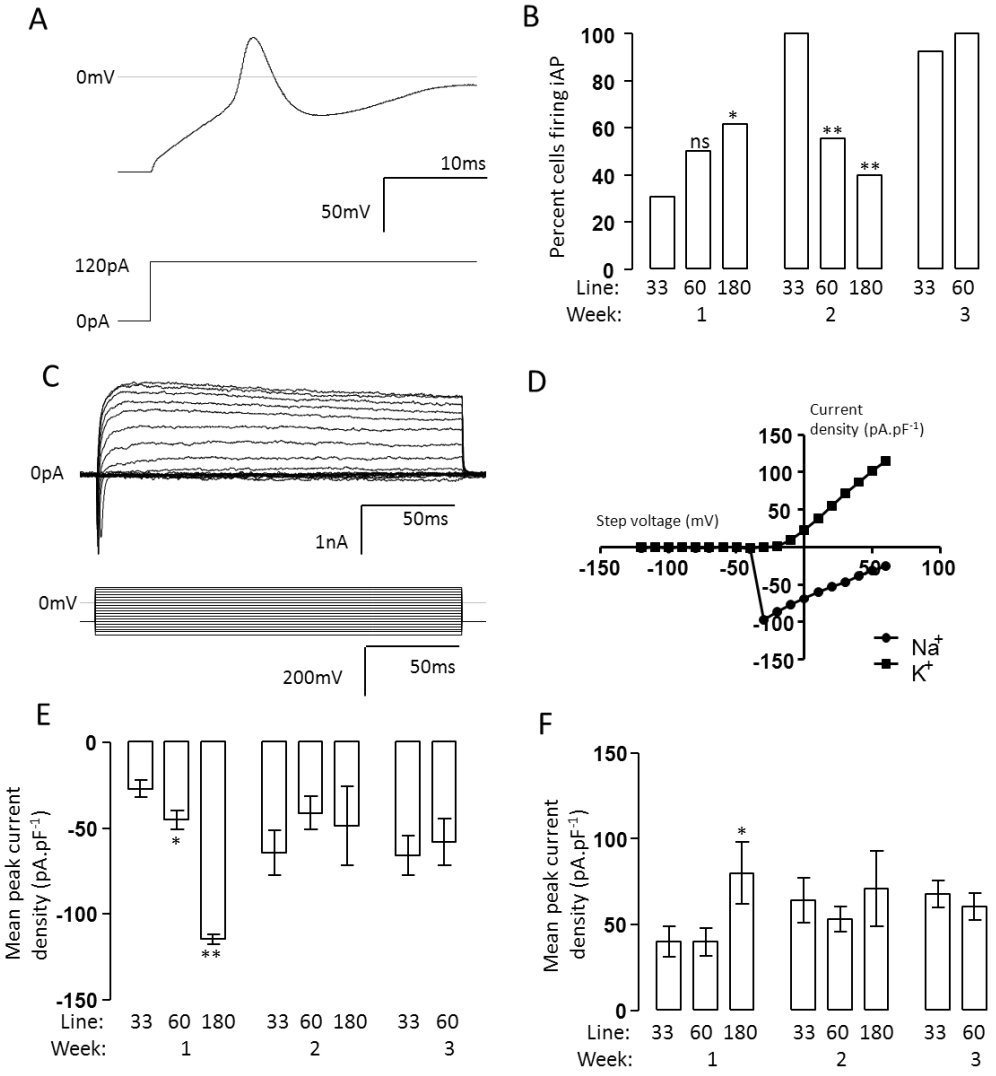

Figure 6.1: Induced action potentials and voltage activated currents in neurons differentiated from the HD lines.

A) An exemplar voltage recording (top) during a current step protocol (bottom) showing an evoked action potential generated in a week 2 Q60 neuron.

B) A bar graph showing the proportion of cells (%) able to fire action potentials in the control (Q33), Q60 and Q180 lines over 3 weeks of differentiation using the standard differentiation protocol.

C) Exemplar current recordings (top) during a voltage clam protocol (bottom) showing evoked voltage activated Na^+ and K^+ currents of a week 2 Q60 neuron.

D) Exemplar current density against step voltage plot for both the peak negative Na^+ current and mean plateaux of the K^+ current of a week 2 Q60 neuron.

E) A bar graph showing the mean K current density (±SEM) in the control (Q33), Q60 and Q180 lines over 3 weeks of differentiation using the standard differentiation protocol.

F) A bar graph showing the mean peak Na current density (±SEM) in the control (Q33), Q60 and Q180 lines over 3 weeks of differentiation using the standard differentiation protocol.

The ability of differentiated cells to fire induced action potentials was assessed using a current steps protocol. In the control cultures (carrying HD33), at week 1 only 30% (n = 13) could fire induced action potentials, but by week 2 that had increased to 100% (n = 12), which was then essentially sustained in week 3 (92.3% n = 13, figure 6.1A). By contrast, more cells differentiated from either of the HD lines were able to fire action potentials by week 1, 50% (n = 10) in the Q60 line and, significantly, 100% (n = 8, $P<0.05$, $Chi^2=3.03$) in the Q180 line. However, at week 2 both of the HD lines showed the opposite trend to control, a static or declining proportion of cells able to fire induced action potentials, only 55.6% (n = 18, $P<0.01$, $Chi^2=7.3$) cells in the Q60 and 40% (n = 10, $Chi^2=9.9$) in the Q180 line could fire action potentials (figure 6.1A). At week 3, the Q60 line had caught up with the control line, showing 100% (n = 13) cells could fire an action potential and cells from the Q180 line had died.

The voltage activated K^+ and Na^+ channels which are required for action potential generation were examined using a voltage step protocol in voltage clamp. Consistent with this notion, the magnitude of Na^+ current densities correlated with the proportions of cells able to generate induced action potentials. As with the proportion firing induced action

potentials the magnitude of Na^+ currents observed correlated with CAG repeat length, such that the Na^+ current densities in the Q180 line were very large compared to the Q60 line, which was still significantly larger than control (-27.6±4.7 $pA \cdot pF^{-1}$ (n = 11) in the control line -45±5 $pA \cdot pF^{-1}$ (n = 10, P<0.05, T=2.6) in the Q60 line and -114.6±28.6 $pA \cdot pF^{-1}$ (n = 9, P<0.01, T=3.6) in the Q180 line, figure 6.1E). Again correlating with the proportion of cells showing induced action potentials, the 180 repeat cell line also showed a much larger K^+ current compared with control (39.5±8.8 $pA \cdot pF^{-1}$ (n = 11) in the control line, 39.9±7.9 $pA \cdot pF^{-1}$ (n = 10, ns) in the Q60 line and 80.1±18.1 $pA \cdot pF^{-1}$ (n = 9, P<0.05, T=2.3) in the Q180 line, figure 6.1F). This suggests the HD cells exhibited an accelerated functional maturation in terms of the functional expression of both Na^+ and K^+ channel function where the control cells showed a more gradual gain of functional Na^+ and K^+ channel function compared with control. This resulted in both HD lines producing more cells capable of firing induced action potentials at week 1. However, from week 1 to 2 the control cells exhibited an appreciable increase in both Na^+ and K^+ current densities, by contrast Na^+ and K^+ currents in the Q60 and Q180 lines had remained static and declined, respectively. This meant no appreciable differences in terms of Na^+ current (-67.9±12.3 $pA \cdot pF^{-1}$ (n = 13) in the control line, -40.9±9.7 $pA \cdot pF^{-1}$ (n = 19) in the Q60 line and -48.3±23 $pA \cdot pF^{-1}$ (n = 8) in the Q180 line) and K^+ current (64.2±12.9 $pA \cdot pF^{-1}$ (n = 13) in the control line, 52.9±7.4 $pA \cdot pF^{-1}$ (n = 19) in the Q60 line and 70.9±22 $pA \cdot pF^{-1}$ (n = 8) in the Q180 line, figure 6.1 E and F) were observed. Interestingly, despite relatively similar mean Na^+ and K^+ currents a significant deficit in the proportion of HD cells able to fire induced action potentials was observed. This appeared to have been as a result of what few cells in the HD lines had Na^+ and K^+ were large enough for action potential generation, but many cells showed neither and were therefore not excitable.

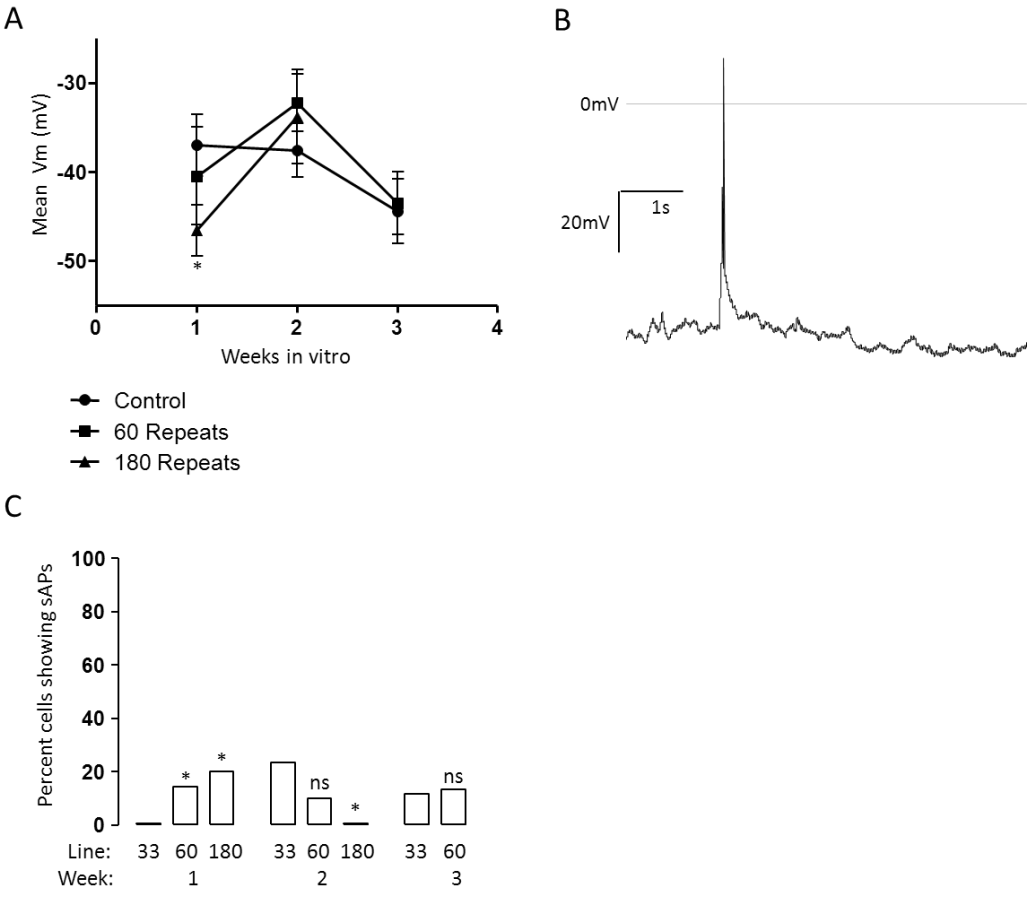

Figure 6.2: Resting membrane potential and spontaneous activity in neurons differentiated from the HD lines.

A) A graph showing the mean resting membrane (±SEM) in the control (Q33), Q60 and Q180 lines over 3 weeks of differentiation using the standard differentiation protocol.

B) An exemplar voltage recording (whilst I=0) showing a spontaneous action potential from a week 2 Q60 neuron.

C) A bar graph showing the proportion of cells (%) firing spontaneous action potentials in the control (Q33), Q60 and Q180 lines over 3 weeks of differentiation using the standard differentiation protocol.

To be an effective model of Huntington's disease in a dish these cells must behave like cells *in vivo*, which means being more than just able to fire action inducible action potentials but firing them spontaneously in response to synaptic input. However, in both the control and HD lines very low rates of spontaneous activity are observed. The control cells showed no spontaneous activity at week 1 (n = 20), but reached their most spontaneously active at week 2 (23.5% (n = 17)) and then declined in week 3 (11.8% (n = 17), 6.2B and C). By contrast, both HD lines showed spontaneous activity at week 1 (14.3% (n = 14) and 20% (n = 15) in the Q60 and Q180 lines respectively, $P<0.05$, $Chi^2>3$). At week 2 however, the Q180 cells lost all spontaneous activity (n = 11, $P<0.05$, $Chi^2=2.4$ compared to control) and were dead by week 3 (figure 6.2C). The Q60 line maintained a low level of spontaneous activity at all 3 weeks (14.3% (n = 14), 10% (N = 30) and 13.3% (n = 15) at weeks 1, 2 and 3, respectively, figure 6.2 B and C). This supports the notion that the high repeat line, Q180, started with a rapidly accelerated development and then declined. However, this also presents a problem for modelling the disease using these lines, there is no one time point where all 3 lines show a significant or consistent level of functional maturity.

Key to firing spontaneous action potentials is the ability to maintain a polarised resting membrane potential. The membrane potential must be sufficiently polarised to remove the inactivation of voltage activated Na^+ channels, leaving a large enough pool of closed and not inactivated Na^+ channels which can respond to a depolarisation. The control neurons showed a steady hyperpolarisation of their membrane potential across all 3 weeks from very depolarised at weeks 1 and 2 (-36.8±3.7 mV (n = 21) and -37.6±3 mV (n = 25) at week 1 and 2 respectively) to being relatively hyperpolarised at week 3 (-43.5±3.4 mV (n = 15), figure 6.2A). The Q60 line derived cells showed very similar membrane potentials to control across all weeks (-40.5 ± 5.5 mV (n = 16 at week 1, -32 ± 3.2 mV (n = 11) at week 2, and -43.5 ±3.5 (n = 15), figure 6.2 A). Compared to a neuron *in vivo,* and more importantly the inactivation voltages of Na^+ channels these membrane voltages are too depolarised, and will not leave a significant pool of Na^+ channels ready for an action potential. Curiously however, it is at week 2 where most spontaneously active control neurons were observed, but the resting membrane potential was most hyperpolarised at week 3. The Q180 line at week 1 showed a hyperpolarised resting membrane potential (-46.7±2.9 (n = 16), $P<0.05$, Mann-Whitney-U = 90.5). However, still depolarised compared to *in vivo,* but sufficiently

hyperpolarised compared to the inactivation voltages of voltage gated Na^+ channels to allow action potential generation, as discussed in chapter 3. At week 2, the Q180 line showed a declining resting membrane potential that could not support spontaneous activity, and then died at week 3.

In addition to voltage activated Na^+ and K^+ channels, neurons also express voltage activated Ca^{2+} channels. These channels function in many ways as a link between electrophysiological function and molecular function, for example regulating gene expression, vesicular release at synapses and cytoskeletal modifications. A voltage ramp protocol with high Ba^{2+} solution was used to measure and identify voltage activated Ca^{2+} channels; from a holding of -70mV, the voltage was stepped down to -120mV which then continuously ramped to +60mV over 1s, which separated the voltage activated Na^+ and Ca^{2+} currents. An inward current observed from around -30mV during the voltage ramp that significantly gained magnitude in the $BaCl_2$ solution was taken to be a voltage activated Ca^{2+} current.

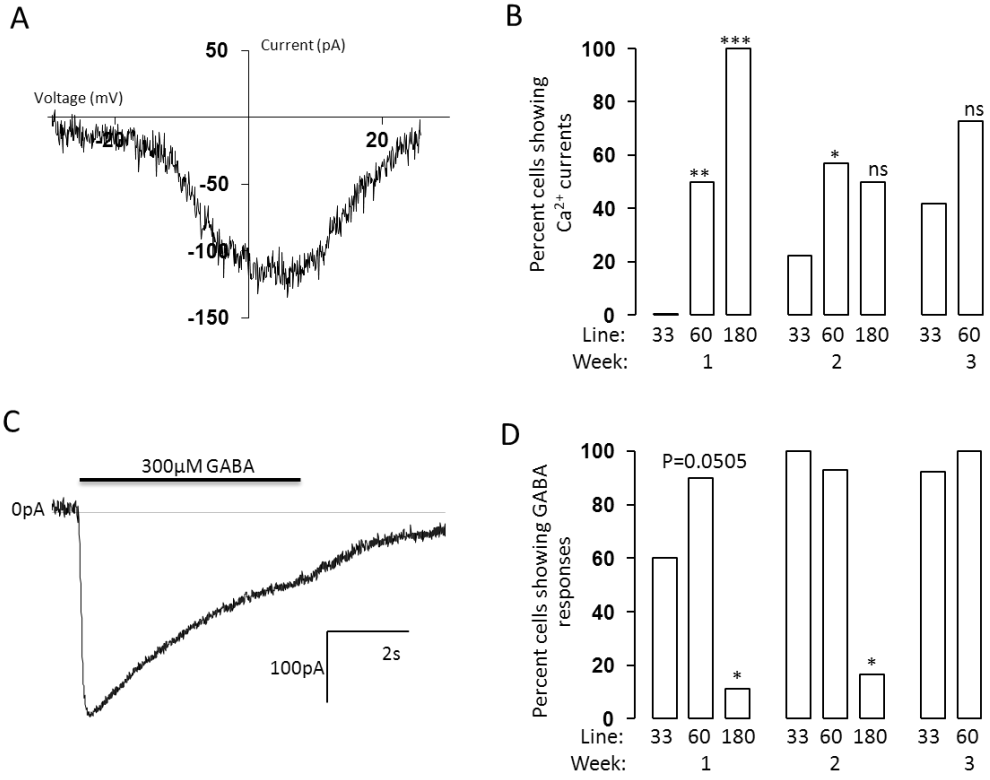

Figure 6.3: Voltage activated Ca^{2+} currents and GABA evoked currents in neurons differentiated from the HD lines.

A) An exemplar current against voltage plot for evoked voltage activated Ca^{2+} channel current during a voltage ramp protocol and enhanced by the addition of Ba^{2+}ions from a week 2 Q60 neuron.

B) A bar graph showing the portion of cells (%) with significant voltage gated Ca^{2+} currents in the control (Q33), Q60 and Q180 lines over 3 weeks of differentiation using the standard differentiation protocol.

C) An exemplar current recording during voltage clamp whilst being held at -70mV, a $GABA_A$ current was evoked by a 5s addition of 300 µM GABA marked above from a week 2 Q60 neuron.

D) A bar graph showing the portion of cells (%) with significant GABA evoked currents in the control (Q33), Q60 and Q180 lines over 3 weeks of differentiation using the standard differentiation protocol.

The control cells showed no voltage (n = 11) activated Ca^{2+} currents at week 1 that were large enough for measurement using this method, this increased significant at week 2 (22.2% (n = 9), figure 6.3B) and again at week 3 (42% (n = 12)). In contrast, both of the HD lines showed a significant number of cells with Ca^{2+} currents by week 1, and most especially in the Q180 line (50% (n = 8, $P<0.01$, $Chi^2=7.2$) in the Q60 line and 100% (n = 8, $P<0.001$, $Chi^2=19$) in the Q180 line, figure 6.3B). This increase was maintained at week 2 in the Q60 line (57% (n = 14), $P<0.05$, $Chi^2=2.7$) and the Q180 line had declined (from 100% to 50% (n = 8)). At week 3 the Q60 line showed a slightly increased proportion of cells showing Ca2+ currents, but the control cells had essentially caught up, and there was no significant difference between the lines (42% (n = 12) and 72% (n = 11), ns).

In addition to voltage activated ion channels a neuron must also be responsive to neurotransmitters, showing functional ligand gated ion channels. GABA is an early-expressed neurotransmitter and key to striatal function. Both the control and the Q60 lines showed significant functional $GABA_A$ currents by week 1 (60% (n = 15) in control and 90% (n = 10) in the Q60 line, $P=0.0505$ $Chi^2=2.7$, figure 6.3D). This increased to almost all cells in

both the Q60 and control lines by week 2 (100% (n = 10) in control and 92.8% (n = 14) in the Q60 line in the control), which continued to week 3 (92% (n = 13) in control and 100% (n = 11) in the Q60 line). In contrast, the Q180 line showed virtually no GABA currents during the two weeks they survived (11.1% (n = 9) and 16.7% (n = 6) at week 1 and week 2 respectively, $P<0.05$, $Chi^2>3.2$, figure 6.3D). This implies a functional abnormality with either the Q180 line specifically, or which occurs with extremely high CAG repeats.

These data demonstrate that all although these 3 are fundamentally capable of generating cells which exhibit basic neuronal electrophysiological features, there are serious potential limitations to using these cells as a disease model. Firstly, the extent of functional maturation is very limited, resulting in few spontaneously active cells and a culture of neurons which do not favourably compare to *in vivo.* Secondly, the profile of functional maturation in many aspects is wildly different for each line across the 3 week protocol, meaning there is no time point where a comparison could be drawn for disease modelling with similarly functional neurons.

Astrocyte conditioned medium and Huntington's disease iPS derived neurons.

Using the control (Q33) line in chapter 3 and ACM, cultures of neurons were generated with significantly enhanced functional properties. Ideally this protocol should be transferable to all 3 lines, producing functionally mature neurons at week 3 for disease modelling. Therefore the HD lines were also treated with mouse ACM developed using the same protocol as in chapter 3, except with a physiological Ca2+ concentration in the medium (1.2mM instead of 0.6).

Interestingly, both of the HD derived lines showed with immediate up-regulation in Ca^{2+} channel expression, which was also observed in the control line when treated with ACM. Consistent with the findings of chapter 4 the HD lines, especially the Q180 line, exhibited a short term functional enhancement in terms of spontaneous and induced action potential generation, and resting membrane potential. The short term nature of this enhancement was entirely consistent with artificial manipulation of Ca^{2+} influx using increased Ca^{2+}

concentration in the medium and the addition of GABA and found to be essentially as a result of the nature of GABA signalling becoming inhibitory over excitatory. However, although ACM acts in part by increasing the magnitude of an endogenous Ca^{2+} influx-dependant mechanism for functional maturation, its effects are sustained and presumably not limited by GABA signalling. The mechanism by which the HD cells exhibit an initial functional benefit is most likely as a result of their increased Ca^{2+} channel function, it is less clear though what causes the functional decline. Firstly, the two HD lines demonstrate very different developmental profiles. Both lines are initially accelerated and show a plateaux or decline at week 2, but at week 3 the Q60 line retained some function whereas the Q180 line died entirely. It is entirely probable that the Q60 line reached a functional plateaux as a result of the GABA switch, however few of the Q180 cells exhibited ionotropic GABA responses. In the case of the Q180 line it is perhaps more plausible that their decline is as a result of selective apoptotic loss of maturing neurons. Therefore, it appears perhaps more plausible that ACM-treatment would be effective on the Q60 line, but perhaps less so with the Q180 line.

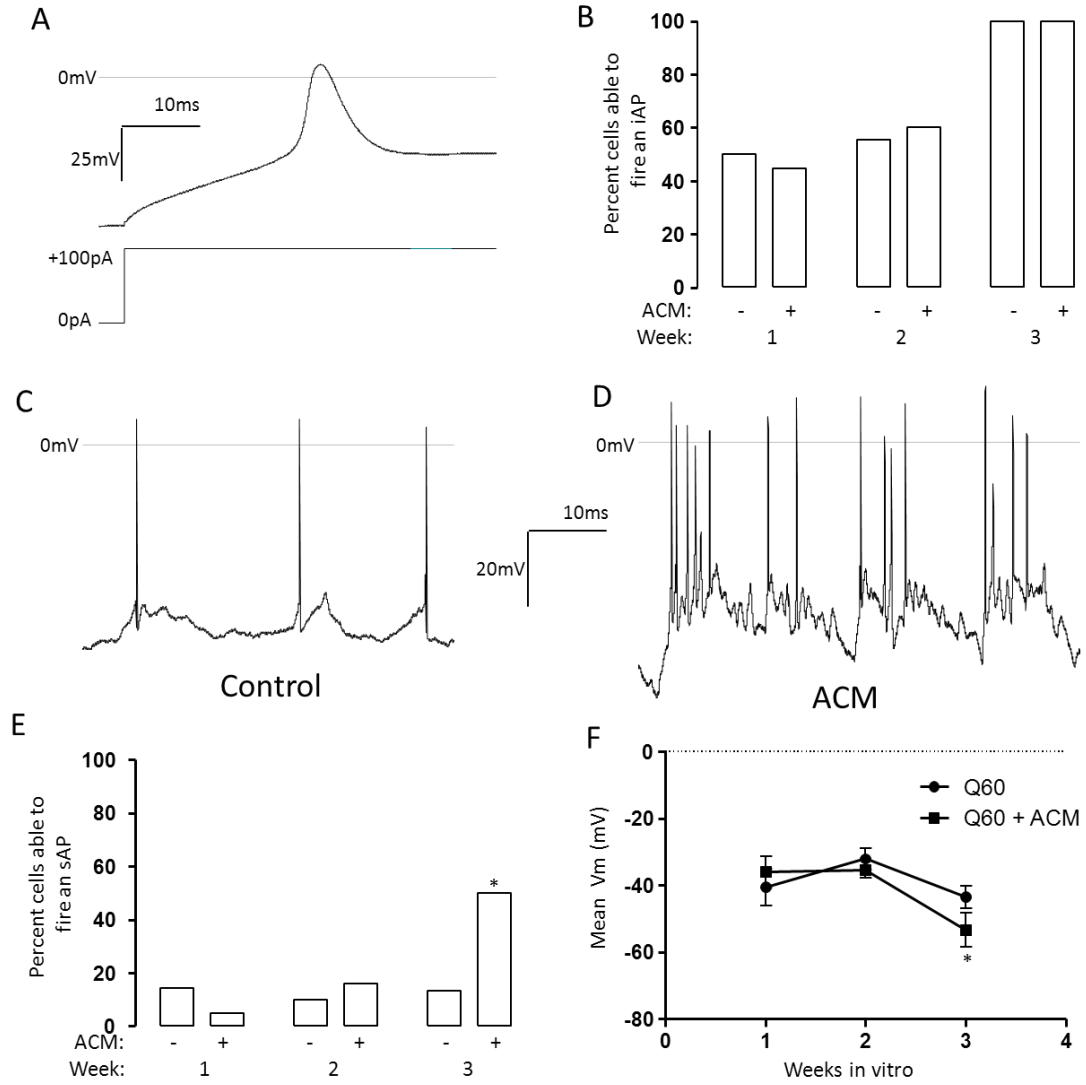

Figure 6.4: The electrophysiological properties of ACM-treated Q60 neurons.

A) An exemplar voltage recording (top) showing an induced action potential during a current step protocol (bottom) from a control Q60 neuron at week 3.

B) A bar graph showing the proportion of cells able to fire and induced action potentials during a current step protocol, from Q60 neurons treated with both control medium and ACM.

C) Exemplar voltage recording during current clamp (I=0) showing spontaneous action potentials from a week 3 control-treated Q60 neuron.

D) Exemplar voltage recording during current clamp (I=0) showing spontaneous action potentials from a week 3 ACM-treated Q60 neuron.

E) A bar graph showing the portion of cells (%) firing spontaneous action potentials in the Q60 line over 3 weeks of differentiation using the standard differentiation protocol and ACM.

F) A graph showing the mean resting membrane potential of Q60 neurons treated with both control medium and ACM over all 3 weeks of differentiation.

Both HD lines were cultured with ACM-treatment using a protocol similar to chapter 3. However, the Q180 line showed insufficient survival at even week 1 to conduct the experiments. Therefore, only the Q60 line could be assessed electrophysiologically over all 3 weeks of differentiation. Like ACM treatment with the control line, no effect on the most basic neuronal electrophysiological phenotype was observed, the ability to fire an action potential. In contrast to the Q33 cells analysed in chapter 3, a slower increase to the majority of cells able to fire induced action potentials was observed, starting with roughly half in week 1 (50% (n = 10) vs. 44% (n = 18) with ACM) and week 2, (55.6% (n = 18) vs. 59% (n = 17) with ACM) increasing to the majority at week 3 (100% (n = 13) vs. 100%(n = 6) with ACM, figure 6.4B).

However, consistent with the notion that ACM improves the extent of functional maturation but does not accelerate it, a significant increase in the portion of cells firing spontaneous action potentials at week 3 (13.3% (n = 15) vs. 50% (n = 6) with ACM, $P<0.05$, $Chi^2=3.9$, figure 6.4E). This correlated with a slightly more polarised membrane potential developed with ACM treatment at week 3 (-44.4±3.6 mV (n = 18) vs. -51.7±6.1 mV (n = 6) in ACM, $P<0.05$, Mann Whitney U = 13.5, figure 6.4F). Also consistent with mouse ACM used in the Q33 (control) cells, a few of the Q60 ACM-treated cells exhibited biphasic resting membrane potentials (33% (n = 6), 6.4C vs D) and enhanced rates of spontaneous activity.

GABA and Ca^{2+} differentiation protocol and HD iPS cell-derived neurons:

As discussed in the specific methods for this chapter an entirely new protocol was investigated, integrating advances in reprogramming, neuralisation and terminal differentiation. Additionally, a second childhood onset HD line (Q109) was incorporated for comparison with the Q180 line which had shown survival issues and very altered functional maturation in previous experiments. Also, amongst these changes, the glutamate concentration in the medium was reduced, which may help to alleviate the survival problems previously observed in the Q180 line. Using this new protocol as a control the functional benefits of using GABA and increased Ca^{2+} in the medium (from 1.2mM to 1.8mM) were assessed, based on data from chapter 5. The hypothesis that a combination of GABA and Ca^{2+} could accelerate and enhance functional maturation, resulting in an early time point which showed consistently mature neurons across all, or most lines. Therefore, cells from all 4 lines (Q33 (control), Q60, Q109 and Q180) were differentiated in the new control medium (using the advanced protocol) and with both 300 µM GABA and 0.6 mM Ca^{2+} added to the medium (resulting in 1.8 mM Ca^{2+}), this medium is further referred to as the GABA + Ca^{2+} medium.

At week 1, the GABA + Ca^{2+} medium evoked a significant increase in the proportion of cells able to fire action potentials across genotypes, other than the Q180 line (100% (n = 8, $P<0.01$, $Chi^2=7.3$) in the Q33 line, 88% (n = 8, $P<0.05$, $Chi^2=3.4$) in Q60 line, 100% (n = 9, $P<0.05$, $Chi^2=2.9$) in the Q109 line and 92% (n = 13, ns) in the Q180 line) compared to control (40% (n = 10) in the Q33 line, 44% (n = 9) in the Q60 line, 73% (n = 15) in the Q109 line and 82% (n = 11) in the Q180 line, figure 6.5B). Further, a similar increase in the rates of spontaneous activity in the GABA + Ca^{2+} medium was observed (25% (n = 8, $P<0.05$, $Chi^2=2.8$) in the Q33 line, 33% (n = 9, $P<0.05$, $Chi^2=3.6$) in the Q60 line, 41% (n = 12, $P<0.05$, $Chi^2=4.7$) in the Q109 line, 31% (n = 13, ns) in Q180 line), compared to control (0% (n = 10) in the Q33 line, 0% (n = 9) in the Q60 line, 7% (n = 15) in the Q109 line and 18% (n = 11) in the Q180 line, figure 6.5E). This correlated with a hyperpolarisation of the resting membrane potential evoked by the GABA + Ca^{2+} medium (-45.1±4.5 mV (n = 8) in the Q33 line, -44.7±3.2 mV (n = 9) in the Q60 line, -47.4±3.2 mV (n = 12) in the Q109 line and -47.0±2.4 mV (n = 13) in the Q180 line) compared to control (-31.1±4.2 mV (n = 10) in the Q33 line, -36.5±2.5 mV (n = 9) in the Q60 line, -41.5±4.3 mV (n = 15) in the Q109 line and -38.8±2.8 mV

(n = 11) in Q180 line, figure 6.5F). By week 2, the control cells had caught up with the GABA and Ca^{2+} treated cells with regards to inducible activity, in the GABA + Ca^{2+} medium (88% (n = 9, ns) in the Q33 line, 86% (n = 7, ns) in the Q60 line, 91% (n = 11, ns) in the Q109 line and 59% (n = 12, ns) in the Q180 line) compared with control (89% (n = 9, ns) in the Q33 line, 100% (n = 10, ns) in the Q60 line, 100% (n = 8, ns) in the Q109 line and 28% (n = 7, ns) in the Q180 line, figure 6.5B). However, in terms of spontaneous activity the GABA + Ca^{2+} medium still evoked an increase (55% (n = 11, $P<0.05$, Chi^2= 3.3) in the Q33 line, 40% (n = 10, ns) in the Q60 line, 75% (n = 8, $P<0.05$, Chi^2=5.1) in the Q109 line, 14% (n = 7, ns) in the Q180 line) compared to control (25% (n = 12) in the Q33 line, 13% (n = 8) in the Q60 line, 30% (n = 10) in the Q109 line and 8% (n = 12) in the Q180 line, figure 6.5E). This correlated with a continued hyperpolarisation of the resting membrane potentials in the GABA + Ca^{2+} medium (-51±3.1 mV (n = 11) in the Q33 line, -48.7±5.2 mV (n = 10) in the Q60 line, -59.4±4.6 mV (n = 8) in the Q109 line and -35.3±7 mV (n = 7) in the Q180 line) compared with control (-39.1±2.7 mV (n = 12) in the Q33 line, -37±5.2 mV (n = 8) in the Q60 line, -43.4±4 mV (n = 10) in the Q109 line and -34.5±2.5 mV (n = 12) in the Q109 line, figure 6.5FC). However, specifically the highest repeat line, the Q180 line showed diminished spontaneous activity and a more depolarised membrane potential. Into week 3 and apart from in the Q180 line, almost all cells were still able to fire action potentials in the GABA + Ca^{2+} medium (100% (n = 8) in the Q33 line, 100% (n = 10) in the Q60 line, 83% (n = 6) in the Q109 line and 66% (n = 3) in the Q180 line) and control (90% (n = 10) in the Q33 line, 86% (n = 7) in the Q60 line, 100% (n = 7) in the Q109 line and 25% (n = 4) in the Q180 line, figure 6.5BA). The Q33, Q60 and Q109 lines also still retained a significant portion of cells showing spontaneous activity at week 3, especially in the GABA+Ca^{2+} medium (50% (n = 8, ns) in the Q33 line, 57% (n = 7, $P<0.05$, Chi^2=2.8) in the Q60 line, 33% (n = 6, ns) in the Q109 line and 0% (n = 4, ns) in the Q180 line) compared with control (33% (n = 9) in the Q33 line, 50% (n = 8) in the Q60 line, 14% (n = 7) in the Q109 line and 0% (n = 5) in the Q180 line, figure 6.5E). Similarly, the resting membrane potential of cells derived from the Q33, Q60 and Q109 lines was still significantly hyperpolarised although there was a smaller difference between the cells differentiated in the GABA + Ca^{2+} medium (-46.2±3.5 mV (n = 8) in the Q33 line, -48.1±2.5 mV (n = 7) in the Q60 line, -45.2±3.1 mV (n = 6) in the Q109 line and -24.5±6 mV (n = 4) in the Q180 line) compared to control (-40.3±2.6 mV (n = 9) in the Q33 line, -39.8±2 mV (n = 7)

in the Q60 line, -40.1±1.7 mV (n = 7) in the Q109 line and -21±7.7 (n = 4) in the Q180 line, figure 6.5F). By contrast the Q180 line showed very significant decline at week 3, in terms of induced action potentials, spontaneous activity and resting membrane potential, which could perhaps attributed to selective loss of mature neurons from this line.

In addition to enhancing the proportion of cells able to fire action potentials the GABA and increased Ca^{2+} also enhanced the shape of evoked action potentials. At week 1, induced action potentials showed immature shape, which is quantitatively compared using the area inside orbital plots (426 ± 59 $mV^2 \cdot ms^{-1}$ (n = 6) in Q33 neurons, 790 ± 197 $mV^2 \cdot ms^{-1}$ (n = 7) in Q60 neurons, 968 ± 208 $mV^2 \cdot ms^{-1}$ (n = 7) in Q109 neurons and 868 ± 114 $mV^2 \cdot ms^{-1}$ (n = 7) in Q180 neurons, figure 6.5C). The GABA and Ca^{2+} medium evoked a significant improvement in the shape of evoked action potentials in the Q33 and Q60 lines, but not the Q109 and Q180 lines (966 ± 169 $mV^2 \cdot ms^{-1}$ (n = 7), $P<0.01$, in the Q33 line, 1349 ± 283 $mV^2 \cdot ms^{-1}$ (n = 8), $P<0.05$, in the Q60 line, 1275 ± 252 $mV^2 \cdot ms^{-1}$ (n = 8), ns, in the Q109 line, and 1107 ± 150 $mV^2 \cdot ms^{-1}$ (n = 8), ns, in the Q180 line, figure 6.5C). At week 2, all of the lines apart from the Q180 line showed more mature action potential shapes (1898 ± 367 $mV^2 \cdot ms^{-1}$ (n = 7) in the Q33 line, 2159 ± 340 $mV^2 \cdot ms^{-1}$ (n = 8) in the Q60 line, 2221 ± 306 $mV^2 \cdot ms^{-1}$ (n = 9) in the Q109 line, and 1034 ± 81 $mV^2 \cdot ms^{-1}$ (n = 6) in the Q180 line). Further, the GABA and Ca^{2+} medium continued to enhance the shape of induced action potentials at week 2 in the Q33, Q60 and Q109 lines (2765 ± 466 $mV^2 \cdot ms^{-1}$ (n = 7), $P<0.05$, in the Q33 line, 2666 ± 441 $mV^2 \cdot ms^{-1}$ (n = 9), $P<0.5$, in the Q60 line, 3220 ± 400 $mV^2 \cdot ms^{-1}$ (n = 6), $P<0.05$, in the Q109 line, and 1107 ± 150 $mV^2 \cdot ms^{-1}$ (n = 5), ns, in the Q180 line, figure 6.5C). At week 3 however, this trend ended, resulting in no appreciable difference evoked by the GABA + Ca^{2+} medium (2310 ± 222 $mV^2 \cdot ms^{-1}$ (n = 5) vs. 2571 ± 241 $mV^2 \cdot ms^{-1}$ (n = 6), ns, in the Q33 line, 1957 ± 494 $mV^2 \cdot ms^{-1}$ (n = 5) vs. 2077 ± 482 $mV^2 \cdot ms^{-1}$ (n = 5), ns, in the Q60 line, 1635 ± 142 $mV^2 \cdot ms^{-1}$ (n = 5) vs. 1572 ± 115 $mV^2 \cdot ms^{-1}$ (n = 5), ns, in the Q109 line), the Q180 line cultures were almost entirely dead by this time point (figure 6.5C).

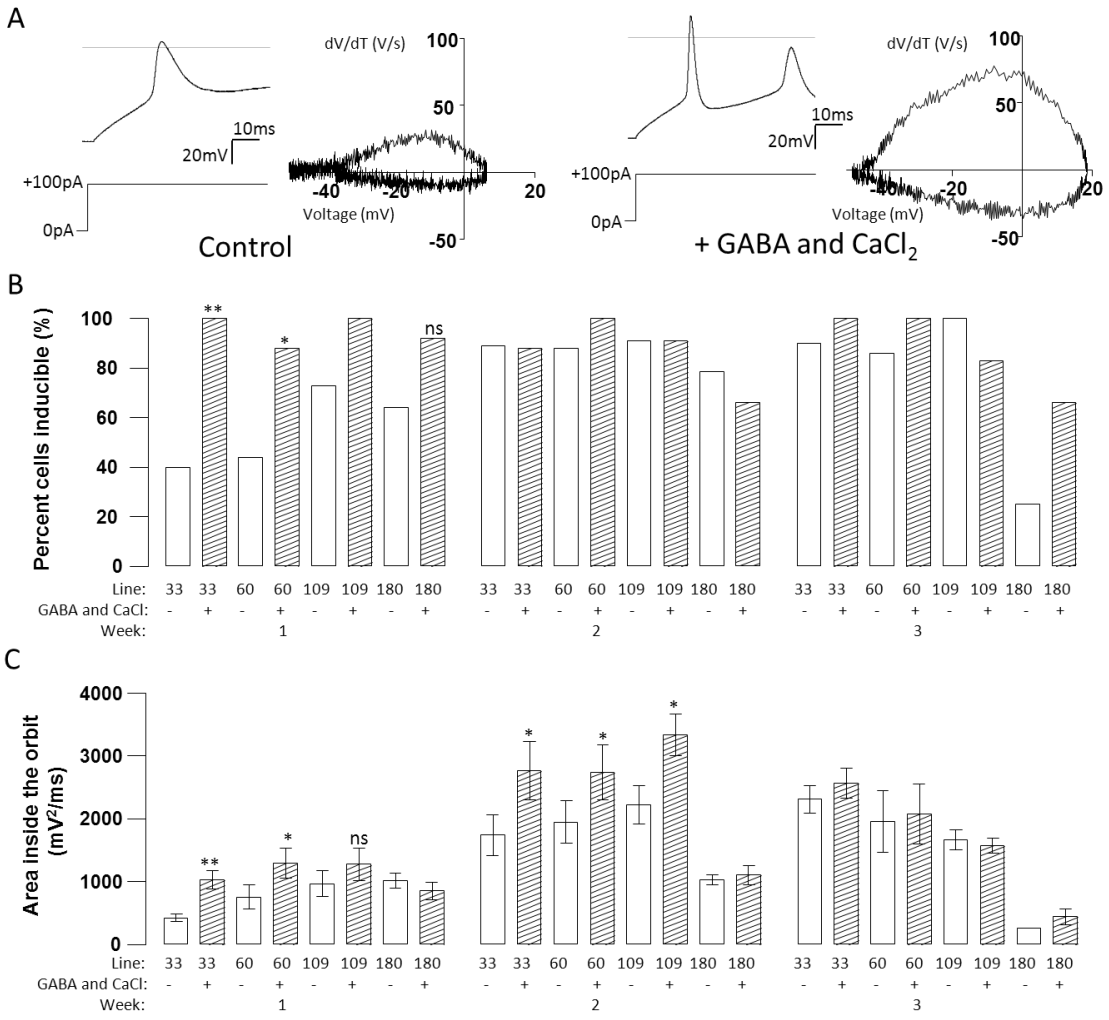
A
dV/dT (V/s)
100
50
-50
-40
-20
20
Voltage (mV)
10ms
20mV
+100pA
0pA
Control
+ GABA and CaCl2
B
Percent cells inducible (%)
100
80
60
40
20
0
**
*
ns
Line: 33 33 60 60 109 109 180 180 33 33 60 60 109 109 180 180 33 33 60 60 109 109 180 180
GABA and CaCl: - + - + - + - + - + - + - + - + - + - + - + - + - +
Week: 1 2 3
C
Area inside the orbit (mV²/ms)
4000
3000
2000
1000
0
**
*
ns
*
*
*
Line: 33 33 60 60 109 109 180 180 33 33 60 60 109 109 180 180 33 33 60 60 109 109 180 180
GABA and CaCl: - + - + - + - + - + - + - + - + - + - + - + - + - +
Week: 1 2 3

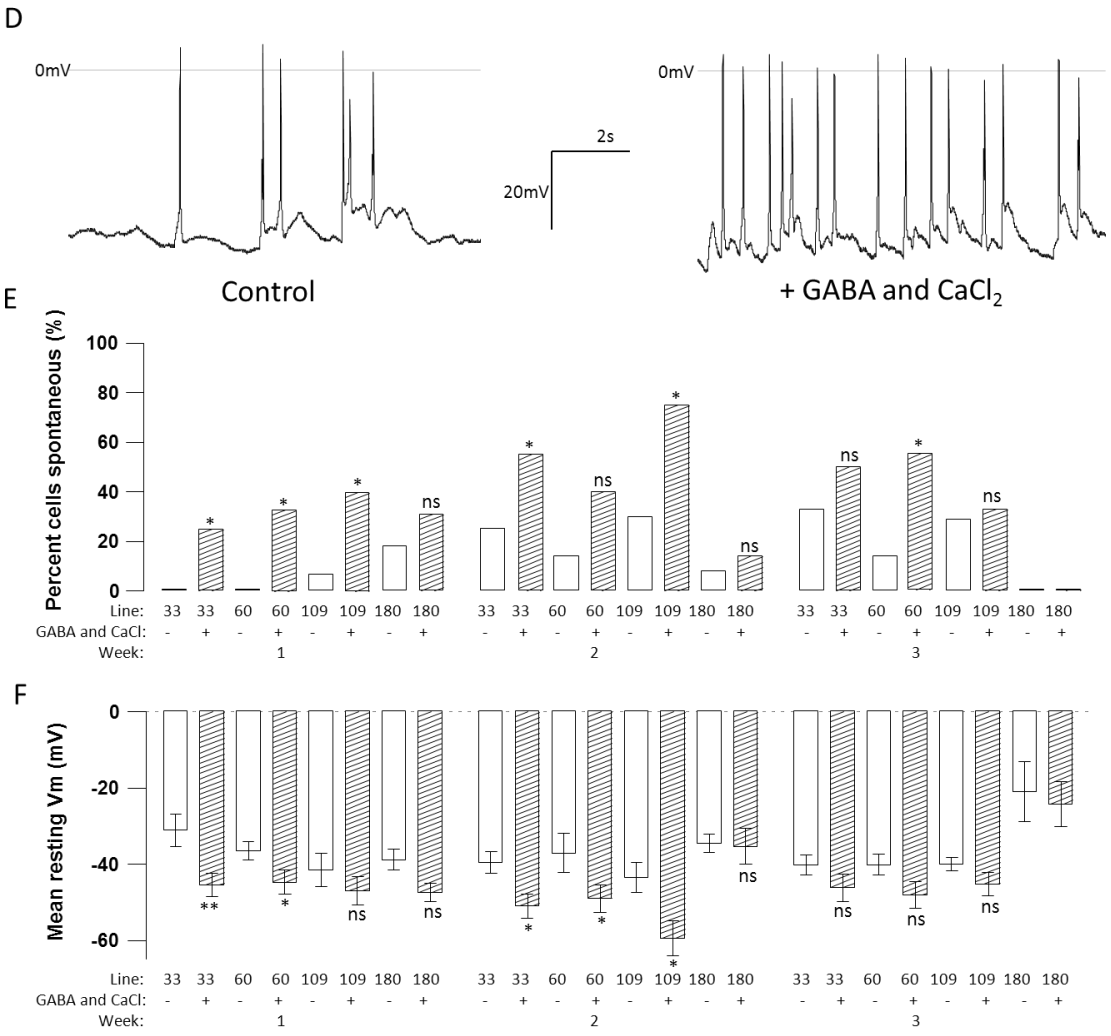

Figure 6.5: Action potential generation and resting membrane potential of HD neurons differentiated in the new protocol, both with and without GABA and increased Ca^{2+}.

A) Exemplar voltage recordings (top) showing induced action potentials during a current step protocol (bottom), also represented as an orbital plot (graphs), for a week 2 Q33 control-treated neuron (right) compared to a week 2 Q33 neuron treated with 300µM GABA and 1.8mM Ca^{2+} (left).

B) A bar graph showing the proportion of cells able to fire induced action potentials across 3 weeks of differentiation treated with control medium and with the addition of 300µM GABA and 1.8mM Ca^{2+}.

C) A bar graph comparing mean area inside orbital graphs (±SEM) which represent induced action potentials from neurons treated and control medium and with the addition of 300µM GABA and 1.8mM Ca^{2+}.

D) Voltage recordings during current clamp (I=0) showing spontaneous action potentials from Q33 neurons at week 2 treated with control medium and with the addition of 300µM GABA and 1.8mM Ca^{2+}.

E) A bar graph showing the proportion of cells showing spontaneous action potentials across 3 weeks of differentiation in control medium and with the addition of 300µM GABA and 1.8mM Ca^{2+}.

F) A bar graph showing the mean resting membrane potential (±SEM) of cells differentiated across 3 weeks of differentiation in control medium and with the addition of 300µM GABA and 1.8mM Ca^{2+}.

Consistent with the observation that the proportion of cells able to fire action potentials and the shape of induced action potentials, the GABA + Ca^{2+} medium also enhanced functional Na^+ and K^+ currents during the course of development. At week 1, Na^+ currents were significantly enhanced in the Q33 and Q60 lines in the GABA + Ca^{2+} medium (-27.7 ± 2.5 pA·pF^{-1} (n = 8) vs. -45 ± 6.3 pA·pF^{-1} (n = 8), P<0.05, in the Q33 line, -32.9 ± 6.3 pA·pF^{-1} (n = 8) vs. -46.3 ± 7 pA·pF^{-1} (n = 8), P<0.05, in the Q60 line, -50.4 ± 9.5 pA·pF^{-1} (n = 9) vs. -45.3 ± 8.6 pA·pF^{-1} (n = 8), ns, in the Q109 line, and -42.8 ± 6.4 pA·pF^{-1} (n = 7) vs. -39.5 ± 3.6 pA·pF^{-1} (n = 8), ns, in the Q180 line, control followed by GABA+ Ca^{2+} in each case, figure 6.6B). Similarly, the magnitude of K^+ currents were also augmented in the Q33 and Q60 lines at week 1 (21.5 ± 2.9 pA·pF^{-1} (n = 8) vs. 45.5 ± 7.9 pA·pF^{-1} (n = 8), P<0.05, in the Q33 line, 27.9 ± 5 pA·pF^{-1} (n = 8) vs. 39 ± 6.1 (n = 8), P<0.05, in the Q60 line, 39.6 ± 8.3 pA·pF^{-1} (n = 8) vs. 49.7 ±11.1 pA·pF^{-1} (n = 8), ns, in the Q109 line, 38.2 ± 7.7 pA·pF^{-1} (n = 7) vs. 43.6 ± 5.3 pA·pF^{-1} (n = 8), ns, in the Q180 line, control followed by GABA+ Ca^{2+} in each case, figure 6.6C). At week 2, Na^+ currents were significantly enhanced in the Q33, Q60 and Q109 lines in the GABA + Ca^{2+} medium (-67.6 ± 6.7 pA·pF^{-1} (n = 8) vs. -84.3 ± 10.2 pA·pF^{-1} (n = 8), P<0.05, in the Q33 line, -66.1 ± 6.7 pA·pF^{-1} (n = 8) vs. -87.5 ± 7.7 pA·pF^{-1} (n = 8), P<0.05, in the Q60 line, -62.1 ± 7.4

$pA \cdot pF^{-1}$ (n = 9) vs. -94.9 ± 6.8 $pA \cdot pF^{-1}$ (n = 8), P<0.05, in the Q109 line, and -43.5 ± 3.5 $pA \cdot pF^{-1}$ (n = 6) vs. -42.2 ± 5 $pA \cdot pF^{-1}$ (n = 7), ns, in the Q180 line, control followed by GABA+ Ca^{2+} in each case, figure 6.6B). Similarly, the magnitude of K^+ currents were also augmented in the Q60 and Q109 lines at week 2 (59.6 ± 10 $pA \cdot pF^{-1}$ (n = 8) vs. 76.8 ± 13 $pA \cdot pF^{-1}$ (n = 8), ns, in the Q33 line, 51.5 ± 9.3 $pA \cdot pF^{-1}$ (n = 8) vs. 81.2 ± 12.5 (n = 8), P<0.05, in the Q60 line, 60.5 ± 9.3 $pA \cdot pF^{-1}$ (n = 9) vs. 79.7 ± 3.9 $pA \cdot pF^{-1}$ (n = 8), P<0.05, in the Q109 line, 41.7 ± 5.3 $pA \cdot pF^{-1}$ (n = 6) vs. 43.6 ± 5.3 $pA \cdot pF^{-1}$ (n = 7), ns, in the Q180 line, control followed by GABA+ Ca^{2+} in each case, figure 6.6C). At week 3, no significant alteration of the Na^+ currents were observed in the GABA + Ca^{2+} medium (-73.3 ± 2.2 $pA \cdot pF^{-1}$ (n = 7) vs. -79.6 ± 9.2 $pA \cdot pF^{-1}$ (n = 7), ns, in the Q33 line, -80.6 ± 6.2 $pA \cdot pF^{-1}$ (n = 8) vs. -78.7 ± 10.8 $pA \cdot pF^{-1}$ (n = 8), ns, in the Q60 line, -56.2 ± 3.8 $pA \cdot pF^{-1}$ (n = 7) vs. -59 ± 4.7 $pA \cdot pF^{-1}$ (n = 7), ns, in the Q109 line, and -13 $pA \cdot pF^{-1}$ (n = 1) vs. -22 ± 10 $pA \cdot pF^{-1}$ (n = 2), ns, in the Q180 line, control followed by GABA+ Ca^{2+} in each case, figure 6.6B). Similarly, no alteration in the magnitude of K^+ currents was observed (76 ± 15.5 pA·pF-1 (n = 7) vs. 73.1 ± 11.2 pA·pF-1 (n = 7), ns, in the Q33 line, 88.5 ± 14 pA·pF-1 (n = 7) vs. 72.3 ± 10.9 (n = 7), ns, in the Q60 line, 44.5 ± 3.9 pA·pF-1 (n = 7) vs. 41.8 ± 3.1 pA·pF-1 (n = 7), ns, in the Q109 line, 10 pA·pF-1 (n = 1) vs. 18.5 ± 3.5 pA·pF-1 (n = 2), ns, in the Q180 line, control followed by GABA+ Ca2+ in each case, 6.6C).

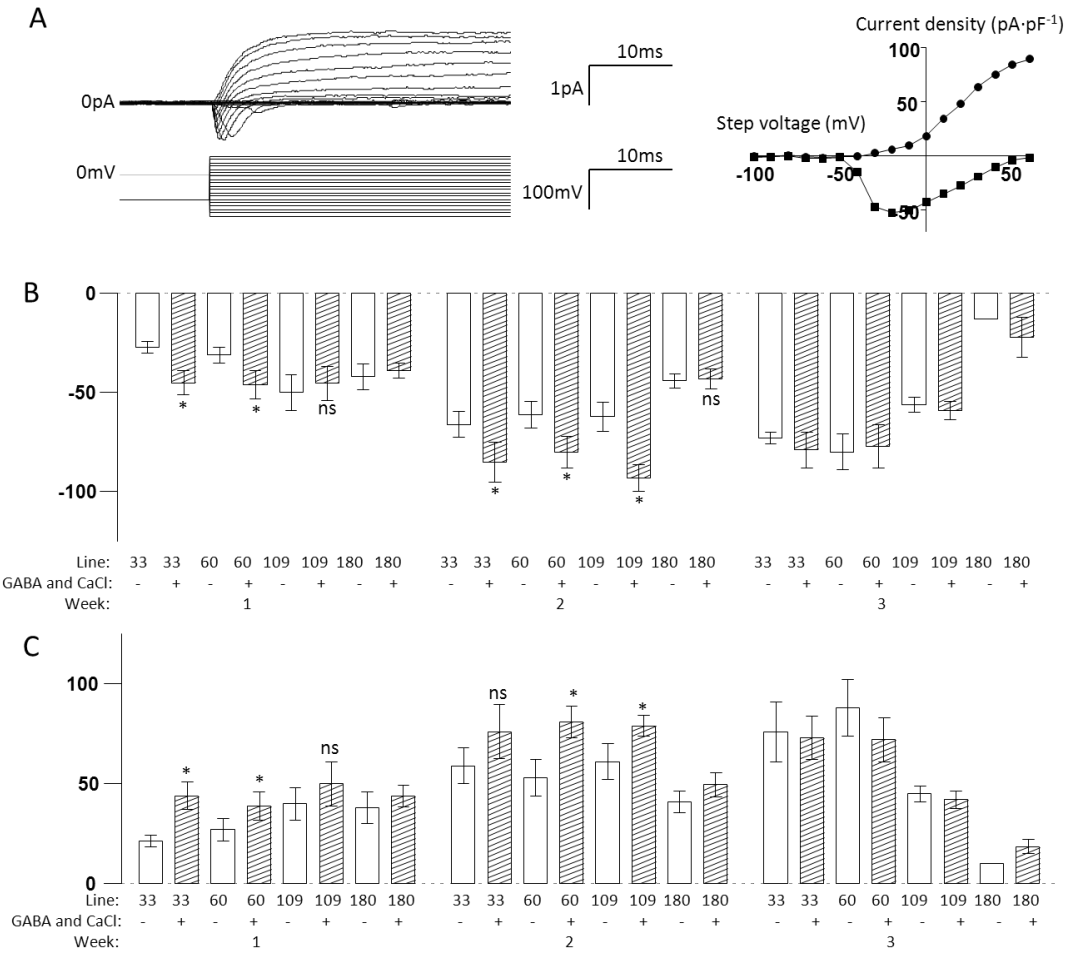

Figure 6.6: Voltage activated Na^+ and K^+ currents evoked in neurons differentiated in the HD lines using the new protocol, and with the addition of GABA and increased Ca^{2+}.

A) Exemplar current recordings from a week 2 control Q33 neuron (top) showing voltage activated Na^+ and K^+ currents evoked by a voltage step protocol (bottom), and represented as a current density against step voltage graph for both currents (Na^+ as circles and K^+ as squares, left).

B) A bar graph comparing the mean magnitude (±SEM) of voltage activated Na^+ currents across all 3 weeks of differentiation, in control medium and with the addition of 300µM GABA and 0.6mM $CaCl_2$.

C) A bar graph comparing the mean magnitude (±SEM) of voltage activated K^+ currents across all 3 weeks of differentiation, in control medium and with the addition of 300µM GABA and 0.6mM $CaCl_2$.

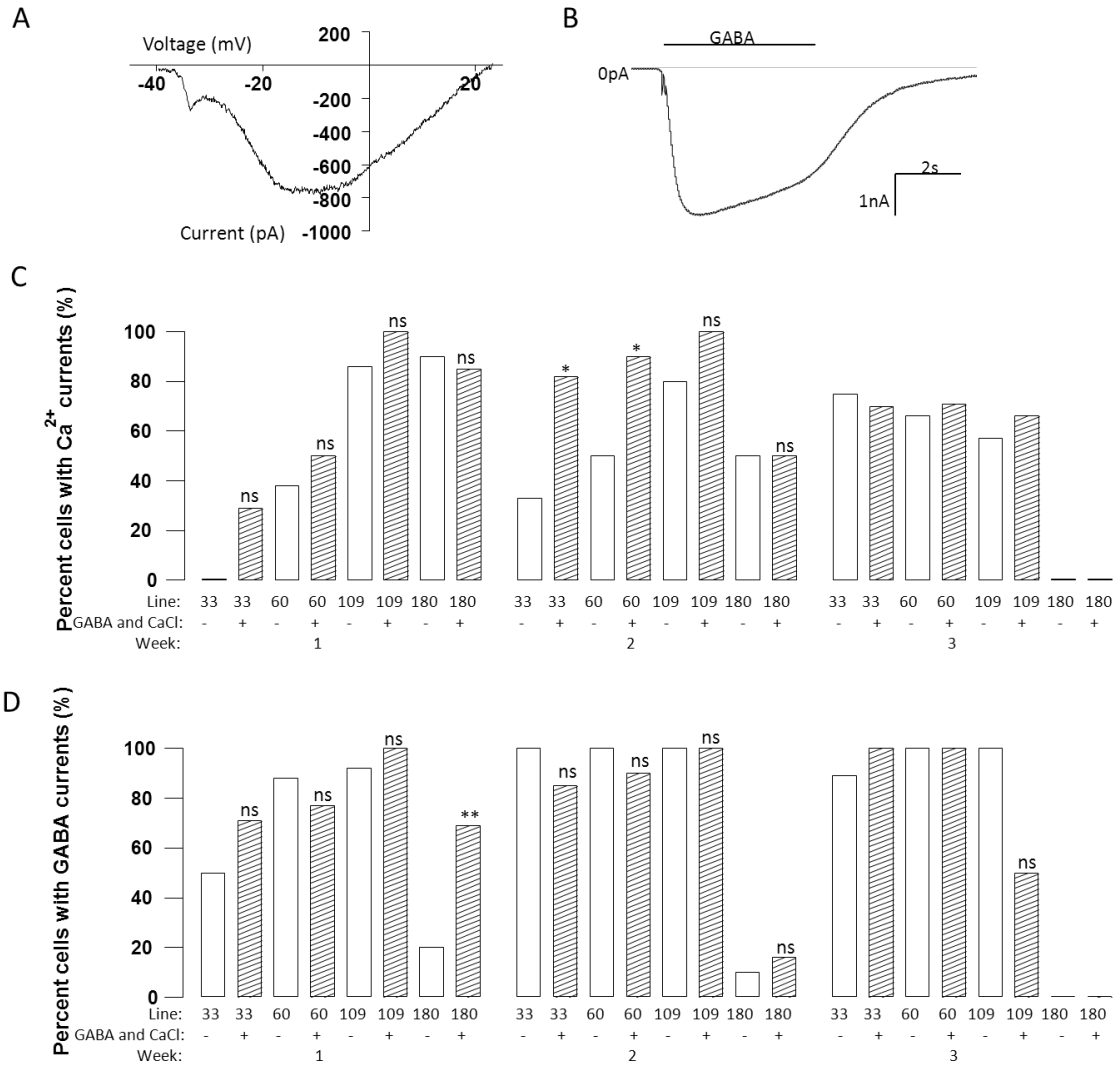

Figure 6.7: Voltage activated Ca^{2+} and $GABA_A$ currents evoked in neurons differentiated in the HD lines using the new protocol, and with the addition of GABA and increased Ca^{2+}.

A) Exemplar current recording during a voltage ramp protocol showing a voltage activated Ca2+ current from a week 2 Q33 neuron treated with 300µM GABA and 0.6mM $CaCl_2$.

B) Exemplar current recording with a 5s application of 300µM GABA whilst being held at -70mV, from a week 2 Q33 neuron treated with 300µM GABA and 0.6mM $CaCl_2$.

C) A bar graph showing the proportion of cells with significant voltage activated Ca^{2+} currents across 3 weeks of differentiation in the new small molecule differentiation, and with the addition of 300µM GABA and 0.6mM $CaCl_2$.

D) A bar graph showing the proportion of cells with significant GABA evoked currents across 3 weeks of differentiation in the new small molecule differentiation, and with the addition of 300µM GABA and 0.6mM $CaCl_2$.

Further, the hypothesis that the GABA and Ca^{2+} medium would increase the functional $GABA_A$ and Ca^{2+} currents across these lines was tested. At week one, consistent with data in the previous differentiation medium an increase the function of Ca^{2+} channels with lines with increasing CAG repeats was observed (0% (n = 8) in the Q33 line, 38% (n = 8) in the Q60 line, 88% (n = 14) in the Q109 line and 90% (n = 10) in the Q180 line, figure 6.7B). No appreciable difference in the function of Ca^{2+} channels was evoked by the GABA + Ca^{2+} medium at week 1 (28% (n = 7) in the Q33 line, 50% (n = 8) in the Q60 line, 100% (n = 8) in the Q109 line and 85% (n = 13) in the Q180 line, figure 6.7B). However, at week 2, the Q33 and Q60 lines showed an increased proportion of cells with Ca^{2+} channels, which was increased further by the GABA + Ca^{2+} medium (82% (n = 11, $P<0.05$, $Chi^2=4.7$) in the Q33 line, 90% (n = 10, $P<0.05$, $Chi^2=3.8$) in the Q60 line, 100% (n = 8, ns) in the Q109 line and 50% (n = 6,ns) in the Q180 line) compared to control (36% (n = 11) in the Q30 line, 50% (n = 10) in the Q60 line, 80% (n = 10) in the Q109 line and 50% (n = 6) in the Q180 line, figure 6.7B). In contrast the Q180 line showed fewer cells with Ca^{2+} currents at week 2. Into week 3 and no appreciable difference was observed between the Q33, Q60 or Q109 lines, or with the application of GABA and Ca^{2+} (75% (n = 8, ns) in the Q33 line, 71% (n = 7, ns) in the Q60 line, 67% (n = 7, ns) in the Q109 line and 0% (n = 3, ns) in the Q180 line in the Q33, Q60, Q109 and Q180 lines respectively) compared to control (66% (n = 9) in the Q33 line, 58% (n = 7) Q60 line, 57% (n = 7) Q109 line and 0% (n = 3) in the Q180 line, figure 6.7B). By contrast the Q180 line showed continuing decline.

No significant differences in the proportion of cells showing functional GABA-evoked currents in the GABA+Ca^{2+} medium compared with control was observed at any week in most of the lines, the one exception being the Q180 line at week 1 (Week 1: 50% (n = 8) vs. 71% (n = 7) in the Q33 line, 88% (n = 9) vs. 77% (n = 9) in the Q60 line, 92% (n = 13) vs. 100% (n = 8) in the Q60 line, 20% (n = 10) vs. 69% (n = 13, $P<0.001$, $Chi^2=5.5$) in the Q180 line; Week 2: 100% (n = 6) vs. 86% (n = 7) in the Q33 line, 100% (n = 7) vs. 90% (n = 10) in the Q60

line, 100% (n = 10) vs. 100% (n = 8) in the Q109 line and 10% (n = 10) vs. 17% (n = 6) in the Q180 line; Week 3: 89% (n = 9) vs. 100% (n = 9) in the Q33 line, 100% (n = 7) vs. 100% (n = 7) in the Q60 line, 83% (n = 6) vs. 50% (n = 6) in the Q109 line and 0% (n = 3) vs. 0% (n = 3) in the Q180 line (control followed by GABA + Ca^{2+} for each), figure 6.7C). Consistent with findings in the standard differentiation an increase in the number of cells with $GABA_A$ currents in the Q60 and Q109 lines was observed compared to Q33. The Q180 lines again showed very few cells with $GABA_A$ currents which was ameliorated by the GABA and Ca^{2+} medium at week 1, but then declined to almost none in week 2 and 3 similar to the Q180 line in the control medium. By week 2, and continuing into week 3 almost all of the cells from the other 3 lines showed functional voltage activated $GABA_A$ currents.

In answer to the hypotheses set, the GABA and Ca^{2+} added to the medium did result in a more mature and consistent electrophysiological phenotype, especially at week 2. At this week cells of all 3 genotypes exhibited consistently hyperpolarised membrane potentials, almost all cells able to fire inducible action potentials, significant Ca^{2+} currents, significant $GABA_A$ currents, and crucially, a significant proportion of cells firing action potentials spontaneously. As an exception, the Q180 line consistently showed a deteriorating function following week two, which was not seen in even the other childhood onset line, the Q109s. However, this could simply be a reflection of the extreme severity of 180 CAG repeats. These data suggest that manipulation of Ca^{2+} influx with GABA and additional Ca^{2+}, or perhaps using Bay K8644, it is possible to functionally enhance neurons for an iPS cell-derived model for Huntington's disease whilst retaining a defined protocol. Further, combining these protocol developments with other technological advances in iPS reprogramming, neuralisation and differentiation it is possible to produce cultures of neurons across multiple disease-lines which are consistently somewhat mature at a set time point. Although this technology has yet to provide enriched cultures of medium spiny neurons, and which are as fully functional as *in vivo*.

Chapter 7: Overall discussions:

Astrocyte conditioned medium and electrophysiological function:

Astrocyte conditioned medium (ACM) was used as a tool for transferring a complete mixture of astrocyte secreted factors as a strategy for enhancing the differentiation of iPS cell-derived neurons in a short protocol. The hypothesis that this cocktail of factors would accelerate the functional development of iPS cell-derived neurons and result in an electrophysiological phenotype which compares better to that seen *in vivo* was tested. Firstly, ACM did not accelerate the development of the fundamental machinery required to generate an action potential. At week 1, both the ACM treated and control cells showed very similar peak voltage activated Na^+ and K^+ currents that were too small to deliver action potentials with a mature shape. Therefore, at week 1 both cultures showed induced action potentials that were slow, with very little overshoot above 0 mV or undershoot below the threshold voltage. This also resulted in no cells at week eliciting a second abortive, or complete, action potential. From week 1 to 2, both ACM treated and control medium appreciably increased the magnitude of their Na^+ and K^+ currents which produced faster induced action potentials with limited attempts at producing a second action potential, as the K^+ current was now significant enough result in the voltage undershooting the threshold voltage significantly. Additionally by week 2, the ACM treated cells showed sharper action potential shapes than control, which correlated with an increase in cells showing abortive second action potentials in ACM. This improvement correlated with an increase in Na^+ current in the ACM treated cells at week 2. However, at week 3 an increased K^+ current was observed in the control cells over the ACM treated cells. More surprisingly, and incongruous with the notion that action potential shape is entirely determined by the magnitude of Na^+ and K^+ currents, more mature and faster action potentials were actually seen in the ACM treated neurons at week 3, of which most cells fired a second full action potential instead of an abortive attempt.

Key to our initial hypothesis that ACM could evoke significantly more functional neurons in this short protocol, was the observation that the ACM evoked a remarkable increase in spontaneous activity by week 3. At week 3 most of the ACM-treated cells showed high rates

of spontaneous activity in short bursts at the top of the up-states of a biphasic membrane potential. This activity is far more reminiscent of the activity expected of neurons *in vivo* or recorded *ex vivo* in slices of neuronal tissue, including medium spiny neurons of the striatum [176]. Multiple parameters of excitability were examined including the threshold for action potentials, voltage dependent profiles for the voltage activated Na^+ current (in terms of both Na^+ activation profile and action potential threshold), membrane input resistance, membrane capacitance and resting membrane potential. No appreciable changes in the threshold voltage, input resistance, membrane capacitance or voltage dependant profiles for activation or inactivation of the Na^+ current were observed. Only the resting membrane potential of ACM-treated neurons showed a significant difference compared to the control cells, a hyperpolarisation of the membrane potential evoked by ACM correlated temporally with the enhanced levels of activity. The resting membrane potential was significantly more polarised at all weeks in ACM-treated cells. However at week 3, this difference was particularly large. This suggests that the resting membrane potential enabled increased spontaneous activity by removing the inactivation of voltage activated Na^+ currents. This notion is supported by comparing the mean resting membrane potential of control and ACM-treated cells with the voltage dependant profile for inactivation of the Na^+ current for these cells. Additionally, the biphasic membrane potential of these cells means that prior to the bursts of action potentials initiated at the start of the up-state, the down-state voltage is further hyperpolarised than the mean resting membrane potential. This provides a best of both voltages situation, where the down-state removes the inactivation of the Na^+ current and the up-state brings the membrane voltage very close to the threshold voltage for an action potential. Examining the voltage dependant profiles for activation and inactivation of these cells Na^+ current, showed these relationships to be highly consistent with the activity of Nav1.2 channels, and not Nav1.6 [167]. This is interesting, because even with the enhanced membrane potential observed in ACM-treated cells, Nav1.6 would be functionally impotent as these channels would be mostly inactivated at the resting membrane potential.

The resting membrane potential alone does not appear to entirely explain the complete contrast in spontaneous activity observed in ACM-treated neurons compared with control. Firstly, although cells showing more hyperpolarised membrane potentials from the control cultures did show spontaneous activity, these were disperse individual events and no

biphasic membrane potentials were observed. This implies another electrophysiological development in ACM-treated cells. The biphasic membrane potential appears to provide a very plausible explanation, where the down-state reduces Na^+ inactivation, followed by the up-state which brings the voltage very close to the threshold for an action potential. Studies agree that biphasic membrane potentials in medium spiny neurons of the striatum are orchestrated and limited by the collective depolarising currents form glutamatergic synaptic drive and the repolarising M-channel K^+ currents [176,209]. However, when recording the synaptic input of ACM-treated cells relatively few cells with spontaneous EPSCs or IPSCs were observed. This is still in contrast to the control-treated cells, where no spontaneous synaptic currents were observed at all. However, it may be possible that these biphasic membrane potentials were actually led by a GABAergic drive. Using Ca^{2+} imaging, a significant switch to inhibitory GABA responses was observed by even week 2. However, during patch clamp experiments GABA stimulation is always excitatory, regardless of developmental stage, because the patch solutions used ensured a Cl^- reversal potential near to 0mV. The notion that spontaneous activity and the biphasic membrane potentials are driven by GABAergic drive is supported by the data showing bicuculline sensitive spontaneous synaptic currents in the week 3 ACM cells. It is also notable that although these membrane potentials were highly polarised compared to the control iPS-derived neurons, they were still relatively depolarised compared to neurons *in vivo.* As an alternative explanation, could the slow activation of T-type Ca^{2+} channels within this voltage range be an alternative explanation for a biphasic membrane potential? In which case these biphasic membrane potentials are as a result of a mechanism more similar to thalmic neurons, but in the absence of the competing voltage regulatory action of glutamatergic and GABAergic synaptic input [43]. However, at present the pharmacological tools used for T-type Ca^{2+} channel blockade, mainly mibedrafil, are not selective enough to test this hypothesis.

A significant increase in the function of voltage activated Ca^{2+} channels was also observed in ACM-treated cells, right from week 1. Further characterisation revealed that L-, N- and R-type Ca^{2+} channels were specifically up-regulated. This temporal increase did not correlate well with the enhanced spontaneous activity in ACM and the control treated cells did catch up in terms of voltage activated Ca^{2+} channel function by week 3. However, this represents a significant functional development since voltage activate Ca^{2+} channels are crucial to linking

electrophysiological activity to multiple other cell-processes, including gene expression, cell-skeletal remodelling, synaptic plasticity and even synaptic vesicular secretion [15,45,157,207]. Both N- and L-type Ca^{2+} channels are present on neurite outgrowths and are likely to play a role in orchestrating synaptic integration [202]. Less is known about R-type Ca^{2+} channels in development, but they have been implicated in synaptic plasticity and are also localised to neurite outgrowths [211]. This is however somewhat inconsistent with the lack of Nav1.6 functional expression observed in these cells, as these Na^{+} channels are localised to dendrites and are implicated in increasing the sensitivity of dendritic membranes to action potential generation, somewhat like a pre-amplifier to the cell [26]. This discrepancy may be explained by the developmental stage, the cells had not yet developed a membrane potential that would be able to support Nav1.6 activity, and we may reasonably speculate that membrane potential development and Nav1.6 expression are in some way synchronised.

The increased rates of spontaneous activity atop a biphasic membrane potential and the recordings of spontaneous synaptic events strongly suggest the existence of functional synapses in ACM-treated cultures. This is functionally very important to modelling neurodegenerative diseases and implies the beginnings of a functional neuronal network *in vitro*. Further characterisation was performed which showed significant bicuculline sensitivity, indicating the presence of GABAergic synapses. This is partially consistent with previous work that showed that ACM or Thrombospondin-1, was sufficient to enhance the development of morphologically distinct synapses of cultured retinal ganglion cells [40]. However, in contrast to astrocyte co-culture, and use of hiPS derived neuronal cultures in ACM reported here, the synapses in the of cultured retinal ganglion cell cultures were silent, showing no post synaptic activity[40].

In addition to driving functional maturity, many reports have also shown that astrocytes promote neuronal survival both *in vivo* and by co-culture *in vitro*[44,127]. Astrocyte secreted factors, including neurotrophins, have also been shown to promote neuronal survival[73]. Wnt proteins are also thought to regulate neuronal differentiation and survival as well as synapse formation and maintenance, and are secreted by adult astrocytes [34,112,150]. This is all consistent with the notion that astrocyte secreted factors are helping neurons to become

integrated synaptically, become spontaneous active and survive much longer, in part due to the increased activity.

Induced pluripotent stem cell derived astrocytes

In addition to the use of mouse isolated astrocytes a protocol for rapidly producing enriched and proliferative populations of hiPS cell-derived astrocytes was developed. Another intention of this protocol was to develop cultures of astrocytes in the absence of neurons, therefore allowing the astrocytes to be used in co-culture experiments with no risk of introducing new neuronal types. This could make these cultures a powerful tool for creating disease models which utilise a mix of wild-type and patient-derived astrocytes (or conditioned medium) with wild-type or patient-derived neurons. The protocol has two stages, and uses iPS-derived EZ-sphere cultures, as the starting cell population [56]. EZ-spheres represent an established and easily grown and expanded source of neural progenitor cells. The first step was to prevent neurogenesis by killing mitotic cells during the first week by treating the cells with Ara-C. During the following week LIF treatment was used to induce astrocyte precursor development [19]. Immunostaining found that by the end of the second week cultures were enriched in GFAP-positive cells, with no obvious population β3-tubulin positive neurons. However, repeating the protocol without Ara-C treatment for the first week yielded a somewhat enriched culture of astrocytes, albeit morphologically different, but also with a high concentration of differentiating neurons. This is consistent with the notion that for a pure population of astrocytes it is necessary to first or simultaneously prevent initially high rates of neurogenesis, and in this protocol we employ the strategy of killing cells that enter mitosis, an essential step in neurogenesis. However, astrogliogenesis also requires cell division, which means that using the tactic of killing mitotic cells at the same time as pushing astrocyte differentiation would be counterproductive. Therefore, the key aspect of Ara-C treatment in this protocol is timing, early neural progenitor cells are readily neurogenic, but due to DNA methylation of certain astrocyte genes cells are insensitive to astrocyte differentiating factors and unable to generate astrocytes. For example, despite a normal response of STAT3 phosphorylation to CNTF/LIF signalling, phospho-STAT3 fails to regulate GFAP gene expression in neurogenic neural progenitors

due to CpG methylation within the STAT3 binding sites in the gene promoter [137]. Over time, notch signalling, retinoic acid signalling and hypoxia inducible factor (HIF) activity participate to regulate the epigenetic chromatin remodelling of gliogenic genes, a process that involves activation of the transcription factor NFIA [6,137]. This means that neural progenitor cells are not immediately responsive to LIF, and not capable of making astrocytes, until NFIA activation has unmethylated gliogenic genes. However, by killing mitotic cells it is possible to prevent a population of neurons being developed. During this time the surviving neuronal progenitor cells become more able to produce astrocytes and responsive to astrocyte differentiation factors, presumably mediated by retinoic acid (AKA. vitamin A, contained in the B27 supplement) and hypoxia inducible factor. A one week delay in Ara-C treatment was sufficient to allow a highly enriched culture of GFAP positive cells without killing too many cells for the culture to be expanded. However, this protocol could potentially have been enhanced by incubation with cilliary neurotrophic factor (CNTF), changing the incubator oxygen concentration and altering the length of time Ara-C is used for [137,165]. BMP-4 also promotes astrocyte differentiation, but results in a different population of astrocytes with less capacity for self-renewal [19,136].

Following the first two weeks, in Ara-C followed by LIF, the iPS cell-derived astrocyte cultures were expanded in a foetal bovine serum (FBS) based medium. This medium is effective for astrocyte growth and is similar to the protocol used to expand the mouse astrocyte cultures. Therefore, this allowed the expansion and continued development of the astrocyte cultures without developing populations of neurons, because FBS based medium is insufficient for efficient neuronal survival and differentiation. Following a further week in the FBS based medium, these cells became almost entirely both GFAP and S100β (a more mature astrocyte marker) positive and could be expanded for at least 8 weeks.

In order to test the function of the iPS cell-derived astrocytes, the same protocol for generating astrocyte conditioned medium as used with the mouse isolated astrocytes to generate conditioned medium from the iPS cell-derived astrocytes. As a primary assay for the effectiveness of this conditioned medium, the levels of spontaneous activity and resting membrane potential were measured in iPS cell-derived neurons treated with this human astrocyte conditioned medium and compared with control. The conditioned medium,

consistent with data using mouse ACM, evoked a significant hyperpolarisation of the membrane potential and increased rates of spontaneous activity. However, in contrast to differentiation using mouse ACM the development of a biphasic membrane potential was not observed. This developmental difference between the iPS-derived ACM and mouse ACM could be as a result of either the developmental stage or regional identity of the iPS cell-derived astrocytes. Less is known about the regional specification of astrocytes compared to neurons. However, using LIF in the absence of BMP-4, most likely produces a population of astrocytes which have astrocyte progenitor traits and self-renewal, and therefore are perhaps not ideal for generating conditioned medium. This is consistent with the ability of these cultures to be passaged at least 8 times without an appreciable loss of markers. Treatment with BMP-4 before being used to condition medium might produce a culture with a larger population of more mature astrocytes [19]. Another potential difference between these iPS cell –derived astrocytes and the mouse isolated astrocytes is that these human astrocytes have developed in the absence of neurons, which are known to influence astrocyte development [31,137,165]. This may suggest that using neuron conditioned medium in the protocol may allow us to generate more mature iPS cell-derived astrocytes.

This new protocol for generating iPS cell-derived astrocytes is potentially very useful for generating iPS cell-derived astrocytes from patient derived iPS lines. Further, the purity of these differentiated astrocyte cultures will allow for the easy integration of neurons and astrocytes differentiated from different iPS cell lines without cell-type contamination. This could provide a powerful tool for modelling mechanisms in neurodegenerative diseases within astrocytes. For example, in Huntington's disease many studies have shown alterations in glutamate and release up-take by astrocytes, however these observations have not yet been observed using human iPS cell-derived cultures[109,113,169]. The ability to test these astrocytic functional deficits on human HD astrocytes in co-culture with wild type human neurons would allow studies to specifically target the mechanisms of the disease in astrocytes.

Manipulating voltage activated Ca^{2+} influx

Ca^{2+} has numerous non-electrophysiological roles in cell signalling and can influence, for example gene transcription and cell morphology[15]. Further, L-type Ca^{2+} channel activity has been shown to exert a pro-neurogenic influence on neural progenitor cell differentiation and further enhance neurogenesis[45]. The ACM evoked an immediate increase in the function of voltage activated Ca^{2+} channels, specifically L-, N- and R-type. This is potentially important, as it suggests more mature development of neurite outgrowths earlier. However, this also presents an activity dependant mechanism for Ca^{2+} influx that is amplified by astrocyte secreted factors, which could be implicated in activity dependant functional development [45,50,51]. Using selective antagonists to these voltage activated Ca^{2+} channels in ACM cultures, blockade of L-, N- or R-type channels entirely blocked the development of spontaneous activity. This showed that all 3 channels were required for the development of spontaneous activity.

Therefore, it was hypothesised that Ca2+ influx could be directly used to enhance functional maturation. In an attempt to directly increase Ca2+ influx, the Ca^{2+} concentration in the culture medium was increased which increased the driving force for Ca^{2+} across the membrane, allowing for larger Ca^{2+} currents when Ca^{2+} channels open. A high concentration (1.8mM Ca^{2+}) caused acceleration in the generation of a generic neuronal phenotype with increased inducible activity and a hyperpolarised resting membrane potential and inducible activity by week 1, and further increased spontaneous activity by week 2. However, in contrast to ACM, by week 3 these same cultures showed a loss of spontaneous activity and membrane depolarisation, similar to the control cultures.

Using subtype-specific antagonists for voltage activated Ca^{2+} channels, it was determined which channels were responsible for the accelerated and enhanced functional development observed with increased Ca^{2+} concentration in the medium. Antagonism of P/Q type Ca^{2+} channels resulted in an inhibition of inducible activity and a slight depolarisation of the membrane potential at week 1, but no effects subsequently. By contrast, addition of antagonists to L- or N- type channels resulted in no significant loss of inducible activity and a slight depolarisation of the membrane at week 1. But at week 2, they significantly depolarised the membrane and blocked the development of all spontaneous activity. Taken

together, these data suggest that P/Q type Ca^{2+} channels could be involved in the very early drive from neural progenitor cells to generic neurons, but not in their functional development. Further supporting this notion, no significant P/Q-type currents were observed when fully characterised at week 1 in the control or ACM-treated cells. By contrast L- and N- type channels are intimately involved in promoting the functional maturation of neurons, were significantly expressed at week 1 and synaptogenesis may require both of these channels.

GABA and functional maturity

In ACM treated cells, an increase in the functional expression of ionotropic GABA receptors at week 2 was observed. Ionotropic GABA receptors ($GABA_A$) are GABA sensitive ligand gated chloride channels and are, therefore, inhibitory or excitatory dependant on the concentration gradient of chloride and the resting membrane potential. During development, GABA stimulation evokes an decrease in the expression of the ionic co-transporter NKCC1, which pumps Cl^- ions out of the cell, and an increase in another ionic co-transporter, KCC2, which pumps Cl^- ions into the cell (figure 7.1 B) [67]. This change in the net direction of Cl^- transport shifts the reversal potential for chloride such that $GABA_A$ currents are hyperpolarising not depolarising (figure 7.1 B). Since GABA is an early excitatory neurotransmitter, it seemed plausible that GABA stimulation could provide an early depolarising stimulus for activation of voltage activated Ca^{2+} channels.

The development of spontaneous activity appears dependent on the function of both L- and N- type Ca^{2+} channels. Therefore, it seems likely that they play different roles in the GABA-dependant mechanism which drives functional maturation. L- type channels tend to be localised near the post synaptic membrane and cause Ca^{2+} influx in response to depolarisation, whilst N- (and P-) type channel activity mediate the release of GABA vesicles in response to depolarisation, and have further been shown to inhibit induced synaptic transmission in hippocampal excitatory synapses[158]. However, in the absence of a depolarising stimulus voltage activated Ca^{2+} channels remain closed, as they are gated by the cell membrane depolarising. Supporting this, the addition of GABA, as an excitatory

stimulus in the control culture medium, was sufficient to evoke an increase in inducible activity and hyperpolarise the resting membrane potential of the cells, similar to that seen with high Ca^{2+}. However, GABA evoked a moderate increase in spontaneous activity at week 1, but not at week 2. This suggests GABA had initially accelerated neuronal maturation at week 1, to a greater extent perhaps than increased extracellular Ca^{2+}. However, this had then declined by week 2, whilst increased Ca^{2+} did not show a decline until week 3. Further, blockade of $GABA_A$ channels in the high Ca^{2+} medium using bicuculline had the same effect as the sum of blockade of P/Q-, L- and N- type channels, in that it depolarised the resting membrane potential, inhibited the generation of induced action potentials and blocked all development of spontaneous activity. This suggests a mechanism whereby N-type Ca^{2+} channels mediate GABA release from very immature synapses, resulting in a GABA elicited depolarisation, dependant on Ca^{2+} influx through L-type Ca^{2+} channels, which is essential for the functional maturation of neurons and early synaptogenesis (figure 7.1 A). This model is consistent with the data showing the requirement of the electrophysiological functions of N- and L- type Ca^{2+} channels and $GABA_A$ being absolutely required for the development of spontaneous activity. Additionally, inhibition of functional maturation, by blockade of N-type Ca^{2+} channels and $GABA_A$, could each be rescued by the addition of GABA and Bay-K (a potent agonist of L- type Ca^{2+} channels), respectively. These data further validate this model by showing that GABA is down stream of N-type Ca^{2+} channel activity and that L-type Ca^{2+} channel activity is down stream of $GABA_A$ dependant depolarisation (figure 7.1 A). Further, this opens a potential mechanism for the apparent plateau of functional maturity seen in the absence of ACM, because as soon as the GABA response becomes inhibitory then the GABA dependant excitation driving functional maturation will cease (figure 7.1 B and C). The timescale of the switch from GABA being excitatory to inhibitory in these iPS-derived neuronal cultures has been found to be between weeks 1 and 2, this is consistent with the loss of function beyond week 2 in the control and high Ca^{2+} treated cells. Therefore it is plausible that in cultures supplemented with Ca^{2+} or GABA, that this switch would occur more rapidly, and that in the presence of antagonists to L- or N- type Ca^{2+} channels, or $GABA_A$ receptors the switch would be delayed or prevented.

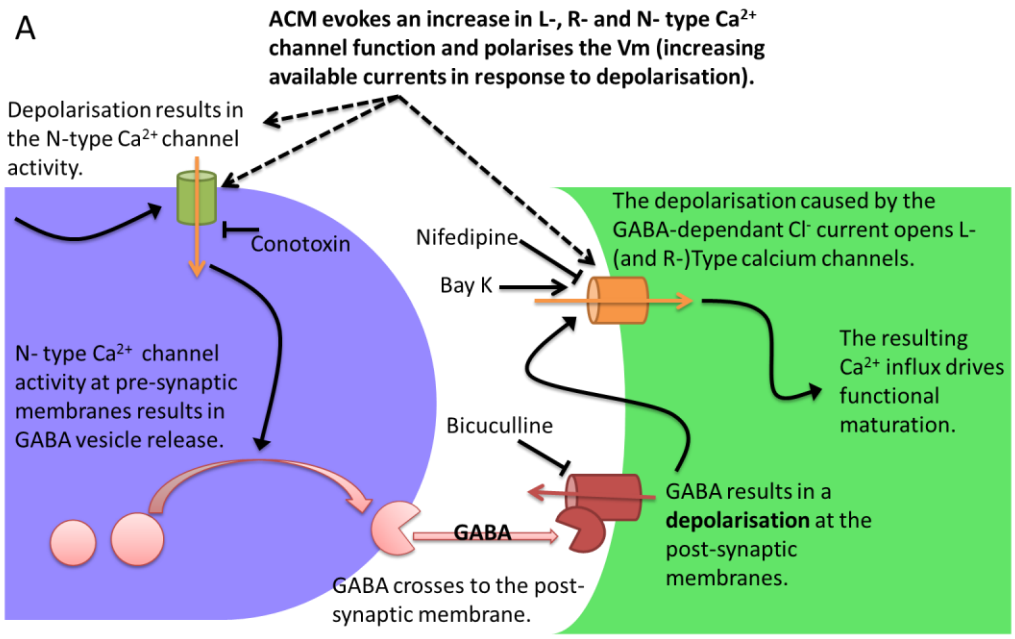
A
ACM evokes an increase in L-, R- and N- type Ca2+ channel function and polarises the Vm (increasing available currents in response to depolarisation).
Depolarisation results in the N-type Ca2+ channel activity.
Conotoxin
N- type Ca2+ channel activity at pre-synaptic membranes results in GABA vesicle release.
GABA
GABA crosses to the post-synaptic membrane.
Nifedipine
Bay K
The depolarisation caused by the GABA-dependant Cl- current opens L- (and R-)Type calcium channels.
The resulting Ca2+ influx drives functional maturation.
Bicuculline
GABA results in a depolarisation at the post-synaptic membranes.

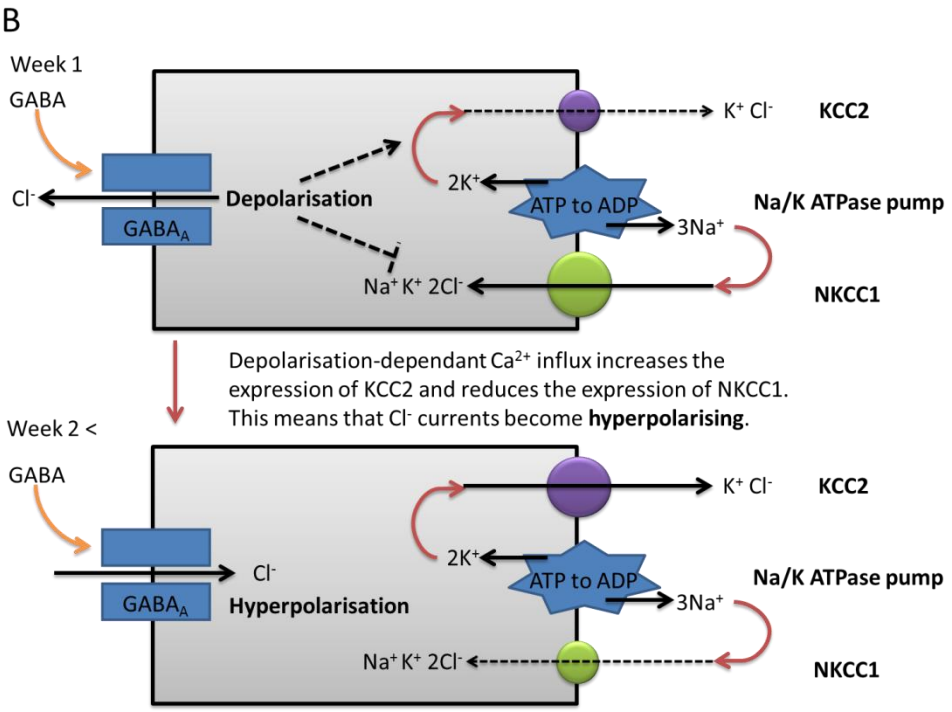
B
Week 1
GABA
Cl-
GABAA
Depolarisation
K+ Cl-
KCC2
2K+
ATP to ADP
3Na+
Na/K ATPase pump
Na+ K+ 2Cl-
NKCC1
Depolarisation-dependant Ca2+ influx increases the expression of KCC2 and reduces the expression of NKCC1.
This means that Cl- currents become hyperpolarising.
Week 2 <
GABA
Cl-
GABAA
Hyperpolarisation
K+ Cl-
KCC2
2K+
ATP to ADP
3Na+
Na/K ATPase pump
Na+ K+ 2Cl-
NKCC1

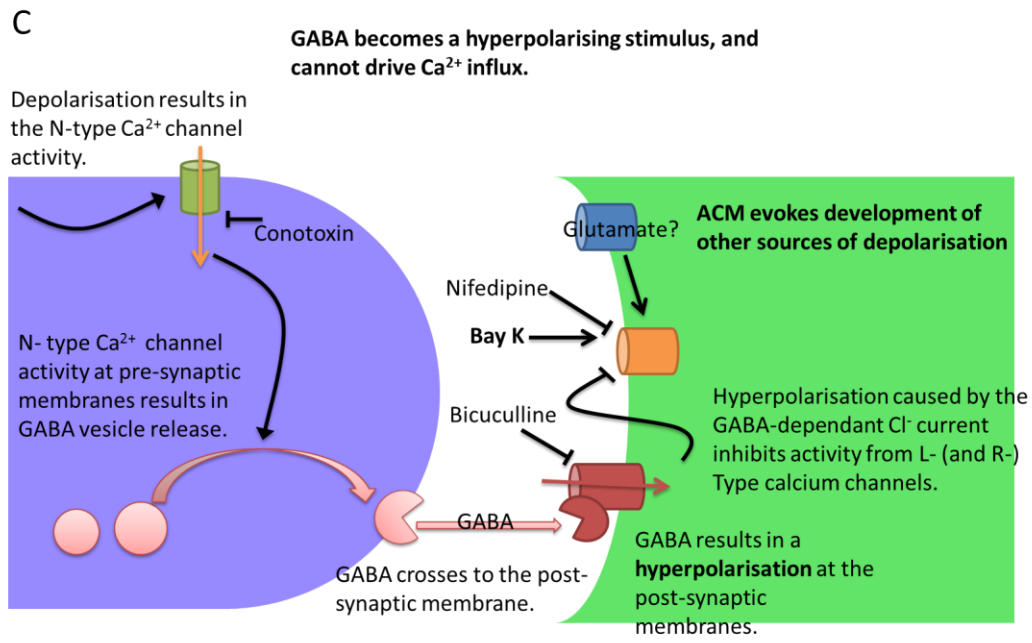

Figure 7.1:

A: A schematic showing a proposed mechanism for GABA evoked depolarisation evoked Ca^{2+} influx-dependant functional maturation, and the potential influence of ACM at week 1.At very early stages P/Q-type Ca^{2+} channels may act in a similar manner as L- or R- type do in this schematic.

B: A schematic showing how alterations to Cl^- transporters result in GABA becoming an inhibitory neurotransmitter.

A: A schematic showing a proposed mechanism for how GABA ceases to be an effective stimulus for Ca^{2+} dependent functional maturation following the GABA switch. Also, potential reasons for BayK 8644 and ACM continuing to be effective.

The effects of Ca^{2+} influx on functional maturation and neuronal differentiation is consistent with work showing that synaptogenesis is activity-dependant in culture[175]. Adult *in vivo* studies in mice have also shown synaptic activity to be crucial to synaptic remodelling and synaptogenesis, repeat stimulation of a specific whisker over a 24 hour time period resulted in a 35% increase in the synaptic density of GABAergic synapses in the layer 5 neuropil when

the animal was dissected[95]. Conversely, removal of specific whiskers, and any stimulation from them, was found to result in the loss of stabilised spines in the neocortex, associated with stable synapses[82]. Further it was found that whisker stimulation induced synaptogenesis was BDNF-dependant, in that increased stimulation was less effective at inducing new synapses in heterozygous BDNF mutants[70]. *In vitro* studies have also demonstrated that BDNF, along with other neurotrophic factors, show greater pro synaptic effectiveness and increased expression as a result of neuronal activity[21,114,174]. Increased BDNF secretion and activity is also linked to excitatory GABA signalling as studies have shown to be reversed when GABA becomes inhibitory and unable to activate voltage activated Ca^{2+} channels by depolarisation[13]. The pro-synaptogenic response from BDNF is as a result of BDNF binding to the TrkB receptor and subsequent phosphorylation of TrkB, activating the receptor. However phosphorylation of TrkB in response to BDNF binding is cAMP (cyclic adenosine monophosphate) dependant; this is a very powerful and specific "gating" mechanism as the absence of c-AMP will stop propagation of a BDNF response at its own receptor[90]. Other studies have shown a depolarisation driven, Ca^{2+} influx dependant increase in cAMP concentration due to calmodulin stimulation of certain adenylyl cyclase isoforms in neurons, as well as an integration between calmodulin and cAMP in driving CREB activity [42,48,159,172]. Membrane recruitment of TrkB has also been shown to be activity and c-AMP dependant[129]. There are also many TrkB-independent links between Ca^{2+} influx and CREB activity that provide activity dependant but BDNF-independent mechanisms for functional maturity [168]. Importantly, Ca^{2+} influx acts as a direct activity dependant stimulus for CREB phosphorylation, which in immature neurons is led by GABA stimulation [18,28,80,99,191]. However, an important distinguishing factor between mature and immature neurons appears to be whether CREB is stably phosphorylated or transiently phosphorylated in response to electrophysiological activity [128]. Therefore, the GABA and Ca^{2+} likely provide a gain in the function of activity-linked CREB phosphorylation which allows functional maturation to proceed when BDNF is alone unable to do so. This is perhaps due to a combination of both the cAMP gating at the TrkB receptor being increasingly activity-dependant, and a change in the role of CREB phosphorylation to become more transient and activity linked. This gain of function is then immediately terminated when GABA becomes an inhibitory neurotransmitter.

In addition to functional maturation, activity and neurotrophins are also required for the survival of mature neurons during development [71,104,126,160]. Which again, when considering the link between neurotrophin receptor activity and electrophysiological activity, this entirely complements studies finding that electrical activity is essential for neuronal survival. This also provides a second implication to activity-dependant maturation; if the neurons are surviving to reach maturity we would expect an increase in functional neurons over time.

ACM and Ca^{2+} influx driven effects

Blocking $GABA_A$, L-, N- or R- type Ca^{2+} channels in the ACM cultures resulted in reduced generation of induced action potentials, depolarised membrane potentials and complete block of spontaneous action potentials by week 2. Therefore, it seems plausible that in the ACM treated cells, R- type Ca^{2+} channels play a similar role to L- type channels in producing $GABA_A$ excitation dependant Ca^{2+} influx, and driving neurogenesis. This shows that there are pro-synaptogenic effects of ACM that are dependent on Ca^{2+} influx. Studies have also showed that ACM-dependant synaptic formation and maintenance in isolated rat hippocampal neurons was dependant on TrkB expression, and therefore BDNF signalling [58]. So ACM dependant synaptogenesis is BDNF dependant and BDNF driven synaptogenesis is dependent on Ca^{2+} influx, which is dependent on some excitatory stimulus. This demonstrates that ACM does not act through similar mechanisms to BDNF, but is actually influencing something downstream.

As previously discussed, ACM evokes functional enhancements in the basic electrophysiological properties of these differentiating neurons. The enhanced resting membrane potential, functional $GABA_A$ expression and functional Ca^{2+} channel expression will have a dramatic effect on activity dependant mechanisms. Taken together these enhanced electrophysiological properties will result in a gain in the GABA evoked depolarisation-dependant Ca^{2+} influx. This provides a novel mechanism for secreted factors by astrocytes to contribute to enhanced neuronal functional maturity of neurons and synaptogenesis by increase in a GABA dependant mechanism.

In addition to ACM increasing the activity-dependant maturation of neurons ACM will also greatly enhance the survival of maturing neurons [198]. ACM itself has been shown to protect neurons from apoptosis through secretion of neurotrophins and wnt [35]. Further, activity is key to neurotrophin dependant survival and therefore through gain of electrophysiological activity-dependant Ca^{2+} influx ACM will enhance activity-dependant neuronal survival as well as functional maturation.

To further develop these protocols, differentiation was tested using the human embryonic stem cell line H9. The EZ-sphere protocol was followed by the standard differentiation protocol, with ACM as a positive control for enhanced functional maturation and BayK 8644 to increase functional maturation by increased L-type Ca^{2+} channel activity. However, the H9 –derived neurons showed a relatively poor profile of functional development compared to the iPS cell-derived neurons and poor survival. This implies that this standard differentiation protocol or EZ sphere generation is poorly optimised for H9 cells. When examining the ACM and BayK 8644-treated cells there was an appreciable hyperpolarisation of the resting membrane potential and increase in the proportion of cells able to fire induced action potentials. Crucially, the BayK 8644-treated cells closely mimicked the ACM-treated cells. This implies that BayK 8644 could provide a powerful, defined, protocol which enhances the extent of functional maturation in stem cell-derived neurons.

Function of iPS cell-derived HD neurons:

The standard differentiation protocol was used to generate cultures of neurons from Huntington's disease iPS cell lines. Interestingly, the HD lines showed significant differences in the profile of electrophysiological development compared with control. Initially, both HD lines exhibited a significant increase in the function of voltage activated Ca^{2+} channels. These data correlated with an increase in the cells able to fire induced action potentials, increase in spontaneous activity and a more polarised membrane potential. This is consistent with increased Ca^{2+} channel function resulting in improved functional maturity. However, although the very high repeat line, the Q180 line, showed the most extreme functional enhancement at week 1, they then rapidly declined and died. Most noticeable

was the almost total lack of cells with a functional $GABA_A$ current in the Q180 line, implying either that the cells were unable to develop this function or that a specific loss of cells which develop GABA currents. This is perhaps consistent with the idea that the differentiated HD-cells are more sensitive to Ca^{2+} influx-dependant apoptosis, which could be driven by GABA excitation driving Ca^{2+} currents. However, synaptic activity appears to be neuroprotective in mature neurons, and extrasynaptic NMDA-receptors activity is considered to be the source of Ca^{2+} driving apoptosis in Huntington's disease, but it is plausible that an entirely immature neuron, without mature dendritic structures might be susceptible to any or other Ca^{2+} influxes. It was also speculated that glutamatergic drive would have the same effect. However, in the absence of the formation of active synapses no balance can develop between synaptic and post-synaptic Ca^{2+} influxes. To augment this imbalance by increasing synaptogesis, the HD cells were differentiated in ACM. However, although ACM-treatment enhanced the functional outcome of iPS cell-derived neurons of the Q60 line, in the Q180 line it resulted in the cells dying.

Using a more up to date small molecule-based differentiation protocol (currently unpublished, developed by A. Harrison, P. Kemp and N. Allen in our lab), non-integrated iPS cells and reduced L-glutamate concentration in the medium. Improved survival was observed across all HD lines. Further, the addition of both GABA and increased Ca^{2+} concentration was tested in the medium as a method for accelerating functional maturation. Using GABA and Ca^{2+} medium, more cells were obseved with functional Ca^{2+} currents, induced action potentials, more mature shaped action potentials, more spontaneous activity and hyperpolarised resting membrane potentials. Contrary to the notion that GABA elicits Ca^{2+} dependant apoptosis in the HD cells, no appreciable loss of survivability was observed in the high repeat lines with the addition of GABA and Ca^{2+}. Also surprisingly, the Q109 line showed no lack of survival compared to the lower repeat lines. Therefore, this high rate of cell death is either specific to the Q180 line in these media or there is an appreciable increase in the severity of phenotype between 109 and 180 CAG repeats.

Most importantly, the new protocol with the GABA and Ca^{2+} resulted in both the greatest consistency and functional maturity across all 4 lines at week 2. This is an important

consideration in developing an iPS cell-derived model for Huntington's disease. Previous studies either haven't sufficiently investigated the functional maturity of iPS-cell derived HD models, or use differentiated cultures which show very different functional development [8,29,217,218]. This presents a challenge in interpreting the results of experiments performed on iPS-cell derived HD models. For example, with a lack of functional maturity might not yield results which are consistent with *in vivo,* and using a model where the control and disease lines exhibit different levels of functional maturity would only add to this problem.

Conclusions

In these experiments it was observed that increased Ca^{2+} influx due to increased driving force for Ca^{2+} across the membrane or increased stimulation by GABA accelerated and enhanced the development of a neuronal phenotype. Further, the development of spontaneous action potentials was found to be dependent on: functional N- type Ca^{2+} channels evoke release of GABA vesicles; $GABA_A$ channels to initiate depolarisation in response to GABA, and; L- or R- type Ca^{2+} channels to provide depolarisation dependant Ca^{2+} influxes and evoke non-electrophysiological responses to intracellular Ca^{2+}. These findings were reproducible in the ACM and high Ca^{2+} medium, which implies that increased functional Ca^{2+} channel expression and increased functional $GABA_A$ expression, elicited by treatment with ACM, acts to amplify GABA evoked depolarisation-dependant Ca^{2+} rises in a similar to increased medium Ca^{2+} concentration in the medium. Astrocyte secreted factors drive the functional expression of $GABA_A$ and specific Ca^{2+} channel subtypes, and it seems very likely that this acts to amplify an intrinsic activity dependant mechanism for functional maturation and survival in neurons. Given that ACM treated cells continue to show increased functional maturity beyond week 2 implies this is only part of the influence provided by ACM. Indeed, in the absence of ACM it is only possible for the above mentioned activity dependant mechanism to function whilst GABA remains an excitatory neurotransmitter. Therefore, it seems plausible that ACM provides another source for continued depolarisation, perhaps rhythmic action potentials due to biphasic resting membrane potentials and more functional synapses, both observed in the ACM-treated cultures. Additionally, it should also be noted that as well as providing an increased activity-

dependant stimulus for functional maturity, ACM could provide increased activity-dependant mechanism for neuronal survival. Therefore an alternative explanation for the functional disparity between ACM, control and high Ca^{2+} treated neurons at week 3 could be that in the presence of ACM more mature neurons are protected from apoptosis which means they become enriched in week 3.

In conclusion, ACM is a powerful means to improving the functional quality of iPS derived neurons, enhancing their accuracy as a model for neurodegenerative diseases. Further, ACM has the capacity to enhance activity-dependant pro-synaptogenic and pro-survival mechanisms and that these are GABA dependant in the early stages of neurogenesis. But, no defined cocktail of astrocyte secreted factors has yet been able to entirely recapitulate these effects, and therefore ACM remains an undefined protocol. This makes manipulating Ca^{2+} concentration, GABA and Bay-K 8644 an attractive option for accelerating functional maturation.

Further, this study demonstrates that GABA and increased Ca^{2+} can be used as a defined addition to existing differentiation protocols. Crucially these additions were able to produce more consistent and mature neurons across different HD lines within only 2 weeks of terminal differentiation. Using this simple protocol, cultures of neurons were generated from multiple HD lines at the same time-point which were mostly able to fire induced action potentials, showed significant rates of spontaneous activity and hyperpolarised membrane potentials. Using both small molecules to synchronise neurogenesis, removing progenitor cell populations and directly stimulating activity-dependant maturation with GABA and Ca^{2+} provides the best current protocol for consistency and maturity of differentiated neurons, without the disadvantages of using an undefined medium such as ACM.

References:

1. Aguado, F., Díaz-Ruiz, C., Parlato, R., Martínez, A., Carmona, M. A., Bleckmann, S., Ureña, J. M., Burgaya, F., del Río, J. A., Schütz, G. & Soriano, E. The CREB/CREM transcription factors negatively regulate early synaptogenesis and spontaneous network activity. *J. Neurosci.* **29,** 328–33 (2009).

2. Ambrosini, A., Bresciani, L., Fracchia, S., Brunello, N. & Racagni, G. Metabotropic glutamate receptors negatively coupled to adenylate cyclase inhibit N-methyl-D-aspartate receptor activity and prevent neurotoxicity in mesencephalic neurons in vitro. *Mol. Pharmacol.* **47,** 1057–1064 (1995).

3. Amenduni, M., De Filippis, R., Cheung, A. Y. L., Disciglio, V., Epistolato, M. C., Ariani, F., Mari, F., Mencarelli, M. A., Hayek, Y., Renieri, A., Ellis, J. & Meloni, I. iPS cells to model CDKL5-related disorders. *Eur. J. Hum. Genet.* **19,** 1246–55 (2011).

4. Andrew, S. E., Goldberg, Y. P., Kremer, B., Telenius, H., Theilmann, J., Adam, S., Starr, E., Squitieri, F., Lin, B. & Kalchman, M. A. The relationship between trinucleotide (CAG) repeat length and clinical features of Huntington's disease. *Nat. Genet.* **4,** 398–403 (1993).

5. Araque, A., Carmignoto, G. & Haydon, P. G. Dynamic signaling between astrocytes and neurons. *Annu. Rev. Physiol.* **63,** 795–813 (2001).

6. Asano, H., Aonuma, M., Sanosaka, T., Kohyama, J., Namihira, M. & Nakashima, K. Astrocyte differentiation of neural precursor cells is enhanced by retinoic acid through a change in epigenetic modification. *Stem Cells* **27,** 2744–52 (2009).

7. Astori, S., Wimmer, R. D., Prosser, H. M., Corti, C., Corsi, M., Liaudet, N., Volterra, A., Franken, P., Adelman, J. P. & Lüthi, A. The Ca(V)3.3 calcium channel is the major sleep spindle pacemaker in thalamus. *Proc. Natl. Acad. Sci. U. S. A.* **108,** 13823–8 (2011).

8. Aubry, L., Bugi, A., Lefort, N., Rousseau, F., Peschanski, M. & Perrier, A. L. Striatal progenitors derived from human ES cells mature into DARPP32 neurons in vitro and in quinolinic acid-lesioned rats. *Proc. Natl. Acad. Sci. U. S. A.* **105,** 16707–12 (2008).

9. Barad, M., Bourtchouladze, R., Winder, D. G., Golan, H. & Kandel, E. Rolipram, a type IV-specific phosphodiesterase inhibitor, facilitates the establishment of long-lasting long-term potentiation and improves memory. *Proc. Natl. Acad. Sci.* **95,** 15020–15025 (1998).

10. Bar-Nur, O., Russ, H. A., Efrat, S. & Benvenisty, N. Epigenetic memory and preferential lineage-specific differentiation in induced pluripotent stem cells derived from human pancreatic islet beta cells. *Cell Stem Cell* **9,** 17–23 (2011).

11. Bekkers, J. M. & Stevens, C. F. NMDA and non-NMDA receptors are co-localized at individual excitatory synapses in cultured rat hippocampus. *Nature* **341,** 230–3 (1989).

12. Ben-Ari, Y. Excitatory actions of gaba during development: the nature of the nurture. *Nat. Rev. Neurosci.* **3,** 728–39 (2002).

13. Berninger, B., Marty, S., Zafra, F., da Penha Berzaghi, M., Thoenen, H. & Lindholm, D. GABAergic stimulation switches from enhancing to repressing BDNF expression in rat hippocampal neurons during maturation in vitro. *Development* **121,** 2327–35 (1995).

14. Berninger, B., Marty, S., Zafra, F., Penha Berzaghi, M., Thoenen, H. & Lindholm, D. GABAergic stimulation switches from enhancing to repressing BDNF expression in rat hippocampal neurons during maturation in vitro. *Development* **121,** 2327–35 (1995).

15. Berridge, M. J., Bootman, M. D. & Roderick, H. L. Calcium signalling: dynamics, homeostasis and remodelling. *Nat. Rev. Mol. Cell Biol.* **4,** 517–29 (2003).

16. Bezprozvanny, I., Scheller, R. H. & Tsien, R. W. Functional impact of syntaxin on gating of N-type and Q-type calcium channels. *Nature* **378,** 623–6 (1995).

17. Biella, G., Di Febo, F., Goffredo, D., Moiana, a, Taglietti, V., Conti, L., Cattaneo, E. & Toselli, M. Differentiating embryonic stem-derived neural stem cells show a maturation-dependent pattern of voltage-gated sodium current expression and graded action potentials. *Neuroscience* **149,** 38–52 (2007).

18. Bito, H., Deisseroth, K. & Tsien, R. W. CREB Phosphorylation and Dephosphorylation: A Ca2+- and Stimulus Duration–Dependent Switch for Hippocampal Gene Expression. *Cell* **87,** 1203–1214 (1996).

19. Bonaguidi, M. A., McGuire, T., Hu, M., Kan, L., Samanta, J. & Kessler, J. A. LIF and BMP signaling generate separate and discrete types of GFAP-expressing cells. *Development* **132,** 5503–14 (2005).

20. Borghese, L., Dolezalova, D., Opitz, T., Haupt, S., Leinhaas, A., Steinfarz, B., Koch, P., Edenhofer, F., Hampl, A. & Brüstle, O. Inhibition of notch signaling in human embryonic stem cell-derived neural stem cells delays G1/S phase transition and accelerates neuronal differentiation in vitro and in vivo. *Stem Cells* **28,** 955–64 (2010).

21. Boulanger, L. M., Boulanger, L. & Poo, M. M. Presynaptic depolarization facilitates neurotrophin-induced synaptic potentiation. *Nat. Neurosci.* **2,** 346–51 (1999).

22. Brennand, K. J., Simone, A., Jou, J., Gelboin-Burkhart, C., Tran, N., Sangar, S., Li, Y., Mu, Y., Chen, G., Yu, D., McCarthy, S., Sebat, J. & Gage, F. H. Modelling schizophrenia using human induced pluripotent stem cells. *Nature* **473,** 221–5 (2011).

23. Buffo, A., Rolando, C. & Ceruti, S. Astrocytes in the damaged brain: molecular and cellular insights into their reactive response and healing potential. *Biochem. Pharmacol.* **79,** 77–89 (2010).

24. Burkhardt, M. F., Martinez, F. J., Wright, S., Ramos, C., Volfson, D., Mason, M., Garnes, J., Dang, V., Lievers, J., Shoukat-Mumtaz, U., Martinez, R., Gai, H., Blake, R., Vaisberg, E., Grskovic, M., Johnson, C., Irion, S., Bright, J., Cooper, B., Nguyen, L., Griswold-Prenner, I. & Javaherian, A. A cellular model for sporadic ALS using patient-derived induced pluripotent stem cells. *Mol. Cell. Neurosci.* **56,** 355–64 (2013).

25. Byers, B., Lee, H. & Reijo Pera, R. Modeling Parkinson's disease using induced pluripotent stem cells. *Curr. Neurol. Neurosci. Rep.* **12,** 237–42 (2012).

26. Caldwell, J. H., Schaller, K. L., Lasher, R. S., Peles, E. & Levinson, S. R. Sodium channel Na(v)1.6 is localized at nodes of ranvier, dendrites, and synapses. *Proc. Natl. Acad. Sci. U. S. A.* **97,** 5616–20 (2000).

27. Campbell, K. H., McWhir, J., Ritchie, W. A. & Wilmut, I. Sheep cloned by nuclear transfer from a cultured cell line. *Nature* **380,** 64–6 (1996).

28. Carlezon, W. A., Duman, R. S. & Nestler, E. J. The many faces of CREB. *Trends Neurosci.* **28,** 436–45 (2005).

29. Carri, A. D., Onorati, M., Lelos, M. J., Castiglioni, V., Faedo, A., Menon, R., Camnasio, S., Vuono, R., Spaiardi, P., Talpo, F., Toselli, M., Martino, G., Barker, R. A., Dunnett, S. B., Biella, G. & Cattaneo, E. Developmentally coordinated extrinsic signals drive human pluripotent stem cell differentiation toward authentic DARPP-32+ medium-sized spiny neurons. *Development* **140,** 301–312 (2012).

30. Chambers, S. M., Fasano, C. A., Papapetrou, E. P., Tomishima, M., Sadelain, M. & Studer, L. Highly efficient neural conversion of human ES and iPS cells by dual inhibition of SMAD signaling. *Nat. Biotechnol.* **27,** 275–80 (2009).

31. Chang, M.-Y., Son, H., Lee, Y.-S. & Lee, S.-H. Neurons and astrocytes secrete factors that cause stem cells to differentiate into neurons and astrocytes, respectively. *Mol. Cell. Neurosci.* **23,** 414–26 (2003).

32. Chartoff, E. H., Papadopoulou, M., Konradi, C. & Carlezon, W. A. Dopamine-dependent increases in phosphorylation of cAMP response element binding protein (CREB) during precipitated morphine withdrawal in primary cultures of rat striatum. *J. Neurochem.* **87,** 107–18 (2003).

33. Charvin, N. Interaction of SNARE Complexes with P/Q-type Calcium Channels in Rat Cerebellar Synaptosomes. *J. Biol. Chem.* **271,** 6567–6570 (1996).

34. Chen, S., Guttridge, D. C., You, Z., Zhang, Z., Fribley, A., Mayo, M. W., Kitajewski, J. & Wang, C. Y. Wnt-1 signaling inhibits apoptosis by activating beta-catenin/T cell factor-mediated transcription. *J. Cell Biol.* **152,** 87–96 (2001).

35. Chen, S., Guttridge, D. C., You, Z., Zhang, Z., Fribley, A., Mayo, M. W., Kitajewski, J. & Wang, C. Y. Wnt-1 signaling inhibits apoptosis by activating beta-catenin/T cell factor-mediated transcription. *J. Cell Biol.* **152,** 87–96 (2001).

36. Chenn, A. A top-NOTCH way to make astrocytes. *Dev. Cell* **16,** 158–9 (2009).

37. Choi, S. H., Li, Y., Parada, L. F. & Sisodia, S. S. Regulation of hippocampal progenitor cell survival, proliferation and dendritic development by BDNF. *Mol. Neurodegener.* **4,** 52 (2009).

38. Chou, B.-K., Mali, P., Huang, X., Ye, Z., Dowey, S. N., Resar, L. M., Zou, C., Zhang, Y. A., Tong, J. & Cheng, L. Efficient human iPS cell derivation by a non-integrating plasmid from blood cells with unique epigenetic and gene expression signatures. *Cell Res.* **21,** 518–29 (2011).

39. Chou, S.-Y., Weng, J.-Y., Lai, H.-L., Liao, F., Sun, S. H., Tu, P.-H., Dickson, D. W. & Chern, Y. Expanded-polyglutamine huntingtin protein suppresses the secretion and production of a chemokine (CCL5/RANTES) by astrocytes. *J. Neurosci.* **28,** 3277–90 (2008).

40. Christopherson, K. S., Ullian, E. M., Stokes, C. C. A., Mullowney, C. E., Hell, J. W., Agah, A., Lawler, J., Mosher, D. F., Bornstein, P. & Barres, B. A. Thrombospondins are astrocyte-secreted proteins that promote CNS synaptogenesis. *Cell* **120,** 421–33 (2005).

41. Chu, Z. & Hablitz, J. J. Quisqualate induces an inward current via mGluR activation in neocortical pyramidal neurons. *Brain Res.* **879,** 88–92 (2000).

42. Cooper, D. M., Mons, N. & Karpen, J. W. Adenylyl cyclases and the interaction between calcium and cAMP signalling. *Nature* **374,** 421–4 (1995).

43. Cueni, L., Canepari, M., Luján, R., Emmenegger, Y., Watanabe, M., Bond, C. T., Franken, P., Adelman, J. P. & Lüthi, A. T-type Ca2+ channels, SK2 channels and SERCAs gate sleep-related oscillations in thalamic dendrites. *Nat. Neurosci.* **11,** 683–92 (2008).

44. Cui, W., Allen, N. D., Skynner, M., Gusterson, B. & Clark, A. J. Inducible ablation of astrocytes shows that these cells are required for neuronal survival in the adult brain. *Glia* **34,** 272–82 (2001).

45. D'Ascenzo, M., Piacentini, R., Casalbore, P., Budoni, M., Pallini, R., Azzena, G. B. & Grassi, C. Role of L-type Ca2+ channels in neural stem/progenitor cell differentiation. *Eur. J. Neurosci.* **23,** 935–44 (2006).

46. Daniel, P. B., Walker, W. H. & Habener, J. F. Cyclic AMP signaling and gene regulation. *Annu. Rev. Nutr.* **18,** 353–83 (1998).

47. Dash, P. K., Karl, K. A., Colicos, M. A., Prywes, R. & Kandel, E. R. cAMP response element-binding protein is activated by Ca2+/calmodulin- as well as cAMP-dependent protein kinase. *Proc. Natl. Acad. Sci.* **88,** 5061–5065 (1991).

48. Dash, P. K., Karl, K. A., Colicos, M. A., Prywes, R. & Kandel, E. R. cAMP response element-binding protein is activated by Ca2+/calmodulin- as well as cAMP-dependent protein kinase. *Proc. Natl. Acad. Sci.* **88,** 5061–5065 (1991).

49. DEISSEROTH, K., BITO, H. & TSIEN, R. Signaling from Synapse to Nucleus: Postsynaptic CREB Phosphorylation during Multiple Forms of Hippocampal Synaptic Plasticity. *Neuron* **16,** 89–101 (1996).

50. Deisseroth, K., Heist, E. K. & Tsien, R. W. Translocation of calmodulin to the nucleus supports CREB phosphorylation in hippocampal neurons. *Nature* **392,** 198–202 (1998).

51. Deisseroth, K., Singla, S., Toda, H., Monje, M., Palmer, T. D. & Malenka, R. C. Excitation-neurogenesis coupling in adult neural stem/progenitor cells. *Neuron* **42,** 535–52 (2004).

52. Du, K. & Montminy, M. CREB is a regulatory target for the protein kinase Akt/PKB. *J. Biol. Chem.* **273,** 32377–9 (1998).

53. Dudman, J. T., Eaton, M. E., Rajadhyaksha, A., Macías, W., Taher, M., Barczak, A., Kameyama, K., Huganir, R. & Konradi, C. Dopamine D1 receptors mediate CREB phosphorylation via phosphorylation of the NMDA receptor at Ser897-NR1. *J. Neurochem.* **87,** 922–34 (2003).

54. Dunnett, A. B. and S. B., Surmeier, D. J., Ding, J., Day, M., Wang, Z. & Shen, W. D1 and D2 dopamine-receptor modulation of striatal glutamatergic signaling in striatal medium spiny neurons. *Trends Neurosci.* **30,** 228–235 (2007).

55. Dworkin, S. & Mantamadiotis, T. Targeting CREB signalling in neurogenesis. *Expert Opin. Ther. Targets* **14,** 869–79 (2010).

56. Ebert, A. D., Shelley, B. C., Hurley, A. M., Onorati, M., Castiglioni, V., Patitucci, T. N., Svendsen, S. P., Mattis, V. B., McGivern, J. V., Schwab, A. J., Sareen, D., Kim, H. W., Cattaneo, E. & Svendsen, C. N. EZ spheres: A stable and expandable culture system for the generation of pre-rosette multipotent stem cells from human ESCs and iPSCs. *Stem Cell Res.* **10,** 417–427 (2013).

57. Ebert, A. D., Yu, J., Rose, F. F., Mattis, V. B., Lorson, C. L., Thomson, J. A. & Svendsen, C. N. Induced pluripotent stem cells from a spinal muscular atrophy patient. *Nature* **457,** 277–80 (2009).

58. Elmariah, S. B., Oh, E. J., Hughes, E. G. & Balice-Gordon, R. J. Astrocytes regulate inhibitory synapse formation via Trk-mediated modulation of postsynaptic GABAA receptors. *J. Neurosci.* **25,** 3638–50 (2005).

59. Endoh, T. Characterization of modulatory effects of postsynaptic metabotropic glutamate receptors on calcium currents in rat nucleus tractus solitarius. *Brain Res.* **1024,** 212–224 (2004).

60. Fabrizio Gabbiani and Steven J. Cox. Mathematics for Neuroscientists - 9780123748829|ScienceDirect.com. at <http://www.sciencedirect.com/science/book/9780123748829>

61. Faideau, M., Kim, J., Cormier, K., Gilmore, R., Welch, M., Auregan, G., Dufour, N., Guillermier, M., Brouillet, E., Hantraye, P., Déglon, N., Ferrante, R. J. & Bonvento, G. In vivo expression of polyglutamine-expanded huntingtin by mouse striatal astrocytes impairs glutamate transport: a correlation with Huntington's disease subjects. *Hum. Mol. Genet.* **19,** 3053–67 (2010).

62. Fan, G., Martinowich, K., Chin, M. H., He, F., Fouse, S. D., Hutnick, L., Hattori, D., Ge, W., Shen, Y., Wu, H., ten Hoeve, J., Shuai, K. & Sun, Y. E. DNA methylation controls the timing of astrogliogenesis through regulation of JAK-STAT signaling. *Development* **132,** 3345–56 (2005).

63. Fellin, T., Pascual, O., Gobbo, S., Pozzan, T., Haydon, P. G. & Carmignoto, G. Neuronal synchrony mediated by astrocytic glutamate through activation of extrasynaptic NMDA receptors. *Neuron* **43,** 729–43 (2004).

64. Ferrer, I., Goutan, E., Marín, C., Rey, M. . & Ribalta, T. Brain-derived neurotrophic factor in Huntington disease. *Brain Res.* **866,** 257–261 (2000).

65. Forsythe, I. D. & Westbrook, G. L. Slow excitatory postsynaptic currents mediated by N-methyl-D-aspartate receptors on cultured mouse central neurones. *J. Physiol.* **396,** 515–533 (1988).

66. Galli, C., Meucci, O., Scorziello, A., Werge, T., Calissano, P. & Schettini, G. Apoptosis in cerebellar granule cells is blocked by high KCl, forskolin, and IGF-1 through distinct mechanisms of action: the involvement of intracellular calcium and RNA synthesis. *J. Neurosci.* **15,** 1172–1179 (1995).

67. Ganguly, K., Schinder, A. F., Wong, S. T. & Poo, M. GABA Itself Promotes the Developmental Switch of Neuronal GABAergic Responses from Excitation to Inhibition. *Cell* **105,** 521–532 (2001).

68. Ge, S., Goh, E. L. K., Sailor, K. A., Kitabatake, Y., Ming, G. & Song, H. GABA regulates synaptic integration of newly generated neurons in the adult brain. *Nature* **439,** 589–93 (2006).

69. Genoud, C., Knott, G. W., Sakata, K., Lu, B. & Welker, E. Altered synapse formation in the adult somatosensory cortex of brain-derived neurotrophic factor heterozygote mice. *J. Neurosci.* **24,** 2394–400 (2004).

70. Genoud, C., Knott, G. W., Sakata, K., Lu, B. & Welker, E. Altered synapse formation in the adult somatosensory cortex of brain-derived neurotrophic factor heterozygote mice. *J. Neurosci.* **24,** 2394–400 (2004).

71. Ghosh, A., Carnahan, J. & Greenberg, M. E. Requirement for BDNF in activity-dependent survival of cortical neurons. *Science* **263,** 1618–23 (1994).

72. Giachino, C., De Marchis, S., Giampietro, C., Parlato, R., Perroteau, I., Schütz, G., Fasolo, A. & Peretto, P. cAMP response element-binding protein regulates differentiation and survival of newborn neurons in the olfactory bulb. *J. Neurosci.* **25,** 10105–18 (2005).

73. Giulian, D., Vaca, K. & Corpuz, M. Brain glia release factors with opposing actions upon neuronal survival. *J. Neurosci.* **13,** 29–37 (1993).

74. Gonzalez, G. A. & Montminy, M. R. Cyclic AMP stimulates somatostatin gene transcription by phosphorylation of CREB at serine 133. *Cell* **59,** 675–680 (1989).

75. Gonzalez, G. A., Yamamoto, K. K., Fischer, W. H., Karr, D., Menzel, P., Biggs, W., Vale, W. W. & Montminy, M. R. A cluster of phosphorylation sites on the cyclic AMP-regulated nuclear factor CREB predicted by its sequence. *Nature* **337,** 749–52 (1989).

76. Hama, H., Hara, C., Yamaguchi, K. & Miyawaki, A. PKC Signaling Mediates Global Enhancement of Excitatory Synaptogenesis in Neurons Triggered by Local Contact with Astrocytes. *Neuron* **41,** 405–415 (2004).

77. Hanoune, J. & Defer, N. Regulation and role of adenylyl cyclase isoforms. *Annu. Rev. Pharmacol. Toxicol.* **41,** 145–74 (2001).

78. Hardingham, G. E., Fukunaga, Y. & Bading, H. Extrasynaptic NMDARs oppose synaptic NMDARs by triggering CREB shut-off and cell death pathways. *Nat. Neurosci.* **5,** 405–14 (2002).

79. Harjes, P. & Wanker, E. E. The hunt for huntingtin function: interaction partners tell many different stories. *Trends Biochem. Sci.* **28,** 425–33 (2003).

80. Herold, S., Jagasia, R., Merz, K., Wassmer, K. & Lie, D. C. CREB signalling regulates early survival, neuronal gene expression and morphological development in adult subventricular zone neurogenesis. *Mol. Cell. Neurosci.* **46,** 79–88 (2011).

81. Hill, B. Ion Channels of Excitable Membranes. at <http://www.sinauer.com/ion-channels-of-excitable-membranes.html>

82. Holtmaat, A., Wilbrecht, L., Knott, G. W., Welker, E. & Svoboda, K. Experience-dependent and cell-type-specific spine growth in the neocortex. *Nature* **441,** 979–83 (2006).

83. Hwang, W. S., Roh, S. Il, Lee, B. C., Kang, S. K., Kwon, D. K., Kim, S., Kim, S. J., Park, S. W., Kwon, H. S., Lee, C. K., Lee, J. B., Kim, J. M., Ahn, C., Paek, S. H., Chang, S. S., Koo, J. J., Yoon, H. S., Hwang, J. H., Hwang, Y. Y., Park, Y. S., Oh, S. K., Kim, H. S., Park, J. H., Moon, S. Y. & Schatten, G. Patient-specific embryonic stem cells derived from human SCNT blastocysts. *Science* **308,** 1777–83 (2005).

84. Inoue, H. & Yamanaka, S. The use of induced pluripotent stem cells in drug development. *Clin. Pharmacol. Ther.* **89,** 655–61 (2011).

85. Ishikawa, T., Kaneko, M., Shin, H.-S. & Takahashi, T. Presynaptic N-type and P/Q-type Ca2+ channels mediating synaptic transmission at the calyx of Held of mice. *J. Physiol.* **568,** 199–209 (2005).

86. Jagasia, R., Steib, K., Englberger, E., Herold, S., Faus-Kessler, T., Saxe, M., Gage, F. H., Song, H. & Lie, D. C. GABA-cAMP response element-binding protein signaling regulates maturation and survival of newly generated neurons in the adult hippocampus. *J. Neurosci.* **29,** 7966–77 (2009).

87. Jakel, R. J., Schneider, B. L. & Svendsen, C. N. Using human neural stem cells to model neurological disease. *Nat. Rev. Genet.* **5,** 136–44 (2004).

88. Jelitai, M. & Madarasz, E. The role of GABA in the early neuronal development. *Int. Rev. Neurobiol.* **71,** 27–62 (2005).

89. Ji, Y., Lu, Y., Yang, F., Shen, W., Tang, T. T.-T., Feng, L., Duan, S. & Lu, B. Acute and gradual increases in BDNF concentration elicit distinct signaling and functions in neurons. *Nat. Neurosci.* **13,** 302–9 (2010).

90. Ji, Y., Pang, P. T., Feng, L. & Lu, B. Cyclic AMP controls BDNF-induced TrkB phosphorylation and dendritic spine formation in mature hippocampal neurons. *Nat. Neurosci.* **8,** 164–72 (2005).

91. Johnson, M. A., Weick, J. P., Pearce, R. A. & Zhang, S.-C. Functional neural development from human embryonic stem cells: accelerated synaptic activity via astrocyte coculture. *J. Neurosci.* **27,** 3069–77 (2007).

92. Kampa, B. M., Clements, J., Jonas, P. & Stuart, G. J. Kinetics of Mg2+ unblock of NMDA receptors: implications for spike-timing dependent synaptic plasticity. *J. Physiol.* **556,** 337–45 (2004).

93. Kaupmann, K., Malitschek, B., Schuler, V., Heid, J., Froestl, W., Beck, P., Mosbacher, J., Bischoff, S., Kulik, A., Shigemoto, R., Karschin, A. & Bettler, B. GABA(B)-receptor subtypes assemble into functional heteromeric complexes. *Nature* **396,** 683–7 (1998).

94. Klempin, F., Babu, H., De Pietri Tonelli, D., Alarcon, E., Fabel, K. & Kempermann, G. Oppositional effects of serotonin receptors 5-HT1a, 2, and 2c in the regulation of adult hippocampal neurogenesis. *Front. Mol. Neurosci.* **3,** (2010).

95. Knott, G. W., Quairiaux, C., Genoud, C. & Welker, E. Formation of dendritic spines with GABAergic synapses induced by whisker stimulation in adult mice. *Neuron* **34,** 265–73 (2002).

96. Koblar, S. A., Turnley, A. M., Classon, B. J., Reid, K. L., Ware, C. B., Cheema, S. S., Murphy, M. & Bartlett, P. F. Neural precursor differentiation into astrocytes requires signaling through the leukemia inhibitory factor receptor. *Proc. Natl. Acad. Sci.* **95,** 3178–3181 (1998).

97. Kondo, T., Asai, M., Tsukita, K., Kutoku, Y., Ohsawa, Y., Sunada, Y., Imamura, K., Egawa, N., Yahata, N., Okita, K., Takahashi, K., Asaka, I., Aoi, T., Watanabe, A., Watanabe, K., Kadoya, C., Nakano, R., Watanabe, D., Maruyama, K., Hori, O., Hibino, S., Choshi, T., Nakahata, T., Hioki, H., Kaneko, T., Naitoh, M., Yoshikawa, K., Yamawaki, S., Suzuki, S., Hata, R., Ueno, S.-I., Seki, T., Kobayashi, K., Toda, T., Murakami, K., Irie, K., Klein, W. L., Mori, H., Asada, T., Takahashi, R., Iwata, N., Yamanaka, S. & Inoue, H. Modeling Alzheimer's disease with iPSCs reveals stress phenotypes associated with intracellular Aβ and differential drug responsiveness. *Cell Stem Cell* **12,** 487–96 (2013).

98. Koós, T. & Tepper, J. M. Dual cholinergic control of fast-spiking interneurons in the neostriatum. *J. Neurosci.* **22,** 529–35 (2002).

99. Kornhauser, J. M., Cowan, C. W., Shaywitz, A. J., Dolmetsch, R. E., Griffith, E. C., Hu, L. S., Haddad, C., Xia, Z. & Greenberg, M. E. CREB Transcriptional Activity in Neurons Is Regulated by Multiple, Calcium-Specific Phosphorylation Events. *Neuron* **34,** 221–233 (2002).

100. Kraev, I. V, Godukhin, O. V, Patrushev, I. V, Davies, H. A., Popov, V. I. & Stewart, M. G. Partial kindling induces neurogenesis, activates astrocytes and alters synaptic morphology in the dentate gyrus of freely moving adult rats. *Neuroscience* **162,** 254–67 (2009).

101. Kreitzer, A. C. Physiology and pharmacology of striatal neurons. *Annu. Rev. Neurosci.* **32,** 127–47 (2009).

102. Krishnan, V., Graham, A., Mazei-Robison, M. S., Lagace, D. C., Kim, K.-S., Birnbaum, S., Eisch, A. J., Han, P.-L., Storm, D. R., Zachariou, V. & Nestler, E. J. Calcium-sensitive adenylyl cyclases in depression and anxiety: behavioral and biochemical consequences of isoform targeting. *Biol. Psychiatry* **64,** 336–43 (2008).

103. Kubo, T., Nonomura, T., Enokido, Y. & Hatanaka, H. Brain-derived neurotrophic factor (BDNF) can prevent apoptosis of rat cerebellar granule neurons in culture. *Brain Res. Dev. Brain Res.* **85,** 249–58 (1995).

104. Kubo, T., Nonomura, T., Enokido, Y. & Hatanaka, H. Brain-derived neurotrophic factor (BDNF) can prevent apoptosis of rat cerebellar granule neurons in culture. *Brain Res. Dev. Brain Res.* **85,** 249–58 (1995).

105. Kusama, T., Spivak, C. E., Whiting, P., Dawson, V. L., Schaeffer, J. C. & Uhl, G. R. Pharmacology of GABA rho 1 and GABA alpha/beta receptors expressed in Xenopus oocytes and COS cells. *Br. J. Pharmacol.* **109,** 200–6 (1993).

106. Lange, C., Mix, E., Frahm, J., Glass, A., Müller, J., Schmitt, O., Schmöle, A.-C., Klemm, K., Ortinau, S., Hübner, R., Frech, M. J., Wree, A. & Rolfs, A. Small molecule GSK-3 inhibitors increase neurogenesis of human neural progenitor cells. *Neurosci. Lett.* **488,** 36–40 (2011).

107. Laube, B., Hirai, H., Sturgess, M., Betz, H. & Kuhse, J. Molecular Determinants of Agonist Discrimination by NMDA Receptor Subunits: Analysis of the Glutamate Binding Site on the NR2B Subunit. *Neuron* **18,** 493–503 (1997).

108. Lee, G., Papapetrou, E. P., Kim, H., Chambers, S. M., Tomishima, M. J., Fasano, C. A., Ganat, Y. M., Menon, J., Shimizu, F., Viale, A., Tabar, V., Sadelain, M. & Studer, L. Modelling pathogenesis and treatment of familial dysautonomia using patient-specific iPSCs. *Nature* **461,** 402–6 (2009).

109. Lee, W., Reyes, R. C., Gottipati, M. K., Lewis, K., Lesort, M., Parpura, V. & Gray, M. Enhanced Ca(2+)-dependent glutamate release from astrocytes of the BACHD Huntington's disease mouse model. *Neurobiol. Dis.* **58,** 192–9 (2013).

110. Li, Q., Lau, A., Morris, T. J., Guo, L., Fordyce, C. B. & Stanley, E. F. A syntaxin 1, Galpha(o), and N-type calcium channel complex at a presynaptic nerve terminal: analysis by quantitative immunocolocalization. *J. Neurosci.* **24,** 4070–81 (2004).

111. Li, S.-H. & Li, X.-J. Huntingtin-protein interactions and the pathogenesis of Huntington's disease. *Trends Genet.* **20,** 146–54 (2004).

112. Lie, D.-C., Colamarino, S. A., Song, H.-J., Désiré, L., Mira, H., Consiglio, A., Lein, E. S., Jessberger, S., Lansford, H., Dearie, A. R. & Gage, F. H. Wnt signalling regulates adult hippocampal neurogenesis. *Nature* **437,** 1370–5 (2005).

113. Liévens, J. C., Woodman, B., Mahal, A., Spasic-Boscovic, O., Samuel, D., Kerkerian-Le Goff, L. & Bates, G. P. Impaired glutamate uptake in the R6 Huntington's disease transgenic mice. *Neurobiol. Dis.* **8,** 807–21 (2001).

114. Lindholm, D., Castrén, E., Berzaghi, M., Blöchl, A. & Thoenen, H. Activity-dependent and hormonal regulation of neurotrophin mRNA levels in the brain--implications for neuronal plasticity. *J. Neurobiol.* **25,** 1362–72 (1994).

115. Lindskog, M., Svenningsson, P., Fredholm, B. B., Greengard, P. & Fisone, G. Activation of dopamine D2 receptors decreases DARPP-32 phosphorylation in striatonigral and striatopallidal projection neurons via different mechanisms. *Neuroscience* **88,** 1005–8 (1999).

116. Lipscombe, D., Helton, T. D. & Xu, W. L-type calcium channels: the low down. *J. Neurophysiol.* **92,** 2633–41 (2004).

117. Lister, R., Pelizzola, M., Kida, Y. S., Hawkins, R. D., Nery, J. R., Hon, G., Antosiewicz-Bourget, J., O'Malley, R., Castanon, R., Klugman, S., Downes, M., Yu, R., Stewart, R., Ren, B., Thomson, J. A., Evans, R. M. & Ecker, J. R. Hotspots of aberrant epigenomic reprogramming in human induced pluripotent stem cells. *Nature* **471,** 68–73 (2011).

118. Maragakis, N. J. & Rothstein, J. D. Mechanisms of Disease: astrocytes in neurodegenerative disease. *Nat. Clin. Pract. Neurol.* **2,** 679–89 (2006).

119. Marchetto, M. C. N., Carromeu, C., Acab, A., Yu, D., Yeo, G. W., Mu, Y., Chen, G., Gage, F. H. & Muotri, A. R. A model for neural development and treatment of Rett syndrome using human induced pluripotent stem cells. *Cell* **143,** 527–39 (2010).

120. Marshall, J., Dolan, B. M., Garcia, E. P., Sathe, S., Tang, X., Mao, Z. & Blair, L. A. C. Calcium Channel and NMDA Receptor Activities Differentially Regulate Nuclear C/EBPβ Levels to Control Neuronal Survival. *Neuron* **39,** 625–639 (2003).

121. Matsuoka, I., Suzuki, Y., Defer, N., Nakanishi, H. & Hanoune, J. Differential Expression of Type I, II, and V Adenylyl Cyclase Gene in the Postnatal Developing Rat Brain. *J. Neurochem.* **68,** 498–506 (2002).

122. Mayer, M., Bhakoo, K. & Noble, M. Ciliary neurotrophic factor and leukemia inhibitory factor promote the generation, maturation and survival of oligodendrocytes in vitro. *Development* **120,** 143–153 (1994).

123. Mayer, M. L., Westbrook, G. L. & Guthrie, P. B. Voltage-dependent block by Mg2+ of NMDA responses in spinal cord neurones. *Nature* **309,** 261–263 (1984).

124. Mayr, B. & Montminy, M. Transcriptional regulation by the phosphorylation-dependent factor CREB. *Nat. Rev. Mol. Cell Biol.* **2,** 599–609 (2001).

125. Meldrum, B. & Garthwaite, J. Excitatory amino acid neurotoxicity and neurodegenerative disease. *Trends Pharmacol. Sci.* **11,** 379–87 (1990).

126. MELE, T., CARMAN-KRZAN, M. & DAMIJANA MOJCA, J. Regulatory role of monoamine neurotransmitters in astrocytic NT-3 synthesis. *Int. J. Dev. Neurosci.* **28,** 13–19

127. Menet, V., Giménez Y Ribotta, M., Sandillon, F. & Privat, A. GFAP null astrocytes are a favorable substrate for neuronal survival and neurite growth. *Glia* **31,** 267–72 (2000).

128. Merz, K., Herold, S. & Lie, D. C. CREB in adult neurogenesis--master and partner in the development of adult-born neurons? *Eur. J. Neurosci.* **33,** 1078–86 (2011).

129. Meyer-Franke, A., Wilkinson, G. A., Kruttgen, A., Hu, M., Munro, E., Hanson, M. G., Reichardt, L. F. & Barres, B. A. Depolarization and cAMP elevation rapidly recruit TrkB to the plasma membrane of CNS neurons. *Neuron* **21,** 681–93 (1998).

130. Miles, G. B., Yohn, D. C., Wichterle, H., Jessell, T. M., Rafuse, V. F. & Brownstone, R. M. Functional properties of motoneurons derived from mouse embryonic stem cells. *J. Neurosci.* **24,** 7848–58 (2004).

131. Mochida, S., Yokoyama, C. T., Kim, D. K., Itoh, K. & Catterall, W. A. Evidence for a voltage-dependent enhancement of neurotransmitter release mediated via the synaptic protein interaction site of N-type Ca2+ channels. *Proc. Natl. Acad. Sci.* **95,** 14523–14528 (1998).

132. Mori, H., Masaki, H., Yamakura, T. & Mishina, M. Identification by mutagenesis of a Mg(2+)-block site of the NMDA receptor channel. *Nature* **358,** 673–5 (1992).

133. Muroyama, Y., Fujiwara, Y., Orkin, S. H. & Rowitch, D. H. Specification of astrocytes by bHLH protein SCL in a restricted region of the neural tube. *Nature* **438,** 360–3 (2005).

134. Murry, C. E. & Keller, G. Differentiation of Embryonic Stem Cells to Clinically Relevant Populations: Lessons from Embryonic Development. *Cell* **132,** 661–680 (2008).

135. Nakagawa, S., Kim, J.-E., Lee, R., Chen, J., Fujioka, T., Malberg, J., Tsuji, S. & Duman, R. S. Localization of Phosphorylated cAMP Response Element-Binding Protein in Immature Neurons of Adult Hippocampus. *J. Neurosci.* **22,** 9868–9876 (2002).

136. Nakashima, K., Yanagisawa, M., Arakawa, H. & Taga, T. Astrocyte differentiation mediated by LIF in cooperation with BMP2. *FEBS Lett.* **457,** 43–46 (1999).

137. Namihira, M. & Nakashima, K. Mechanisms of astrocytogenesis in the mammalian brain. *Curr. Opin. Neurobiol.* **23,** 921–7 (2013).

138. Nelson, B. R., Hartman, B. H., Georgi, S. A., Lan, M. S. & Reh, T. A. Transient inactivation of Notch signaling synchronizes differentiation of neural progenitor cells. *Dev. Biol.* **304,** 479–498 (2007).

139. Nguyen, H. N., Byers, B., Cord, B., Shcheglovitov, A., Byrne, J., Gujar, P., Kee, K., Schüle, B., Dolmetsch, R. E., Langston, W., Palmer, T. D. & Pera, R. R. LRRK2 mutant iPSC-derived DA neurons demonstrate increased susceptibility to oxidative stress. *Cell Stem Cell* **8,** 267–80 (2011).

140. Nicol, X., Muzerelle, A., Bachy, I., Ravary, A. & Gaspar, P. Spatiotemporal localization of the calcium-stimulated adenylate cyclases, AC1 and AC8, during mouse brain development. *J. Comp. Neurol.* **486,** 281–94 (2005).

141. Nishi, A., Snyder, G. L. & Greengard, P. Bidirectional regulation of DARPP-32 phosphorylation by dopamine. *J. Neurosci.* **17,** 8147–55 (1997).

142. Nishida, H. & Okabe, S. Direct astrocytic contacts regulate local maturation of dendritic spines. *J. Neurosci.* **27,** 331–40 (2007).

143. Niswender, C. M. & Conn, P. J. Metabotropic glutamate receptors: physiology, pharmacology, and disease. *Annu. Rev. Pharmacol. Toxicol.* **50,** 295–322 (2010).

144. Nonaka, M. A Janus-like role of CREB protein: enhancement of synaptic property in mature neurons and suppression of synaptogenesis and reduced network synchrony in early development. *J. Neurosci.* **29,** 6389–91 (2009).

145. Ohnuma, S. & Harris, W. A. Neurogenesis and the Cell Cycle. *Neuron* **40,** 199–208 (2003).

146. Okamoto, A., Pouladi, M. a, Talantova, M., Yao, D., Xia, P., Ehrnhoefer, D. E., Zaidi, R., Clemente, A., Kaul, M., Graham, R. K., Zhang, D., Vincent Chen, H.-S., Tong, G., Hayden, M. R. & Lipton, S. a. Balance between synaptic versus extrasynaptic NMDA receptor activity influences inclusions and neurotoxicity of mutant huntingtin. *Nat. Med.* **15,** 1407–13 (2009).

147. Orrenius, S., Zhivotovsky, B. & Nicotera, P. Regulation of cell death: the calcium-apoptosis link. *Nat. Rev. Mol. Cell Biol.* **4,** 552–65 (2003).

148. Parajuli, L. K., Nakajima, C., Kulik, A., Matsui, K., Schneider, T., Shigemoto, R. & Fukazawa, Y. Quantitative regional and ultrastructural localization of the Ca(v)2.3 subunit of R-type calcium channel in mouse brain. *J. Neurosci.* **32,** 13555–67 (2012).

149. Patapoutian, A. & Reichardt, L. F. Trk receptors: mediators of neurotrophin action. *Curr. Opin. Neurobiol.* **11,** 272–280 (2001).

150. Patapoutian, A. & Reichardt, L. F. Roles of Wnt proteins in neural development and maintenance. *Curr. Opin. Neurobiol.* **10,** 392–9 (2000).

151. Peltier, J., O'Neill, A. & Schaffer, D. V. PI3K/Akt and CREB regulate adult neural hippocampal progenitor proliferation and differentiation. *Dev. Neurobiol.* **67,** 1348–61 (2007).

152. Perez-Reyes, E. Molecular physiology of low-voltage-activated t-type calcium channels. *Physiol. Rev.* **83,** 117–61 (2003).

153. Perez-Reyes, E., Cribbs, L. L., Daud, A., Lacerda, A. E., Barclay, J., Williamson, M. P., Fox, M., Rees, M. & Lee, J. H. Molecular characterization of a neuronal low-voltage-activated T-type calcium channel. *Nature* **391,** 896–900 (1998).

154. Pfrieger, F. W. Synaptic Efficacy Enhanced by Glial Cells in Vitro. *Science (80-.).* **277,** 1684–1687 (1997).

155. Platel, J.-C., Dave, K. A., Gordon, V., Lacar, B., Rubio, M. E. & Bordey, A. NMDA receptors activated by subventricular zone astrocytic glutamate are critical for neuroblast survival prior to entering a synaptic network. *Neuron* **65,** 859–72 (2010).

156. Polo, J. M., Liu, S., Figueroa, M. E., Kulalert, W., Eminli, S., Tan, K. Y., Apostolou, E., Stadtfeld, M., Li, Y., Shioda, T., Natesan, S., Wagers, A. J., Melnick, A., Evans, T. & Hochedlinger, K. Cell type of origin influences the molecular and functional properties of mouse induced pluripotent stem cells. *Nat. Biotechnol.* **28,** 848–55 (2010).

157. Poncer, J. C., McKinney, R. A., Gähwiler, B. H. & Thompson, S. M. Either N- or P-type calcium channels mediate GABA release at distinct hippocampal inhibitory synapses. *Neuron* **18,** 463–72 (1997).

158. Poncer, J. C., McKinney, R. A., Gähwiler, B. H. & Thompson, S. M. Either N- or P-type calcium channels mediate GABA release at distinct hippocampal inhibitory synapses. *Neuron* **18,** 463–72 (1997).

159. Poser, S., Impey, S., Xia, Z. & Storm, D. R. Brain-derived neurotrophic factor protection of cortical neurons from serum withdrawal-induced apoptosis is inhibited by cAMP. *J. Neurosci.* **23,** 4420–7 (2003).

160. Poser, S., Impey, S., Xia, Z. & Storm, D. R. Brain-derived neurotrophic factor protection of cortical neurons from serum withdrawal-induced apoptosis is inhibited by cAMP. *J. Neurosci.* **23,** 4420–7 (2003).

161. Puri, M. C. & Nagy, A. Concise review: Embryonic stem cells versus induced pluripotent stem cells: the game is on. *Stem Cells* **30,** 10–4 (2012).

162. Ransom, B., Behar, T. & Nedergaard, M. New roles for astrocytes (stars at last). *Trends Neurosci.* **26,** 520–2 (2003).

163. Rigamonti, D., Sipione, S., Goffredo, D., Zuccato, C., Fossale, E. & Cattaneo, E. Huntingtin's neuroprotective activity occurs via inhibition of procaspase-9 processing. *J. Biol. Chem.* **276,** 14545–8 (2001).

164. Rosen, L. B., Ginty, D. D., Weber, M. J. & Greenberg, M. E. Membrane depolarization and calcium influx stimulate MEK and MAP kinase via activation of Ras. *Neuron* **12,** 1207–1221 (1994).

165. Rowitch, D. H. & Kriegstein, A. R. Developmental genetics of vertebrate glial-cell specification. *Nature* **468,** 214–22 (2010).

166. Rubinsztein, D. C. & Carmichael, J. Huntington's disease: molecular basis of neurodegeneration. *Expert Rev. Mol. Med.* **5,** 1–21 (2004).

167. Rush, A. M., Dib-Hajj, S. D. & Waxman, S. G. Electrophysiological properties of two axonal sodium channels, Nav1.2 and Nav1.6, expressed in mouse spinal sensory neurones. *J. Physiol.* **564,** 803–15 (2005).

168. Saneyoshi, T., Wayman, G., Fortin, D., Davare, M., Hoshi, N., Nozaki, N., Natsume, T. & Soderling, T. R. Activity-dependent synaptogenesis: regulation by a CaM-kinase kinase/CaM-kinase I/betaPIX signaling complex. *Neuron* **57,** 94–107 (2008).

169. Santello, M. & Volterra, a. Synaptic modulation by astrocytes via Ca2+-dependent glutamate release. *Neuroscience* **158,** 253–9 (2009).

170. Sassone-Corsi, P. Coupling gene expression to cAMP signalling: role of CREB and CREM. *Int. J. Biochem. Cell Biol.* **30,** 27–38 (1998).

171. Sattler, R., Xiong, Z., Lu, W.-Y., MacDonald, J. F. & Tymianski, M. Distinct Roles of Synaptic and Extrasynaptic NMDA Receptors in Excitotoxicity. *J. Neurosci.* **20,** 22–33 (2000).

172. Schröder-Lang, S., Schwärzel, M., Seifert, R., Strünker, T., Kateriya, S., Looser, J., Watanabe, M., Kaupp, U. B., Hegemann, P. & Nagel, G. Fast manipulation of cellular cAMP level by light in vivo. *Nat. Methods* **4,** 39–42 (2007).

173. Seibler, P., Graziotto, J., Jeong, H., Simunovic, F., Klein, C. & Krainc, D. Mitochondrial Parkin recruitment is impaired in neurons derived from mutant PINK1 induced pluripotent stem cells. *J. Neurosci.* **31,** 5970–6 (2011).

174. Seil, F. J. & Drake-Baumann, R. TrkB Receptor Ligands Promote Activity-Dependent Inhibitory Synaptogenesis. *J. Neurosci.* **20,** 5367–5373 (2000).

175. Seil, F. J. & Drake-Baumann, R. Reduced cortical inhibitory synaptogenesis in organotypic cerebellar cultures developing in the absence of neuronal activity. *J. Comp. Neurol.* **342,** 366–77 (1994).

176. Shen, W., Hamilton, S. E., Nathanson, N. M. & Surmeier, D. J. Cholinergic suppression of KCNQ channel currents enhances excitability of striatal medium spiny neurons. *J. Neurosci.* **25,** 7449–58 (2005).

177. Sheng, M., Thompson, M. & Greenberg, M. CREB: a Ca(2+)-regulated transcription factor phosphorylated by calmodulin-dependent kinases. *Science (80-.).* **252,** 1427–1430 (1991).

178. Sheng, Z.-H., Rettig, J., Takahashi, M. & Catterall, W. A. Identification of a syntaxin-binding site on N-Type calcium channels. *Neuron* **13,** 1303–1313 (1994).

179. Shigemoto, R., Kinoshita, A., Wada, E., Nomura, S., Ohishi, H., Takada, M., Flor, P. J., Neki, A., Abe, T., Nakanishi, S. & Mizuno, N. Differential Presynaptic Localization of Metabotropic Glutamate Receptor Subtypes in the Rat Hippocampus. *J. Neurosci.* **17,** 7503–7522 (1997).

180. Singh, S. K., Wilczynska, K. M., Grzybowski, A., Yester, J., Osrah, B., Bryan, L., Wright, S., Griswold-Prenner, I. & Kordula, T. The unique transcriptional activation domain of nuclear factor-I-X3 is critical to specifically induce marker gene expression in astrocytes. *J. Biol. Chem.* **286,** 7315–26 (2011).

181. Sladeczek, F., Momiyama, A. & Takahashi, T. Presynaptic inhibitory action of a metabotropic glutamate receptor agonist on excitatory transmission in visual cortical neurons. *Proc. Biol. Sci.* **253,** 297–303 (1993).

182. Stipursky, J., Romão, L., Tortelli, V., Neto, V. M. & Gomes, F. C. A. Neuron-glia signaling: Implications for astrocyte differentiation and synapse formation. *Life Sci.* **89,** 524–31 (2011).

183. Stuart, G. J. & Häusser, M. Dendritic coincidence detection of EPSPs and action potentials. *Nat. Neurosci.* **4,** 63–71 (2001).

184. Sunahara, R. K. & Taussig, R. Isoforms of mammalian adenylyl cyclase: multiplicities of signaling. *Mol. Interv.* **2,** 168–84 (2002).

185. Sweatt, J. D. Toward a Molecular Explanation for Long-Term Potentiation. *Learn. Mem.* **6,** 399–416 (1999).

186. Szebenyi, G., Morfini, G. A., Babcock, A., Gould, M., Selkoe, K., Stenoien, D. L., Young, M., Faber, P. W., MacDonald, M. E., McPhaul, M. J. & Brady, S. T. Neuropathogenic forms of huntingtin and androgen receptor inhibit fast axonal transport. *Neuron* **40,** 41–52 (2003).

187. Szydlowski, S. N., Pollak Dorocic, I., Planert, H., Carlén, M., Meletis, K. & Silberberg, G. Target selectivity of feedforward inhibition by striatal fast-spiking interneurons. *J. Neurosci.* **33,** 1678–83 (2013).

188. Tachibana, M., Amato, P., Sparman, M., Gutierrez, N. M., Tippner-Hedges, R., Ma, H., Kang, E., Fulati, A., Lee, H.-S., Sritanaudomchai, H., Masterson, K., Larson, J., Eaton, D., Sadler-Fredd, K., Battaglia, D., Lee, D., Wu, D., Jensen, J., Patton, P., Gokhale, S., Stouffer, R. L., Wolf, D. & Mitalipov, S. Human embryonic stem cells derived by somatic cell nuclear transfer. *Cell* **153,** 1228–38 (2013).

189. Takahashi, K., Tanabe, K., Ohnuki, M., Narita, M., Ichisaka, T., Tomoda, K. & Yamanaka, S. Induction of pluripotent stem cells from adult human fibroblasts by defined factors. *Cell* **131,** 861–72 (2007).

190. Takazawa, T., Croft, G. F., Amoroso, M. W., Studer, L., Wichterle, H. & Macdermott, A. B. Maturation of spinal motor neurons derived from human embryonic stem cells. *PLoS One* **7,** e40154 (2012).

191. Tao, X., Finkbeiner, S., Arnold, D. B., Shaywitz, A. J. & Greenberg, M. E. Ca2+ Influx Regulates BDNF Transcription by a CREB Family Transcription Factor-Dependent Mechanism. *Neuron* **20,** 709–726 (1998).

192. Tashiro, A., Sandler, V. M., Toni, N., Zhao, C. & Gage, F. H. NMDA-receptor-mediated, cell-specific integration of new neurons in adult dentate gyrus. *Nature* **442,** 929–33 (2006).

193. Tepper, J. M., Koós, T. & Wilson, C. J. GABAergic microcircuits in the neostriatum. *Trends Neurosci.* **27,** 662–9 (2004).

194. Tobey, R. A. Effects of Cytosine Arabinoside, Daunomycin, Mithramycin, Azacytidine, Adriamycin, and Camptothecin on Mammalian Cell Cycle Traverse. *Cancer Res.* **32,** 2720–2725 (1972).

195. Tojima, T., Kobayashi, S. & Ito, E. Dual role of cyclic AMP-dependent protein kinase in neuritogenesis and synaptogenesis during neuronal differentiation. *J. Neurosci. Res.* **74,** 829–37 (2003).

196. Toyoda, H., Yamada, J., Ueno, S., Okabe, A., Kato, H., Sato, K., Hashimoto, K. & Fukuda, A. Differential functional expression of cation-Cl- cotransporter mRNAs (KCC1, KCC2, and NKCC1) in rat trigeminal nervous system. *Brain Res. Mol. Brain Res.* **133,** 12–8 (2005).

197. Tozuka, Y., Fukuda, S., Namba, T., Seki, T. & Hisatsune, T. GABAergic excitation promotes neuronal differentiation in adult hippocampal progenitor cells. *Neuron* **47,** 803–15 (2005).

198. Trendelenburg, G. & Dirnagl, U. Neuroprotective role of astrocytes in cerebral ischemia: focus on ischemic preconditioning. *Glia* **50,** 307–20 (2005).

199. Tu, H., Rondard, P., Xu, C., Bertaso, F., Cao, F., Zhang, X., Pin, J.-P. & Liu, J. Dominant role of GABAB2 and Gbetagamma for GABAB receptor-mediated-ERK1/2/CREB pathway in cerebellar neurons. *Cell. Signal.* **19,** 1996–2002 (2007).

200. Ullian, E. M., Christopherson, K. S. & Barres, B. A. Role for glia in synaptogenesis. *Glia* **47,** 209–16 (2004).

201. Ullian, E. M., Sapperstein, S. K., Christopherson, K. S. & Barres, B. A. Control of synapse number by glia. *Science* **291,** 657–61 (2001).

202. Vigers, A. J. & Pfenninger, K. H. N-type and L-type calcium channels are present in nerve growth cones. Numbers increase on synaptogenesis. *Brain Res. Dev. Brain Res.* **60,** 197–203 (1991).

203. Volterra, A. & Meldolesi, J. Astrocytes, from brain glue to communication elements: the revolution continues. *Nat. Rev. Neurosci.* **6,** 626–40 (2005).

204. Walaas, S. I. & Greengard, P. DARPP-32, a dopamine- and adenosine 3':5'-monophosphate-regulated phosphoprotein enriched in dopamine-innervated brain regions. I. Regional and cellular distribution in the rat brain. *J. Neurosci.* **4,** 84–98 (1984).

205. Wang, D. D., Krueger, D. D. & Bordey, A. GABA depolarizes neuronal progenitors of the postnatal subventricular zone via GABAA receptor activation. *J. Physiol.* **550,** 785–800 (2003).

206. Wassef, M., Berod, A. & Sotelo, C. Dopaminergic dendrites in the pars reticulata of the rat substantia nigra and their striatal input. combined immunocytochemical localization of tyrosine hydroxylase and anterograde degeneration. *Neuroscience* **6,** 2125–2139 (1981).

207. Wheeler, D., Randall, A. & Tsien, R. Roles of N-type and Q-type Ca2+ channels in supporting hippocampal synaptic transmission. *Science (80-.).* **264,** 107–111 (1994).

208. Wickens, J. R. & Wilson, C. J. Regulation of Action-Potential Firing in Spiny Neurons of the Rat Neostriatum In Vivo. *J Neurophysiol* **79,** 2358–2364 (1998).

209. Wickens, J. R. & Wilson, C. J. Regulation of action-potential firing in spiny neurons of the rat neostriatum in vivo. *J. Neurophysiol.* **79,** 2358–64 (1998).

210. Wollmuth, L. P., Kuner, T. & Sakmann, B. Adjacent asparagines in the NR2-subunit of the NMDA receptor channel control the voltage-dependent block by extracellular Mg2+. *J. Physiol.* **506,** 13–32 (1998).

211. Yasuda, R., Sabatini, B. L. & Svoboda, K. Plasticity of calcium channels in dendritic spines. *Nat. Neurosci.* **6,** 948–55 (2003).

212. Zeron, M. M., Fernandes, H. B., Krebs, C., Shehadeh, J., Wellington, C. L., Leavitt, B. R., Baimbridge, K. G., Hayden, M. R. & Raymond, L. A. Potentiation of NMDA receptor-mediated

excitotoxicity linked with intrinsic apoptotic pathway in YAC transgenic mouse model of Huntington's disease. *Mol. Cell. Neurosci.* **25,** 469–79 (2004).

213. Zeron, M. M., Hansson, O., Chen, N., Wellington, C. L., Leavitt, B. R., Brundin, P., Hayden, M. R. & Raymond, L. A. Increased Sensitivity to N-Methyl-D-Aspartate Receptor-Mediated Excitotoxicity in a Mouse Model of Huntington's Disease. *Neuron* **33,** 849–860 (2002).

214. Zhang, S. C., Wernig, M., Duncan, I. D., Brüstle, O. & Thomson, J. A. In vitro differentiation of transplantable neural precursors from human embryonic stem cells. *Nat. Biotechnol.* **19,** 1129–33 (2001).

215. Zhou, X., Hollern, D., Liao, J., Andrechek, E. & Wang, H. NMDA receptor-mediated excitotoxicity depends on the coactivation of synaptic and extrasynaptic receptors. *Cell Death Dis.* **4,** e560 (2013).

216. Zimmermann, D., Zhou, A., Kiesel, M., Feldbauer, K., Terpitz, U., Haase, W., Schneider-Hohendorf, T., Bamberg, E. & Sukhorukov, V. L. Effects on capacitance by overexpression of membrane proteins. *Biochem. Biophys. Res. Commun.* **369,** 1022–1026 (2008).

217. Zuccato, C., Valenza, M. & Cattaneo, E. Molecular Mechanisms and Potential Therapeutical Targets in Huntington ' s Disease. *Reporter* 905–981 (2010). doi:10.1152/physrev.00041.2009.

218. Induced pluripotent stem cells from patients with Huntington's disease show CAG-repeat-expansion-associated phenotypes. *Cell Stem Cell* **11,** 264–78 (2012).